UNIVERSITY OF COPENHAGEN
FACULTY OF SCIENCE
PHD SCHOOL OF SCIENCE

KØBENHAVNS
UNIVERSITET

KU LEUVEN
FACULTY OF SCIENCE
ARENBERG DOCTORAL SCHOOL

KU LEUVEN

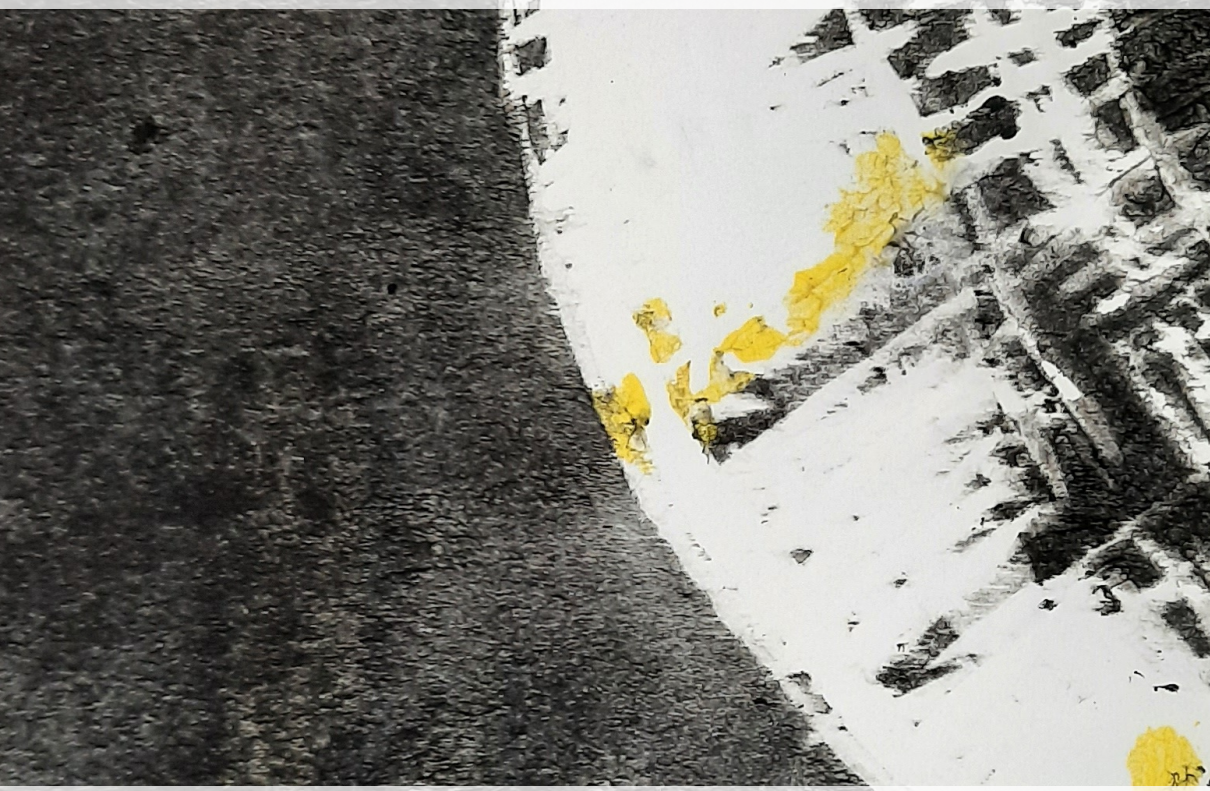

PhD Thesis

Bridging Atmospheres and Interiors: Exploring Exoplanetary Gas Giants

Advancing Theoretical Models for Future Observations

Aaron David Schneider
Advisor: Uffe Gråe Jørgensen, Leen Decin, Ludmila Carone

Submitted: February 11, 2024

Bridging Atmospheres and Interiors: Exploring Exoplanetary Gas Giants

Advancing Theoretical Models for Future Observations

Aaron David Schneider

PhD thesis
Submitted: February 11, 2024

This PhD thesis has been submitted to the Arenberg Doctoral School, KU Leuven, in partial fulfillment of the requirements for the degree of Doctor of Science (PhD): Astronomy and Astrophysics.
This PhD thesis has been submitted to the PhD school of The Faculty of Science, University of Copenhagen, Denmark.

Examination Committee:
Chair: Prof. dr. Troels Haugbølle (University of Copenhagen)
Supervisor: Prof. dr. Uffe Gråe Jørgensen (University of Copenhagen)
Supervisor: Prof. dr. Leen Decin (KU Leuven)
Supervisor: Dr. Ludmila Carone (Österreichische Akademie der Wissenschaften)
Co-Supervisor: Prof. dr. Anja Andersen (University of Copenhagen)
Co-Supervisor: Prof. dr. Jon Sundqvist (KU Leuven)
Assessor: Dr. David Gobrecht (Gothenburg University)
Referee: Dr. Joanna Barstow (The Open University)
Referee: Prof. dr. Denis Defrère (KU Leuven)

Funding acknowledgement: Aaron Schneider is part of the CHAMELEON MC ITN EJD which received funding from the European Union's Horizon 2020 research and innovation programme under the Marie Sklodowska-Curie grant agreement no. 860470.

Cover art by Joachim Riehle

Für meine Familie.

ACKNOWLEDGEMENTS

First and foremost, I would like to thank God for providing health and mind, as well as the beauty and mystery of creation to discover.

I would like to mention special thanks to Ludmila Carone, who was my primary supervisor and has always been very friendly, knowledgeable, cooperative and helpful. Our weekly meetings provided a solid foundation to my work and were an important basis of my research planning. I would also like to thank Bertram Bitsch for continuing to work with me, even after my master thesis was finished, and for exposing `chemcomp` to so many of his students. Furthermore, I would like to thank Leen Decin for her valuable ideas and comments on my papers and for the good discussions on radiative transfer that helped a lot with my understanding of the physics. I want to express my gratitude to Uffe Gråe Jørgensen, who continuously trusted in my capabilities more than I could and who always had an open door, when I needed someone to talk to about my research or bureaucratic issues. Furthermore, I would like to thank Paul Mollière for his help with `petitRADTRANS` and for all the nice and technical meetings we had. I would like to acknowledge the contributions of ChatGPT and the language editors of A&A in providing language editing assistance during the preparation of this thesis and its chapters. I would also like to thank Mathijs Vanrespaille and Nanna Bach-Møller for translating my abstract.

Finally, I would like to thank my family for supporting me along the way. I would like to thank my mother for sparking my interest in physics and my father for always being proud of me. I would like to thank my parents in law for welcoming me into their family and my father-in-law for providing the cover art. I would like to put special thanks to my wife Helen for continuously supporting me during these three years. If I hadn't known that you would enjoy living abroad together with me, I would not have been writing this thesis. Last, but certainly not least, I would like to thank my son Immanuel for teaching me that there are more important things in life than a thesis.

ABSTRACT

With advancing observations of exoplanets, there is a pressing need for models that can explain observation trends. Detailed spectra of exoplanetary atmospheres reveal their chemical composition, while radius and mass measurements provide information about the planet's bulk composition. The composition of planets is strongly influenced by their formation process, making it useful to compare theories of planet formation with present-day observations. Hot Jupiters, gas giant planets located close to their star, always face the star with the same side. Due to their proximity and asymmetric illumination, hot Jupiters experience strong winds that shape their climate. Additionally, many of these hot Jupiters have lower densities compared to the gas giants in our solar system, suggesting an unknown mechanism that inflates these planets. Previous studies have proposed that atmospheric dynamics could deposit a fraction of the stellar irradiation deep enough in the atmosphere to cause these planets to exhibit these inflated radii.

We used planet formation models to investigate how pebble drift in protoplanetary disks affects the composition of planets that form in these disks. Using these models, we discovered that the composition of atmospheres of gas giant planets can be significantly influenced by the evaporation of pebbles in the disk. Pebbles drifting inward cross evaporation lines, causing parts of their composition to evaporate. This leads to the pollution of the gas phase of the disk with heavy elements and the enrichment of forming planet with volatile species like H_2O and CO_2. These insights from pebble evaporation are important for putting the carbon to oxygen ratio and possibly the volatile to refractory ratio in the atmosphere of exoplanets into the correct formation context. However, only the uppermost 1% of the planetary radius are accessible via detailed observations, whereas understanding planet formation requires an understanding of the planetary bulk composition. Thus, a better connection between the observable atmosphere and the deeper layers is a pressing need.

We then coupled an efficient radiative transfer solver to a 3D climate model, to study the link between the deeper atmospheric layers and the radiative upper atmosphere. A long-term study showed that we can indeed realize a first link between the observable atmosphere and deeper layers for the example of WASP-76b . We find that it is possible to transport energy from the irradiated photosphere downwards, potentially explaining inflated radius.

However, since this process of energy disposition is very slow, temperature convergence in deep atmospheric layers is out of reach for climate models of hot Jupiters. Future atmospheric models of hot Jupiters should thus base their initial temperature profile in the deep layers on reasonable interior structure model estimates. With a tighter link to the interior, detailed spectra from James Webb Space Telescope (JWST), will hopefully provide a window into the formation of these planets.

RESUMÉ

Med fremadskridende observationer af exoplaneter er der et presserende behov for modeller, der kan forklare de tendenser vi observerer. Detaljerede spektre af exoplanetatmosfærer afslører deres kemiske sammensætning, mens radius- og massemålinger giver information om planetens hovedsammensætning. Sammensætningen af planeter er stærkt påvirket af deres dannelsesproces, hvilket gør det nyttigt at sammenligne teorier om planetdannelse med nutidens observationer. Hot Jupiters, gas planeter i et tæt kredsløb om deres stjerne, har altid samme side vendt mod stjernen. Grundet deres nærhed til stjernen og asymmetrien i deres bestråling oplever Hot Jupiters stærke vinde, der påvirker deres klima.

Derudover har mange af disse Hot Jupiters lavere densiteter sammenlignet med gasgiganterne i vores solsystem, hvilket tyder på, at en ukendt mekanisme får disse planeter til at udvide sig. Tidligere studier har foreslået, at atmosfæredynamik vil kunne afsætte en del af energien fra stjernes bestrålingen dybt nok i atmosfæren til at få disse planeter til at udvide sig til de observerede oppustede radier.

Vi benyttede modeller for planetdannelse til at undersøge, hvordan småstensdrift i protoplanetariske diske påvirker sammensætningen af planeterne, der dannes i disse diske. Ved hjælp af vores modeller opdagede vi, at sammensætningen af gasplaneters atmosfærer kan påvirkes betydeligt af fordampningen af småsten i disken. Småsten, der driver indad i disken, vil krydser fordampningslinjer, hvilket får dele af deres sammensætning til at fordampe. Dette fører til en forøgelse af tunge grundstoffer til diskens gasfase og vil forårsage, at planeter dannet i disken vil være beriget med volatile arter som H_2O og CO_2.

Denne forøgede indsigt i fordampning af småsten er vigtig for at forstå sammenhængen mellem processerne for planetdannelse og de resulterende forhold mellem karbon og oxygen og muligvis også forholdet mellem volatile og refraktære arter i exoplanetatmosfærer. Imidlertid er kun den øverste 1% af planetens radius, der kan observeres i detaljer, mens det er nødvendigt at have en dybdegående viden om hele planets sammensætning for at forstå dens dannelsesproces. Der er derfor et stort behov for en bedre forståelse af sammenhængen mellem den observerbare atmosfære og planetens dybere lag.

Derefter koblede vi en effektiv radiative transfer solver til en 3D klimamodel for at studere sammenhængen mellem de dybere lag af atmosfæren og den

strålingsdominerede øvre atmosfære. En længerevarende undersøgelse viste os en første sammenhæng mellem den observerbare atmosfære og dybere lag ved at bruge WASP-76 b som eksempel. Vi finder, at det er muligt at transportere energi nedad fra den bestrålede fotosfære, hvilket potentielt kan forklare den oppustede radius. Men da denne proces med energideponering er meget langsom, kan temperaturkonvergensen i de dybe atmosfæriske lag ikke reproduceres med klimamodeller af Hot Jupiters. Fremtidige atmosfæremodeller af Hot Jupiters bør derfor basere deres indledende temperaturprofil i de dybe lag på pålidelige estimater fra modeller over indre strukturer. Med et tættere link til planeternes indre, kan detaljerede spektre fra James Webb Space Telescope (JWST) forhåbentlig give en bedre indsigt i dannelsen af disse planeter.

BEKNOPTE SAMENVATTING

Er is een dringende nood aan modellen om de steeds meer geavanceerde observaties van exoplaneten te verklaren. Gedetailleerde spectra van exoplaneetatmosferen onthullen hun chemische samenstelling terwijl metingen van de straal en massa aanwijzingen over de compositie van de gehele planeet bieden. De samenstelling van planeten is sterk beïnvloed door hun vormingsproces, wat het de moeite waard maakt om theorieën van planeetvorming met moderne observaties te testen. Hete Jupiters, gasreuzen in een baan dichtbij hun moederster, tonen altijd dezelfde kant aan de ster. Als gevolg worden ze erg krachtig en ongelijk bestraald, wat leidt tot sterke winden die hun klimaat vorm geven. Bovendien hebben hete Jupiters een lagere massadichtheid dan de gasreuzen in ons zonnestelsel, wat suggereert dat een momenteel onbekend proces de planeten doet uitzetten. Eerdere onderzoeken stelden voor dat atmosfeerdynamieken een deel van de sterrenstraling omlaag dragen en zodoende deze planeten opblaast.

We gebruikten modellen van planeetvorming om te onderzoeken hoe kiezeldrift in protoplanetaire schijven de samenstelling van de daarin vormende planeten die aantast. Met deze modellen ontdekten we dat de compositie van atmosferen van gasreuzen significant beïnvloed wordt door de verdamping van de kiezels. Bij het inwaarts afdrijven steken de kiezels verdampingslijnen over, waardoor delen van hun compositie verdampen. Dit vervuilt de gassen in de schijf met zware elementen en verrijkt zodoende vormende planeten met vluchtige stoffen zoals H_2O en CO_2. Dit inzicht op kiezelverdamping is van belang om de verhouding van koolstof tot zuurstof en mogelijks ook van vluchtige tot refractaire stoffen in de atmosfeer correct te interpreteren. Helaas is enkel de bovenste 1% van de straal van de planeet is beschikbaar voor gedetailleerde observaties, terwijl we om de planeetvorming te begrijpen de volledige planeetcompositie dienen te kennen. Daarom is er een dringende nood om het verband tussen de observeerbare atmosfeer en de diepe, verborgen lagen te vatten.

We verbonden een efficiënte stralingstransportcode aan een 3D klimaatmodel om de link tussen de diepe atmosfeerlagen en de radiatieve buitenlagen te onderzoeken. Een langdurige studie toonde dat we inderdaad een eerste verband tussen de observeerbare atmosfeer en de diepe lagen in bijvoorbeeld WASP-76b opmerken. We merken dat het mogelijk is om energie van de bestraalde fotosfeer neerwaarts te transporteren, wat mogelijks de opgeblazen

straal verklaart. Het proces van energie deponeren is echter zeer traag, dus temperatuursconvergentie in de diepste lagen van de atmosfeer ligt buiten het bereik van klimaatmodellen van hete Jupiters. Toekomstige atmosfeermodellen dienen dus hun initieel temperatuursprofiel in de diepe lagen te baseren op redelijke schattingen van structuurmodellen. Samen met de nauwere link tot het interieur zullen gedetailleerde spectra van de James Webb Space Telescope (JWST) hopelijk een venster op planeetvorming bieden.

PUBLICATIONS

Bitsch, B., **Schneider, A. D.**, & Kreidberg, L. 2022, A&A, 665, A138

Sainsbury-Martinez, F., Tremblin, P., **Schneider, A. D.**, et al. 2023, MNRAS, 524, 1316

Schneider, A. D. & Bitsch, B. 2021a, A&A, 654, A71

Schneider, A. D. & Bitsch, B. 2021b, A&A, 654, A72

Schneider, A. D., Carone, L., Decin, L., Jørgensen, U. G., & Helling, C. 2022a, A&A, 666, L11

Schneider, A. D., Carone, L., Decin, L., et al. 2022b, A&A, 664, A56

OTHER PUBLICATIONS (NOT PART OF THIS THESIS)

Baeyens, R., Désert, J.-M., Petrignani, A., Carone, L., & **Schneider, A. D.** 2023, arXiv e-prints, arXiv:2309.00573

Bitsch, B., Raymond, S. N., Buchhave, L. A., **et al.** 2021, A&A, 649, L5

Carone, L., Lewis, D. A., Samra, D., **Schneider, A. D.**, & Helling, C. 2023, arXiv e-prints, arXiv:2301.08492

Mollière, P., Molyarova, T., Bitsch, B., **et al.** 2022, ApJ, 934, 74

Samra, D., Helling, C., Chubb, K. L., **et al.** 2023, A&A, 669, A142

Schneider, A. D., Dullemond, C. P., & Bitsch, B. 2018, A&A, 617, L7

Schneider, A. D., Mollière, P., Louppe, G., et al. 2024, A&A, 682, A79

ABBREVIATIONS

ALI approximate Lambda iteration

CFL Courant-Friedrich-Lewy

CIA collision induced absorption

GCM General Circulation Model

HPC high performance computer

HPE hydrostatic primitive equations

HST Hubble Space Telescope

JWST James Webb Space Telescope

LTE local thermodynamic equilibrium

RCB radiative convective boundary

RE radiative equilibrium

RT radiative transfer

TOA the top of the atmosphere

UHJ ultra-hot Jupiter

CONTENTS

1

INTRODUCTION

1.1 OBSERVING EXOPLANTES

The existence of planets outside our solar system (extra solar planets or exoplanets) has long been a subject of speculation. In 1952, Struve (1952) proposed that these objects could be observed indirectly by measuring variations in the radial velocity of planet-hosting stars, caused by the Doppler effect. He also suggested that planets passing between the observer and their host star would occult some fraction of the stellar light, resulting in the dimming of the star. These two methods have emerged as the most promising approaches to detect and characterize exoplanets. However, it was not until 1992 that the first exoplanet was actually detected (Wolszczan & Frail, 1992). This planetary system, unlike those in our own solar system, was found around a pulsar star. Shortly after, in 1995, 51 Pegasi b became the first planet detected around a sun-like star (Mayor & Queloz, 1995). 51 Pegasi b is unlike any other planet in our solar system. With a mass of roughly half the mass of Jupiter, 51 Pegasi b falls in the category of gas giant planets. However, with an orbit closer to its host star than Mercury to the sun, 51 Pegasi b established a new category of planets, called hot Jupiters, whose existence was a big challenge for theories of planet formation at that time.

1.1.1 *Observational methods*

Exoplanets are small and dim compared to their host stars, making it difficult to directly image them (see Currie et al., 2023, for a recent review on direct imaging). It is therefore currently only possible to image young and hot objects with leftover heat from their formation. Promising results have been achieved, such as the studies by Müller et al. (2018) and Keppler et al. (2018), who were the first to image an exoplanet while it is forming in a protoplanetary disk. Thus, since direct measurements of exoplanets are difficult, mostly indirect

methods are nowadays used to observe exoplanets. As originally argued by Struve (1952), the transit method as well as the spectroscopic radial velocity method are currently the most reliable methods to characterize exoplanets in terms of mass, radius, and orbital separation. State-of-the-art telescopes such as the JWST are revealing fascinating details about transiting exoplanet (e.g., JWST Transiting Exoplanet Community Early Release Science Team et al., 2023). But how do these methods work? We will now give some basic introduction into how planets can be observed using these two methods.

Doppler method

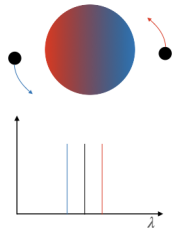

The solution of the two body problem of one planet and one star is given by both planet and star orbiting around a common center of mass. Due to the difference in mass between a star and a planet, the center of mass is typically located inside the star or close to it. Observing the star, one can notice its wobbling motion. According to Kepler's third law, the distance between a planet and a star a_{pl} relates to the orbital period P by

$$a_{pl}^3 = \frac{GM_\star}{4\pi^2} P^2, \tag{1.1}$$

where G is the gravitational constant and $M_\star$ is the mass of the star. Equating Newtons law of gravitation with the equation for the centripetal force, leads to the velocity v_{pl} of the planet on its orbit around the star

$$v_{pl} = \sqrt{\frac{GM_\star}{a_p}}. \tag{1.2}$$

Inserting Eq. 1.1 into Eq. 1.2 and using the center of mass equation, we can find the stellar velocity $v_\star$ as

$$v_\star = \frac{M_{pl}}{M_\star} v_{pl}, \tag{1.3}$$

which means that the orbital velocity of the star, caused by the companion planet increases with planetary mass M_{pl} and decreasing orbital separation. This effect is obviously very minimal, where a Jupiter like planet located fifty times closer to the star than our earth would cause a velocity of $0.2\,\mathrm{km\,s^{-1}}$ (Struve, 1952).

Since the star is periodically orbiting around the common center of mass, the Doppler effect causes the stellar light to periodically shift in wavelength as the planet orbits the star. Measuring the period of the shift and the maximum displacement of the wavelength, which is proportional to the stellar velocity, allows us to solve Eq. 1.3 for the planetary mass, given that the stellar mass is known. However, since only the line-of-sight component of the velocity contributes to the Doppler shift, the planetary mass can only be measured modulo the inclination of the planetary orbit relative to the line of sight. This limitation of the Doppler method can be resolved if we observe the planet passing in front of the star, which is known as a transit. Observing the transit of the planet can be done in two ways. First via photometric measurements of the intensity of the light, which is dimmed by the transiting planet, which will be discussed below, and secondly in the spectrum, via the Rossiter-McLaughlin effect, where the spin of the star and its resulting blue and redshifted parts of the stellar photosphere are blocked at different times during the transit.

Doppler spectroscopy is thus a powerful method, especially in combination with the transit method (discussed below). In fact, the first discovery of an exoplanet has been made possible with the Doppler method (Mayor & Queloz, 1995). Follow-up Doppler measurements of exoplanets detected with the transit method yield a way to independently confirm planets and give precise measurements of their mass (e.g., Bouchy et al., 2009).

Transit method

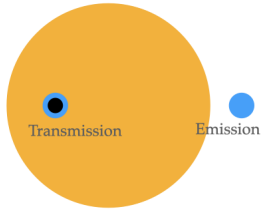

If a planet transits the star, a fraction of the stellar light will be blocked for the time of the transit. Looking at the star, the measured intensity will thus

decrease, when the planet transits. The photometric transit depth $\Delta f/f$, is thus given by (Sing, 2018)

$$\frac{\Delta f}{f} = \left(\frac{R_{pl}}{R_\star}\right)^2, \tag{1.4}$$

where R_{pl} and $R_\star$ are the planetary and stellar radius respectively. The first exoplanet that has been confirmed by looking for such a dip in the light curve is HD 209458 b (Charbonneau et al., 2000; Henry et al., 2000), which was previously found by the Doppler method (Mazeh et al., 2000). Follow-up Hubble Space Telescope (HST) observations of HD 209458 b (Brown et al., 2001), revealed an unusually high absorption of the alkali metal Na during the transit (Charbonneau et al., 2002), which has been previously predicted to be present in the atmosphere of HD 209458 b (Seager & Sasselov, 2000). Their pioneering work showed that the transit method could not only be useful to constrain the radius of a planet and confirm its existence, but instead could also be used for atmospheric characterization, which will be discussed below in Sect. 1.3.

1.1.2 *Exoplanet demographics*

Thanks to advancing technology and space telescopes such as Kepler, the number of exoplanets observed has risen to over 5,200 (Akeson et al., 2013), and continues to grow thanks to ongoing and upcoming missions like TESS and PLATO. Since both of the above-mentioned methods are subject to a significant observational bias towards massive and close planets, it is not surprising that many of the discovered exoplanets are hot gas giant exoplanets. However, the real fraction of hot gas giants is small, when accounting for this observational bias (e.g., Howard et al., 2012). The majority of the observed exoplanet population can be grouped into two classes (see Fig. 1.1). The above discussed hot gas giants and an even larger population of planets with radii between the radius of Earth and Neptune of $0.05\,R_{jup}$ to $0.3\,R_{jup}$. Like for the hot gas giants, we do not have any equivalent for these type of planets in our solar system.

There are two distinct features in the population of these $0.05\,R_{jup}$ to $0.3\,R_{jup}$ planets: The sub-Jovian desert for planets on short orbital period and the radius gap in occurrence rate between what is believed to be rocky and mini-Neptune planets (see review of Zhang, 2020, for references). The planetary desert describes the slope with which the population is cut towards low orbital period, whereas the radius gap describes the loosely visible vertical separation of the population into two groups, where one group has planets

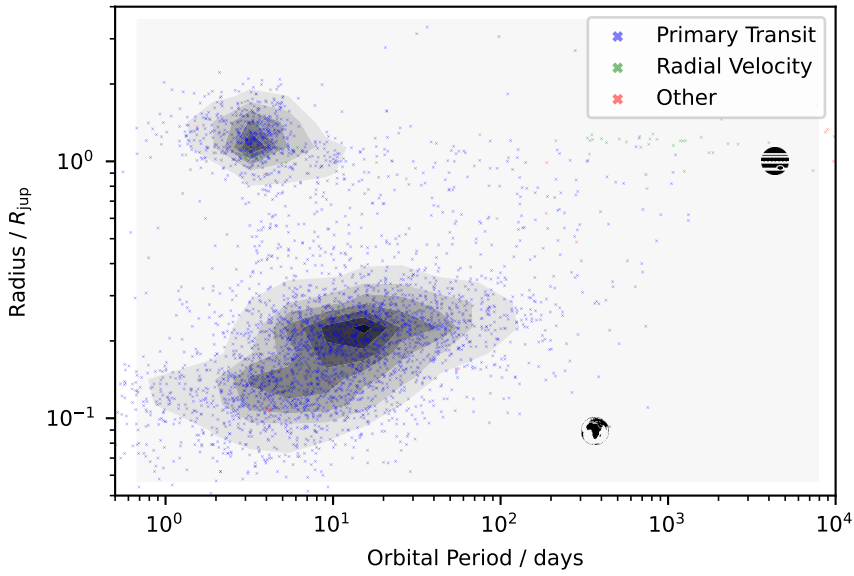

Figure 1.1: The blue crosses indicate observed exoplanets by their radius and orbital period, with Jupiter and Earth marked above. The contour faces are calculated by binning the number of observed exoplanets in a 2D histogram. Data was collected from `http://exoplanet.eu` using `pyExoplaneteu` on 03.07.2023.

with radii smaller $\approx 1.5 R_{earth}$ and one with planets larger than that (see Fig. 1.1). Owen & Wu (2013) and Lopez & Fortney (2013) found that planets could lose their atmosphere due to photoevaporation after the planet has formed. By this process, high energy photons from the host star heat up the hydrogen-helium atmosphere. Due to the high temperature, part of the gas reaches the escape velocity and thus essentially evaporates, leaving a bare core. These planets are thus often called super Earths, whereas their non evaporated counterparts, with larger radii, are called sub Neptunes. Photo evaporation seems to be able to explain the observed desert, where smaller distance to the star results in higher energy deposition in the atmosphere and thus higher mass loss due to photoevaporation. It is, however, an ongoing debate, whether photoevaporation is sufficient to explain the radius gap as well (Van Eylen et al., 2018; Martinez et al., 2019).

This thesis focuses on hot Jupiters rather than sub Neptunes or super-Earths. These planets are larger and more massive than sub Neptunes, but still not massive enough to burn deuterium, which is typically assumed to require a mass of $13\,M_{jup}$ (Spiegel et al., 2011). Hot Jupiters are thought to be tidally locked (Guillot et al., 1996; Rasio et al., 1996; Showman & Guillot, 2002). This means that their spinning rate is aligned with the orbital frequency due to the proximity to the star, where tidal effects are very important. Consequently, like the moon, hot Jupiters have permanent day and nightsides, which makes them very interesting targets for atmospheric studies (Madhusudhan, 2019). Hot Jupiters come in two types: Ordinary hot Jupiters and ultra-hot Jupiters. Ultra-hot Jupiters can be separated from ordinary hot Jupiters by their temperature, where ultra-hot Jupiters are defined as planets with temperatures above $\approx 2200\,K$. These high temperatures enable processes such as dissociation of water and H_2, as well as the formation of hydride (H^-). These processes significantly impact both the thermal structure and the observed spectrum (Parmentier et al., 2018; Tan & Komacek, 2019; Helling et al., 2021b).

Furthermore, most of the detected hot gas giants tend to have anomalously large radii (low density), compared to Jupiter (Thorngren & Fortney, 2018), which is often called the problem of radius inflation. In order to explain an inflated radius, energy needs to be deposited at depths below the layers of thermal emission. Thus, the question of radius inflation can be formulated as a question of high internal temperature. Guillot & Showman (2002) was the first to suggest that the state of inflation might correspond to the incident stellar flux, where planets receiving more stellar flux would be more inflated. Further studies confirmed this trend (Laughlin et al., 2011; Thorngren et al., 2019; Sarkis et al., 2021), but also found that the amount of inflation peaks at $\approx 3 \times 10^9\,erg\,s^{-1}\,cm^{-2}$ (see Fig. 1.2). Understanding the mechanisms that

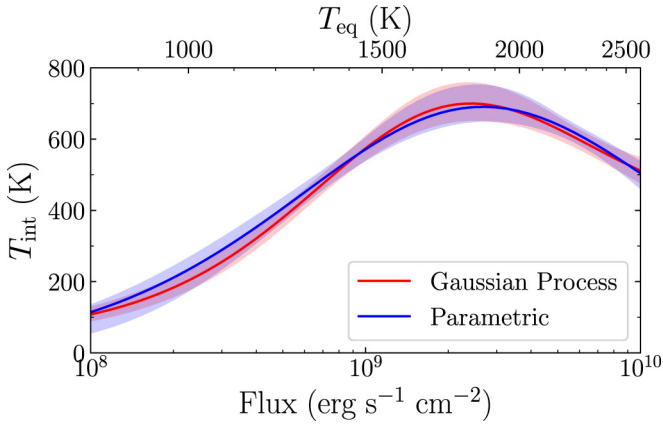

Figure 1.2: Intrinsic temperatures of hot Jupiters in equilibrium as a function of incident flux (bottom) or equilibrium temperature (top). These were derived from the two favored heating models (Gaussian process and Gaussian parametric) of Thorngren & Fortney (2019), using Equation (2), with corresponding uncertainties. The two models yield nearly identical results. Importantly, the intrinsic temperatures must be quite high — up to 700 K — to match the hot interiors required to explain the radii of hot Jupiters. Figure and caption taken from Thorngren et al. (2019), ©AAS. Reproduced with permission.

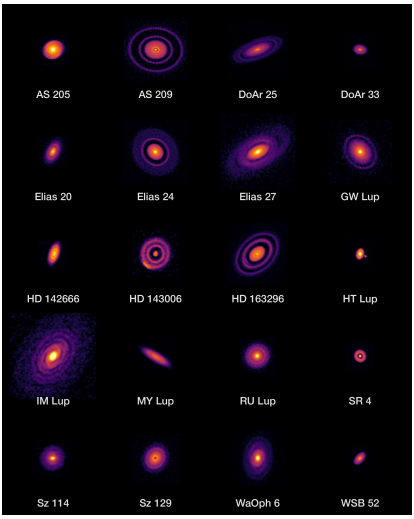

Figure 1.3: ALMA's high-resolution images of nearby protoplanetary disks, which are results of the Disk Substructures at High Angular Resolution Project (DSHARP). Credit: ALMA (ESO/NAOJ/NRAO), S. Andrews et al.; N. Lira

form these inflated radii is an ongoing subject of research, which will be discussed in more detail in Chapters 6, 7 and 8.

1.2 LINKING EXOPLANET OBSERVATIONS TO PLANET FORMATION

Stars are thought to form from gravitational collapse within a molecular cloud. This collapse occurs when the molecular cloud's density exceeds a certain critical value (the Jeans limit). To conserve angular momentum, the newly born star rotates rapidly. Due to the gravitational pull of the newborn star, surrounding material from the molecular cloud forms a rotating disk around the star, called a protoplanetary disk. Such a protoplanetary disk consists of gas (mostly hydrogen and helium) and small solid particles. Depending on the size of these solid particles, they are either referred to as dust or pebbles.

Promising observations of the dust thermal emission of protoplanetary disks with ALMA (e.g., Andrews et al., 2018; Dullemond et al., 2018) reveal a variety of features in these disks, including asymmetries, rings and spiral arms, as can be seen in Fig. 1.3. Such features can be caused by the interaction of the gaseous disk with planets forming in these disks (e.g., Zhang et al., 2018). However, ring like features are not only found in the thermal emission of these disks, they are also frequently found in images of the stellar reflected

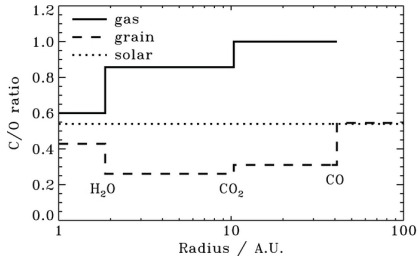

Figure 1.4: C/O ratio in the gas and in grains, assuming the temperature structure of a "typical" protoplanetary disk around a solar-type star (T_0 is 200 K and $q = 0.62$). The H_2O, CO_2, and CO snowline are marked for reference. Figure and caption taken from Öberg et al. (2011), ©AAS. Reproduced with permission.

light of disks, which probe the surface of the protoplanetary disk (e.g., de Boer et al., 2016). These shallow ring structures may be caused from stellar outbursts (Schneider et al., 2018) or self shadowing effects (e.g., D'Alessio et al., 1999).

Protoplanetary disks vary in size and mass, extending from dozens to hundreds of astronomical units (AU). The temperature in the midplane of the disks decreases from hundreds of Kelvin in the inner disk to a few Kelvin in the outer parts, crossing multiple condensation curves of molecular species. Thus, the chemical composition of the disk is highly dependent on the radius. In a basic protoplanetary disk model, consisting of gas and grains (water, carbon dioxide and carbon monoxide), water freezes out closest to the star, usually around 1 AU to 2 AU. Carbon dioxide tends to freeze out at around 10 AU, followed by carbon monoxide at a few dozen AU. We show the effect of the different freeze out locations on the carbon to oxygen (C/O) ratio in Fig. 1.4. The C/O ratio greatly varies with distance from the star, where the ratio is determined only by carbon monoxide in the outer parts of the disk, and thus the C/O number ratio is one. This ratio, however, changes towards the inner parts of the disk, where the temperature increases and thus first carbon dioxide (C/O number ratio of 0.5) and then water become available to the gas phase. The opposite is then true for the chemistry of the grains.

The importance of this differences in C/O for the formation of planets has first been pointed out by Öberg et al. (2011), who suggested that the C/O ratio of planetary atmospheres could be useful to constrain the location at which planets form inside a protoplanetary disk. One major advantage of the C/O ratio is that it not only varies in the protoplanetary disk, but also strongly regulates the chemistry inside planetary atmospheres (Lodders, 2010; Mollière

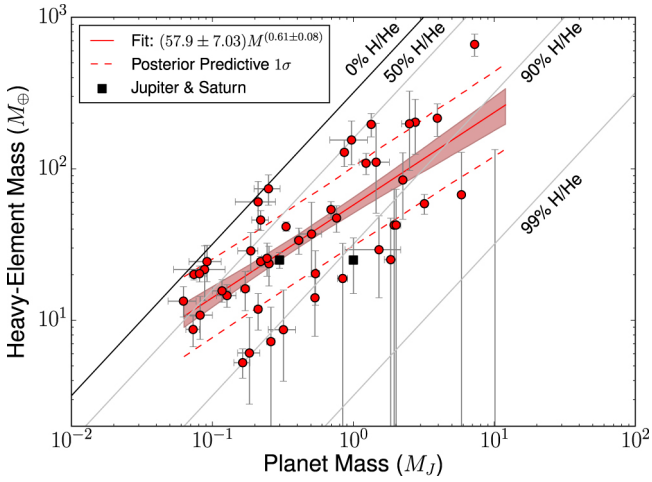

Figure 1.5: Heavy element masses of planets and their masses. The lines of constant Z_{planet} are shown at values of 1 (black), 0.5, 0.1, and .01 (Gray). Distributions for points near $Z_{planet} = 1$ tend to be strongly correlated (have well-defined Z_{planet} values) but may have high-mass uncertainties. No models have a Z_{planet} larger than one. The distribution of fits (see Thorngren et al., 2016, Section 4 for discussion) is shown by a red median line with 1, 2, and 3σ contours. Note Kepler-75b at 10.1M_J, which only has an upper limit. Figure and caption taken from Thorngren et al. (2016), ©AAS. Reproduced with permission.

et al., 2015). Subsequent observations of exoplanets have been able to retrieve first constraints on the C/O ratio (Brewer et al., 2017; GRAVITY Collaboration et al., 2020, e.g.,), suggesting a variety of different values. Unfortunately, the promise of the C/O ratio as a reliable proxy for the location of planet formation is further complicated, because the simple picture of a protoplanetary disk, drawn by Öberg et al. (2011) is not accurate. Instead, the C/O ratio in grains and gas of protoplanetary disks is time-dependent, where different processes such as chemical processes (Eistrup et al., 2016) and kinematic processes (drift of grains and advection of gas) (Booth et al., 2017; Schneider & Bitsch, 2021a) further complicate the picture. Different chemical ratios such as the volatile to refractory ratio (Lothringer et al., 2021; Schneider & Bitsch, 2021b) have thus been proposed to solve the problem of the C/O ratio degeneracy.

A different useful tool to possibly constrain the formation of gas giant exoplanets in protoplanetary disks is given by comparing the observed planetary radii with their masses (e.g., Thorngren et al., 2016; Zakhozhay et al., 2022).

Thorngren et al. (2016) showed that the planetary heavy element mass content[1] can be fitted to the radius and masses of planets using interior models of gas giants (see Fig. 1.5). Using multiple observed non-inflated gas giants, they then found a relation between the masses of gas giants and their heavy element content, in which the amount of heavy elements in gas giants roughly scales with the root of the planetary mass. This finding can thus yield a useful constraint to planet formation synthesis models that predict the heavy element content for gas giants.

1.3 ATMOSPHERIC CHARACTERIZATION

1.3.1 *Transmission spectroscopy*

The transit method allows us to determine not only the radius of a planet but also provides valuable insights into its atmosphere. By analyzing the transmitted light spectroscopically, we can gather significant information about the planet's atmospheric composition. When a planet with an atmosphere undergoes a transit in front of its host star, the planetary atmosphere causes the absorption of a portion of the star's light. The opacity of a planet's atmosphere varies with wavelength, so the amount of light that passes through it will also vary. The transit depth is then clearly affected by Rayleigh scattering, UV absorbers, that block the stellar light, such as alkali metals, or high altitude clouds, as already pointed out by Seager & Sasselov (2000). Probing different parts of the spectrum gives a window into different altitudes, because the path length and thickness of the atmosphere increase towards the center of the planet. Line cores of strong absorbers, such as Alkali metals, have high opacity and will thus block the light throughout the atmosphere, whereas line wings, with lower opacity can be used to trace intermediate regions in the atmosphere (Sing, 2018).

Observing the combined light curve, however, reveals more than just the transmission spectrum. A secondary eclipse occurs when a planet passes behind its star, also known as an eclipse event. The eclipse is particularly useful, as it gives the unperturbed stellar spectrum, without the contribution of the planetary emission and reflection. This deficit thus yields another type of planetary spectrum: The emission spectrum. The spectrum will be affected by reflection in the optical wavelength ranges, and will encode the thermal emission of the planet in the infrared (Sing, 2018). If a planet is tidally locked, which is often the case for hot Jupiters, the emission spectrum will probe

1 We follow the typical notation in astrophysics, in which heavy elements are defined as elements heavier than Helium.

the dayside of the planet. The pathways of the emitted light in the emission spectrum are shorter, compared to the transmission spectrum, and as such probe deeper layers of the planetary atmosphere. Whether molecular lines can be seen in emission or in absorption depends on the slope of the temperature profile in the atmosphere. If cooler gas is on top of hotter gas, less and less light is emitted towards the observer, but the absorption stays constant, and thus the molecular gas will be seen in absorption. However, if warmer gas lies on top of cooler gas, which is called a stratosphere, less will be absorbed than emitted towards the observer and thus the molecular feature will be switched around and in emission. Such a stratosphere could be possible if strong UV absorbers like TiO and VO are present in the upper layers of the atmosphere (Fortney et al., 2008a). Knutson et al. (2008) found that HD 209458 b would feature such an excess of emission and could thus have a stratosphere. This finding was later ruled out when observations revealed a better measurement of the eclipse (Line et al., 2016).

In general, the planet can also be followed between the transit and eclipse, revealing the phase curve of the planet. Assuming that the planet is tidally locked, such an observation enables an all-around view of the planet, rendering them particularly useful for the study of atmospheric dynamics on gas giants. However, this type of observation is a technically very challenging task, since it involves, observing the target with high precision for multiple days. Therefore, only few phase curve observations exist, which have been very important for the comparison with atmospheric models, for example in revealing day night temperature contrasts and hot spot offsets (e.g., Knutson et al., 2007; Stevenson et al., 2014, 2017).

Transit observations have typically been performed with space telescopes, since the observations of transits and eclipses require focusing on targets for a long time, especially for phase curves. Furthermore, Earth's atmosphere blocks a large portion of the planetary emission in infrared, thus rendering it difficult to perform emission spectroscopy of planetary atmospheres (for a review see Zhang, 2020). Nevertheless, space telescopes are often more expensive than ground based telescopes, and can only perform low resolution observations, whereas the spectral resolution of ground based telescopes can be much higher. Moreover, by correlating the known absorption profile of molecules with high-resolution spectra of exoplanets observed from ground-based telescopes, we can obtain accurate predictions for the presence of these molecules with high signal-to-noise ratio. (Snellen et al., 2015). Various species have been discovered in planetary atmospheres using this method (e.g., Snellen et al., 2010; Brogi et al., 2012, 2016; Hoeijmakers et al., 2018, 2019). High-resolution spectra also provide information on planetary winds

by observing the Doppler broadening of individual lines (e.g., Snellen et al., 2010; Seidel et al., 2020; Savel et al., 2022; Wardenier et al., 2021, 2023).

1.3.2 *Atmospheric dynamics in hot Jupiters*

The short orbital period of hot Jupiters suggest that these planets are tidally locked (Showman et al., 2020). This means that in the planet's reference frame, there is one side that is constantly irradiated from the star (dayside) and one that never receives radiation from the star (nightside). Both of these have a unique point whose atmospheric normal is parallel to the closest path between the star and the planet. These points are often referred to as the substellar and antistellar points, with the substellar point being the location on the planet that receives the most irradiation.

Classical radiative equilibrium (RE) models of hot Jupiters, that solve the radiative transfer problem in 1D without taking atmospheric dynamics into account, thus predict the hottest temperatures around the substellar point. However, already using a simple parametric temperature forcing coupled to a climate model, originally developed for Earths atmosphere, Showman & Guillot (2002) predicted that the temperature would be far from RE. Instead, a strong zonal wind jet for HD 209458b, was predicted, which carries away hot air from the dayside towards the nightside. Such a strong wind jet phenomenon, called superrotation, occurs when the wind speed is faster than the planet's background rotation. Subsequent Spitzer IR observations (Knutson et al., 2007) of the full orbital phase of the hot gas giant HD 189733b confirmed the predicted hotspot offset, which was then understood by subsequent theoretical work (e.g., Showman & Polvani, 2011).

Showman & Polvani (2011) showed that the asymmetric forcing (heating on the dayside and cooling on the nightside) induces two types of planetary-scale waves. An eastward propagating Kelvin wave trapped in the equatorial region and westward propagating Rossby waves trapped in the subtropics (outside the equatorial region). The Kelvin wave is essentially a horizontally propagating buoyancy (gravity) wave, and the Rossby waves are a result of the tendency of fluid parcels to conserve vorticity on a rotating sphere. This can be understood by the meridionally increasing strength of the Coriolis force. Due to the Coriolis force, fluid parcels near the poles have higher vorticity than those near the equator. To conserve absolute vorticity, these parcels must change direction. On the Northern Hemisphere, fluid parcels propagating northward are deflected clockwise, and those going southward, anti-clockwise. The opposite is true on the Southern Hemisphere. This has two effects: For the Kelvin wave, the Coriolis force bends the Kelvin wave to the equatorial

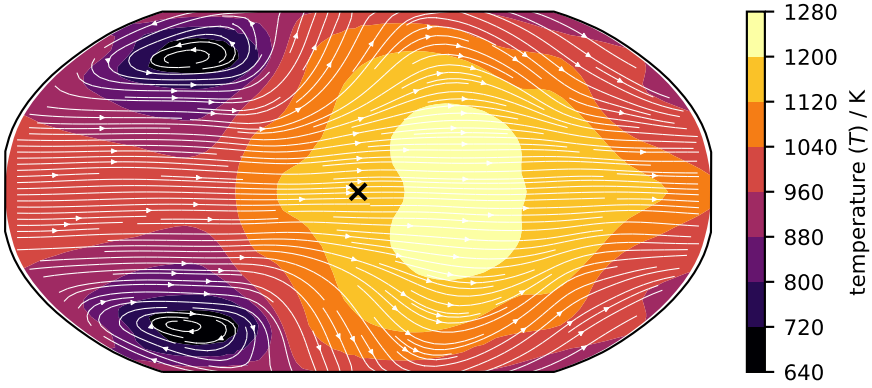

Figure 1.6: Temperature contour face map at $p = 5 \times 10^{-2}$ bar of HD 189733b, simulated with `expeRT/MITgcm` (Schneider et al., 2022b). The substellar point (point of maximum stellar illumination) is marked by a black cross.

region. For the Rossby wave, however, the change of direction results in its wave pattern, where in the Northern Hemisphere, northward propagating gas parcels turn clockwise until they propagate southward, which turns them anti-clockwise until the parcel propagates northward again. Thus, the different location and propagation direction implies a tilt of atmospheric temperature, where the Kelvin wave shifts the hottest point eastwards in the equatorial region and the Rossby wave tilts it back towards the west. Matsuno (1966) and Gill (1980) first found that such a combination of Rossby and Kelvin waves could be an idealized solution to fluid dynamics on a rotating sphere. A pattern, similar to this idealized pattern, can be seen in almost all hot Jupiter simulations (e.g., Showman et al., 2009; Heng et al., 2011a; Rauscher & Menou, 2012; Kataria et al., 2016; Amundsen et al., 2016; Carone et al., 2020; Baeyens et al., 2021; Mendonça et al., 2018b; Lee et al., 2021; Deitrick et al., 2022), and is caused by the strong forcing gradient between the day and nightside. In Fig. 1.6, we show the temperature and winds from a simulation of the hot Jupiter HD 189733b at a pressure of 5×10^{-2} bar, which is close to the pressure at which the planet might emit thermal radiation. The temperature looks similar to the original Matsuno-Gill solution (see e.g., Matsuno, 1966, Fig. 9), where the above discussed tilt between the Rossby wave and the Kelvin wave results in a cold gyre and a hot spot offset towards the east, together with a strong jet.

Finally, the superrotating jet, is a result of the above discussed tilted temperature structure, which tilts the eddy velocities, and thus converges zonal

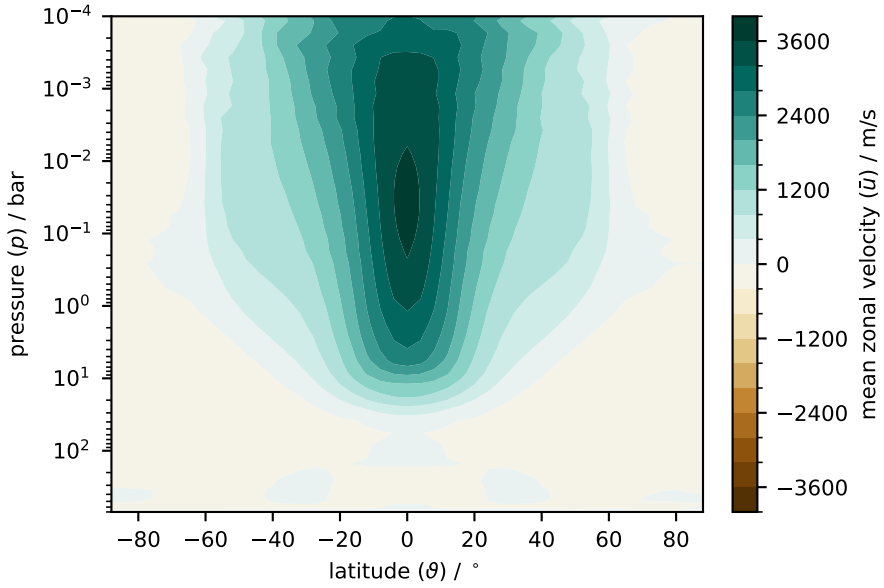

Figure 1.7: zonally averaged wind speeds as a function of pressure and latitude for the same simulation of HD 189733b as in Fig. 1.6.

momentum from the poles towards the equator, accelerating the jet. This is counteracted by nightside cooling, which results in downward flux of momentum. This downward flux takes away some eastward momentum and decelerates the jet. This downward flux of air at the east terminator[2] and upward flux of cold air at the western terminator, closes off the jet and may have a strong impact on the temperature structure in the deep atmosphere (e.g., Tremblin et al., 2017; Carone et al., 2020), which will be discussed in Chapter 8.

The exact velocity of the superrotating jet in climate models of hot Jupiters is dependent on a variety of numerical and physical effects. However, the peak zonal averaged wind speeds of typical hot Jupiters is often in the range of $1\,\mathrm{km\,s^{-1}}$ to $10\,\mathrm{km\,s^{-1}}$ (e.g., Dobbs-Dixon & Agol, 2013; Amundsen et al., 2016; Kataria et al., 2016; Deitrick et al., 2020; Lee et al., 2021; Baeyens et al., 2021). We show a typical zonal wind profile of a hot Jupiter in Fig. 1.7, which displays the mean zonal wind speed as a function of latitude and pressure. The jet extends deep into the atmosphere, where the exact depth of the cutoff likely depends on the rotation rate, gravity and numerical assumptions (Carone

2 Here terminator describes the region of transition between the nightside and dayside

et al., 2020). The strength of the wind jet is important for the day-night temperature contrast. Strong winds carry away hot air from the dayside to the nightside, before the air can be cooled from radiation. However, the temperature contrast between dayside and nightside likewise influences the strength of the wind jet, as discussed above. Clouds on the nightside can act as blankets that keep the radiation inside and hinder the air to cool (e.g., Roman & Rauscher, 2017). Furthermore, magnetic fields, deeply rooted in the atmosphere, assert a drag on ionized gas particles, slowing down the wind (e.g., Perna et al., 2010a; Rauscher & Menou, 2013). This is particularly relevant for ultra-hot Jupiters with partly ionized daysides. Finally, different numerical approximations, needed to solve the governing equations of radiative transfer and fluid dynamics, have a large impact as well (e.g., Mayne et al., 2014, 2019; Deitrick et al., 2020; Noti et al., 2023).

1.4 GOALS AND OUTLINE

The main objective of this thesis is to construct theoretical models that can provide explanations for questions arising from observations of exoplanetary atmospheres. Our goal is to enhance our understanding of the connection between the interior structure of gas giant exoplanets and their observable atmospheres. To accomplish this, we will develop numerical models to track the composition of gas giant planets formed through pebble and gas accretion. Additionally, we will expand a climate model by incorporating consistent radiative transfer. Through the utilization of these models, we aim to investigate the impact of specific parameters on observable phenomena.

1.4.1 *Research context and science questions*

The goal of this thesis can be outlined by the following two research questions.

How do drifting and evaporating pebbles shape giant planets? What are the observable implications?

Observations of exoplanets have revealed super solar abundances, leading to a large variety of different possible C/O ratios (Madhusudhan et al., 2011; Lee et al., 2013; Brewer et al., 2017; GRAVITY Collaboration et al., 2020, e.g.,). C/O ratios are well traceable in planetary atmospheres, because of their profound impact on the atmospheric chemistry (e.g., Fortney et al., 2008b; Lodders, 2010; Mollière et al., 2015). Similarly, giant planets in our solar system feature super solar abundances (Owen et al., 1999; Atreya et al., 2016). Öberg et al.

(2011) realized that these atmospheric constraints could be used to constrain planet formation models. Subsequently, some planet formation models have included predictions for the chemical compositions of planets formed in their model (Mordasini et al., 2009; Madhusudhan et al., 2017; Cridland et al., 2019; Mollière et al., 2022). Additionally, tracing the heavy element content of planets, forming in planet formation models, has also been suggested as a possible way to compare planets with precise mass and radius measurements from transit and Doppler measurements Thorngren et al. (2016).

Generally speaking, planet formation models in the core accretion paradigm can be split into two types of models. These models form planetary cores either by the accretion of planetesimals (e.g., Ida & Lin, 2004, 2008a,b, 2010; Alibert et al., 2005; Mordasini et al., 2012; Alibert et al., 2013; Cridland et al., 2019; Emsenhuber et al., 2021, 2023) or by the accretion of pebbles (e.g., Bitsch et al., 2015b, 2019; Lambrechts & Johansen, 2012, 2014; Ali-Dib, 2017; Ndugu et al., 2018; Brügger et al., 2018; Lambrechts et al., 2019b). The advantage of pebble accretion is that pebbles can be accreted efficiently (e.g., Bitsch et al., 2015b), whereas efficient planetesimal accretion requires the presence of small planetesimals (e.g., Tanaka & Ida, 1999; Johansen & Bitsch, 2019). One way to do comparisons between predictions from planet formation models with observations of exoplanets and demographic statistics is to perform population synthesis (e.g., Ida & Lin, 2004; Mordasini et al., 2009; Emsenhuber et al., 2021, 2023). Populations synthesis models usually couple planet formation models with N-body integrators that trace the evolution of planetary systems from birth to observation. However, one of the disadvantages of these models is that it is often difficult to constrain the exact priors, needed to start models.

Lastly, the final chemical composition of exoplanets is influenced by many physical and chemical mechanisms. Chemical reactions in protoplanetary disks will influence the chemical composition of protoplanetary disks (e.g., Eistrup et al., 2016; Cridland et al., 2019). However, the chemical composition is likely also influenced by the drift of pebbles, which leads to evaporation and thus enrichment around evaporation lines (Cuzzi & Zahnle, 2004; Booth et al., 2017; Ciesla & Cuzzi, 2006; Stammler et al., 2017; Krijt et al., 2018; Kalyaan et al., 2021, 2023). No study thus far has studied the effect of pebble evaporation and condensation on the composition of gas giant planets.

How is the deep atmosphere hydrodynamically connected to the radiative parts of the atmosphere? Can atmospheric dynamics cause the inflation of hot Jupiters?

Hot Jupiter research faces the challenge of explaining the observed inflated radii of these planets. Generally, there is a trend between the incident stellar flux and the level of radius inflation, with some exceptions (e.g., Laughlin

et al., 2011; Thorngren & Fortney, 2018; Sarkis et al., 2021). Early models by Guillot et al. (1996) suggested that hot gas giants cool down over time, causing their radii to shrink. However, present-day planetary evolution models contradict this by concluding that the current population of hot gas giants would have cooler interiors and smaller radii, typically less than 1.2 Jupiter radii (e.g., Fortney et al., 2007). Recent studies by Komacek & Youdin (2017) and Komacek et al. (2020) suggest that heating in deep layers, below the radiative convective boundary, plays a crucial role in maintaining the inflated radius, while heating above this boundary has minimal impact on radius evolution.

In order to match the observed inflated radii, 1D RE models often use the concept of intrinsic temperature. Intrinsic temperature can be defined as the black body temperature that the planet would have from thermal emission, if it would not be irradiated. It is thus the analogue of the stellar effective temperature. Increasing the intrinsic temperature/flux in these models has the effect of increasing the temperature in the deep atmosphere (e.g., Guillot, 2010). If a planet lacked an internal heat source and maintained radiative energy balance with its star (input equals output), the planet's intrinsic temperature would be 0 K. However, it is important to note that the intrinsic temperature is not a physical concept that explains the reason for the extra heating term that leads to the hot temperature in the deep atmosphere. Instead, the intrinsic temperature is just a concept that can be used in 1D RE models to match the inflated radii of hot gas giants.

Many mechanisms have been proposed to explain the inflated radii of hot Jupiters. The cooling of the interior from an initial hot state could be delayed by compositional gradients in the interior (Chabrier & Baraffe, 2007) or by enhanced opacities in the atmosphere (Burrows et al., 2007). Planet-planet interactions that cause tidal heating have been put forward as one of the first mechanisms to explain the inflated radii (Bodenheimer et al., 2001; Arras & Socrates, 2010; Socrates, 2013). However, processes that rely on stellar energy deposition are more likely to fit the observed relation between inflation and stellar flux. Already Guillot & Showman (2002) proposed that depositing 1% of the incoming stellar flux at pressures higher than 100 bar could explain the inflated radius of HD 209458 b. However, the question remains, which process could be responsible to transport the stellar energy to these deep layers, since radiation is absorbed much higher up in the atmosphere and convection can only transport heat upwards and not downwards (e.g., Fortney et al., 2021). One of the processes that has been suggested to deposit energy at greater depths is Ohmic dissipation. Ohmic dissipation is the process of kinetic energy dissipation of charged particles that feel a drag from the magnetic fields in the

planetary atmospheres (e.g., Batygin & Stevenson, 2010; Batygin et al., 2011; Perna et al., 2010b; Rauscher & Menou, 2013; Knierim et al., 2022). Thorngren & Fortney (2018) showed that the amount of inflation peaks at an incident flux of $\approx 1 \times 10^9$ erg s^{-1} cm^{-2}, which could be an indication of Ohmic dissipation, which has been proposed to also peak at similar incident fluxes (Menou, 2012; Rogers & Showman, 2014; Ginzburg & Sari, 2016).

Finally, Tremblin et al. (2017) suggested a mechanism that is similar to the mechanism proposed by Guillot & Showman (2002), but differs as it does not require an additional process for the downward transport of heat, and instead relies only on the overturning caused by the atmospheric circulation, which brings warm air down to deeper layers, thus heating the deeper layers. The idea of this theory is especially attractive, as in it only requires the atmospheric circulation to work, which is different to all other theories that require additional physical mechanisms such as magnetic fields, tidal interaction or microturbulance. Whereas, the 2D model of Tremblin et al. (2017) could not demonstrate this mechanism selfconsistantly, because it required a parameterization for the vertical transport, Sainsbury-Martinez et al. (2019) followed up on this idea and performed General Circulation Model (GCM) simulations with a parametric temperature forcing to show that the atmospheric circulation would indeed deposit energy in the deeper atmosphere. Showman et al. (2020) has questioned, whether the parametric approach of the heating and cooling would capture the reality good enough. Additionally, Sainsbury-Martinez et al. (2019) showed that the efficiency of this process strongly depends on numerical parameters, such as the strength of numerical diffusion. Moreover, the suggested process acts on long timescales, inaccessible to most contemporary GCMs of hot Jupiters.

GCMs of hot Jupiters are available in three different categories, based on the way they treat the thermal forcing. The numerically fastest method, yet at the same time the most inaccurate method, is Newtonian cooling, which uses a prescribed temperature profile together with radiative timescales (e.g., Showman et al., 2008; Sainsbury-Martinez et al., 2019; Carone et al., 2020). Using such a Newtonian cooling approach is extremely useful for the inter comparison of different dynamical cores (e.g., Held & Suarez, 1994; Polichtchouk et al., 2014; Christie et al., 2022). In order to gain more realistic heating and cooling, radiative transfer solvers are needed. The computational cost of these models scales with the number of frequency points used. The simplest solution is to use mean opacities (e.g., Rauscher & Menou, 2012; Heng et al., 2011a; Deitrick et al., 2020; Lee et al., 2021). Since a true frequency resolved radiative transfer solver would require millions of frequency points (see Amundsen et al., 2014, for a discussion), previous GCMs with accurate

radiative transfer have relied on the correlated-k method (Goody et al., 1989) (see Section 2.3.3). Showman et al. (2009) was the first to introduce this method in a hot Jupiter GCM, which is now used by a number of the other GCMs (Amundsen et al., 2016; Lee et al., 2021; Schneider et al., 2022b; Deitrick et al., 2022). Very long runtimes of thousands of days are needed, in order to run a model until it reaches steady state (e.g., Sainsbury-Martinez et al., 2019). Because of the computational cost of multiband radiative transfer, most other multiband GCMs could not be used to perform these long-running studies of the convergence behavior of hot Jupiter GCMs.

Some studies have already suggested that the temperature in the deep atmosphere will have observable effects on the atmospheric circulation (e.g., Mayne et al., 2017; Carone et al., 2020; Komacek et al., 2022; Schneider et al., 2022b,a). Sainsbury-Martinez et al. (2019) suggests to start models hotter than their expected outcome, because they claim that it is faster to cool a model than to heat it. Carone et al. (2020) and Komacek et al. (2022) proposed that the best solution to the problem would be to anchor the temperature in the deep layers of the GCM onto a 1D model calculation of an interior model. However, while such an approach is certainly useful for models that are to be compared to observations, doing so requires a guess for the amount of inflation to be inputted into these models. Thus, it is an open question how the atmospheric dynamics of the upper layers of the atmosphere connects to the deeper layers of the atmosphere.

1.4.2 *Outline of the thesis*

The theoretical background of the models developed for this thesis is presented in Chapter 2. In Chapter 3, we examine the influence of pebble drift and evaporation on the composition of exoplanets, comparing it to current models of the interior structure of exoplanets and observations of the C/O ratio in the atmosphere. Chapter 4 introduces the volatile to refractory ratio as an observational constraint for understanding formation processes. In Chapter 5, we explore potential formation pathways based on observations of two specific planets. The remaining chapters of this thesis focus on how atmospheric dynamics affect the observed radius of hot gas giants. In Chapter 6, we integrate a modern radiative transfer solver with a climate model to study long-term atmospheric dynamics on hot gas giants. Chapters 7 and 8 discuss the possibility of energy deposition in deeper atmospheric layers due to atmospheric dynamics. Chapter 8 provides an updated interpretation of the analysis presented in Chapter 7. Finally, we summarize and discuss future prospects in Chapter 9.

2

THEORY AND METHODS

Understanding astrophysical observations requires comparison of observables to predictions of models. These models may be either of analytical or numerical nature and build on our knowledge about physical processes that generate these observables. In the scope of this thesis, we have used semi-analytical models that describe how planets form in protoplanetary disks. Furthermore, we have coupled a sophisticated radiative transfer solver to hydrodynamical models of planetary atmospheres to understand the dynamics and inflation mechanisms that govern hot gas giants. In this chapter we will explain and introduce the underlying theory of both planet formation in the core accretion paradigm (Section 2.1), and the hydrodynamical models used to study planetary atmospheres (Section 2.2), and how radiation can be coupled to such models (Section 2.3).

2.1 PLANET FORMATION

Observations of protoplanetary disks and extrasolar planets are becoming increasingly common, allowing us to better understand the theory of planet formation. In this section, we will give a brief summary of planet formation in the core accretion paradigm and how planet formation is modeled in `chemcomp`, which was first introduced in Schneider & Bitsch (2021a). The basis of any good planet formation model is a good model of a protoplanetary disk in which the planets can be born, as such, we will start by introducing a theory of the evolution of protoplanetary disks in Section 2.1.1 and continue with the theory of accretion based planet formation in Section 2.1.2. A more detailed introduction to planet formation is given in Armitage (2013) and the code `chemcomp` is discussed in detail in Schneider & Bitsch (2021a). We will thus limit the introduction in this section to a brief summary of the most important concepts handled in `chemcomp`.

2.1.1 *Disk structure*

In the viscous disk evolution theory (Lynden-Bell & Pringle, 1974; Bell et al., 1997), which describes gas in a disk, dominated by viscous accretion to a central star, the kinematic viscosity ν, which is the ratio between the dynamic viscosity μ and the density ρ, can be expressed using a parametric approach, the so-called alpha viscosity prescription (Shakura & Sunyaev, 1973). In the alpha viscosity prescription, the kinematic viscosity is given as a function of a dimensionless parameter α as

$$\nu = \alpha \frac{c_s^2}{\Omega_K}, \tag{2.1}$$

where Ω_K is the Kepler orbital frequency and c_s is the isothermal sound speed, given by

$$c_s = \sqrt{\frac{k_B T}{\mu_{MMW} m_p}}, \tag{2.2}$$

where $k_B = 1.3807 \times 10^{-16}\,cm^2\,g\,s^{-2}\,K^{-1}$ is the Boltzmann constant, T is the temperature, μ_{MMW} is the mean molecular weight, and $m_p = 1.6726 \times 10^{-24}\,g$ is the mass of a proton. Assuming that the disk is azimuthally isotropic and in hydrostatic equilibrium, Pringle (1981) derived an equation of the evolution of such a viscous disk from mass and angular momentum conservation. The evolution of the column density $\Sigma_{gas,Y}$ of a species Y is then given by

$$\frac{\partial \Sigma_{gas,Y}}{\partial t} - \frac{3}{r}\frac{\partial}{\partial r}\left[\sqrt{r}\frac{\partial}{\partial r}\left(\sqrt{r}\nu\Sigma_{gas,Y}\right)\right] = \dot{\Sigma}_Y, \tag{2.3}$$

where ν is the kinematic viscosity, r is the radius (e.g., the radial coordinate), and $\dot{\Sigma}_Y$ denotes a source/sink term, which will be discussed below.

The pressure force acting on the gas accommodates for a sub-Keplerian azimuthal speed v_φ. The velocity difference Δv to the Keplerian velocity is then given by

$$\Delta v = v_K - v_\varphi = -\frac{1}{2}\frac{d\ln p}{d\ln r}\left(\frac{H_{gas}}{r}\right)^2 v_K, \tag{2.4}$$

where $H_{gas} = \frac{c_s}{\Omega_K}$ is the disk scale height and p is the pressure.

Whereas the gas is pressure supported and therefore orbits the star with the sub-Keplerian velocity, the dust is not pressure supported and wants to orbit with Keplerian velocity. However, the dust particles are coupled to the

gas, which will therefore assert a drag on the dust particles. As a result, the dust particles spiral inwards with radial velocity u_Z, depending on the size of the particles, where large particles are less coupled to the gas and thus feel more headwind. The dust velocity is thus given by (Weidenschilling, 1977; Brauer et al., 2008; Birnstiel et al., 2012)

$$u_Z = \frac{1}{1+St^2} u_{gas} - \frac{2}{St^{-1}+St} \Delta v, \tag{2.5}$$

with the Stokes number St, which is a unitless quantity that describes the friction in the Epstein drag regime (Brauer et al., 2008; Birnstiel et al., 2010), and is given by the particle size a and density $\rho_\bullet$ as

$$St = \frac{\pi}{2} \frac{a \rho_\bullet}{\Sigma_{gas}}, \tag{2.6}$$

where $\Sigma_{gas} = \sum_Y \Sigma_{gas,Y}$ is the total gas column density.

The size of dust particles is not trivial and in reality follows a non-trivial size distribution (Birnstiel et al., 2010). Birnstiel et al. (2012) showed that the dust evolution can be approximated within some percent accuracy by distinguishing between two size limits: pebbles and small dust particles. The size of the pebbles is then given by the limits to which they can grow before collisions destroy them or radial drift would remove them too efficiently. Using this model, Birnstiel et al. (2012) formulated the evolution of the mass weighted dust column density (small dust + pebbles). The dust column density $\Sigma_{Z,Y}$ of species Y is then given by solving

$$\frac{\partial \Sigma_{Z,Y}}{\partial t} + \frac{1}{r} \frac{\partial}{\partial r} \left\{ r \left[\Sigma_{Z,Y} \cdot \bar{u_Z} - \frac{\partial}{\partial r} \left(\frac{\Sigma_{Z,Y}}{\Sigma_{gas}} \right) \cdot \Sigma_{gas} \nu \right] \right\} = -\dot{\Sigma_Y}. \tag{2.7}$$

In Schneider & Bitsch (2021a), we have introduced pebble evaporation and condensation as a source and sink term ($\dot{\Sigma_Y}$) in Eqs. 2.3 and 2.7. The mechanism works by removing a chemical species Y from the solid phase ($\Sigma_{Z,Y}$) and at the same time adding to the gas phase ($\Sigma_{gas,Y}$) or the reverse, depending on the location in the disk with respect to the ice line of species Y. However, also other mechanisms such as photoevaporation and accretion of material onto a planet would be treated as a sink term in these equations.

2.1.2 *The core accretion paradigm*

Two theories compete to explain the formation of gas giant exoplanets: core accretion and in situ formation. The core accretion theory suggests that planets form from large planetesimals (called "embryos") that accumulate

other planetesimals and pebbles. When the core is large enough, it starts to attract the gas from the protoplanetary disk. The in situ formation theory proposes that planets emerge from an instability that leads to a spontaneous collapse of a gas cloud.

In the core accretion paradigm, dust grows to pebbles, which then gather by disk instabilities to form planetesimals. Several mechanisms have been proposed for planetesimal formation such as turbulent clustering (Cuzzi et al., 2010; Hartlep & Cuzzi, 2020), trapping in vortices (Raettig et al., 2015; Lyra et al., 2018), trapping in zonal flows (Johansen & Youdin, 2007; Johansen et al., 2011; Dittrich et al., 2013; Drążkowska & Alibert, 2017), and the streaming instability (Johansen et al., 2009; Schäfer et al., 2017). These planetesimals will then interact dynamically, collide and finally form a planetary embryo (e.g., Voelkel et al., 2021a,b, 2022). Once the embryo has formed, planetesimal accretion (e.g., Ida & Lin, 2004) and pebble accretion (Lambrechts & Johansen, 2012; Bitsch et al., 2015b) onto the embryo will grow the planetary core until the disk has dissipated, the planet migrated (see below) to the inner disk or has collided with other embryos. The accumulation of pebbles will cease when the pebble isolation mass is reached (e.g., Bitsch et al., 2018). This happens when the planet is sufficiently large to cause a pressure bump in the disk, which stops pebbles from moving inward. The pebble isolation mass is typically at a few Earth masses, depending on the planetary location in the disk (e.g., Bitsch et al., 2018). Once the supply of pebbles stops, the planet will start to cool down and the surrounding gas will start to contract onto the planet (e.g., Ikoma et al., 2000; Piso & Youdin, 2014), followed by a direct supply of gas from the disk (e.g., Machida et al., 2010; Bergez-Casalou et al., 2020; Ndugu et al., 2021).

During its growth, the planet will gravitationally interact with the disk (Goldreich & Tremaine, 1979, 1980), exerting a torque on the disk, which causes an angular momentum transfer between disk and planet, leading to migration of the planet inside the disk (for a review see Kley & Nelson, 2012; Baruteau et al., 2014). When the planet is still small, type I migration (e.g., Paardekooper et al., 2011) will drag the planet towards the star, due to the gravitational interaction of the planet with the disk. The thermal heating of the planet due to its accretion of pebbles, will warm the surrounding disk, which may counteract this drastic inward drift (Masset, 2017; Baumann & Bitsch, 2020). When the planet is large enough, it will carve a gap into the disk (e.g., Crida et al., 2006), which locks the planet inside the gap. The planet will then transition to type II migration, which is given by the viscous radial gas velocity from Eq. 2.3.

How efficient each of these mechanisms is, is an ongoing debate. Recent studies (e.g., Johansen & Bitsch, 2019), as well as a lack of observational evidence for small-sized planetesimals (Bottke et al., 2005; Morbidelli et al., 2009), doubt the efficiency of planetesimal accretion for the formation of planets. It is thus to be determined by observational signatures such as the refractory to volatile ratio (e.g., Lothringer et al., 2021; Schneider & Bitsch, 2021b; Bitsch et al., 2022), which of the growth mechanisms are the most efficient ones.

2.1.3 *chemcomp*

The code `chemcomp`, introduced in Schneider & Bitsch (2021a), and used in Bitsch et al. (2021); Schneider & Bitsch (2021b); Bitsch et al. (2022); Mollière et al. (2022); Mah & Bitsch (2023); Hühn & Bitsch (2023); Bitsch & Mah (2023); Savvidou & Bitsch (2023); Chatziastros et al. (2024); Müller et al. (in review); Mah et al. (2023); Danti et al. (2023); Eberlein et al. (in prep); Andama & Bitsch (in prep); Lienert et al. (in prep); Ndugu & Bitsch (in prep); Savvidou & Bitsch (in prep), is a 1D model that solves the equations of dust and gas evolution (Eqs. 2.7 and 2.3) on a discrete radial grid. It uses the implicit donorcell scheme of Birnstiel et al. (2010) and the two population dust growth model of Birnstiel et al. (2012). The model also partitions molecular species into the solid phase (dust + pebbles) and the gas phase, based on the position and temperature in the disk.

The kinematic approach to chemistry, developed in Schneider & Bitsch (2021a), transports individual species (Eqs. 2.7 and 2.3) and condenses/evaporates them based on the disk temperature. The code further models the growth of planets from embryos (approximately moon mass) to gas giants in the core accretion scenario. This is achieved by placing the embryo at a given time into the disk and by growing the planet by accreting pebbles until it reaches the pebble isolation mass, while keeping track of the accreted composition and advancing the planet's position by migration. Once the planet is large enough, the `chemcomp` model simulates the gap carved into the disk, which stops pebbles from drifting inwards and influences the disk structure and chemistry. The planet then starts to accrete gas from its surroundings until the disk has dissipated, or the planet reaches the inner disk, where the model stops. A more detailed explanation of the code and its underlying assumptions is given in Schneider & Bitsch (2021a).

2.2 GENERAL CIRCULATION MODELS (GCMS)

A General Circulation Model (GCM) is a computational model that solves the equations of hydrodynamics for a planet's atmosphere and ocean. GCMs are often used to understand Earth's climate and weather, but they can also be specifically developed for other planets (e.g., Mendonça et al., 2016; Deitrick et al., 2020). Because of the 3D nature of planets and the non-linearity of the equations of hydrodynamics, GCMs are often very complex and highly optimized models, developed over many years, and often deployed to run in parallel on high performance computer (HPC) clusters.

In the following sections, we will first introduce the equations of hydrodynamics and the simplifications that can be made to simulate planetary atmospheres (Section 2.2.1). We will then discuss the model used in this thesis, the `MITgcm`.

2.2.1 *Hydrodynamics*

In order to describe the flow of gas in a planetary atmosphere, certain assumptions are useful. In this chapter, we will summarize the assumptions needed to derive the hydrostatic primitive equations (HPE), a set of equations often solved in GCMs. Many of the derivations in this section follow the derivations shown in the book by Marshall & Plumb (2007).

Hydrodynamics can be employed to characterize a collection of gas, provided that the system is primarily influenced by collisions. This assumption is valid if the mean free path of a gas particle is significantly smaller than the spatial extent of the region under investigation. We can then combine mass conservation, momentum conservation and energy conservation together with an equation of state to describe the gas.

Using Gauss theorem, we can write the equation of mass conservation (also called continuity equation) and the equation of momentum conservation in Eulerian form as

$$\left(\frac{\partial \rho}{\partial t}\right) = \nabla \cdot (\rho \mathbf{u}), \tag{2.8}$$

$$\rho \left(\frac{\partial \mathbf{u}}{\partial t} + \mathbf{u} \cdot \nabla \mathbf{u}\right) = -\nabla p + \mu(\nabla \cdot \nabla \mathbf{u}) + \mathbf{f}. \tag{2.9}$$

Here ρ is the density, t is the time, $\mathbf{u}$ is the velocity, p is the pressure, μ is the dynamic viscosity, $\mathbf{f}$ denotes external forces, ∇ is the gradient operator, and $\nabla\cdot$ is the divergence operator.

In order to close these two equations, it is necessary to have a relation between pressure p and density ρ. In the upper parts of planetary atmospheres, it is fine to assume that collisions in the gaseous atmosphere are dominated by two body encounters. Furthermore, we may assume that intermolecular forces are not important, because the gas particles are too far separated from each other. We can then describe the gas as an ideal gas, which yields a relation between pressure and density

$$p = \rho R_s T, \tag{2.10}$$

where $R_s = \frac{R}{m}$ is the specific gas constant, with the universal gas constant $R = 8.31 \times 10^7 \, \mathrm{erg\,K^{-1}\,mol^{-1}}$ and m the molar mass of the gas under consideration.

Finally, we may combine the momentum equation and continuity equation with the first law of thermodynamics

$$\delta Q = dU - p\,dV, \tag{2.11}$$

which states that a parcel of gas needs to either be heated (δQ) or perform work by expanding/contracting to change its internal energy $dU = c_V dT$, where c_V is the heat capacity at constant volume.

It is often useful to write the equations of motion using a total derivative, also often called material derivative. The total derivative is given by

$$\frac{D}{Dt} = \frac{\partial}{\partial t} + \mathbf{u} \cdot \nabla, \tag{2.12}$$

and describes the motion of the gas by following a fluid parcel with velocity, which we will refer to as the Lagrangian form. We can thus write Eq. 2.8 as

$$\frac{D\rho}{Dt} + \rho \nabla \cdot \mathbf{u} = 0, \tag{2.13}$$

and the equation of momentum conservation as

$$\rho \frac{D\mathbf{u}}{Dt} = -\nabla p + \mu(\nabla \cdot \nabla \mathbf{u}) + \mathbf{f}. \tag{2.14}$$

Momentum Conservation

For planetary atmospheres, we can often assume that the viscosity is negligible. We will thus drop $\mu(\nabla \cdot \nabla \mathbf{u})$ from Eq. 2.14. This assumption does not imply that general circulation models are free of viscosity. In fact, every algorithm that solves an advection problem always imposes a numerical viscosity, caused

by the underlying discretization of the problem. However, for the scope of this thesis, we will assume that the physical viscosity in planetary atmospheres is zero.

The above Eqs. 2.14 and 2.13 are only valid in a non-rotating (inertial) frame of reference. Since the equations are invariant to translation, we only have to take acceleration terms into account, when switching to a rotating frame of reference. We can thus switch between a rotating frame of reference and an inertial frame of reference by formulating the velocity in the inertial frame of reference u_{ini} as a sum of the contribution due to rotation and a co-rotating velocity u_{rot}

$$\mathbf{u}_{ini} = \mathbf{u}_{rot} + \Omega \times \mathbf{r}, \tag{2.15}$$

where $\mathbf{r}$ is the position vector, $\times$ is the cross-product, and Ω is the vector of the angular velocity.

Inserting u_{ini} into the material derivative, we can derive (Marshall & Plumb, 2007)

$$\frac{D\mathbf{u}_{ini}}{Dt} = \frac{D\mathbf{u}_{rot}}{Dt} + 2\Omega \times \mathbf{r} + \Omega \times \Omega \times \mathbf{r}, \tag{2.16}$$

which yields the extra terms $2\Omega \times \mathbf{r}$ and $\Omega \times \Omega \times \mathbf{r}$, where the former is the Coriolis force and the latter is the centrifugal force. Since the centrifugal force points into the opposite direction of the gravity and since we can write the centrifugal force as a gradient of a potential, we can absorb gravity and centrifugal force into an effective gravity

$$\nabla\phi \equiv g\mathbf{e}_z + \Omega \times \Omega \times \mathbf{r} = \nabla(gz - \frac{\Omega^2}{2r^2}), \tag{2.17}$$

where we then use $\nabla\phi$ in Eq. 2.14 as part of the external forces $\mathbf{f}$.

We can often assume that the vertical acceleration and vertical Coriolis force are negligible, since the vertical scale height is much smaller than the horizontal scale of the atmosphere. Thus, the z-component of the momentum equation can be written as

$$\begin{aligned} \underbrace{\rho\left(\frac{\partial u_z}{\partial t} + \left[u_x\frac{\partial u_z}{\partial x} + u_y\frac{\partial u_z}{\partial y} + u_z\frac{\partial u_z}{\partial z}\right]\right)}_{\approx 0} &= -\frac{\partial p}{\partial z} - \rho g \\ \rightarrow \left(\frac{\partial p}{\partial z}\right) &= -\rho g. \end{aligned} \tag{2.18}$$

This assumption is called hydrostatic equilibrium or assumption of hydrostasy and will be applied throughout this thesis. We note, however, that it has been

shown that the assumption of hydrostasy breaks down for sub Neptunes and super Earths (Mayne et al., 2014, 2019).

Transforming into spherical coordinates (φ, ϑ, r) and velocities (u, v, ω), we can write the momentum equation as (e.g., Holton, 1992; Mayne et al., 2014)

$$\begin{aligned}
\frac{Du}{Dt} - \frac{uv\tan\varphi}{r} + \frac{uw}{r} &= -\frac{1}{\rho}\frac{\partial p}{\partial x} + 2\Omega v\sin\varphi - 2\Omega\omega\cos\varphi + F_x \\
\frac{Dv}{Dt} + \frac{u^2\tan\varphi}{r} + \frac{vw}{r} &= -\frac{1}{\rho}\frac{\partial p}{\partial y} - 2\Omega u\sin\varphi + F_y \\
\frac{D\omega}{Dt} + \frac{u^2+v^2}{r} &= -\frac{1}{\rho}\frac{\partial p}{\partial z} - \frac{\partial\phi}{\partial z} + 2\Omega u z\cos\varphi + F_z.
\end{aligned} \tag{2.19}$$

Additionally, to the assumption of hydrostasy (Eq. 2.18), two more assumptions are useful and valid in planetary atmospheres. The first additional assumption is the so-called traditional assumption (for a review see Mayne et al. (2014, 2019)), which drops negligible terms, including terms with vertical velocity: $\frac{\omega u}{r}, \frac{v\omega}{r}, \frac{u^2+v^2}{r}, 2\Omega u\cos\varphi, 2\Omega\omega\cos\varphi$. The second additional assumption is the assumption of a shallow fluid, where we assume that the atmosphere is thin in comparison to the planetary radius such that we can approximate $r = R_p + a \approx R_p$. Putting these assumptions together, we yield the hydrostatic primitive equations (HPE) as shown below.

Mass Conservation

It is often less optimal to use geometric coordinates in atmospheric dynamics, since the mass of a given volume ($\delta V = \delta x\,\delta y\,\delta z$) of a compressible fluid parcel is not conserved in geometric coordinates. This is because the mass of the parcel (δM) depends on the density as

$$\delta M = \rho\,\delta x\,\delta y\,\delta z, \tag{2.20}$$

which can vary and so the mass is not conserved in the volume δV. However, if we can assume hydrostatic equilibrium, we can use Eq. 2.18 and show that

$$\begin{aligned}
\delta M &= \rho\left(\frac{\partial p}{\partial z}\right)^{-1}\delta x\,\delta y\,\delta p \\
&= -\frac{1}{g}\,\delta x\,\delta y\,\delta p,
\end{aligned} \tag{2.21}$$

and thus the mass in pressure coordinates (x, y, p) is conserved, since g is a constant. Thus, if we use pressure coordinates, we can write the continuity equation in a much simpler form

$$\nabla_p \cdot \mathbf{u}_p = 0, \tag{2.22}$$

where ∇_p is the gradient in pressure coordinates and $\mathbf{u}_p$ is the velocity in pressure coordinates.

Energy Conservation

Following a gas parcel of unit mass ($M = \rho V = 1$), we can find that the inner energy ($dU = c_V\, dT$) of a gas parcel can either perform work by contracting ($p\, dV$) or cool/heat by external heating δQ, leading to the first law of thermodynamics (Eq. 2.11). By repeatedly using the ideal gas equation (Eq. 2.10) on the first law of thermodynamics, we find that we can express the work $p\, dV$ as

$$\begin{aligned} p\, dV &= p\, d\left(\frac{1}{\rho}\right) = -\frac{p}{\rho^2} d\rho \\ &= -\frac{p}{\rho^2}\left[\frac{\rho}{p} dp - \frac{\rho}{T} dT\right] \\ &= \frac{1}{\rho} dp - R\, dT. \end{aligned} \tag{2.23}$$

Using the heat capacity at constant pressure, $c_p = c_V + R$, we can thus find that Eq. 2.11 can be written as

$$\delta Q = c_p\, dT - \frac{1}{\rho} dp. \tag{2.24}$$

If the parcel is adiabatically heated, $\delta Q = 0$, and by applying the ideal gas law and using $d \log x = \frac{dx}{x}$, we can rewrite Eq. 2.24 as

$$\begin{aligned} 0 &= c_p\, dT - \frac{RT}{p} dp \\ &= d \log T - \frac{R}{c_p} d \log p \end{aligned} \tag{2.25}$$

and we can thus find that in the absence of external heating $\delta Q = 0$:

$$p^{\frac{R}{c_p}} \propto T \tag{2.26}$$

It is thus useful to define the potential temperature Θ that satisfies Eq. 2.26

$$\Theta \equiv \left(\frac{p_0}{p}\right)^{\frac{R}{c_p}} T. \tag{2.27}$$

Inserting Θ and by dividing by an infinitesimal small δt, we can rewrite the first law of thermodynamics from Eq. 2.24 to

$$\frac{D\Theta}{Dt} = \frac{1}{c_p}\left(\frac{p}{p_0}\right)^{-\frac{R}{c_p}} \frac{DQ}{Dt}. \tag{2.28}$$

Throughout this work, we follow the common assumption that radiative transport in planetary atmospheres can be solved in independent 1D vertical atmospheric columns, thus assuming that radiation mainly travels upward and downwards (e.g., Showman et al., 2009; Rauscher & Menou, 2012; Komacek et al., 2017; Amundsen et al., 2016; Lee et al., 2021; Deitrick et al., 2022). The change of temperature in an atmospheric layer, that absorbs a different amount of radiation than it emits, can be related to the difference between the flux F_{net} that passes into the layer and what comes out of the layer. We can write the heating/cooling of the layer $\frac{DQ}{Dt}$ as

$$\begin{aligned}\frac{DQ}{Dt} &= -\frac{1}{\rho}\frac{\partial F_{net}}{\partial z} \\ &= g\frac{\partial F_{net}}{\partial p},\end{aligned} \tag{2.29}$$

where we assumed hydrostatic equilibrium in the last step (Eq. 2.18). Other heating and cooling terms may be given by dissipation, such as Ohmic dissipation. This occurs when the magnetic field of the planet slows down ions in the atmospheric flow, thus exerting a friction on the wind flow, which leads to heating (e.g., Perna et al., 2010b; Rauscher & Menou, 2012; Beltz et al., 2022a).

Hydrostatic primitive equations

The hydrostatic primitive equations (HPE) are derived by combining the above-mentioned approximation of hydrostasy, traditional approximation, and shallow fluid approximation for an inviscid ideal gas. Taking together Eq. 2.22 for the mass conservation in p-coordinates, Eq. 2.28 as a version of the first law of thermodynamics, we yield

$$\begin{aligned}\nabla_p \cdot \mathbf{v}_h + \frac{\partial \omega}{\partial p} &= 0 \\ \frac{D\mathbf{v}_h}{Dt} + 2\Omega \sin\varphi\, \mathbf{e}_z \times \mathbf{v}_h + \nabla_p \phi &= \mathbf{F} \\ \frac{\partial \phi}{\partial p} + \frac{1}{\rho} &= 0 \\ \frac{D\Theta}{Dt} &= \frac{1}{c_p}\left(\frac{p}{p_0}\right)^{-\frac{R}{c_p}} \frac{DQ}{Dt},\end{aligned} \tag{2.30}$$

where $\mathbf{v}_h$ is the horizontal velocity and $\mathbf{e}_z$ is the unit vector in the vertical direction. This is the set of equations, which is solved in the `MITgcm`, which will be used throughout this thesis to model the atmospheric dynamics of hot gas

giant exoplanets. It is important to note that the HPE assume that the vertical wind is a diagnostic of the horizontal wind. Thus, gravity waves, shocks, convection, and other small scale non-hydrostatic behavior can not be modeled by the HPE. Most of these effects, however, require a very fine resolution to be properly resolved, and are thus impossible to resolve with the coarse resolution typically applied in GCMs of hot Jupiters.[1] Deitrick et al. (2020) and Noti et al. (2023) show that GCM simulations with fewer approximations compared to the HPE have differences in the vertical temperature profile and wind speeds. These differences seem to be especially important for fast rotation rates, low gravity, and strong stellar irradiation (Noti et al., 2023).

2.2.2 *MITgcm*

The `MITgcm` (Marshall et al., 1997a,b; Adcroft et al., 2004) is a General Circulation Model (GCM), developed by scientists at the Massachusetts Institute of Technology to model the dynamics of Earth's atmosphere and ocean. The `MITgcm` includes a dynamical core that solves the equations of hydrodynamics, as well as packages for physical parameterization of the atmosphere and ocean. Finite volume methods used to treat the topography of oceans and mountains (Adcroft et al., 1997). It is optimized for a variety of computing architectures and can employ parallel computing to speed up computations (Marshall et al., 1997a; Hill et al., 1999). Furthermore, automatic differentiation enables sensibility studies (Heimbach et al., 2002).

Naive gridding of the sphere, such as spherical longitude latitude grids, result in singularities at the poles, where the density of grid points rises to infinity and thus the size of grid cells goes to zero. This then raises a problem with the explicit time stepping, because the size of the time step needs to be proportional to the size of the grid according to the Courant-Friedrich-Lewy (CFL) condition of stability in hydrodynamic simulations. To circumvent this issue, GCMs often either use a different grid type or apply smoothing over the singularities to stabilize the model. In this work, we use the `MITgcm` with a cubed sphere grid (see Fig. 2.1), which can be constructed by projecting a cube on a sphere. The advantage of such a grid is that it does not cause singularities, but instead has similar sized grid cells on the full globe. The disadvantage, however, is that numerical instabilities can arise at the edges and corners of the cube. Furthermore, it is generally inconvenient to work with cubed-sphere coordinates, when analyzing model outputs. We have thus

1 In order to mimic convection, which can not be selfconsistenly resolved with the resolution of a GCM, some models (e.g., Lee et al., 2021) include a convective adjustment scheme, which forces the pressure temperature profile to be adiabatic, when it becomes super adiabatic.

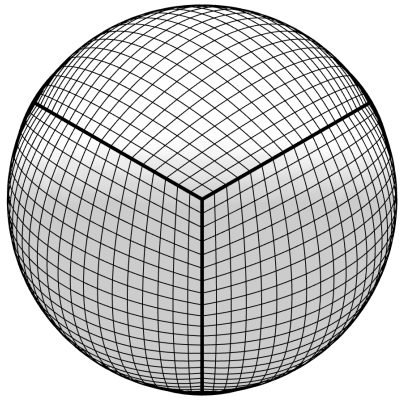

Figure 2.1: Visualization of the cubed sphere geometry. The plot has been generated using the code from https://github.com/JiaweiZhuang/Plotly_CubedSphere

developed the python package `cubedsphere`[2], a tool to regrid model outputs to a longitude-latitude grid. We use a version of the cubed sphere grid with 32×32 grid cells (hereafter C32) in each of the 6 faces. This corresponds to a resolution of approximately $2.8° \times 2.8°$ in longitude and latitude.

We use several smoothing schemes to make the model more stable. A fourth-order Shapiro filter (Shapiro, 1970) is applied to reduce grid-scale noise, associated with the corners of the cubed sphere grid. Additionally, drag in the upper and deepest layers prevents instabilities that create wave-like structures, such as gravity waves. Since the HPE does not permit gravity waves as a solution, these must be avoided. The use of these schemes is further detailed and explained in Carone et al. (2020) and Schneider et al. (2022b,a).

2.3 RADIATIVE TRANSFER IN PLANETARY ATMOSPHERES

One of the main contributions of this thesis is the implementation of radiative transfer into `MITgcm`. Accurate radiative transfer is needed to line up observations of exoplanets with their models. It is thus arguably the most important tool in astrophysics, because it is vital not only to understand what we observe, but also for the understanding of how things work. The following section aims to introduce the most important concepts in the context of planetary atmospheres and explains how radiative transfer is solved in `expeRT/MITgcm`

2 https://cubedsphere.readthedocs.io/en/latest/

(Schneider et al., 2022b). Most of the derivations shown in this section base on the lecture about radiative transfer by Cornelis Dullemond (Dullemond, 2012).

2.3.1 *The radiative transfer approximation*

The propagation of light is subject to the Maxwell equations. However, in many cases in astrophysics we are interested in the macroscopic propagation of light, where macroscopic means that the wavelength of the light is much shorter than the size of the medium through which it propagates. In such cases, we can treat the propagation of light in terms of geometric optics. Furthermore, in planetary atmospheres and stellar atmospheres, we can often assume that the refractive index of the medium is close to one (e.g., not like a surface). This is the basis of the radiative transfer approximation.

A photon with frequency ν traveling along a straight line through a medium (e.g., a planetary atmosphere) can be absorbed or scattered. Furthermore, new photons can be created. Absorption and scattering events can be described in terms of a mean free path ($l_{\nu,\text{free}}$) that a photon travels until such an event happens. The inverse of $l_{\nu,\text{free}}$ is called extinction coefficient α_ν. The extinction coefficient is given as

$$\alpha_\nu = \kappa_\nu \rho, \tag{2.31}$$

where ρ is the density of the medium and κ_ν is the opacity or cross-section.[3]

The energy per unit area and time into a given direction is often referred to as intensity in astrophysical applications. The intensity (I_ν) is in principle a 7 dimensional quantity, with 3 spatial coordinates, 2 angular dependencies, a time dependency and a frequency dependency. In this thesis, we can omit the time dependency of the problem, since light travels with the speed of light, which is fast enough to propagate information almost instantly in a planetary atmosphere.

For convenience, we will work in angular coordinates, where we can write the unit vector of the direction of the light $\mathbf{n}$ as

$$\mathbf{n} = \begin{pmatrix} \cos(\phi)\sin(\theta) \\ \sin(\phi)\sin(\theta) \\ \cos(\theta) \end{pmatrix}. \tag{2.32}$$

We can now formulate the formal equation of radiative transfer as

$$\mathbf{n} \cdot \nabla I_\nu(\mathbf{n}, \mathbf{x}) = j_\nu(\mathbf{x}) - \alpha_\nu(\mathbf{x}) I_\nu(\mathbf{n}, \mathbf{x}), \tag{2.33}$$

3 The term opacity is also often used for the extinction coefficient. In this thesis, we will refer to opacity as cross-section and not as inverse mean free path.

where j_ν is the emissivity (e.g., the photons created). The formal equation of radiative transfer tells us that a change in intensity occurs by extinction ($\alpha_\nu I_\nu$) or emission (j_ν). We can define the source function S_ν as

$$S_\nu \equiv \frac{j_\nu}{\alpha_\nu}, \tag{2.34}$$

and write Eq. 2.33 in terms of the change of intensity along a straight path s

$$\frac{dI_\nu(\mathbf{n}, s)}{ds} = \alpha_\nu[S_\nu(s) - I_\nu(\mathbf{n}, s)], \tag{2.35}$$

in a differential form or

$$I_\nu(\mathbf{n}, s_1) = I_\nu(\mathbf{n}, s_0)e^{-\tau_\nu(s_0,s_1)} + \int_{s_0}^{s_1} \alpha_\nu(s)S_\nu(s)e^{-\tau(s,s_1)}ds \tag{2.36}$$

in an integral form. Here, we defined the optical depth τ as

$$\tau_\nu(s_0, s_1) \equiv \int_{s_0}^{s_1} \alpha_\nu ds. \tag{2.37}$$

The intensity in a medium (e.g., a gas) with homogeneous temperature T in local thermodynamic equilibrium (LTE) in all direction is given by the Planck function.

$$B_\nu(T) = \frac{2h\nu^3}{c^2}\frac{1}{e^{\frac{h\nu}{k_B T}} - 1}, \tag{2.38}$$

where $h = 6.626\,070\,15 \times 10^{-27}$ erg s is the Planck constant,
$c = 2.997\,924\,58 \times 10^{10}$ cm s^{-1} is the speed of light, and
$k_B = 1.3807 \times 10^{-16}$ cm^2 g s^{-2} K^{-1} is the Boltzmann constant. For such a homogeneous medium in LTE, we can insert $I_\nu(\mathbf{n}, s) = B_\nu(T)$ in Eq. 2.35 and then get

$$\frac{dI_\nu(\mathbf{n}, s)}{ds} = 0 = \alpha_\nu[S_\nu(s) - B_\nu(T)], \tag{2.39}$$

which is equivalent to Kirchhoff's law of thermal radiation

$$S_\nu = B_\nu(T). \tag{2.40}$$

Planetary atmospheres are thin shells, where the height of the shell (e.g., along the z-axis) is much smaller in comparison to the horizontal dimensions (longitude and latitude). We therefore assume that the x, y-plane is locally

parallel to the longitude-latitude plane, or more qualitatively that the atmosphere is locally flat. Furthermore, we will assume local translational and rotational symmetry (e.g., no dependence on x, y and no dependence on the angle ϕ in Eq. 2.32). Putting these assumptions together, we end up with the plane-parallel assumption, and we can formulate Eq. 2.35 as

$$\mu \frac{dI_\nu(z,\mu)}{dz} = \alpha_\nu(z)[S_\nu(z) - I_\nu(z,\mu)], \tag{2.41}$$

where we defined

$$\mu = \cos(\theta). \tag{2.42}$$

The plain parallel assumption reduces the problem from 3 spatial dimensions to 1 spatial dimension and from 2 angular dependencies to 1 angular dependency. In the scope of this thesis, we will only work with the plane parallel assumption, assuming that the mentioned assumptions hold.

It is often useful to define moments of the intensity. We can define the zeroth and first moment as

$$J_\nu \equiv \frac{1}{4\pi} \int_\Omega I_\nu(\mathbf{n}) d\Omega \tag{2.43}$$

$$\mathbf{H} \equiv \frac{1}{4\pi} \int_\Omega I_\nu(\mathbf{n}) \mathbf{n} d\Omega, \tag{2.44}$$

where we used Ω as the solid angle. If we use the plane parallel assumption, we get

$$J_\nu = \frac{1}{2} \int_{-1}^{1} I_\nu(\mu) d\mu \tag{2.45}$$

$$H_\nu = \frac{1}{2} \int_{-1}^{1} I_\nu(\mu) \mu d\mu. \tag{2.46}$$

The zeroth moment is simply the mean of the intensity in all directions and is thus called mean intensity and describes the amount of photons available at a given position $\mathbf{x}$. The first moment is proportional to the Flux:

$$\mathbf{F} = -4\pi\mathbf{H} \tag{2.47}$$

Multiple scattering

If we have both scattering and absorption/emission, we can split the emissivity j_ν into two parts

$$j_\nu = j_\nu^{\text{emis}} + j_\nu^{\text{scat}}, \tag{2.48}$$

and similarly the extinction coefficient can be split into two parts

$$\alpha_\nu = \alpha_\nu^{\text{abs}} + \alpha_\nu^{\text{scat}}, \tag{2.49}$$

Thus, inserting j_ν and α_ν into Eq. 2.34, we yield

$$S_\nu = \frac{j_\nu}{\alpha_\nu} = \frac{j_\nu^{\text{emis}} + j_\nu^{\text{scat}}}{\alpha_\nu^{\text{abs}} + \alpha_\nu^{\text{scat}}}. \tag{2.50}$$

It will now be useful to define the albedo η_ν and the photon destruction probability ϵ_ν as

$$\begin{aligned} \eta_\nu &\equiv \frac{\alpha_\nu^{\text{scat}}}{\alpha_\nu^{\text{abs}} + \alpha_\nu^{\text{scat}}} \\ \epsilon_\nu &\equiv \frac{\alpha_\nu^{\text{abs}}}{\alpha_\nu^{\text{abs}} + \alpha_\nu^{\text{scat}}}. \end{aligned} \tag{2.51}$$

According to Eq. 2.40, we know that $\frac{j_\nu^{\text{emis}}}{\alpha_\nu^{\text{abs}}} = B_\nu(T)$. If the scattering is isotropic, we further find that $\frac{j_\nu^{\text{scat}}}{\alpha_\nu^{\text{scat}}} = J_\nu$. Using the definitions in Eq. 2.51, the source function can be rewritten as

$$S_\nu = \epsilon_\nu B_\nu(T) + (1 - \epsilon_\nu) J_\nu. \tag{2.52}$$

In other words, a photon might scatter multiple times and travel multiple $l_{\nu,free}$ before it either escapes or gets destroyed by absorption. The solution to the problem thus becomes harder the smaller ϵ_ν gets, because J_ν depends on I_ν, which depends on S_ν. We will discuss a possible numerical solution to this problem below in Section 2.3.3.

Stellar irradiation

There are two ways of including stellar irradiation impinging the planet into Eq. 2.33. Either by setting the boundary condition when integrating the radiative transfer equation (Eq. 2.41) such that the intensity at the top of the atmosphere (TOA) is given by the stellar irradiation, or by separating the

intensity from the stellar radiation field ($I_\nu^\star$) from the planetary radiation field (I_ν^{pla}) as

$$I_\nu = I_\nu^\star + I_\nu^{pla}. \tag{2.53}$$

Since the radiative transfer equation (Eq.2.35) is linear in I_ν, the problem separates into two separate problems, with the advantage that the anisotropy of the stellar radiation field is easier to treat compared to the coupled boundary condition approach.

Suppose, the planet is irradiated at an angle $\Omega_\star$ with respect to the atmospheric normal. Using this approach, we can split 2.41 into two equations.

$$\mu_\star \frac{dI_\nu^\star}{dz} = -\alpha_\nu(z) I_\nu^\star(z, \mu_\star) \tag{2.54}$$

and

$$\mu \frac{dI_\nu^{pla}}{dz} = \alpha_\nu(z)[S_\nu(z) - I_\nu^{pla}(z, \mu)], \tag{2.55}$$

where Eq. 2.52 becomes

$$S_\nu = \epsilon_\nu B_\nu(T) + (1 - \epsilon_\nu)(J_\nu^{pla} + J_\nu^\star), \tag{2.56}$$

which will be used to find the solution to the planetary radiation field.

If we assume that the star is a point source, illuminating the planet[4], we find that the received flux at TOA is given by

$$F_\nu^\star(TOA) = -\mu_\star \frac{L_\nu^\star}{4\pi d^2}. \tag{2.57}$$

Using the z-component of the moment definitions in Eq. 2.44 and using that the stellar intensity is only non-zero for one specific angle ($\Omega = \Omega_\star$ or equivalently $\mu = \mu_\star$)

$$I_\nu^\star(z, \Omega) = \begin{cases} I_\nu^\star(z) & \text{if } \Omega = \Omega_\star \\ 0 & \text{else} \end{cases}. \tag{2.58}$$

We can thus find that

$$F_\nu^\star(z) = -4\pi \frac{1}{4\pi} \int_\Omega \delta(\Omega - \Omega_\star) \mu I_\nu^\star(z, \Omega) d\Omega = -\mu_\star I_\nu^\star(z, \mu_\star) \tag{2.59}$$

4 Note that a similar derivation with assuming that the star has some angular size $\Delta\Omega$, yields the same result, see e.g., Mollière et al. (2015)

and for the mean intensity we find that

$$J^{\star}_{\nu}(z) = \frac{1}{4\pi}\int_{\Omega} \delta(\Omega - \Omega_{\star}) I^{\star}_{\nu}(z,\Omega) d\Omega = \frac{I^{\star}_{\nu}(z,\mu_{\star})}{4\pi}. \tag{2.60}$$

Furthermore Eq. 2.54 is a simple differential equation with analytical solution, when using Eq. 2.57 as a boundary condition:

$$I^{\star}_{\nu}(z,\mu_{\star}) = \frac{L^{\star}_{\nu}}{4\pi d^2} \exp\left(-\frac{\tau(0,z)}{\mu_{\star}}\right). \tag{2.61}$$

Putting together Eqs. 2.59 and 2.60 with Eq. 2.61, we find that

$$\begin{aligned} J^{\star}_{\nu}(z) &= \frac{L^{\star}_{\nu}}{(4\pi)^2 d^2} \exp\left(-\frac{\tau(0,z)}{\mu_{\star}}\right) \\ F^{\star}_{\nu}(z) &= -\mu_{\star}\frac{L^{\star}_{\nu}}{4\pi d^2} \exp\left(-\frac{\tau(0,z)}{\mu_{\star}}\right). \end{aligned} \tag{2.62}$$

2.3.2 *Opacities*

As we have seen in 2.3.1, we need to know about the optical properties of the medium in order to be able to tell how the intensity changes along the ray. There are multiple sources of absorption and emission that play a role in planetary atmospheres. The main constituents are gas absorption and emission, small particles in the form of clouds or hazes that scatter the light, Rayleigh scattering and collision induced absorption (CIA). Since our models do not yet include clouds and hazes, we will limit the discussion to lines (gas absorption and emission) and continuum sources (Rayleigh scattering, CIA).

Lines

Molecules and atoms can absorb and emit radiation by increasing and lowering quantum mechanical states. In case of atoms, these are electronic transitions, where electrons get promoted to higher energy levels by absorbing a photon and subsequently emitting a photon when descending back to the ground state. Due to the geometry of molecules, rotational and vibrational transitions dominate in the case of molecules.

A molecule or atom can be excited from one energy level (E_j) to a higher one (E_i) by absorbing a photon with frequency

$$\nu_{ij} = \frac{E_i - E_j}{h}. \tag{2.63}$$

Similarly, the reverse process of deexcitation from E_i to E_j emits a photon of frequency ν_{ij}. As such, in this simple approximation, this form of emission and absorption, called line emission/absorption needs an exact match of the frequency ν_{ij} with the energy levels of the molecule or atom. This is, however, not exactly true since lines are broadened by various physical mechanisms, which we will discuss below.

In LTE, we find that the probability $n_i = \frac{N_i}{N}$ to find an atom or molecule in state i is given by

$$n_i = \frac{g_i \exp\left(\frac{-E_i}{k_B T}\right)}{\sum_j g_j \exp\left(\frac{-E_j}{k_B T}\right)}, \tag{2.64}$$

where g_i is the statistical weight of level i (e.g., how many independent quantum states yield the same energy level).

The emissivity $j_{ij,\nu}$ and extinction coefficient $\alpha_{ij,\nu}$ of a spontaneous transition from i to j is given by

$$\begin{aligned} j_{ij,\nu} &= \frac{h\nu_{ij}}{4\pi} N_i A_{ij} \Phi_{ij}(\nu) \\ \alpha_{ij,\nu} &= \frac{h\nu_{ij}}{4\pi} \Phi_{ij}(\nu)(N_j B_{ji} - N_i B_{ij}), \end{aligned} \tag{2.65}$$

where $\Phi(\nu)$ is the line profile (see below in Section 2.3.2), B_{ij}, B_{ji} and A_{ij} are the Einstein coefficients for which one is sufficient to know to get the other two using the Einstein relations

$$A_{ij} = \frac{2h\nu_{ij}^3}{c^2} B_{ij} \qquad\qquad g_i B_{ij} = g_j B_{ji}. \tag{2.66}$$

It is common to have tabulated values (so-called line lists) for Einstein coefficients A_{ij} along with the corresponding energy level E_i, frequency of the transition ν_{ij} and the statistical weights g_i and g_j. The exomol project (Tennyson et al., 2016)[5] is currently the best option for lines of molecules in exoplanetary atmospheres.

Continuum

In addition to the narrow line emission and absorption, molecules can also give rise to broader opacities.

In the limit of particle sizes much smaller than the wavelength ($a \ll \lambda$), light will scatter elastically with particles, causing the particles to be excited

5 www.exomol.com

to oscillate and thus inducing a dipole moment. This so-called Rayleigh scattering has a dependence on the wavelength with $\alpha \propto \frac{1}{\lambda^4}$ and thus creates a slope (the so called Rayleigh-slope) in spectra of exoplanetary atmospheres. In the case of hydrogen dominated atmospheres, such as those of hot gas giants, Rayleigh scattering will be dominated by scattering with H_2 and He.

If two molecules collide with each other, van der Waals forces will create a dipole field, allowing previously inaccessible energy transitions in the collision partners. This so called collision induced absorption (CIA) is typically dominated by collisions between the most prominent molecules in the gas mixture, such as H_2 in a hydrogen dominated atmosphere. Furthermore, CIA is pressure dependent, since more collision events take place at higher densities.

Lineprofiles

There are four basic mechanisms that broaden the frequency at which emission and absorption is possible. These mechanisms can be divided into two different line profiles (Gaussian and Lorentzian). We will start by summarizing natural line broadening and pressure broadening, which give rise to a Lorentzian shape in the line profile.

The transition to a higher energy level can be described as a damped harmonic oscillator, where the damping encapsulates the spontaneous decay of the energy level (natural broadening) or the disturbance of the phase by collision (collisional broadening). The Fourier transform of the damped harmonic oscillator then yields the line profile and is given by a Lorentzian

$$\Phi(\nu) = \frac{1}{\pi} \frac{\gamma_i}{(\nu - \nu_i)^2 + \gamma_i^2}, \tag{2.67}$$

where γ_i is given by natural broadening and collisional broadening

$$\gamma_i = \gamma_{i,nat} + \gamma_{i,col}. \tag{2.68}$$

The coefficient for natural broadening ($\gamma_{i.nat}$) is proportional to the spontaneous decay rate of E_i, whereas the coefficient for collisional broadening ($\gamma_{i,col}$) depends on the amount of collision events and is thus proportional to the pressure.

Since the gas particles follow a Gaussian velocity distribution, the light will be naturally Doppler shifted with respect to the co-moving frame of a gas particle. The resulting line profile is thus given by a Gaussian

$$\Phi(\nu) = \frac{1}{\gamma_{i,dop}\sqrt{\pi}} \exp\left(-\frac{(\nu - \nu_i)^2}{\gamma_{i,dop}^2}\right), \tag{2.69}$$

where $\gamma_{i,dop}$ is given by

$$\gamma_{i,dop} = \frac{\nu_i}{c}\sqrt{\sigma^2}, \tag{2.70}$$

where σ^2 is the velocity variance of the gas particles. The velocity variance of the gas can be given by two components: A thermal component (σ_{th}) and a component that captures turbulent sub-grid processes (σ_m). The variance of the velocity distribution can then be written as

$$\sigma^2 = \sigma_{th}^2 + \sigma_m^2. \tag{2.71}$$

The thermal part of this equation σ_{th} comes from the thermal motion of the gas and is given by the single directional (along the line of sight) variance of the gas velocity distribution as

$$\sigma_{th} = \sqrt{\frac{2k_B T}{m}}. \tag{2.72}$$

The turbulent sub-grid component, also called microturbulance, is often used in stellar atmosphere models (e.g., Gustafsson et al., 2008) to mimic physical processes that are not resolved in a model. It is thus also often used as a free fitting parameter to match model predictions to observations.

Combining all of these four different line broadening mechanisms can be done by convolving the two line profiles (Gaussian and Lorentzian), which yields a Voigt profile. We show the opacity of H_2O, sampled with a wavenumber resolution of $0.01\,cm^{-1}$, for two pressure values at a temperature of 1500 K in Figure 2.2 to demonstrate the effect of line broadening on the opacity. The figure has been created with the lines for water from Polyansky et al. (2018), which are broadened by a Voigt profile using the `HELIOS-K`(Grimm & Heng, 2015; Grimm et al., 2021) opacity calculator.[6] Figure 2.2 demonstrates that the opacity of water consists of millions of lines, which at higher pressure overlap in their line profiles (also called wings).

Equilibrium Chemistry

The total opacity of a gas mixture is the sum of mass-weighted contributions of the individual molecules and atoms. We can thus write the total opacity $\kappa_{\nu,tot}$ as

$$\kappa_{\nu,tot} = \sum_i X_i \kappa_{\nu,i}, \tag{2.73}$$

6 The opacity files have been downloaded from the DACE database (https://dace.unige.ch/opacityDatabase/).

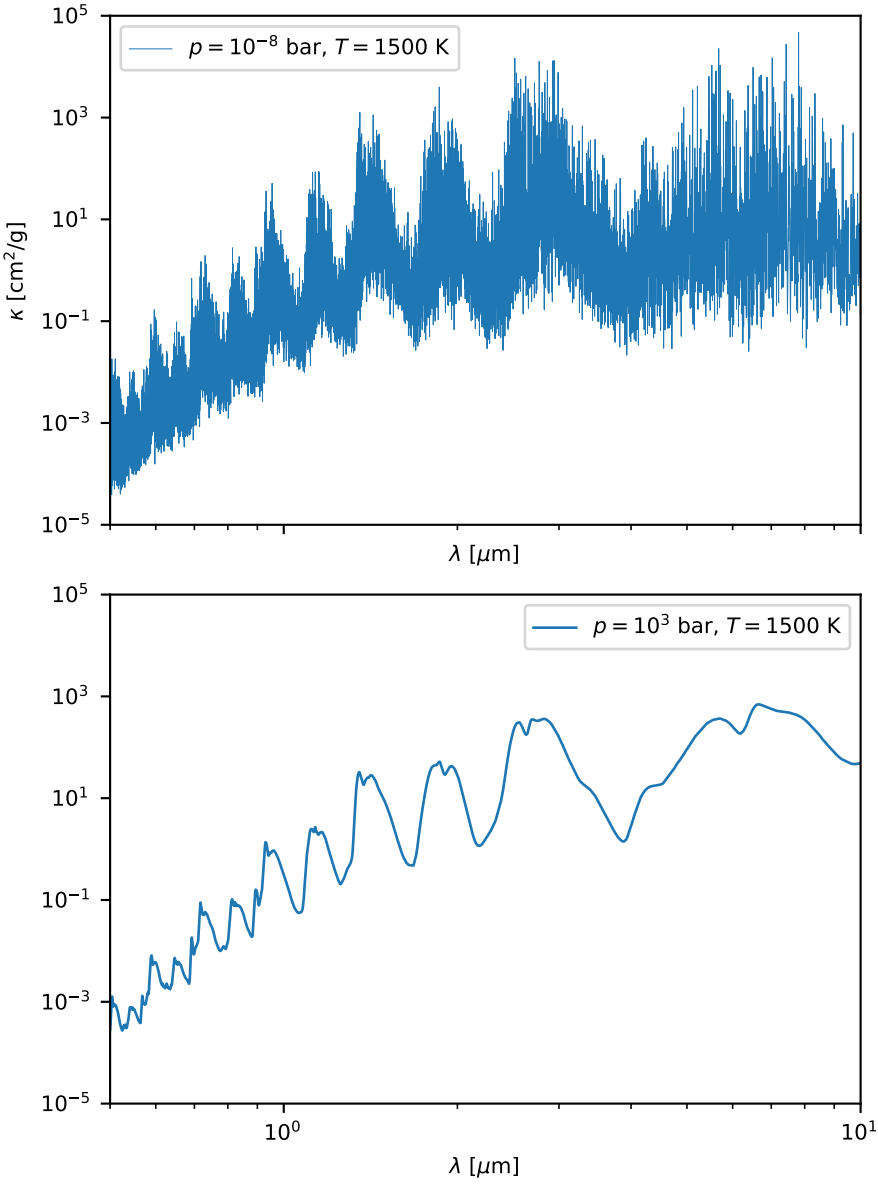

Figure 2.2: Opacity of H_2O at two different pressure values at T = 1500 K.

where X_i denotes the mass mixing ratio (abundance hereafter) of species (molecule or atom) i and $\kappa_{\nu,i}$ is its respective opacity. We therefore need to know the abundances of species in the gas. In the scope of this thesis, we will use equilibrium abundances, we note however, that chemical processes such as photochemistry and transport can significantly alter abundances from their equilibrium abundances (e.g., Drummond et al., 2018b, 2020; Baeyens et al., 2021, 2022; Lee et al., 2023).

To find chemical equilibrium, we start by describing chemical reactions at constant pressure and constant temperature thermodynamically using the Gibbs free energy G

$$dG = dU + pdV - TdS, \tag{2.74}$$

where T is the temperature, S is the entropy, U is the inner energy, and V is the volume.

The first law of thermodynamics states that for a closed system in which only mechanical work is possible, the change of the inner energy is given by the energy being added to the system in the form of heat (δQ) and the work performed by the system pdV:

$$dU = \delta Q - pdV \tag{2.75}$$

Thus, inserting this into the Gibbs free energy (Eq. 2.74) yields

$$dG = \delta Q - TdS. \tag{2.76}$$

According to the second law of thermodynamics, in a closed system $TdS \geqslant \delta Q$, therefore Eq. 2.76 yields

$$dG \leqslant 0. \tag{2.77}$$

Thus, the chemical reaction can only decrease the Gibbs free Energy, meaning that chemical equilibrium implies minimal Gibbs free energy. Solving such a system for equilibrium based on a set of (temperature and pressure dependent) net reaction rates is fast and easy to do, and several efficient solvers have been proposed for planetary atmospheres (e.g., Gordon & McBride, 1994; Mollière et al., 2015; Woitke et al., 2018)

2.3.3 *Numerical solutions*

correlated-k

One of the main computational issues in line radiative transfer lies in resolving the frequency dependence of the opacity. As discussed in Section 2.3.2,

spontaneous emission and absorption of gas results in many (sometimes millions) individual lines that form the opacity. The resulting chromatic opacity often varies many orders of magnitude and is thus difficult to sample. Additionally, it is important to sample small opacity values well, because these so-called windows, have a tremendous impact on the resulting radiation field, which can be seen in the exponential dependency of the optical depth τ_ν in the radiative transfer equation (Eq. 2.36). Thus, in practice, tens of thousands to millions of frequency points are needed to accurately compute spectra and even integrated fluxes.

One numerical solution proposed in planetary science literature is the correlated-k method (Goody et al., 1989), aimed to be used when fine wavelength resolutions are too computationally expensive for rapid radiative transfer computations. The correlated-k method divides the spectrum into coarse bins ($\approx 10^1$ to 10^3). In such a bin i with bin-size $\Delta\nu$, the integral over an arbitrary function L_i of the opacity κ_i is given by

$$\begin{aligned}\bar{L}_i &= \int_0^1 L_i(\kappa_{\nu,i})\mathrm{d}(\nu/\Delta\nu) \\ &= \int_0^\infty f_i(\kappa_\nu) L_i(\kappa_{\nu,i})\mathrm{d}\kappa \\ &= \int_0^1 L_i(\kappa_{g,i})\mathrm{d}g,\end{aligned} \tag{2.78}$$

where $f_i(\kappa)$ is the distribution function of κ and g_i is the cumulative distribution function, given by

$$g_i(\kappa) = \int_0^\kappa f_i(\kappa')\mathrm{d}\kappa'. \tag{2.79}$$

In practice, one thus sorts the opacity in a bin i to find the cumulative distribution function $g_i(\kappa')$, where $g_i(\kappa')$ gives the fraction of the bin i, for which $\kappa < \kappa'$. The advantage of this approach is that $g_i(\kappa)$ is easy to discretize. These $\kappa_{g,i}$ values (often called k-tables) are then used instead of the opacity to calculate the radiative transfer. We show such a k-table of water for a wavelength bin between 1.0 μm and 1.1 μm in Figure 2.3, where due to less spread of the opacity (as seen in Figure 2.2) the higher pressure k-table is flatter compared to the low pressure k-table.

The radiative transfer equation is then first solved in each of the discrete g-coordinates individually, where the Planck function is assumed to be constant in bin i. This then yields the intensity (and its moments) and the source function as a function of frequency and g-coordinate. The final step is then to

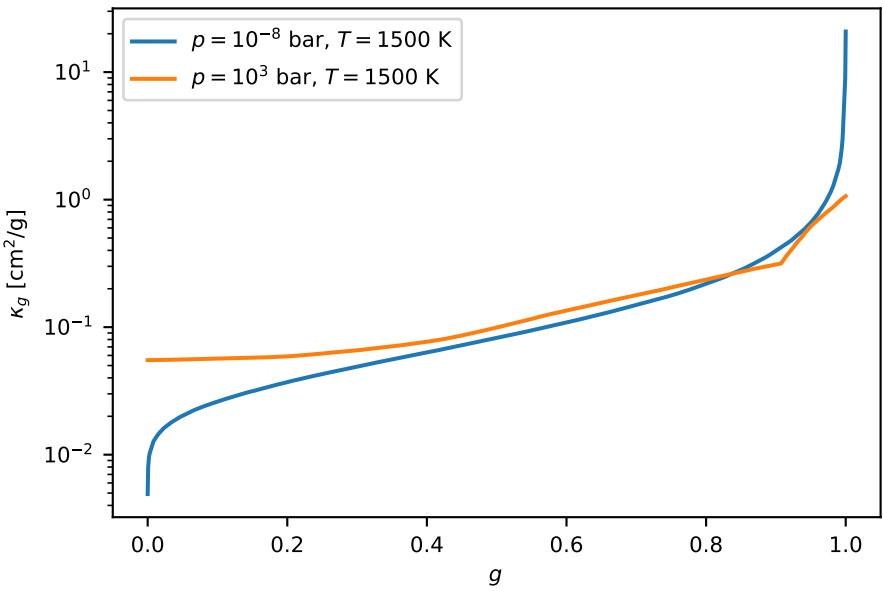

Figure 2.3: k-table for H_2O between 1.0 µm and 1.1 µm for two different pressure values at T = 1500 K

yield the semi-chromatic radiative quantities, such as the intensity of frequency bin i as

$$I_{\nu_i} = \int_0^1 I_{\nu_i, g} \, dg \tag{2.80}$$

and similarly for the flux and mean intensity.

The main disadvantage of this approach is that the mapping between frequency and g is different for different atmospheric layers, because different opacities have different distribution functions. Therefore, using the correlated-k approach means loosing information about the frequency space. Put in simple terms, this means that it is not possible to simply add up different opacities of different species in order to get the total opacity of a gas mixture. Instead, one needs to convolve all opacity distribution functions with each other, which is numerically expensive (Amundsen et al., 2017). Due to these disadvantages, climate models applying the correlated-k method, usually rely on look up tables for the correlated-k opacities. These look up tables are a function of pressure and temperature (e.g., Showman et al., 2009; Lee et al., 2021; Schneider et al., 2022b), assuming that the gas is in chemical equilibrium (see above).

Feautrier method

One of the most prominent methods to solve the radiative transfer equation in stellar atmospheres, which has also been applied to planetary atmospheres (Mollière et al., 2015; Schneider et al., 2022b), is the Feautrier method (Feautrier, 1964). The Feautrier method works by separating the angle dependence of the intensity field into an upper half ($I_+ = I_{\mu \geqslant 0}$) of the sphere and a lower half ($I_- = I_{\mu < 0}$), where μ is the cosine of the angle, as defined in Eq. 2.42, and where we omitted ν for notational convenience. We then get two radiative transfer equations (Eq. 2.35), one for the upper half and one for the lower half:

$$\begin{aligned} \frac{dI_+}{ds} &= \alpha(S - I_+) \\ \frac{dI_-}{ds} &= -\alpha(S - I_-). \end{aligned} \tag{2.81}$$

We now introduce a symmetric and antisymmetric combination of I_+ and I_-:

$$\begin{aligned} I_s &= \frac{1}{2}\left[I_+ + I_-\right] \\ I_a &= \frac{1}{2}\left[I_+ - I_-\right]. \end{aligned} \tag{2.82}$$

Inserting these in Eq. 2.81 yields

$$\begin{aligned} \frac{dI_s}{ds} &= -\alpha I_a \\ \frac{dI_a}{ds} &= -\alpha(I_s - S), \end{aligned} \tag{2.83}$$

which can be merged into one second order differential equation

$$\mu^2 \frac{d^2 I_s}{d\tau^2} = I_s - S, \tag{2.84}$$

where we used the plane parallel assumption and $d\tau = \frac{1}{\mu}\alpha ds$.

Using Eq. 2.45, the mean intensity can then be calculated as

$$J = \int_0^1 I_s d\mu \tag{2.85}$$

The advantage of solving for the upward and downward stream at the same time is that Eq. 2.84 can be easily cast into a matrix equation, which is efficiently solved by inverting a tridiagonal matrix. Furthermore, since Eq. 2.84 takes the form of a diffusion equation, it naturally recovers the optically thick diffusion limit, which is the most difficult part of solving multiple scattering. Solving Eq. 2.85 requires a boundary condition for the first layer and the last layer. The first one is given by the requirement that the planetary radiation field is zero in downward direction at the uppermost layer (e.g., no planetary light enters the computational domain from outside the planet). The second boundary condition is to assume that the radiation field is diffusive at the bottom boundary, such that $I_+ = I_-$ in all directions.

Lambda iteration

As mentioned in 2.3.1, the source function S_ν depends on the solution of the radiative transfer equation (Eq. 2.35). We can thus formulate the solution to Eq. 2.35 as

$$J_\nu = \Lambda[S_\nu], \tag{2.86}$$

where Λ is an operator (e.g., a matrix or numerical subroutine) that acts on the source function and outputs the mean intensity. In practice, however, we do not need to know all components of Λ at the same time when solving the radiative transfer equation.

Inserting J_ν from Eq. 2.52, we can write Eq. 2.86 as

$$S_\nu = \epsilon_\nu B_\nu(T) + (1 - \epsilon_\nu)\Lambda[S_\nu]. \tag{2.87}$$

The easiest solution to solve this is by computing the inverse of Λ, which would directly reveal the correct source function. However, it turns out that this is too computationally expensive for most applications, since Λ is a $N_\mu \times N_{\text{layers}} \times N_{\text{layers}}$ tensor. Thus, iterating over the radiative transfer equation is a better solution. The source function at iteration step $n+1$ is then given as

$$S_\nu^{n+1} = \epsilon_\nu B_\nu(T) + (1-\epsilon_\nu)\Lambda[S_\nu^n], \tag{2.88}$$

which is called Lambda iteration.

Lambda iteration is very slow, because the number of iterations needed to find convergence N_{iter} is typically much higher than the expected scattering events of a photon before it gets destroyed (see Section 2.3.1). We can thus estimate N_{iter} by (Dullemond, 2012)

$$N_{\nu,\text{iter}} \gg \min\left(\tau_{\nu,\text{scat}}^2, \frac{1}{\epsilon_\nu}\right). \tag{2.89}$$

We will briefly summarize two methods to circumvent the convergence issues of Lambda iteration: Approximate Lambda iteration (ALI) and Ng-acceleration. In ALI (Olson et al., 1986), we separate the Lambda operator into an approximate operator $\Lambda^\star$, which is ideally easy to invert, and solve the rest by iterating. Assuming that Λ can be represented by a matrix, we can write Λ as

$$\Lambda = (\Lambda - \Lambda^\star) + \Lambda^\star. \tag{2.90}$$

A typical choice of $\Lambda^\star$ is the local Lambda approximator, often called OAB, which is given by

$$\Lambda^\star = \text{diag}(\Lambda). \tag{2.91}$$

We can then write Eq.2.87 as

$$\begin{aligned} S_\nu &= \epsilon_\nu B_\nu(T) + (1-\epsilon_\nu)(\Lambda-\Lambda^\star)S_\nu + (1-\epsilon_\nu)\Lambda^\star S_\nu \\ \Rightarrow [E-(1-\epsilon_\nu)\Lambda^\star]\, S_\nu &= \epsilon_\nu B_\nu(T) + (1-\epsilon_\nu)(\Lambda-\Lambda^\star)S_\nu \\ \Rightarrow S_\nu &= M^{-1}\left[\epsilon_\nu B_\nu(T) + (1-\epsilon_\nu)(\Lambda-\Lambda^\star)S_\nu\right], \end{aligned} \tag{2.92}$$

where E is the diagonal matrix of ones, and with

$$M = E - (1-\epsilon_\nu)\Lambda^\star, \tag{2.93}$$

which is diagonal and therefore trivial to invert. Using Eq. 2.86, we can finally derive

$$S_\nu^{n+1} = M^{-1}\left[\epsilon_\nu B_\nu(T) + (1-\epsilon_\nu)(J_\nu^n - \Lambda^\star S_\nu^n)\right], \tag{2.94}$$

as the Equation to iterate on instead of the normal Lambda iteration (Eq. 2.88). This is useful, because by iterating over Eq.2.94, we effectively exclude the self coupling inside a cell from iterating and instead focus on getting the coupling between different grid cells correct.

One of the main disadvantages of Lambda iteration and ALI is its linear convergence behavior, which is a consequence of the linear dependence of S_ν^{n+1} on S_ν^n. Therefore, one method to speed up the convergence of the source function is to extrapolate this linear improvement of the source function. The most common algorithm aimed to do that uses a linear combination of the previous three iterations and is called Ng-acceleration (Ng, 1974). The source function at iteration $n+1$ can be written as a linear combination of S_ν^n, S_ν^{n-1}, S_ν^{n-2}

$$S_\nu^{n+1} = (1-a-b)S_\nu^n + aS_\nu^{n-1} + bS_\nu^{n-2}, \tag{2.95}$$

where a and b are the values that minimize $|S_\nu^{n+1} - S_\nu^n|$. We use the values from Dullemond (2012), which can be derived by using Eq. 2.95 for step n and $n+1$ and solving for a and b. Thus, in order to use Ng-acceleration we have to first compute the previous three iterations using three ALI steps. Once the prediction from the Ng-acceleration step is calculated, we use this prediction as the source function, and perform another three ALI steps before we calculate the next Ng step.

2.3.4 *Radiative transfer inside the GCM*

In order to obtain heating rates and spectra, we first need to solve the above-mentioned equations. We summarize the general radiative transfer routine, used throughout this work and continue then to explain how their respective results are applied, to compute heating and cooling in the GCM. Post-processing to calculate planetary spectra uses the same methodology but with a higher frequency resolution (see Schneider et al. (2022b) for more details).

We solve Eq. 2.84 for I_s by discretizing the equation onto a vertical grid with grid index i as

$$I_i - \frac{1}{\Delta\tau_0}\left(\frac{I_{i+1} - I_i}{\Delta\tau_p} - \frac{I_i - I_{i-1}}{\Delta\tau_m}\right) = S_i, \tag{2.96}$$

where we wrote $I_{s,\nu}(p_i) = I_i$ for notational convenience, and where we introduced three differences $(\Delta\tau_p, \Delta\tau_m, \Delta\tau_0)$ of the optical depth τ as

$$\begin{aligned}\Delta\tau_p &= \tau_{i+1} - \tau_i \\ \Delta\tau_m &= \tau_i - \tau_{i-1} \\ \Delta\tau_0 &= \frac{1}{2}(\tau_{i+1} + \tau_{i+\frac{1}{2}}) - \frac{1}{2}(\tau_i + \tau_{i-\frac{1}{2}}) = \frac{1}{2}(\tau_{i+1} - \tau_{i-1}).\end{aligned} \tag{2.97}$$

The result can be put into a matrix equation

$$P_{i,j} I_j = S_i, \tag{2.98}$$

which takes the form of a tridiagonal matrix given by

$$\begin{aligned}P_{i,i} &= 1 + \frac{\mu^2}{\Delta\tau_0}\left(\frac{1}{\Delta\tau_p} + \frac{1}{\Delta\tau_m}\right) \\ P_{i,i+1} &= -\frac{\mu^2}{\Delta\tau_0 \Delta\tau_p} \\ P_{i,i-1} &= -\frac{\mu^2}{\Delta\tau_0 \Delta\tau_m}\end{aligned} \tag{2.99}$$

for $i \in [2, ..., N-1]$. Further, in the same way, according to Eq. 2.86 and Eq. 2.91, we may then find $\Lambda^\star$ for $i \in [2, ..., N-1]$ as

$$\Lambda^\star_{i,i} = \sum_j^{N_\mu} \frac{\Delta\mu_j}{P_{i,i}}. \tag{2.100}$$

The edges of P and $\Lambda_\star$ (e.g., $P_{0,1}$) are derived in the same way by inserting the boundary conditions (see Section 2.3.3).

Given the optical depths, calculated from the opacities, we construct the matrix elements of P, according to Eq. 2.99 and $\Lambda^\star$ according to Eq. 2.100. The first ALI iteration starts out with an initial guess of the source function (e.g., assuming that the previous source function was in LTE, see Eq. 2.40). We can then solve Eq. 2.98 for a set of angles using a adaptation of the `tridag` routine from Press et al. (1992) to obtain the I_s. The full intensity I in all directions, and I_a can then be recovered from Eq. 2.83. This is followed by calculating the next guess of the source function according to Eq. 2.94, where J_ν is given as the sum of the planetary and stellar mean intensity (see Eq. 2.60). In this manner, we iterate by performing ALI steps and doing Ng-acceleration, every fourth iteration, until convergence is reached.

In the GCM, we solve the 1D plane parallel radiative transfer using the above description of the algorithm. We divide the 3D grid into vertical columns

and call the radiative transfer routine every radiative timestep (usually every fourth dynamical timestep). We then perform the ALI steps until convergence is reached. We assume that convergence is reached when

$$\frac{\Delta S_\nu}{S_\nu} < 0.02 \times \frac{1}{\Lambda^*}, \tag{2.101}$$

following Rutten (2003). The reason for this approach on convergence can be found in the linear convergence behavior of ALI, which may lead to results that look almost converged, even though they are completely wrong, because Λ is small, and the source function therefore does not change, hence the $\frac{1}{\Lambda^*}$ to make sure we land on a correct solution. The converged source function is then saved for later use as the initial guess for the source function at the next radiative time step.

For computational reasons, radiative transfer calculations are performed every other horizontal grid point and linearly interpolated in between. From the resulting intensity field, bolometric fluxes are calculated according to Eq. 2.47. The net flux is then given by the sum of the planetary and stellar flux and is used to determine the heating rate (see Eq. 2.29).

There are multiple options for k-tables in the GCM. The fastest option is to use a lookup table. The k-tables of the individual species are then premixed beforehand for a grid of pressure and temperature, assuming equilibrium chemistry and stored in a lookup table, which is then loaded into the GCM. The opacity in the GCM is then given by interpolation. The disadvantage of this approach, however, is its flexibility. If the abundances in the GCM were to differ from chemical equilibrium, opacities can not be used self consistently with the abundances in the GCM.

In Schneider et al. (2022b) and Schneider et al. (2022a) we have used such lookup tables. In recent work, however, which is not part of this thesis, we have extended the options in the GCM to allow for on-the-fly k-table mixing using different methods. These methods are reviewed and discussed in Schneider et al. (2024).

3

HOW DRIFTING AND EVAPORATING PEBBLES SHAPE GIANT PLANETS I: HEAVY ELEMENT CONTENT AND ATMOSPHERIC C/O

Aaron David Schneider & Bertram Bitsch

Published in Astronomy & Astrophysics, Volume 654, id.A71, October 2021

Author contributions:
Aaron Schneider conducted the research, developed the numerical model, and wrote most of the paper. Bertram Bitsch supervised the project and contributed significantly to the writing of the manuscript, the interpretation, and discussion of the results.

Material in the paper from another degree / thesis:
The publication (Schneider & Bitsch, 2021a) is in large parts based on Aaron Schneider's master thesis, which was titled "Chemical composition of exoplanets due to pebble, planetesimal and gas accretion" and presented at the University of Heidelberg's Department of Physics and Astronomy in 2020. The review process for (Schneider & Bitsch, 2021a) required significant changes to the numerical model and to the manuscript and continued for one year after the completion of the master thesis. While some parts of the methodology, analysis, and figures in (Schneider & Bitsch, 2021a) are original and have not been presented before, much of the work builds on the master thesis.

Notes:
The published version of Schneider & Bitsch (2021a) and Schneider & Bitsch (2021b) made use of a chemical partitioning model that did not conserve the nitrogen abundance. Subsequent corrections to Schneider & Bitsch (2021a), that have been published in a corrigendum (Schneider & Bitsch, 2022) are applied to this version of Schneider & Bitsch (2021a).

Original Abstract
Recent observations of extrasolar gas giants suggest super-stellar C/O ratios in planetary atmospheres, while interior models of observed extrasolar giant planets additionally suggest high heavy element contents. Furthermore, recent observations of protoplanetary disks revealed super-solar C/H ratios, which are explained by inward drifting and evaporating pebbles enhancing the volatile content of the disk. We investigate in this work how the inward drift and evaporation of volatile-rich pebbles influences the atmospheric C/O ratio and heavy element content of giant planets growing by pebble and gas accretion. To achieve this goal, we perform semi-analytical 1D models of protoplanetary disks, including the treatment of viscous evolution and heating, pebble drift, and simple chemistry to simulate the growth of planets from planetary embryos to Jupiter-mass objects by the accretion of pebbles and gas while they migrate through the disk. Our simulations show that the composition of the planetary gas atmosphere is dominated by the accretion of vapor that originates from inward drifting evaporating pebbles at evaporation fronts. This process allows the giant planets to harbor large heavy element contents, in contrast to models that do not take pebble evaporation into account. In addition, our model reveals that giant planets originating farther away from the central star have a higher C/O ratio on average due to the evaporation of methane-rich pebbles in the outer disk. These planets can then also harbor super-solar C/O ratios, in line with exoplanet observations. However, planets formed in the outer disk harbor a smaller heavy element content due to a smaller vapor enrichment of the outer disk compared to the inner disk, where the very abundant water ice also evaporates. Our model predicts that giant planets with low or large atmospheric C/O should harbor a large or low total heavy element content. We further conclude that the inclusion of pebble evaporation at evaporation lines is a key ingredient for determining the heavy element content and composition of giant planets.

3.1 INTRODUCTION

The number of observed exoplanets is increasing every day, with now more than 4000 observed exoplanets (Akeson et al., 2013). However, how exactly the planets form and how some of their properties can be explained (e.g., the C/O ratio and their heavy element content) is still unclear. Observed

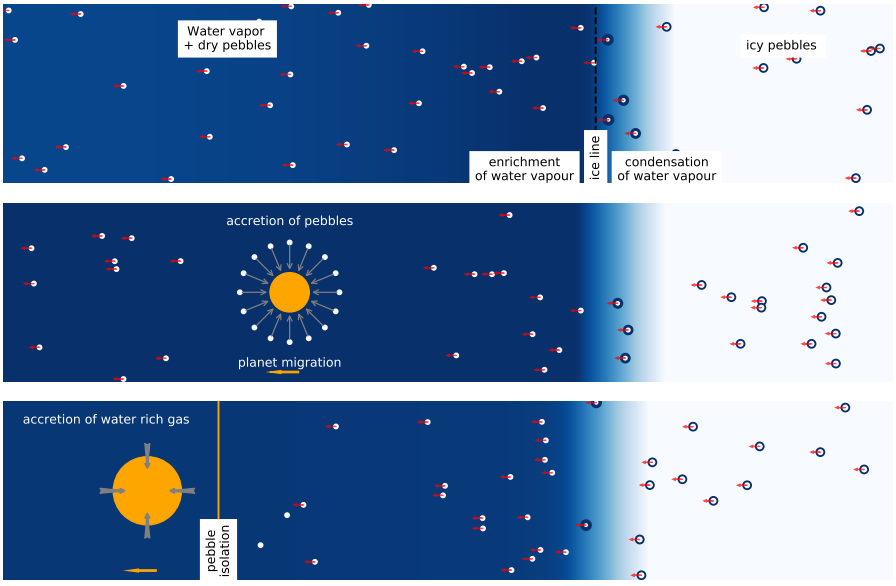

Figure 3.1: Phases of planetary growth.
Top: Dust particles grow to pebbles (small dots) and drift toward the star. Icy pebbles that cross the water ice line (dashed line) evaporate their water content and enrich the gas with water vapor. Water vapor that crosses the ice line condenses onto pebbles, increasing their water content.
Middle: The core of the planet is formed by pebble accretion while the planet migrates. Depending on the formation path, the core composition can be icy or dry. In the cartoon shown here, the core would be water poor.
Bottom: Once the planet is heavy enough to reach pebble isolation and form a pressure bump, pebbles are stopped and cannot be accreted by the planet. The planet will then start to accrete gas that is enriched with water vapor.
The water content of the disk (in solid or gaseous form) is color coded, where a darker color indicates a higher water content. We restrict ourselves in this cartoon to the water evaporation front, but the same applies for the evaporation of all solids in our model.

atmospheric abundances of exoplanets could thus be used to constrain the planet formation pathway (e.g., Mordasini et al. 2016; Madhusudhan et al. 2017; Cridland et al. 2019).

One quantity to constrain the planet formation pathway could be the atmospheric C/O ratios, which can be measured to high precision (Mollière et al., 2015). It has been clear since the pioneering works of Öberg et al. (2011) that atmospheric C/O ratios strongly depend on the formation environment of the planet. Although atmospheric measurements are still imprecise, Brewer et al. (2017) constrain atmospheric C/O ratios for different observed hot gas giants and find that C/O ratios differ from the host star's C/O ratio. Some might even be enhanced by more than a factor of two compared to the host star's value. However, these data will hopefully be improved with the *James Webb Space Telescope* (JWST) and the *Atmospheric Remote-sensing Infrared Exoplanet Large-survey* (ARIEL) by the end of the decade.

If the mass and radius of an observed planet are known, one can also apply interior models to constrain the amount of heavy elements (elements with atomic numbers higher than two) that is needed to match those parameters (e.g., Miller & Fortney 2011). Thorngren et al. (2016) uses a sample of non-inflated hot gas giants to relate the amount of heavy elements to the planetary mass and radius. They find that the heavy element mass is approximately proportional to the square root of the planetary mass and that an average Jupiter-mass planet should harbor 57.9 $M_\oplus$ of heavy elements. However, recent work by Müller et al. (2020) questions whether some of the planets from the catalog of Thorngren et al. (2016) are inflated, thus making the analysis of Thorngren et al. (2016) less applicable. In any case, the origin of this large heavy element content is still unknown.

From the formation side, models either include the growth of planetary cores via planetesimals (Ida & Lin, 2004; Alibert et al., 2005; Ida & Lin, 2008a,b, 2010; Mordasini et al., 2012; Alibert et al., 2013; Cridland et al., 2019; Emsenhuber et al., 2021) or pebbles (Bitsch et al., 2015b, 2019; Lambrechts & Johansen, 2012, 2014; Lambrechts et al., 2019b; Ndugu et al., 2018; Ali-Dib, 2017; Brügger et al., 2018). Even though there are plenty of models that deal with the formation aspect, only a few models include the chemical composition that allows a more detailed comparison to observations. For example, Venturini & Helled (2020) investigates the heavy element content of planets built by pebbles or planetesimals but do not treat multiple chemical species. On the other hand, Booth et al. (2017) include the physics of radial dust drift and pebble evaporation at evaporation lines to infer the C/O ratios of planets built by pebble and gas accretion but do not include condensation and do not investigate the heavy element content of gas giants.

Other approaches focus solely on the disk chemistry and handle the chemical reactions on the surface of dust grains (Semenov et al., 2010; Eistrup et al., 2016; Notsu et al., 2020). It is, however, difficult to include the physical processes of grain growth and radial dust drift in these models, though first attempts have been made (e.g., Booth & Ilee, 2019). A recent work by Krijt et al. (2020) also expands this in much more detail for a 2D disk model. However, it seems that chemical reactions operate on longer timescales compared to the radial drift of millimeter- and centimeter-sized pebbles (e.g., Booth & Ilee, 2019).

In this work we focus thus on a disk model that includes the growth and drift of pebbles (Birnstiel et al., 2012) as well as evaporation and condensation at evaporation fronts. We then model the growth of planets via the accretion of pebbles (Johansen & Lambrechts, 2017) and gas (Ndugu et al., 2021) inside these disks, while tracing the chemical composition of the accreted material to derive the atmospheric C/O ratio as well as the heavy element content. Our model approach is outlined in the cartoon shown in Fig. 3.1.

Our newly developed code `chemcomp` simulates the formation of planets in viscously evolving protoplanetary disks by the accretion of pebbles and gas. The chemical composition of planetary building blocks (pebbles and gas) is traced by including a physical approach of the evaporation and condensation of volatiles at evaporation lines.

This paper is structured as follows: The first part includes the outline of the disk model and the description of the planetary formation model. We then explain the numerical methods (Sect. 3.2) used in `chemcomp` and show results that have been obtained (Sects. 3.3 and 3.4). We then discuss the shortcomings and implications of our simulations in Sect. 3.5 before concluding in Sect. 3.6.

3.2 MODEL

In this section we discuss the different ingredients and parameters of our model. We list all variables and their meaning in Tables 3.6,3.7,3.8 and 3.9. We start by discussing first the parts of our model that are relevant for the disk structure and evolution, namely the dust growth and the chemical composition of the disk followed by the viscous evolution, including pebble evaporation and condensation as well as the disk dispersal. Our model regarding planetary growth includes planet migration, pebble and gas accretion, and gap opening in our disk model. We then close this section by discussing the operating principle of our newly developed code `chemcomp`.

We follow here a classic viscous disk evolution model (e.g., Lynden-Bell & Pringle, 1974; Bell et al., 1997), utilizing the alpha-viscosity prescription (Shakura & Sunyaev, 1973). The viscosity is then given by

$$\nu = \alpha \frac{c_s^2}{\Omega_K}, \tag{3.1}$$

where α is a dimensionless factor that describes the turbulent strength and $\Omega_K = \sqrt{\frac{GM_\star}{r^3}}$ is the Keplerian angular frequency. The isothermal sound speed c_s can be linked to the midplane temperature T_{mid} (see Appendix B for details of our disk temperature calculation) by

$$c_s = \sqrt{\frac{k_B T_{mid}}{\mu m_p}}, \tag{3.2}$$

where μ is the mean molecular weight, which can change due to the enrichment of the disk's gas with vapor, as we discuss below, and m_p is the proton mass. For simplicity, we keep the disk's temperature fixed in time.

3.2.1 *Dust growth*

We followed the two populations approach from Birnstiel et al. (2012) to model the growth of dust to pebbles limited by fragmentation, drift, and drift-induced fragmentation. We compare the gas and solid evolution of our code to the code of Birnstiel et al. (2012) in Appendix C. Since solid particles try to move Keplerian, the gas asserts an aerodynamic headwind on the solid particles due to the sub-Keplerian azimuthal speed Δv of the gas given by

$$\Delta v = v_K - v_\varphi = -\frac{1}{2}\frac{d \ln P}{d \ln r}\left(\frac{H_{gas}}{r}\right)^2 v_K, \tag{3.3}$$

where $v_K = \Omega_K r$ is the Keplerian velocity, $H_{gas} = \frac{c_s}{\Omega_K}$ is the scale height of the disk, and P is the gas pressure. This friction can be quantified in the Epstein drag regime (Brauer et al., 2008; Birnstiel et al., 2010) by quantifying the friction time, τ_f, and the Stokes number, St, of a particle

$$St = \Omega_K \tau_f = \frac{\pi}{2}\frac{a \rho_\bullet}{\Sigma_{gas}}, \tag{3.4}$$

where a and $\rho_\bullet$ denote the radius of the solid particle and its density.[1] Σ_{gas} corresponds to the gas surface density. Small particles have low friction times

1 We follow the approach outlined in Eq. 12 of Drążkowska & Alibert (2017) and calculate $\rho_\bullet$ dynamically according to the abundance of ices in solids, which changes due to condensation, where silicates have a density of $3 g/cm^3$ and ices a density of $1 g/cm^3$.

and are therefore strongly coupled to the gas, whereas large particles have large friction times and therefore only couple weakly to the gas. Due to this headwind, dust grains will spiral inward with the radial velocity u_Z (Weidenschilling, 1977; Brauer et al., 2008; Birnstiel et al., 2012)

$$u_Z = \frac{1}{1+St^2} u_{gas} - \frac{2}{St^{-1}+St} \Delta v. \tag{3.5}$$

Thus, growing from small grains to large grains implies an increase in the radial dust velocity. Growth can therefore be limited by radial drift (larger grains "drift away"), especially in the outer disk regions. When the velocity of the dust grains exceeds a certain velocity boundary (Birnstiel et al., 2009), the dust will fragment (and therefore decrease its size) upon collision. This fragmentation velocity is normally measured in laboratory experiments that yield fragmentation velocities of $1\,m\,s^{-1}$ to $10\,m\,s^{-1}$ for silicate and ice particles, respectively (Gundlach & Blum, 2015). In our model we always use a fixed fragmentation velocity of 5m/s.

The solid to gas ratio ϵ is defined as

$$\epsilon = \frac{\Sigma_Z}{\Sigma_{gas}}, \tag{3.6}$$

where Σ_Z denotes the total solid surface density (composed of dust and pebbles). The pebble surface density can be constrained from the solid surface density by multiplication with a numerical factor f_m taken from the two population model (Birnstiel et al., 2012):

$$\Sigma_{peb} = f_m \times \Sigma_Z, \tag{3.7}$$

where $f_m = 0.97$ in the drift limited case and $f_m = 0.75$ in the fragmentation limited case.

We can now calculate the mass averaged dust velocity (important for dust transport; see Sect. 3.2.3):

$$\bar{u}_Z = (1 - f_m) u_{dust} - f_m u_{peb} \,. \tag{3.8}$$

However, other growth limiting mechanisms such as the bouncing barrier (Güttler et al., 2010) or the charging barrier (Okuzumi, 2009) exist but are, for the sake of simplicity, not considered in this work. In principle, bouncing would lead to smaller particle sizes compared to a fragmentation or drift-limited particle size (e.g., Lorek et al., 2018).

This approach to the dust evolution is within a few percent compared to a "full" model, which includes individual velocities for all grains within the grain

Species (X)	Abundance
He/H	0.085
O/H	4.90×10^{-4}
C/H	2.69×10^{-4}
N/H	6.76×10^{-5}
Mg/H	3.98×10^{-5}
Si/H	3.24×10^{-5}
Fe/H	3.16×10^{-5}
S/H	1.32×10^{-5}
Al/H	2.82×10^{-6}
Na/H	1.74×10^{-6}
K/H	1.07×10^{-7}
Ti/H	8.91×10^{-8}
V/H	8.59×10^{-9}

Table 3.1: Elemental number ratios used in our model, corresponding to the abundance of element X compared to hydrogen in the solar photosphere (Asplund et al., 2009).

size distribution (Birnstiel et al., 2012). Previous planetesimal (Drążkowska et al., 2016; Drążkowska & Alibert, 2017) and planet formation simulations (Guilera et al., 2020) have used this full model. While the full model allows for a slightly larger accuracy for the dust evolution, the here used approach of Birnstiel et al. (2012) results in a shorter computational run time, needed to probe all the different disk and planetary parameters (Table 3.3) in our work. We further note that our approach does not take into account the reduction of the dust and pebble velocities due to increases in the local dust-to-gas ratio, as considered in other works (e.g., Nakagawa et al. 1986; Drążkowska et al. 2016).

3.2.2 *Compositions*

We make the assumption that the original chemical composition of the disk is similar to the host star composition. We use here the solar abundances [X/H] from Asplund et al. (2009) (see also Table 3.1), whereas our chemical model is based on the model presented in Bitsch & Battistini (2020). The disk

Species (Y)	T_{cond} [K]	$\nu_{Y,\,no\,C}$	$\nu_{Y,\,with\,C}$
CO	20	$0.45 \times C/H$	$0.45 \times C/H$
N_2	20	$0.45 \times N/H$	see $\nu_{Y,\,no\,C}$
CH_4	30	$0.45 \times C/H$	$0.25 \times C/H$
CO_2	70	$0.1 \times C/H$	$0.1 \times C/H$
NH_3	90	$0.1 \times N/H$	see $\nu_{Y,\,no\,C}$
H_2S	150	$0.1 \times S/H$	see $\nu_{Y,\,no\,C}$
H_2O	150	$O/H - (3 \times MgSiO_3/H + 4 \times Mg_2SiO_4/H + CO/H + 2 \times CO_2/H + 3 \times Fe_2O_3/H + 4 \times Fe_3O_4/H + VO/H + TiO/H + 3 \times Al_2O_3 + 8 \times NaAlSi_3O_8 + 8 \times KAlSi_3O_8)$	see $\nu_{Y,\,no\,C}$
Fe_3O_4	371	$(1/6) \times (Fe/H - 0.9 \times S/H)$	see $\nu_{Y,\,no\,C}$
C (carbon grains)	631	0	$0.2 \times C/H$
FeS	704	$0.9 \times S/H$	see $\nu_{Y,\,no\,C}$
$NaAlSi_3O_8$	958	Na/H	see $\nu_{Y,\,no\,C}$
$KAlSi_3O_8$	1006	K/H	see $\nu_{Y,\,no\,C}$
Mg_2SiO_4	1354	$Mg/H - (Si/H - 3 \times K/H - 3 \times Na/H)$	see $\nu_{Y,\,no\,C}$
Fe_2O_3	1357	$0.25 \times (Fe/H - 0.9 \times S/H)$	see $\nu_{Y,\,no\,C}$
VO	1423	V/H	see $\nu_{Y,\,no\,C}$
$MgSiO_3$	1500	$Mg/H - 2 \times (Mg/H - (Si/H - 3 \times K/H - 3 \times Na/H))$	see $\nu_{Y,\,no\,C}$
Al_2O_3	1653	$0.5 \times (Al/H - (K/H + Na/H))$	see $\nu_{Y,\,no\,C}$
TiO	2000	Ti/H	see $\nu_{Y,\,no\,C}$

Table 3.2: Condensation temperatures and volume mixing ratios of the chemical species.

Notes: Condensation temperatures for molecules are taken from Lodders (2003). For Fe_2O_3 the condensation temperature for pure iron is adopted (Lodders, 2003). Volume mixing ratios ν_Y (i.e., by number) are adopted for the species as a function of disk elemental abundances (see, e.g., Madhusudhan et al. 2014). We expand here on the different mixing ratios from Bitsch & Battistini (2020). Results in this work apply the model without pure carbon grains. A comparison with a model that includes carbon grains can be found in Appendix D.

temperature is dependent on the orbital distance (see Appendix B and Fig. 3.16) and therefore the composition of dust and gas is likewise dependent on the orbital distance. We used a simple chemical partitioning model to distribute the elements into molecules, Y (see Table 3.2; extended from Bitsch & Battistini 2020).

Based on the condensation temperature, a molecule of species Y will generally either be available in gas form (evaporated) when the disk temperature is above the condensation temperature or in solid form (condensated) when the disk temperature is below the condensation temperature. The transition point, where the midplane temperature equals the condensation temperature of species Y, is referred to as the evaporation line of species Y.

Sulfur is mostly available in refractory form in protoplanetary disks (Kama et al., 2019), leaving only a small component in volatile form. For nitrogen we use N_2 and NH_3, where most of the nitrogen should be in the form of N_2 (e.g., Bosman et al., 2019). Even though Ti, Al, K, Na, and V are not very abundant and thus do not contribute significantly to the planetary accretion rates, we include these elements in our model because they can be observed in the atmospheres of hot Jupiters and could also play a crucial role for the chemical evolution inside the atmospheres (Ramírez et al., 2020).

The above-described partitioning model is used for the initial chemical composition in our disk (e.g., Fig. 3.2) as well as the chemical composition at all times for our simplest model, which is basically an extension of the step-function-like compositions in the work of Öberg et al. (2011). In the course of this work we also include the evaporation of drifting grains at evaporation lines, which will change the chemical composition of the disk (see below).

With this we can define the elemental number ratio

$$X1/X2 = \frac{m_{X1}}{m_{X2}} \frac{\mu_{X2}}{\mu_{X1}}, \tag{3.9}$$

where m_{X1} and m_{X2} is the mass fraction of the elements X1 and X2, respectively, in a medium of mass or density m (e.g., $m = \Sigma_{gas}$) and μ_{X1} and μ_{X2} are the atomic masses of the specific element. In our work we mainly use this definition to calculate C/O.

In our model, we include the change of the mean molecular weight μ due to evaporation of inward drifting pebbles that increase the vapor content in the gas phase in time. This can lead to an increase in μ from 2.3 (standard hydrogen-helium mixture) up to 4, if the disk is heavily enriched in vapor. We show the derivation of how we calculate μ in our model in Appendix E.

For all icy species (H_2O, H_2S, NH_3, CO_2, CH_4, N_2, and CO) we assume a pebble density of $\rho_{\bullet,ice} = 1\,g\,cm^{-3}$, while refractory species (Fe_3O_4 and higher condensation temperatures) have a pebble density of $\rho_{\bullet,ref} = 3\,g\,cm^{-3}$.

The exact pebble density is then computed dynamically during the simulation via their composition

$$\rho_\bullet = (m_{\text{ref}} + m_{\text{ice}}) \cdot \left(\frac{m_{\text{ref}}}{\rho_{\bullet,\text{ref}}} + \frac{m_{\text{ice}}}{\rho_{\bullet,\text{ice}}} \right)^{-1} . \tag{3.10}$$

This process accounts automatically for a change in the pebble density due to condensation or evaporation of volatile species.

3.2.3 *Viscous evolution*

Given mass conservation and conservation of angular momentum, one can derive (Pringle, 1981; Armitage, 2013) the viscous disk equation

$$\frac{\partial \Sigma_{\text{gas,Y}}}{\partial t} - \frac{3}{r} \frac{\partial}{\partial r} \left[\sqrt{r} \frac{\partial}{\partial r} \left(\sqrt{r} \nu \Sigma_{\text{gas,Y}} \right) \right] = \dot{\Sigma}_Y, \tag{3.11}$$

where $\dot{\Sigma}_Y$ is a source term for a given species Y described later on. The viscous disk equation describes how the gas surface density evolves in time. With this equation we yield the radial gas velocity, given by

$$u_{\text{gas}} = -\frac{3}{\Sigma_{\text{gas}} \sqrt{r}} \frac{\partial}{\partial r} \left(\nu \Sigma_{\text{gas}} \sqrt{r} \right) . \tag{3.12}$$

We compare the radial velocities of the gas, dust and planets in Appendix F.

For the initialization of simulations we used the analytical solution (without the source term $\dot{\Sigma}_Y$) found by Lynden-Bell & Pringle (1974), which is dependent on a scaling radius R_0 and the initial disk mass M_0 and can be expressed as (Lodato et al., 2017)

$$\Sigma_{\text{gas}}(r,t) = \frac{M_0}{2\pi R_0^2} (2-\psi) \left(\frac{r}{R_0} \right)^{-\psi} \xi^{\frac{5/2-\psi}{2-\psi}} \times \exp\left(-\frac{(r/R_0)^{2-\psi}}{\xi} \right), \tag{3.13}$$

where t is the time, $\psi = \left(\frac{d \ln \nu}{d \ln r} \right)_{r=r_{\text{in}}} \approx 1.08$, which is evaluated at the inner edge of the disk (r_{in}) and $\xi = 1 + \frac{t}{t_\nu}$ with the viscous time t_ν

$$t_\nu = \frac{R_0^2}{3(2-\psi)^2 \nu(R_0)}. \tag{3.14}$$

We used the numerical approach described in Birnstiel et al. (2010) to solve the evolution of the gas surface density.

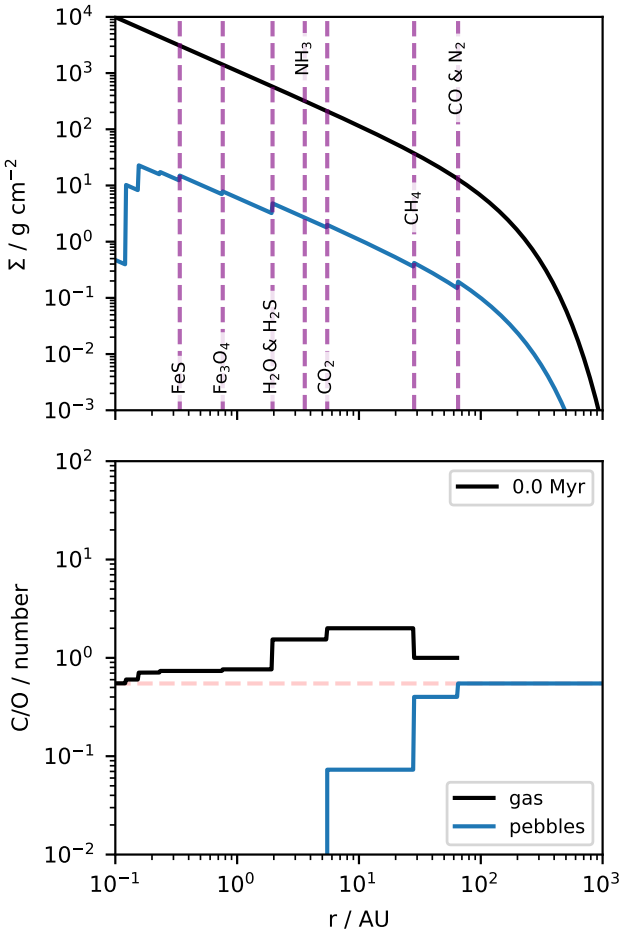

Figure 3.2: Initial surface density and C/O ratio. Top: Initial surface density of pebbles (blue line) and gas (black line). Bottom: C/O number ratio in the disk in pebbles and gas. Evaporation lines are labeled and indicated as dashed purple lines. Evaporation lines for molecular species with condensation temperatures higher than 704 K are not shown for simplicity (see Table 3.2). The solar C/O value of 0.54 is indicated as a red horizontal dashed line. We use our standard disk parameters with $\alpha = 5 \times 10^{-4}$ for this simulation, as stated in Table 3.3.

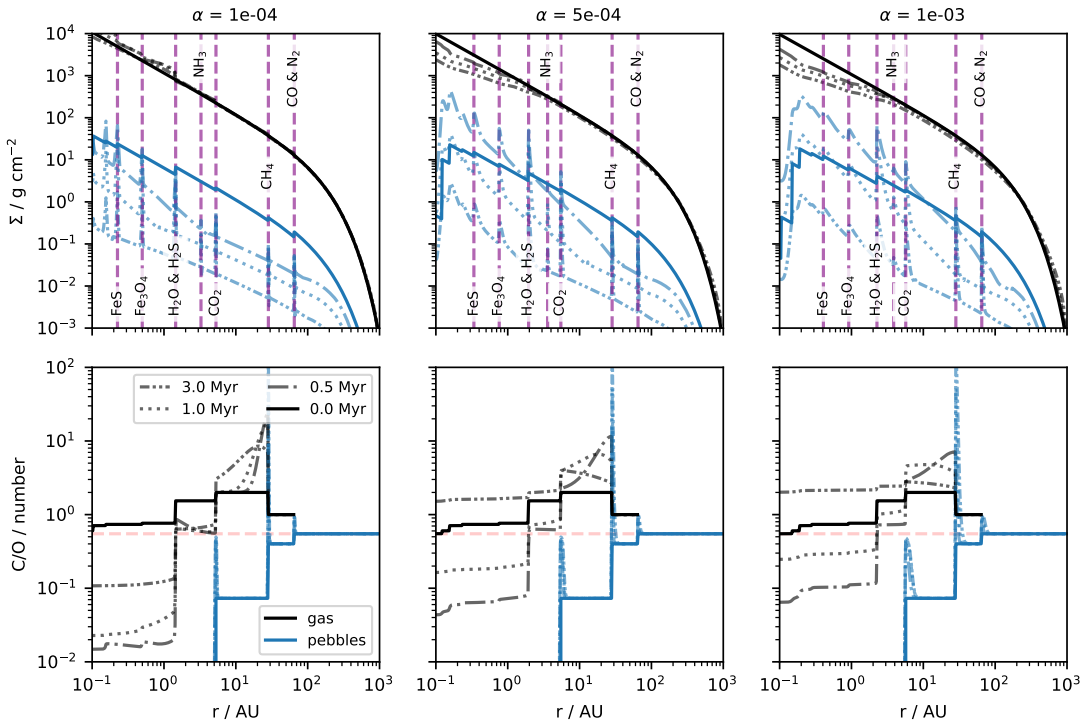

Figure 3.3: Like Fig. 3.2 but now including the time evolution of the disk, also for $\alpha = 10^{-4}$ (left) and $\alpha = 10^{-3}$ (right). Evaporation line positions are shown with vertical lines, which are different for the different simulations due to an increase in viscous heating with increasing α (Appendix B). We use the same disk parameters (except α) as in Fig. 3.2, corresponding to the standard parameters shown in Table 3.3.

Considering the inward drift of pebbles (Eq. 3.8), the evolution of the solid surface density can be described by (Birnstiel et al., 2010, 2012, 2015)

$$\frac{\partial \Sigma_{Z,Y}}{\partial t} + \frac{1}{r}\frac{\partial}{\partial r}\left\{ r\left[\Sigma_{Z,Y}\cdot \bar{u}_Z - \frac{\partial}{\partial r}\left(\frac{\Sigma_{Z,Y}}{\Sigma_{gas}}\right)\cdot \Sigma_{gas}\nu \right]\right\} = -\dot{\Sigma}_Y - \dot{\Sigma}_Y^{acc,peb}, \quad (3.15)$$

where $\dot{\Sigma}_Y^{acc,peb}$ is the source term that accounts for the discount of accreted pebbles from the dust surface density in the grid cell of the planet. The source term $\dot{\Sigma}_Y$ originates from pebble evaporation and condensation and is given by

$$\dot{\Sigma}_Y = \begin{cases} \dot{\Sigma}_Y^{evap} & r < r_{ice,Y} \\ \dot{\Sigma}_Y^{cond} & r \geqslant r_{ice,Y}. \end{cases} \quad (3.16)$$

Here $\dot{\Sigma}_Y^{evap}$ and $\dot{\Sigma}_Y^{cond}$ are the evaporation and condensation source terms of species Y for the two transport Eqs. 3.11 and 3.15.

In order to allow for mass conservation we require that no more than 90% of the local surface density is evaporated or condensed in one time step Δt:

$$|\dot{\Sigma}_Y| = \min\left[|\dot{\Sigma}_Y|, 0.9\frac{\min\left(\Sigma_{gas,Y}, \Sigma_{Z,Y}\right)}{\Delta t}\right]. \quad (3.17)$$

We used a fixed timestep of $\Delta t = 10\,yr$ for all of our models.

For the condensation term we assume that gas can only condensate by sticking on the surface (with efficiency $\epsilon_p = 0.5$) of existent solids. The condensation term is then given by

$$\dot{\Sigma}_Y^{cond} = \frac{3\epsilon_p}{2\pi\rho_\bullet}\Sigma_{gas,Y}\left(\frac{\Sigma_Z}{a_{dust}} + \frac{\Sigma_{peb}}{a_{peb}}\right)\Omega_k\sqrt{\frac{\mu}{\mu_Y}}, \quad (3.18)$$

where μ_Y is the mass (in proton masses) of a molecule of species Y. Here a_{dust} and a_{peb} are the particle sizes of the small and large dust distribution, respectively (see Sect. 3.2.1). A derivation of the above equation can be found in Appendix G.

For the evaporation term we assumed that the flux of solids that drifts through the evaporation line is evaporated into the gas within 1×10^{-3} AU

$$\dot{\Sigma}_Y^{evap} = \frac{\Sigma_{Z,Y}\cdot \bar{u}_Z}{1\times 10^{-3}\,AU}. \quad (3.19)$$

We show how the water ice fraction evolves in time for disks with different viscosities in Appendix H.

The time evolution of the gas and pebble surface density as shown in Fig. 3.3 reveals that due to the inward drift of pebbles, the gas surface density changes on longer timescales compared to the solid surface density. This effect is enhanced for low viscosities, which allow larger grains and thus faster drift as well as slower viscous gas evolution.

The low viscosity has two main effects regarding the C/O ratio of the protoplanetary disk. At low viscosity, the pebbles grow larger (e.g., Birnstiel et al. 2012), which allows faster radial drift of the pebbles, enriching the gas with vapor when the pebbles evaporate at evaporation lines. As a consequence, the C/O ratio in the very inner disk is very low initially, due to the evaporation of water-rich pebbles. The low viscosity is then inefficient in diffusing the vapor inward, so that it takes several megayears to diffuse the gaseous methane inward, resulting in an increase in C/O only at late times. This effect is further aided by the inward diffusion of water vapor, which also increases the C/O in the gas phase. We discuss more about the water content in the protoplanetary disk below. This effect clearly depends on the disk's viscosities, where larger viscosities allow an increase to super-solar C/O values, while disks with low viscosities ($\alpha = 10^{-4}$) always have sub-solar C/O values interior of the water ice line (Fig. 3.3). Furthermore, the evaporation of inward drifting pebbles does not only influence the C/O ratio in the disk, but also the heavy element content in the gas phase (Fig. 3.4), which is larger in the initial phase, but then decreases in time, as the pebble supply originating from the outer disk diminishes in time.

The heavy element enrichment of the gas phase of the disk interior to the evaporation lines is key to understand the heavy element enrichment of gas accreting planets. Hints for this icy pebble migration across evaporation lines could also explain features of observed protoplanetary disks (Banzatti et al., 2020; Zhang et al., 2020).

Gas diffuses and spreads outward, crossing the evaporation lines where it can condense, leading to pebble pileups that can be seen especially around the water ice line in the pebble surface density (Fig 3.3). This process is also invoked by Aguichine et al. (2020) to explain the composition of refractory materials in the solar systems at so-called rock lines. Mousis et al. (2021) uses the same processes, but around volatile lines, to explain the chemical composition of the comet C/2016 R2. The results of our simulations are in line with theirs.

3.2.4 *Disk lifetime*

Observations of disks indicate that disks live for a few million years (Mamajek, 2009). The final stages of the disk is determined by photoevaporation (e.g., Ercolano et al., 2009; Pascucci & Sterzik, 2009; Ercolano & Clarke, 2010; Owen et al., 2012, 2013). We did not include an exact photoevaporation model here but instead began to drastically decay the gas surface density once it reached a critical time. We used a sink term in the viscous evolution (Eq. 3.11) given by

$$\dot{\Sigma}^{W}_{\mathrm{gas,Y}} = \begin{cases} 0 & t < t_{\mathrm{evap}} \\ \frac{\Sigma_{\mathrm{gas,Y}}}{\tau_{\mathrm{decay}}} & t \geqslant t_{\mathrm{evap}} \end{cases}. \tag{3.20}$$

The starting time of the disk clearance t_{evap} was generally set to 3 Myr and the decay timescale τ_{decay} to 10 kyr. A similar approach is used in the N-body simulations of Izidoro et al. (2021b) and Bitsch et al. (2019). We discuss more about how photoevaporation would influence our results in Sect. 3.5.

3.2.5 *Migration*

Growing planets with mass M naturally interact gravitationally with the ambient disk, which causes the planet to change its orbital elements (for a review, see Kley & Nelson 2012 and Baruteau et al. 2014). This migration process depends on the angular momentum of the planet

$$J_p = M a_p^2 \Omega_K. \tag{3.21}$$

The change of orbital position a_p is then given as (Armitage, 2013)

$$\dot{a_p} = \frac{da_p}{dt} = \frac{a_p}{\tau_M} = 2a_p \frac{\Gamma}{J_p}, \tag{3.22}$$

where τ_M is the migration timescale and Γ the torque that acts on the planet. Low mass planets only disturb the disk slightly and migrate in the type-I fashion, where the torque acting on the planet is a combination of the Lindblad and corotation torques. We used here the torque formula by Paardekooper et al. (2011), which includes the Lindblad as well as as the barotropic and entropy related corotation torques.

Besides these classical torque, new studies reveal that the thermal torque (Lega et al., 2014; Benítez-Llambay et al., 2015; Masset, 2017), originating from density perturbations close to the planet due to thermal heat exchange between

the planet and the disk, as well as the dynamical torque (Paardekooper, 2014; Pierens, 2015), originating from feedback processes of the migration rate of the planet on the torque, can play a vital role in the orbital evolution of the planet.

The thermal torque consists of a cooling torque and a heating torque due to the bombardment and ablation of solids. We followed the description of Masset (2017) to include the thermal torque using the accretion luminosity as defined by Chrenko et al. (2017)

$$L = \frac{GM}{a_p}\dot{M}_{peb}, \tag{3.23}$$

where $\dot{M}_{peb}$ is the accretion rate of pebbles onto the planet (see below). Depending on the accretion efficiency of the planet, this thermal torque can lead to outward migration (Guilera et al., 2019; Baumann & Bitsch, 2020).

For the dynamical torque we followed Paardekooper (2014) and replaced Eq. 3.22 by

$$\frac{da_p}{dt} = \frac{a_p}{\tau_M} = 2a_p\Theta\frac{\Gamma}{J_p}, \tag{3.24}$$

where Θ is the numerical parameter that determines the effects of migration onto the migration rate (Eqs. 31 and 32 from Paardekooper (2014)). The dynamical torque can also help to significantly slow down inward migration of low mass planets, preventing large-scale migration of planets (Ndugu et al., 2021).

Planets that start to accrete gas efficiently, open gaps in the protoplanetary disk (Crida et al. 2006; Crida & Morbidelli 2007). The gap opening is caused by gravitational interactions between the disk and the planet, but can also be aided by gas accretion itself (Crida & Bitsch, 2017; Bergez-Casalou et al., 2020). A combined approach of gap opening via gravity and gas accretion is implemented in Ndugu et al. (2021) and we follow their approach. We first describe here the gap opening by gravity and include later on the gap opening via gas accretion.

A gap by gravity can be opened (with $\Sigma_{Gap} < 0.1\Sigma_{gas}$), when

$$\mathcal{P} = \frac{3}{4}\frac{H_{gas}}{R_H} + \frac{50}{q\mathcal{R}} \leqslant 1\,, \tag{3.25}$$

where $R_H = a_p \left(\frac{M}{3M_\star}\right)^{1/3}$ is the planetary Hill radius, $q = M/M_\star$, and $\mathcal{R}$ the Reynolds number given by $\mathcal{R} = a_p^2 \Omega_K / \nu$ (Crida et al., 2006). The depth of the gap caused by gravity is given in Crida & Morbidelli (2007) as

$$f(\mathcal{P}) = \begin{cases} \frac{\mathcal{P}-0.541}{4} & \text{if} \quad \mathcal{P} < 2.4646 \\ 1.0 - \exp\left(-\frac{\mathcal{P}^{3/4}}{3}\right) & \text{otherwise} \end{cases} . \tag{3.26}$$

We note that the gap depth can also be influenced by gas accretion, so we used in our code

$$f_{gap} = f(\mathcal{P}) f_A \tag{3.27}$$

to calculate the gap depth relevant to switch from type-I to type-II migration. Here f_A corresponds to the contribution of accretion to the gap depth (see below in Sect. 3.2.6), as discussed in Ndugu et al. (2021).

If the planet becomes massive enough to achieve a gap depth of 10% of the unperturbed gas surface density, it opens up a gap in the disk, and it migrates in the pure type-II regime, where the migration timescale is given as $\tau_{visc} = a_p^2/\nu$. However, if the planet is much more massive than the gas outside the gap, it will slow down. This happens if $M > 4\pi\Sigma_{gas} a_p^2$, which leads to the migration timescale of

$$\tau_{II} = \tau_\nu \times \max\left(1, \frac{M}{4\pi\Sigma_{gas} a_p^2}\right) , \tag{3.28}$$

resulting in slower inward migration for more massive planets (Baruteau et al., 2014).

In addition, we used a linear smoothing function for the transition between planets that open partial gaps inside the disk (that migrate with the reduced type-I speed by the factor f_{gap}) and planets that migrate with type-II, because even the reduced type-I migration rate (if the gap is fully opened with $\mathcal{P} < 1$) is different from the nominal type-II rate. This approach is also used in Bitsch et al. (2015b).

3.2.6 *Accretion*

We illustrate the planetary growth in our model in Fig. 3.1. Planetary embryos are planted into the disk with masses, where pebble accretion starts to become efficient (e.g., Lambrechts & Johansen, 2012; Johansen & Lambrechts, 2017):

$$M_t = \sqrt{\frac{1}{3}} \frac{\Delta v^3}{G\Omega_K}, \tag{3.29}$$

with a typical value of $M_t \approx 5 \times 10^{-3} M_\odot$ at 10 AU. Our planets then start to accrete pebbles (see Sect. 3.2.6). When the planet is massive enough to form a pressure bump in the gas surface density, pebbles are hindered from reaching the planet. This transition occurs at the pebble isolation mass M_{iso} (see Morbidelli & Nesvorny, 2012; Lambrechts et al., 2014; Ataiee et al., 2018; Bitsch et al., 2018), where we follow the pebble isolation mass prescription of Bitsch et al. (2018).

At $M = M_{iso}$ the accretion of pebbles ends and the core is completely formed. Core accretion is then followed by envelope contraction and envelope accretion (see Sect. 3.2.6).

During the buildup of the core, we set the fraction of matter that is accreted to the core (with mass M_c) at $M < M_{iso}$ to 90% of the total accreted matter (10% of accreted pebbles contribute to the primary envelope). This approach is supposed to account for pebble evaporation into the planetary envelope during core buildup in a simplified way compared to more sophisticated models (e.g., Brouwers & Ormel 2020; Ormel et al. 2021), who actually show that even less than 50% of the solids accreted via pebbles make up the core and the evaporated pebbles make up most of the heavy element content of these forming planets (Ormel et al., 2021). The initial growth during the core buildup in our model is thus simply described via

$$\dot{M}_{core} = 0.9 \dot{M}_{peb}; \quad \dot{M}_{gas} = 0.1 \dot{M}_{peb} \, , \tag{3.30}$$

where $\dot{M}_{peb}$ describes the pebble accretion rate onto the planetary core (see below). We discuss this assumption, which mainly influences the atmospheric C/O, but not the total heavy element content, in more detail in Appendix I. After the pebble isolation mass is reached, all material is accreted into the planetary envelope M_a.

Pebble accretion

The accretion of small millimeter to centimeter sized objects, so-called pebbles, is thought to significantly accelerate the growth process of planetary cores (Ormel & Klahr, 2010; Johansen & Lacerda, 2010; Lambrechts & Johansen, 2012). Here, we follow the pebble accretion rates derived in Johansen & Lambrechts (2017). The accretion rate of pebbles on a growing protoplanet is determined by the azimuthal flux of pebbles $\rho_{peb} \delta v$ through the cross section of the accretion sphere πR_{acc}^2 of the planet:

$$\dot{M}_{peb} = \begin{cases} \pi R_{acc}^2 \rho_{peb} \delta v & \text{3D accretion} \\ 2 R_{acc} \Sigma_{peb} \delta v & \text{2D accretion} \end{cases} . \tag{3.31}$$

The radius of the accretion sphere R_{acc} strongly depends on the Stokes number of the pebbles:

$$R_{acc} \propto \left(\frac{\Omega_K St}{0.1}\right)^{1/3} R_H, \tag{3.32}$$

where R_H is the planetary hill radius. The optimal Stokes number for pebble accretion is approximately 0.1.

The transition criterion for the transition from 3D to 2D accretion is given by (Morbidelli et al., 2015)

$$H_{peb} < \frac{2\sqrt{2\pi}R_{acc}}{\pi}, \tag{3.33}$$

where we use the pebble scale height $H_{peb} = H_{gas}\sqrt{\alpha_z/St}$ and the relation $\rho_{peb} = \Sigma_{peb}/(\sqrt{2\pi}H_{peb})$. In the case of 2D pebble accretion, the planetary accretion radius is larger than the midplane pebble scale height of the disk, so that the planet can accrete from the full pebble flux passing the planetary orbit. This is not the case in the 3D pebble accretion regime, where the planetary accretion radius is smaller than the pebble scale height and only a fraction of the pebble flux passing the planet can contribute to the accretion. We use here $\alpha_z = 1 \times 10^{-4}$ for all our simulations (Table 3.3), motivated by the constraints from protoplanetary disk observations, which show low level of vertical stirring (Dullemond et al., 2018). Motivated by simulations (Nelson et al., 2013; Turner et al., 2014; Flock et al., 2015) and observations (Dullemond et al., 2018; Flaherty et al., 2018), Pinilla et al. (2021) study how different sources and values of turbulence for vertical stirring, radial diffusion, and gas viscous evolution influence grain growth and drift, finding that indeed different values for these parameters allow a better match to the observations. For simplicity we thus keep α_z fixed in our simulations and only vary α, responsible for the disk evolution, gas accretion and migration.

The pebble surface density and the Stokes number are a natural outcome of our disk evolution model (see Sect. 3.2.1) and depend on the initial solid to gas ratio (ϵ_0). This approach is an improvement compared to previous planet formation simulations via pebble accretion, where mostly a simplified pebble growth and drift model is used (e.g., Lambrechts & Johansen 2014; Bitsch et al. 2015b; Ndugu et al. 2018), but approaches using a model with accretion rates depending on a full pebble size distribution have also been implemented in other works (Guilera et al., 2020; Venturini et al., 2020; Savvidou & Bitsch, 2021; Drążkowska et al., 2021).

Gas accretion

In reality, gas contraction can already happen during the buildup of the core, where the efficiency increases once the heat released by infalling solids stops. We follow here a simple two-step process, where the planetary envelope can quickly contract and runaway gas accretion can start once the planet has reached its pebble isolation mass, where the accretion of solids stop.

In our model, the gas accretion onto the planet is given by the minimum between the accretion rates given by Ikoma et al. (2000), Machida et al. (2010) and by the gas the disk can viscously provide into the horseshoe region after the planet has emptied the horseshoe region (Ndugu et al., 2021). We follow here the approach outlined in Ndugu et al. (2021), which is derived for H-He gas. We discuss how vapor-enriched gas accretion (e.g., Hori & Ikoma 2011; Venturini et al. 2015) could influence our results in Sect. 3.5.

The gas accretion rates of Ikoma et al. (2000) are given by

$$\dot{M}_{\rm gas,Ikoma} = \frac{M}{\tau_{\rm KH}}, \tag{3.34}$$

where $\tau_{\rm KH}$ is the Kelvin-Helmholtz contraction rate and scales as

$$\tau_{\rm KH} = 10^3 \left(\frac{M_c}{30 M_E}\right)^{-2.5} \left(\frac{\kappa_{\rm env}}{0.05 {\rm cm^2 g^{-1}}}\right) {\rm year}. \tag{3.35}$$

Here M_c is the mass of the planet's core; this is in contrast with M, which is the full planet mass (core plus envelope). We set the envelope opacity for simplicity to 0.05 cm^2/g for all our planets.

Machida et al. (2010) give the gas accretion rate $\dot{M}_{\rm gas,Machida}$ as the minimum of:

$$\dot{M}_{\rm gas,low} = 0.83 \Omega_k \Sigma_{\rm gas} H_{\rm gas}^2 \left(\frac{R_H}{H_{\rm gas}}\right)^{\frac{9}{2}} \tag{3.36}$$

and

$$\dot{M}_{\rm gas,high} = 0.14 \Omega_k \Sigma_{\rm gas} H_{\rm gas}^2 \, . \tag{3.37}$$

The Machida et al. (2010) rate is derived from shearing box simulations, where gap formation is not taken fully into account. However, once a gap is opened, obviously the planet cannot accrete more gas than the disk can supply. Throughout our simulations, we modeled the disk supply rate

$$\dot{M}_{\rm disk} = -2\pi r \Sigma_{\rm gas} u_{\rm gas}, \tag{3.38}$$

where u_{gas} is the radial gas velocity (Eq. 3.12). The radial gas velocity depends linearly on α, which therefore sets the accretion flow in the disk, so it provides the gas accretion rate to the planet. Therefore, a change in α would imply a different accretion flow through the disk and thus sets a different limit on the planet accretion rate. In summary, our gas accretion rate, $\dot{M}_{gas}$ onto the planet is taken as

$$\dot{M}_{gas} = \min\left(\dot{M}_{gas,Ikoma}, \dot{M}_{gas,Machida}, \dot{M}_{disk} + \dot{M}_{HS}\right), \tag{3.39}$$

where $\dot{M}_{HS}$ is the horseshoe depletion rate, given by

$$\dot{M}_{HS} = M_{HS}/(2T_{HS}), \tag{3.40}$$

where M_{HS} is the mass of the horseshoe region, $T_{HS} = 2\pi/\Omega_{HS}$ is the synodic period at its border with $\Omega_{HS} = 1.5\pi\Omega r_{HS}/a_p$, $r_{HS} = x_s a_p$ is its half-width (with x_s from Paardekooper et al., 2011, Eq. 48). At each time step Δt we compute the mass accretion rate $\dot{M}_{HS}$ that could be provided by the horseshoe region.

Following the same philosophy as for gravitational gap opening, we introduce an additional parameter f_A, initially equal to 1, which is computed every time step. f_A scales as

$$f_A = 1 - \frac{\dot{M}_{gas}\delta t}{f(\mathcal{P})\hat{M}_{HS}}. \tag{3.41}$$

Here $\hat{M}_{HS}$ is the mass inside the horseshoe region in the absence of gas accretion onto the planet and in absence of gravitational gap opening. $\hat{M}_{HS}$ is given by

$$\hat{M}_{HS} = 2\pi a_p r_{HS}\hat{\Sigma}_{HS}. \tag{3.42}$$

The full depth of the gap is therefore

$$f_{gap} = f(\mathcal{P})f_A. \tag{3.43}$$

The formulae above (Eq. 3.41) requires us to monitor the mass of the horseshoe region M_{HS} as a function of time. By definition of the $f(\mathcal{P})$ and f_A factors, the mass of the horseshoe region scales as

$$M_{HS} = f(\mathcal{P})f_A\hat{M}_{HS}. \tag{3.44}$$

The quantity $\hat{M}_{HS}$ evolves over time because the width of the horseshoe region r_{HS} changes with the planet mass and location. For simplicity, we assume

that the vortensity in the horseshoe region is conserved (strictly speaking this is true only in the limit of vanishing viscosity), so that if the location of the planet changes from a_p to a'_p, the horseshoe gas density changes from

$$\hat{\Sigma}_{HS} = \hat{M}_{HS}/(4\pi a_p r_{HS}) \tag{3.45}$$

to

$$\hat{\Sigma}'_{HS} = \hat{\Sigma}_{HS}(a_p/a'_p)^{3/2}. \tag{3.46}$$

Thus, when r_{HS} changes to r'_{HS}, we compute the quantity

$$\hat{M}'_{HS} = 4\pi a'_p r'_{HS} \hat{\Sigma}'_{HS}. \tag{3.47}$$

If $\hat{M}'_{HS} < \hat{M}_{HS}$, we refill the horseshoe region at the disk's viscous spreading rate and recompute $\hat{M}'_{HS}$ as

$$\hat{M}'_{HS} = \hat{M}_{HS} + (\dot{M}_{disk} - \dot{M}_{gas})\Delta t, \tag{3.48}$$

where $\dot{M}_{disk}$ and $\dot{M}_{gas}$ are defined in Eqs. 3.38 and 3.39, respectively. If the opposite is true, it means that the horseshoe region has expanded and must have captured new gas from the disk, with a density Σ_{gas}. Thus, we compute the new value of $\hat{M}_{HS}$ as:

$$\hat{M}'_{HS} = \hat{M}_{HS} + \left(4\pi a'_p r'_{HS} - \frac{\hat{M}_{HS}}{\hat{\Sigma}'_{HS}}\right)\Sigma_{gas}\ . \tag{3.49}$$

Once $\hat{M}'_{HS}$ is computed, the new value of $\hat{\Sigma}'_{HS}$ is recomputed as $\hat{\Sigma}'_{HS} = \hat{M}'_{HS}/(4\pi a'_p r'_{HS})$. This procedure is then repeated at every time step. This procedure automatically captures the gas surface density decay during the disk's evolution because Σ_{gas} is evaluated at each time step. This approach is outlined, as described, in Ndugu et al. (2021).

3.2.7 *Gap profile*

Pebbles will stop drifting inward when the planet is massive enough to open a small gap in the protoplanetary disk. In reality, the torque from the planet acting on the disk is responsible for the opening of the gap (e.g., Crida et al. 2006). For simplicity, we chose an approach with varying viscosity to mimic the effect of a pressure bump caused by a growing planet (e.g., Pinilla et al. 2021). We did so by applying a gap profile inversely to the viscosity once the planet has reached the pebble isolation mass in order to keep the mass

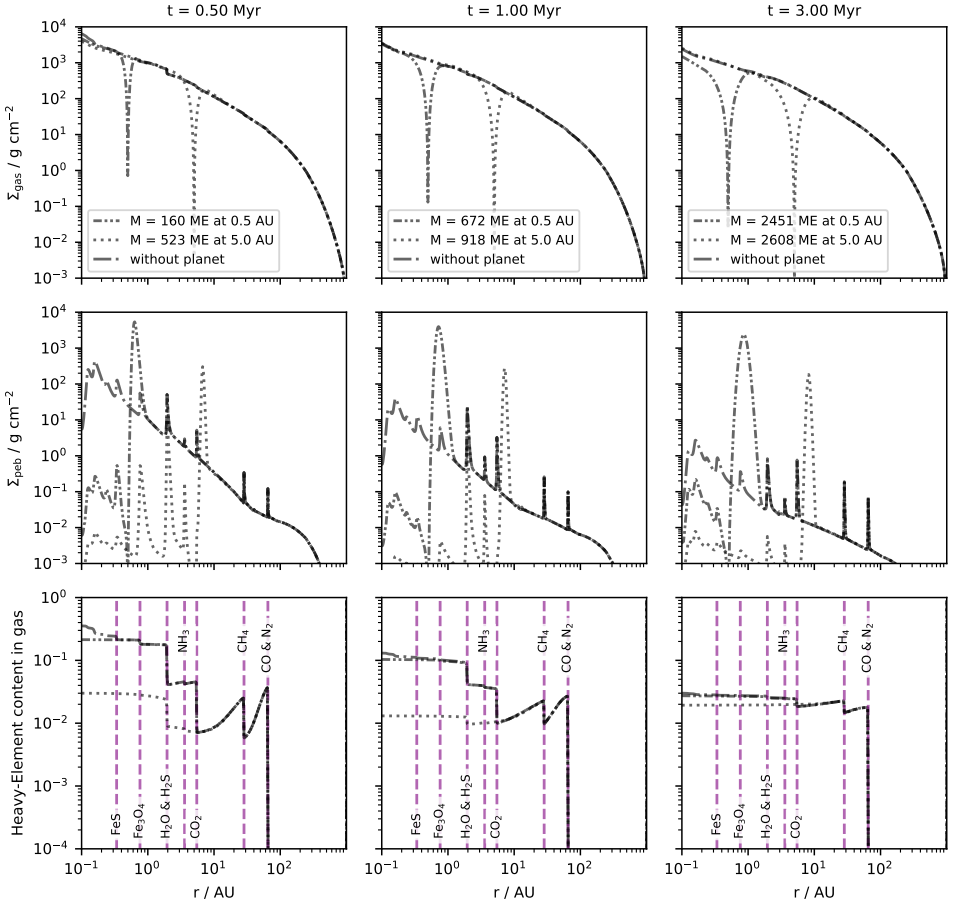

Figure 3.4: Gas surface density (top), pebble surface density (middle), and heavy element content $\Sigma_{gas,Y}/\Sigma_{gas}$ of the gas surface density as a function of radius for different times using the evaporation and condensation treatment described in Sect. 3.2.3 in the case of either no planet or planets fixed at 0.5 or 5 AU. These planets are either located interior (0.5 AU) or exterior (5 AU) to the water ice line. Disk parameters can be found in Table 3.3; here we use $\alpha = 0.0005$.

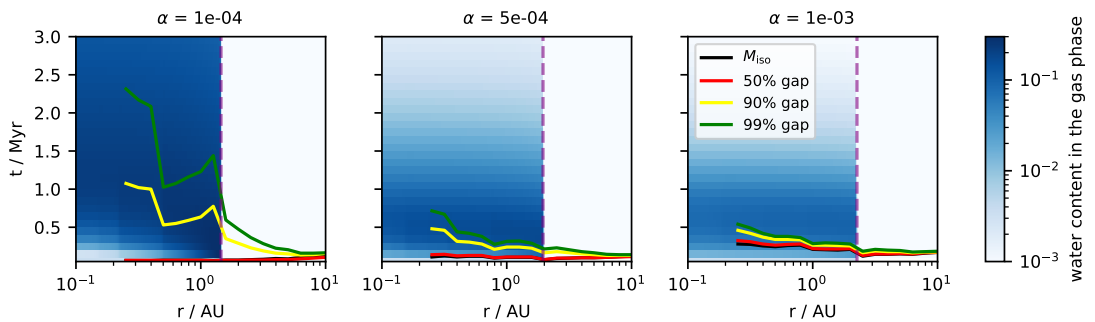

Figure 3.5: Water content in the gas phase as a function of time for different disk viscosities. The black line marks the time a non-migrating growing planet starting at $t = 0.05\,Myr$ needs to reach the pebble isolation mass, while the red, yellow, and green lines indicate the time the same growing planet needs to reach a certain gap depth.

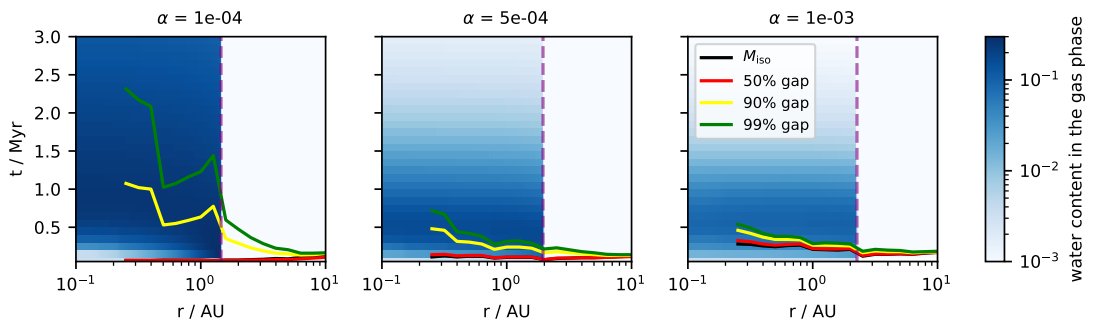

Figure 3.6: Same as Fig. 3.5 but with a growing non-migrating planet placed at 0.5 AU. The water content of the growing planet is displayed in Fig. 3.9. The planet growing interior to the water ice line has only a little influence on the disk's water vapor content.

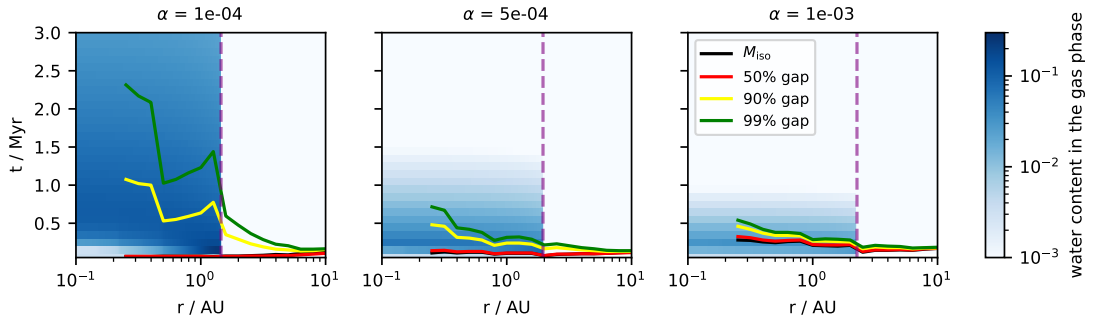

Figure 3.7: Same as Fig. 3.5 but with a growing non-migrating planet placed at 5.0 AU. The water content of the growing planet is displayed in Fig. 3.9. The planet exterior to the water ice line has a strong influence on the water vapor content in the inner disk, compared to planets interior to the water ice line (Fig. 3.6) or if there are no planets (Fig. 3.5).

accretion rate of the gas phase of the protoplanetary disk constant. The viscous α parameter in Eq. 3.11 is then given at the planet's location by

$$\alpha = \alpha / \aleph(r), \tag{3.50}$$

where the numerical factor $\aleph(r)$ describes the gap profile, which is approximated by a Gaussian distribution

$$\aleph(r) = 1 - [1 - f_{gap}] \exp\left(0.5\,[(r - a_p)/\sigma]^2\right) \tag{3.51}$$

around the planetary position with a width given by the horseshoe width

$$\sigma = 2r_{HS}/[2\sqrt{2\log(2)}]. \tag{3.52}$$

This increased α parameter is then only used to calculate the gap in the gas surface density profile. All other calculations within the code use the default α parameter. We interpolate quantities to the planetary position by excluding the gap (i.e., use only those grid cells that satisfy $\aleph < 1\%$), since our descriptions of the migration and accretion rates depend on the unperturbed disk.

The effects of the planetary gap on the gas surface density, the heavy element content and the pebble distribution can be seen in Fig. 3.4, where we compare simulations of a protoplanetary disk that include non-migrating planets at 0.5 or 5 AU with a protoplanetary disk that does not host a planet. The gap generated by the growing planet results in deep deletions in the gas surface density, where consequently pressure bumps exterior to the planetary orbit are formed. The gap widens in time, as the planet grows. We additionally show in Figs. 3.5, 3.6, and 3.7 the water vapor content in disks without and with planets (at 0.5 and 5.0 AU) as a function of time for different disk viscosities.

It is clear from Fig. 3.4 that the growing planets cause pressure bumps exterior to their orbits in the protoplanetary disk, where pebbles can accumulate. These pile-ups in the pebble surface density are much larger than the pile-ups caused by condensation in the outer disk regions. Exterior to the pressure bump exerted by the planet, the disk structure is not affected and the pile-ups in the pebble surface density are caused by condensation and evaporation. Furthermore, the planets are very efficient at blocking the pebbles, resulting in low pebble surface densities interior to the planetary orbits, because our pebble evolution model does not contain multiple pebble species during the pebble drift step, which prevents a detailed filtering mechanism at pressure bumps (e.g., Weber et al. 2018). Interior to the pressure bump generated by the giant planet, spikes in the pebble distribution at the evaporation lines are

still present, especially around the water ice line[2]. This spike in the pebble distribution is fuelled by outward diffusing condensing vapor. However, in time, the vapor has diffused inward, hindering efficient condensation, diminishing the pebble pile-up at the evaporation fronts interior to the giant planet, resulting in a very low pebble density. This effect can be seen clearly in the middle panel with $\alpha = 5 \times 10^{-4}$ of Fig. 3.7, where the water vapor content decreases sharply after 1 Myr.

The heavy element content in the gas phase in the inner disk increases toward the star because pebbles drift inward very efficiently, where they evaporate once they cross the evaporation lines aided by the fact that gas diffusion is initially inefficient at low viscosities. This can be seen in Fig. 3.5 where the water vapor content is initially larger close to the water ice line, but then slowly increases in the whole inner disk as water vapor diffusion becomes efficient after a few 100 kyr. The same effect is shown in the simulations of Gárate et al. (2020).

Especially at the water ice line, a jump in the heavy element content of the gas phase is observed, due the large water ice abundance. This is not only the case for the simulations without planets, but is also the case if the planet is interior to the water ice line, which only blocks the inward drifting pebbles once they have evaporated at the water ice line. Especially the water vapor content in the inner disk is very similar in both cases (Figs. 3.5 and 3.6). In contrast, the heavy element content in the gas is much lower, if a planet starts to block pebbles exterior to the water ice line. Nevertheless, our simulations still show initially a small jump in the heavy element content of the gas phase for this case because the inward drifting pebbles enrich the gas before the planet generates a pressure bump to block the inward drifting pebbles. The water vapor then diffuses inward, reducing the heavy element content (Fig. 3.4). At very late times, however, the heavy element content in the gas phase rises again due to the inward diffusion of methane and CO, while the water vapor content is depleted (Fig. 3.7). Consequently, the C/O ratio in the gas phase also increases (see Fig. 3.3 for the case without planet). It is clear that the positions of planets relative to the evaporation fronts influences the heavy element content in the gas phase (see also Bitsch et al. 2021).

In time the heavy element content of the gas in the inner regions diminishes because the volatile vapor is slowly accreted onto the star and the disk has transported most of its pebbles into the inner disk (Fig. 3.3), cutting the supply of new pebbles that could evaporate and contribute to the heavy element content of the gas.

2 At this point in the disk, the water ice makes up 33% of the total solid mass, clearly overpowering the contribution of H_2S.

The enrichment in heavy elements in the inner disk regions is a strong function of the disk's viscosity. At low viscosities, the pebbles grow larger and thus drift faster inward where they evaporate, increasing the heavy element content in the gas phase. In addition, the low viscosity is very inefficient in removing the volatile-rich gas onto the star. At high viscosity, pebbles are smaller and the disk is more efficient in diffusing the vapor-rich gas inward. As a consequence, the heavy element enrichment in the inner disk decreases with increasing viscosity. This effect can be seen very clearly for the evolution of the water vapor content in time (Figs. 3.5, 3.6, and 3.7). This clearly indicates that the enrichment of the inner disk, and consequently planetary atmospheres, as discussed below, is a strong function of the disk's viscosity, where lower viscosities will allow a larger enrichment of the disk with vapor and consequently of planetary atmospheres with vapor. Observations of the water vapor content in the inner disk, could thus be helpful to constrain the disk's viscosity.

3.2.8 *Operating principle*

Calculations in this paper are performed using the newly developed 1D code `chemcomp`. It provides a platform to simulate the above described physics. It includes a disk module (attributes are defined on a log-radial grid) that deals with the formation of pebbles (see Sect. 3.2.1) as well as the dynamics of gas and pebbles (see Sect. 3.2.3). It calculates the temperature of the disk (see Appendix B) and the temperature-dependent compositions of gas and pebbles (see Sect. 3.2.2) by also including effects induced by the existence of evaporation lines (see Sect. 3.2.3).

The code also contains a planet module that handles growth (see Sect. 3.2.6) and migration (see Sect. 3.2.5) of a single planet. The planet module acts as the supervisor of the disk module and "collects" the matter available in the disk.

The operating principle of the code can also be divided into these two modules. As Fig. 3.8 shows, each time step begins ($\Delta t = 10\,\mathrm{yr}$) with the disk step. The disk step begins by computing the pebble growth and then computing the sink and source terms for the viscous evolution (Eqs. 3.16 and 3.20). We then have everything in place to evolve the surface densities in time. We use a modified version of the donor-cell scheme outlined in Birnstiel et al. (2010) to solve Eqs. 3.15 and 3.11 for every molecular species. The realization in `chemcomp` is an adapted version from the implementation in the unpublished code `DISKLAB` (Dullemond & Birnstiel, 2018). The inner disk boundary for the gas and solid evolution is treated using a Neumann

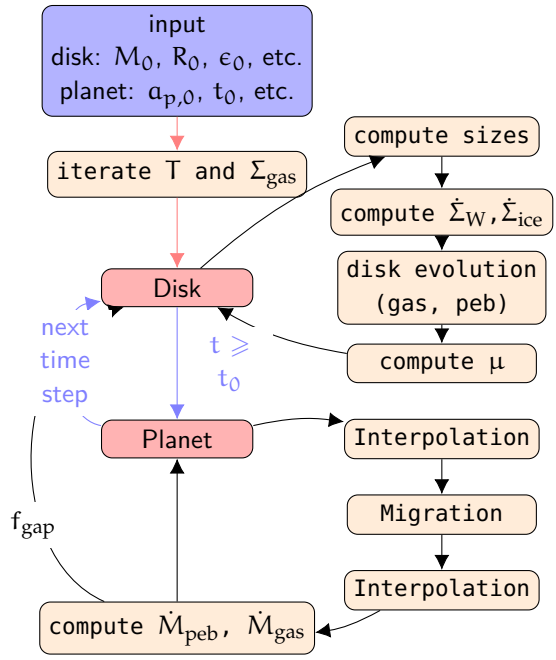

Figure 3.8: Operating principle of `chemcomp`. The main loop is shown in blue. Black arrows connect the individual steps (beige nodes) that are performed in each time step. Red arrows indicate initialization steps.

Quantity	Value	
$a_{p,0}$	$3, 10, 30\,AU^{\star}$	initial position
t_0	$0.05\,Myr^{\star}$	starting time
κ_{env}	$0.05\,cm^2\,g^{-1}$	envelope opacity

(a) Planet

Quantity	Value	
r_{in}	$0.1\,AU$	inner edge
r_{out}	$1000\,AU$	outer edge
N_{Grid}	500	Number of gridcells

(b) Grid

Quantity	Value	
α	$(1, 5, 10) \times 10^{-4}$	viscous alpha parameter
α_z	1×10^{-4}	vertical mixing
M_0	$0.128\,M_{\odot}$	initial disk mass
R_0	$137\,AU$	initial disk radius
[Fe/H]	0	host star metallicity
t_{evap}	$3\,Myr$	disk lifetime
ϵ_0	$2\,\%^{\star}$	solid to gas ratio
u_{frag}	$5\,m\,s^{-1}$	fragmentation velocity

(c) Disk

Table 3.3: Parameters used throughout this paper.

Notes: The star symbol indicates those parameters whose values are varied in the figures associated with Table 3.5.

boundary condition for $\Sigma_{gas,Y}$ and $\frac{\Sigma_{Z,Y}}{\Sigma_{gas}}$, respectively. The outer boundary uses a fixed Dirichlet boundary condition.

We now have a disk that is advanced in time in which we calculate the torques acting on the planet by interpolating the disk quantities from the radial grid to the planetary position and then advancing its position (Eq. 3.24). After a next interpolation of the disk quantities to the new position of the planet, accretion rates for pebble accretion (Eq. 3.31) and gas accretion (Eq. 3.39), are calculated. The calculated accretion rates already include the chemical composition of the disk because the surface densities are treated as vectors, meaning that the resulting accretion rates are also given as compositional vectors. These accretion rates are now added to the planets composition

$$M_Y \rightarrow M_Y + \dot{M}_Y \cdot \Delta t. \tag{3.53}$$

The pebble and gas accretion rates are additionally converted to sink terms that are then added to the viscous evolution for the next time step. We remove the accreted pebbles only from the cell where the planet is located, since we do not numerically resolve the Hill sphere during pebble accretion. If the planet migrates down to 0.2 AU[3], we stop the accretion of gas because recycling flows penetrating into the Hill sphere of the planet prevent efficient gas accretion (Ormel et al., 2015; Cimerman et al., 2017; Lambrechts & Lega, 2017). Finally, we also check whether the disk has disappeared (disk mass below $1 \times 10^{-6}\,M_\odot$). If both checks evaluated negative we start a new time step.

3.2.9 *Initialization*

All disk quantities are defined on a logarithmically spaced grid with $N_{grid} = 500$ cells between $r_{in} = 0.1\,AU$ and $r_{out} = 1000\,AU$. The code is initialized with the initial gas surface density. Followed by the knowledge of the solid to gas ratio (ϵ_0) it computes the dust- and pebble surface densities. The code will then compute the temperature profile using the surface densities. In this paper we use the analytical solution for the gas surface density (Eq. 3.13) to initialize the code. Since this is based on the viscosity, which depends on the temperature, we iterate the above steps until the temperature has converged to 0.1% accuracy. When the disk has been initialized the code begins the viscous evolution. The planetary seed is then placed at $t = t_0$ into the disk. We stop the planetary integration at the end of the disk's lifetime or if the planet reaches 0.2 AU.

3 This is beyond the inner edge of our disk because grid cells interior of the planet are needed to calculate gradients relevant for planet migration and gap opening.

Abbreviation	Meaning for simulations
evap / evaporation	evaporation and condensation at evaporation lines included
plain	evaporation and condensation is not included

Table 3.4: Meaning of used model abbreviations in Figs. 3.11, 3.12, 3.13, 3.14, and 3.15.

3.3 GROWTH TRACKS

We discuss in this section the results of our models, where we first focus on the water content of growing giant planets and then discuss the atmospheric C/O ratio of growing planets. The disk parameters are the same as for the disk simulations discussed before and we only vary the viscosity parameter.

3.3.1 *Planetary water content*

In Fig. 3.9 we show the water content of non-migrating planets placed at 0.5 AU and 5.0 AU for different viscosities. These planets are placed interior and exterior to the water ice line. Initially only the core is formed, so that the water content is determined only by solid accretion. Due to our assumption for the buildup of the planetary atmosphere during this phase, the water content is the same for the atmosphere and the core. During the core buildup phase, the water ice fraction of the core forming at 0.5 AU is zero because no water ice penetrates that deeply into the disk from the water ice line (see Appendix H). Once the planetary core is fully formed, gas accretion can start (indicated by the deviation of the different curves in Fig. 3.9). Due to the planet's location interior to the water ice line, the planet accretes a lot of water vapor, increasing the planet's atmospheric and total water fraction for all different viscosities.

However, the different viscosities have an influence on the exact water content of the growing planets. At low viscosities, the planet can reach larger water contents compared to high viscosities. This is caused by the larger enrichment with vapor of the inner disk in the case of low viscosity due to the more efficient pebble drift and less efficient vapor diffusion (see also Fig. 3.6). Toward the end of the disk's lifetime, the water content in the planetary atmosphere decreases again because the supply of pebbles that enrich the disk has run out, preventing a continuous water vapor enrichment of the accreting planet. This effect is also stronger for higher viscosities because water vapor diffuses away faster.

A planetary embryo growing at 5.0 AU, has initially a large water content in the core due to the accretion of water ice. As soon as the planet starts to accrete gas efficiently, the water content in the planetary atmosphere decreases because the gas is water poor. The kink in the atmospheric and total water abundance around 100 kyr to 200 kyr is caused by a change in the planetary gas accretion rate, after the planet has emptied its horseshoe region and the planetary growth is limited by the supply rate of the disk (Eq. 3.39), reducing the gas accretion rate onto the planet. Consequently the dilution of the water vapor in the atmospheres slows down in time. This effect is not visible for the planet growing at 0.5 AU, because the water content is increasing as the planet grows and the small deviation in the accretion rate is not visible within the log-scale of the plot.

We note that the growth rate of the planetary core is reduced for larger viscosities. This is caused by the decreasing pebble sizes for increasing viscosities, resulting in lower pebble accretion rates, independent of whether the planet is interior or exterior of the water ice line.

In Fig. 3.10 we show the atmospheric water content of growing and migrating planets in disks with different viscosities. We place the planetary embryos initial interior, exterior, and close to the water ice line. The position of the water ice line is farther away from the star for disks with larger viscosities due to the increase in viscous heating.

As the planetary core grows, the water content of the planetary atmosphere is determined by the composition of the solids that evaporate in the initial atmosphere. This leads to initially water-poor planets interior to the water ice line and to initially water-rich planets exterior to the ice line, as for the non-migrating planets (Fig. 3.9). As soon as the planets start to accrete gas (marked by the dot in Fig. 3.10), the water content of the planetary atmosphere changes. Planets interior to the water ice line accrete water vapor, while planets exterior to the water ice line accrete water-poor gas. If the planets migrate across the water ice line, we observe again a change in the atmospheric water content. The final water content in the atmosphere is then an interplay between the accreted mass interior and exterior to the water ice line.

3.3.2 *Atmospheric C/O ratio*

In our model planets grow and migrate at the same time. We do not take scattering effects happening after the gas disk phase (e.g., Raymond et al., 2009b; Sotiriadis et al., 2017; Bitsch et al., 2020) into account because our model can only include one planetary embryo at a time. We show the growth tracks of three different planets starting at different positions for three different disk

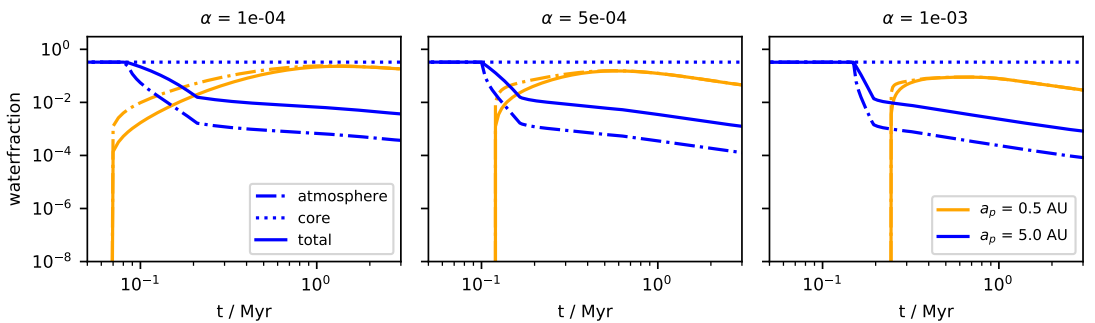

Figure 3.9: Water content of non-migrating planets as a function of time for different disk viscosities, displayed for the core (dotted), the atmosphere (dashed), and the whole planet (solid). The corresponding water content of the protoplanetary disk as a function of time is displayed in Figs. 3.6 and 3.7.

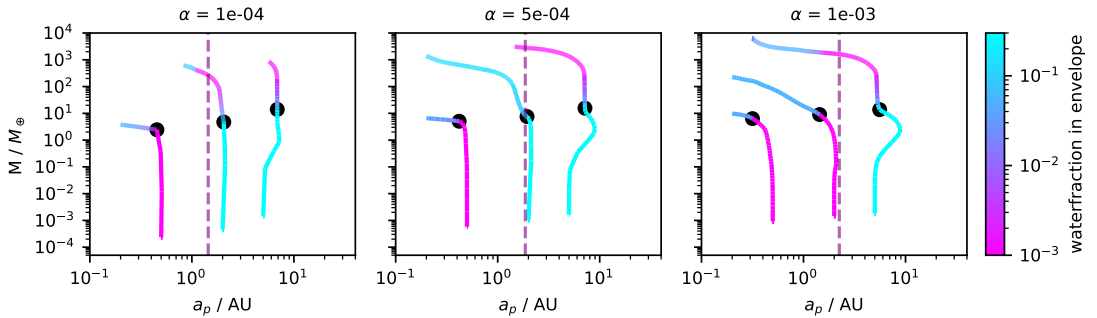

Figure 3.10: Atmospheric water content (in color) of migrating planets in disks with different viscosities. The dot marks the pebble isolation mass, where the planet switches to gas accretion, while the vertical line marks the water ice line.

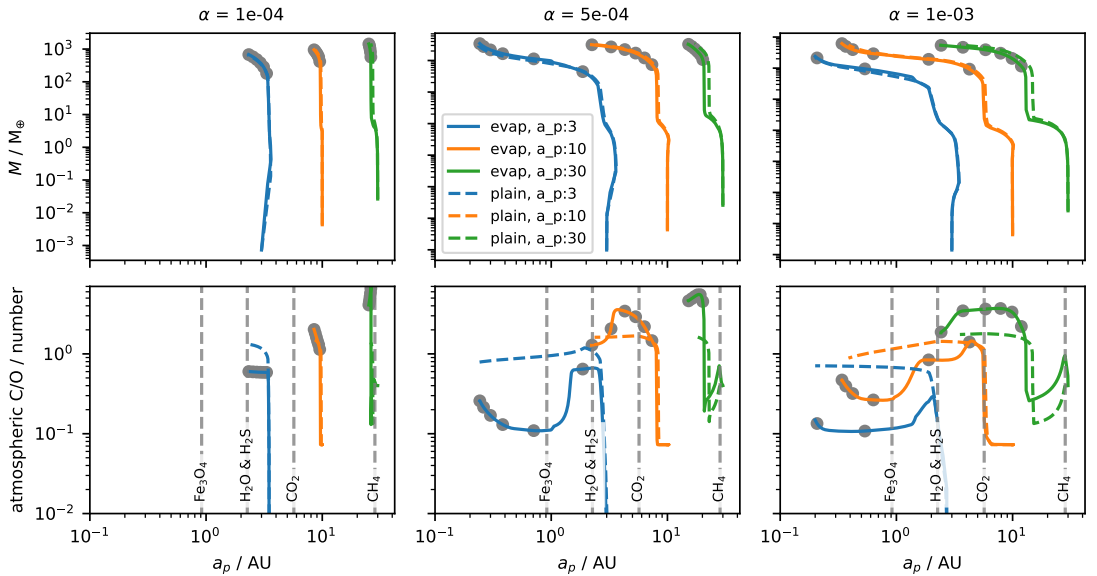

Figure 3.11: Evolution of planets that accrete pebbles and gas starting at different initial positions. Top: Growth tracks displaying the planetary mass as a function of its position. The dashed line indicates planets that grow in disks with a static composition model (see Sect. 3.2.2), while the solid lines include the evaporation of pebbles at the evaporation lines. Bottom: Atmospheric C/O content of the same planets as a function of their position. The dashed gray lines mark the positions of evaporation lines. The gray dots mark time steps of 0.5 Myr. We use here our standard parameters as stated in Table 3.3, corresponding to the disk evolution shown in Fig. 3.3, and abbreviations of the labels can be found in Table 3.4.

viscosities in Fig. 3.11. The disk parameters used for this example correspond to the disk evolution shown in Figs. 3.3 and 3.4.

The blue line depicts the evolution of planets starting at 0.05 Myr and 3 AU, which rapidly accrete pebbles and then gas and migrate inward to become hot Jupiters if the viscosity is large enough, allowing an efficient migration in the type-II regime. Because of the high pebble accretion rates the planet migrates only slightly or even outward during core formation (Fig. 3.11) due to the heating torque. The heating torque does not contribute any more once the planet has reached a few Earth masses and the planet moves inward in type-I migration. Within 0.05 Myr (at $t = 0.1$ Myr) the planet has already started to accrete gas and reached roughly $100\,M_\oplus$ after 0.2 Myr, which happens slightly later in disks with higher viscosities due to the slower pebble accretion rates. During this phase, the planet accretes faster than it migrates because it feeds off the gas supply inside the planetary horseshoe region. Once the horseshoe region is emptied, the planetary accretion is slowed down and the planet migrates inward in the slower type-II migration regime, which is slower for lower viscosities, resulting in only a marginal inward migration in this case. Especially in the case of $\alpha = 10^{-3}$ the inward migration is very efficient, so that the planet reaches the inner edge of the protoplanetary disk well before the end of its lifetime.

In Fig. 3.11 we also compare how evaporation and condensation at evaporation lines affect the formation and composition of the growing planets. The difference is minimal in the growth tracks (upper panel). However, the C/O ratio (bottom panel) shows significant differences for the two model approaches. Water ice line crossing pebbles enrich the gas in oxygen and therefore greatly reduce the C/O ratio interior to the water ice line compared to the static model approach (Fig. 3.3). Furthermore, the evaporation of the methane content of drifting pebbles increases the C/O ratio in the gas significantly at late times, especially for larger viscosities, as the methane vapor diffuses inward.

The C/O ratio of the planet forming at 3 AU in the disk with $\alpha = 10^{-4}$ stays around solar, corresponding to the disk's C/O content (Fig. 3.3). Its migration across the water ice line happens so late that there is no significant change in the planet's C/O. The C/O of the planet forming in the disk with $\alpha = 5 \times 10^{-4}$ shows a more complicated pattern, originating from crossing various ice lines. After the planet crossed the water ice line, the planetary C/O drops (with a slight delay caused by the slower gas accretion rate, as the planetary gap is already formed) and only increases at late times again when inward diffusing carbon-rich gas reaches the planet. The planet forming in the disk with $\alpha = 10^{-3}$ migrates across the water ice line very quickly and

thus harbors a low C/O ratio. In contrast, the planets forming in the model without evaporation of inward drifting pebbles show C/O ratios close to solar, corresponding to the values of the inner disk regions without evaporation (Fig. 3.3).

The origin of the planets forming at 10 AU (orange line) is farther away from the central star, where less solids and gas are available in the disk. This slows down the accretion rate of solids and gas as well as the migration rate. The cores of these planets form beyond the CO_2 evaporation line, resulting in low C/O ratios during the core accretion phase. When the planet has reached the pebble isolation mass and begins to accrete gas, the C/O ratio increases and stays approximately constant because the gas in the range between 2-10 AU, features a relatively constant C/O (Fig. 3.3). Only at late times does the C/O ratio increase further due to the inward diffusing methane vapor. However, the planet forming in the disk with $\alpha = 10^{-3}$ migrates also significantly during its gas accretion phase, crossing several evaporation fronts. At each evaporation front, the planetary C/O ratio changes correspondingly, but also increases slightly toward the end of the disk's lifetime due the inward diffusion of carbon-rich gas.

The planets forming at 30 AU (green lines) needs more time to accrete material, resulting in further inward migration during the type-I regime, especially in disks with high viscosities, which have the lowest pebble accretion rates due to the smallest particles. However, these planets have a very efficient envelope contraction phase due the higher pebble isolation mass, which leads to core masses of $20 M_\oplus$ (twice the core mass of the inner planets) and thus shorter contraction times. This efficient contraction phase boosts the planet into rapid gas accretion, which then slows down the planet into the type-II migration phase.

The C/O ratio looks initially very similar if evaporation of pebbles is considered or not. This is related to the formation position of the planet close to the methane evaporation front, where the C/O in the gas and solid phase does not change very much (Fig. 3.3). Only once the planet crosses the methane evaporation line a significant change of the planetary C/O ratio can be observed. In the cases without evaporation, the planetary C/O ratio increases slightly above 1, while including evaporation can boost the atmospheric C/O ratio up to a value of 5. However, toward later times, the C/O ratio decreases slightly because the supply of carbon-rich pebbles that fuel the carbon vapor, diminishes in time, resulting in a decrease in the C/O ratio of the disk (Fig. 3.3) and consequently in the planetary atmosphere.

We note that the exact change of the atmospheric C/O ratio in the planetary atmosphere when crossing an evaporation front also depends on the gas mass

parameter	values
ϵ_0	0.01, 0.015, 0.02 and 0.025
α	1×10^{-4}, 5×10^{-4} and 1×10^{-3}
t_{evap}	1 Myr, 2 Myr and 3 Myr
t_0	0.05 Myr, 0.15 Myr, 0.25 Myr, 0.35 Myr and 0.45 Myr
$a_{p,0}$	1 AU, 2 AU, 3 AU, 5 AU, 10 AU, 15 AU, 20 AU, 25 AU and 30 AU

Table 3.5: Parameters different from the standard parameters in Table 3.3 that are used for simulations in Sect. 3.4. Simulations are performed on a grid by simulating each of the 1620 possible combinations. Like Thorngren et al. (2016), only planets with final masses in the range of $20 M_\oplus$ and $20 M_J$ and stellar insulations less than $F_\star < 2 \times 10^8$ erg s^{-1} cm^{-2} and additionally only planets with final orbits with less than 1 AU are considered (except in Fig. 3.15).

the planet accretes. If the planet is already very massive and only accretes a tiny fraction of gas with a different composition, the change of the planetary C/O ratio is small.

We conclude that the inclusion of pebble evaporation effects make a huge difference in the atmospheric elemental ratios of gas giants. Our simulations show that the C/O ratio increases with orbital distance, for all disk viscosities. Observed hot Jupiter planets that have formed as cold Jupiters and were scattered to sub AU orbits might therefore have significantly larger C/O ratios compared to planets that formed by smooth inward migration from initially closer-in orbits.

3.4 HEAVY ELEMENT CONTENT

Thorngren et al. (2016) derived the heavy element content for giant exoplanets by comparing the observed planetary masses and radii with interior models. In this section we explore how the effects of pebble evaporation at evaporation lines influences the heavy element content of growing gas giants. We performed simulations on a grid of parameters given in Table 3.5 by simulating every possible combination (in total 1620).

We follow Thorngren et al. (2016) and only include planets in our analysis with final masses in the range of $20 M_\oplus$ and $20 M_J$ and stellar insulations

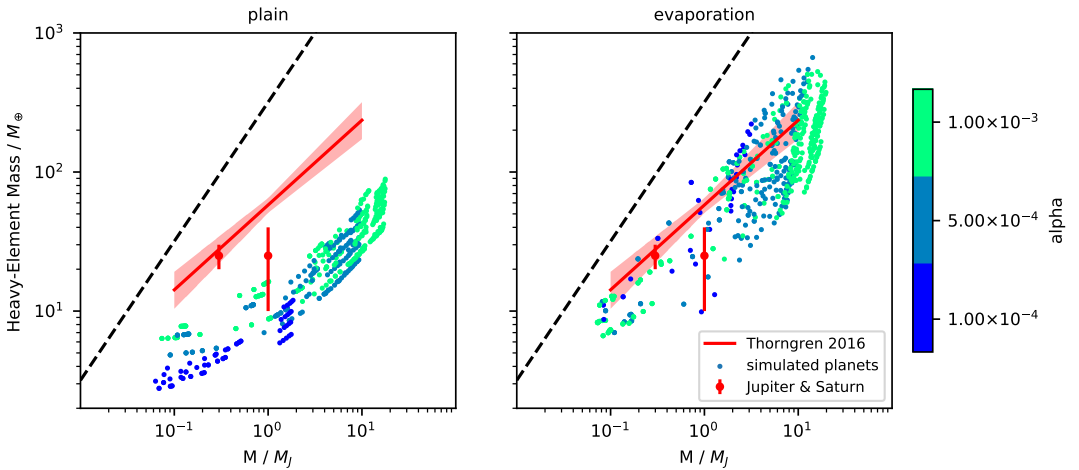

Figure 3.12: Total heavy element mass (core plus envelope) as a function of planetary mass. Simulated planets (see Table 3.5) are compared to interior models of observed hot Jupiters from Thorngren et al. (2016), marked with the red line. The color coding in this figure shows the dependence on α. The different panels indicate whether evaporation line effects have been taken into account for the simulations (see Table 3.4).

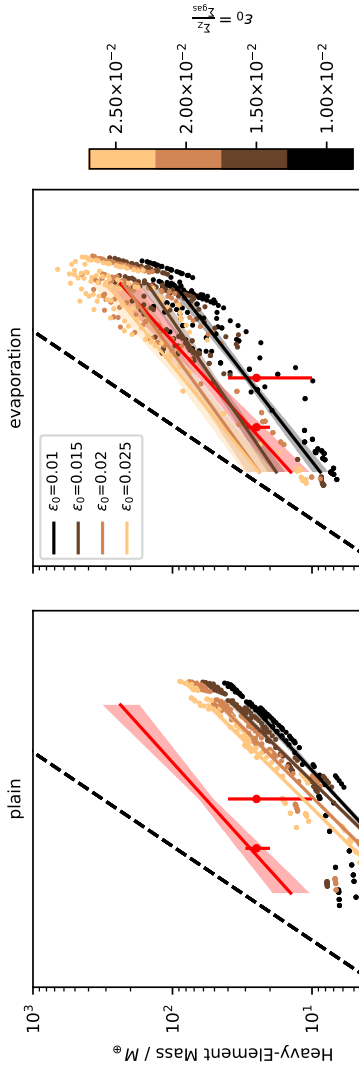

Figure 3.13: Like Fig. 3.12 but using the solid to gas ratio ϵ_0 for the color coding. Each solid to gas ratio has been fitted for comparison to the original fit from Thorngren et al. (2016). Fit results can be found in Table 3.11.

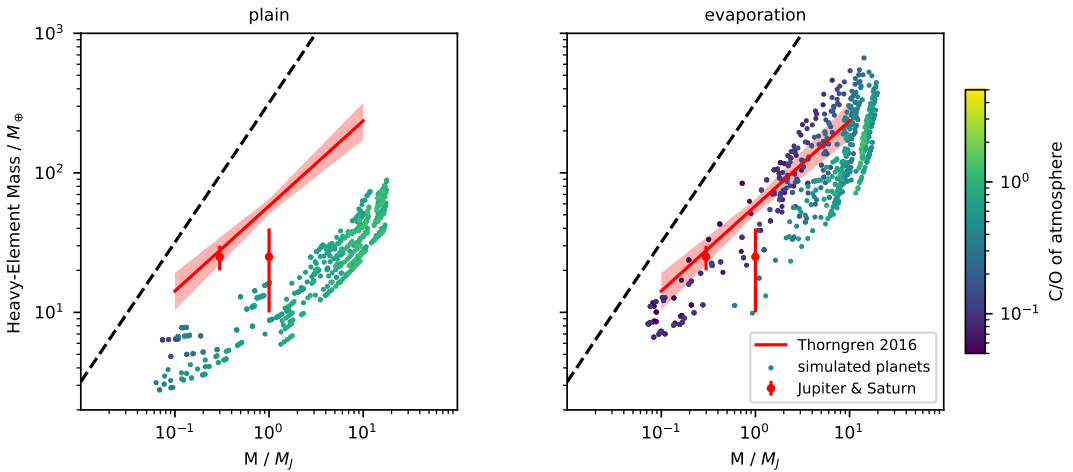

Figure 3.14: Like Fig. 3.12 but using the atmospheric C/O ratio for the color coding.

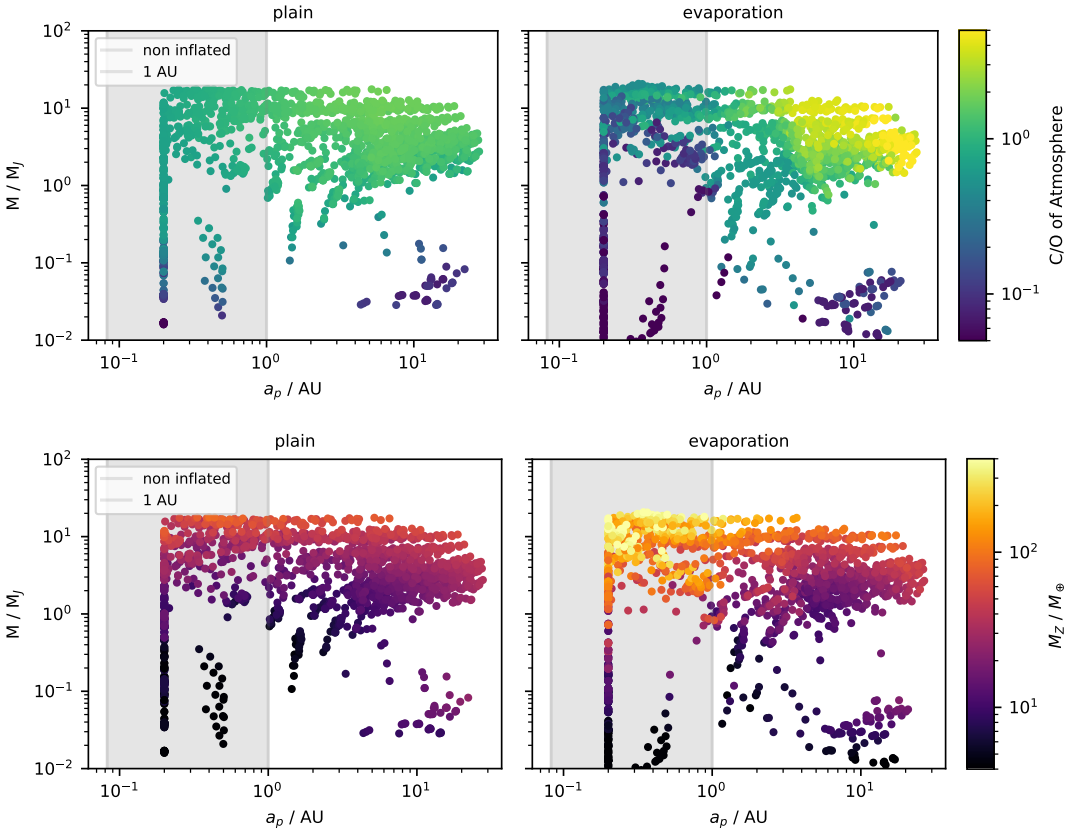

Figure 3.15: Final position and masses of planets formed with the initial conditions stated in Table 3.5, color coded by their atmospheric C/O (top) and their heavy element content (bottom). We mark in the gray band the planets that are featured in Figs. 3.12, 3.13, and 3.14. The different bands of the formed planets in the a-M space are caused by the initial spacing of the embryos with $a_{p,0}$ and t_0, as described in Table 3.5.

less than $F_\star < 2 \times 10^8\,\mathrm{erg\,s^{-1}\,cm^{-2}}$. Stellar insulations are converted to final positions using the relation

$$r < \sqrt{\frac{L_\star}{4\pi F_\star}}, \tag{3.54}$$

where $L_\star = 1 L_\odot$ is the stellar luminosity. We also select only those planets that have final orbits with less than 1 AU because the planetary radii, needed for the model of Thorngren et al. (2016) become increasingly difficult to determine for planets farther away.

We show in Figs. 3.12, 3.13, and 3.14 the results of our simulations, where we color code different properties of the planets formed in our simulations. In Fig. 3.12 we color code the disk's viscosity, in Fig. 3.13 we color code the dust-to-gas ratio, and in Fig. 3.14 we show the atmospheric C/O ratio.

These results clearly show that the inclusion of evaporation and condensation at evaporation lines enhances the total heavy element content of the formed giant planets (right panels). The heavy element content of the giant planets is dominated by the accretion of evaporated volatiles residing in the gas.

While the value of α seems to determine the final mass of planets (horizontal shifting of planets in Fig. 3.12) we can directly link the solid to gas ratio to the magnitude of the heavy element content (vertical shifting in Fig. 3.13). This can best be shown if the fit from Thorngren et al. (2016) is reproduced for the different solid to gas ratios. We can match these quantities using a power law relation for the heavy element content and final mass (Thorngren et al., 2016) of

$$M_Z = \gamma_a \cdot \left(\frac{M}{M_J}\right)^{\gamma_b}, \tag{3.55}$$

where γ_a and γ_b are fit constants (results see Table 3.11).

We note that the slope of the heavy element content of the giant planets depends on the exact dust-to-gas ratio in the case of pebble evaporation. For $\epsilon_0 = 2.5\%$, the slope is slightly steeper than inferred from Thorngren et al. (2016), while lower ϵ_0 values result in flatter slopes. For low planetary masses, the heavy element content is very similar for the different initial dust-to-gas ratios because the heavy element content is dominated by the planetary core mass, which is set by the pebble isolation mass. The pebble isolation mass, however, does not depend on the dust-to-gas ratio, resulting in the similar heavy element contents of the small mass planets. More massive planets are dominated by gas accretion. Thus the heavy element content is dominated by the vapor content in the gas phase of the disk, which increases for increasing

initial dust-to-gas ratios (see also Gárate et al. 2020 for the water content). Consequently the slope of the heavy element content as a function of planetary mass increases for increasing ϵ_0.

The dependence on the solid to gas ratio is only seen if the evaporation of pebbles is taken into account. This means that the solid to gas ratio mainly influences how many heavy elements can be evaporated into the gas and consequently accreted onto the planet. The heavy element content of the low mass giant planets (below 0.2 Jupiter masses) is very similar regardless of whether pebble evaporation is taken into account or not because the heavy element content for these planets is dominated by the core, which is independent of pebble evaporation at ice lines.

It seems that $\epsilon_0 = 2.5\%$ allows the data from Thorngren et al. (2016) to be reproduced best. Under the assumption that the solid to gas ratio can be linked to the solar solid to gas ratio of $\approx 1.5\%$ (Lodders, 2003; Asplund et al., 2009) and the value for the iron abundance [Fe/H]$= 0$, this would relate to a value for [Fe/H]$= \log_{10}(2.5/1.5) \approx 0.22$.[4] The sample of planets that has been used in Thorngren et al. (2016) has a wide range of metallicities with a mean value of [Fe/H]$= 0.1 \pm 0.2$. Buchhave et al. (2018) have shown that hot Jupiters are more likely to be found among metal-rich stars with a mean metallically of [Fe/H]$= 0.25 \pm 0.03$. This indicates that a solid to gas ratio of 2.5% might be a realistic proposal for the formation of these hot gas giants in line with our model.

The atmospheric C/O ratio of the planets with very large heavy element contents is mostly below 1 (Fig. 3.14), due to the efficient accretion of water vapor for these close in planets. In contrast, observations of hot Jupiters show that the C/O ratio could be super-stellar (Brewer et al., 2017). In Figs. 3.12, 3.13, and 3.14, we show the results from planets that migrated via planet-disk interactions into the inner regions of the protoplanetary disk. However, planets can also finish their formation farther away from the central star and then scatter inward to form hot Jupiters (for a recent review of hot Jupiter formation see Dawson & Johnson (2018)).

In Fig. 3.15 we show the final orbital positions and masses of all the planets formed in our simulations with the initial conditions stated in Table 3.5. With the gray band we mark the planets that fulfill the stellar insulation criterion and are within 1 AU, corresponding to the planets shown in Figs. 3.12, 3.13, and 3.14. The orbital evolution of the planets ends at 0.2 AU, resulting in the vertical band at that position.

4 We note that we do not change the chemical composition when increasing the dust-to-gas ratio, as observations indicate (e.g., Buder et al., 2018; Bitsch & Battistini, 2020)

The planetary distributions show also specific bands in the mass-orbital distance plane. This is caused by the initial conditions ($a_{p,0}$ and t_0) of the planets, which are, for the sake of simplicity, not randomized as in population synthesis simulations, because we want to investigate general trends and not match the exact exoplanet populations. Furthermore, our simulations show a large fraction of giant planets, which is also caused by the setup of our simulations. Placing planetary seeds in the outer regions of the disk allows a more efficient growth of gas giants compared to growth in the inner disk (e.g., Ndugu et al. 2018; Bitsch & Johansen 2017).

Due to this artificial setup, we do not compare the final positions and masses of our planets to observations as in population synthesis simulations that are specifically designed for this task (e.g., Ida & Lin 2004; Mordasini et al. 2016; Ndugu et al. 2018; Cridland et al. 2019). Furthermore, the planet population synthesis simulations probe different parameters (e.g., disk mass) that we did not change within our simulations (see Sect. 3.5). Our focus here is on how the evaporation of pebbles influences the heavy element content and the C/O ratio of giant planets, which is independent of the exact comparison of our synthetic planet populations to exoplanet occurrence rates.

The atmospheric C/O ratios in Fig. 3.15 follow the trends already outlined before (Fig. 3.11), namely that planets accreting their gaseous envelope farther away from the central star have a larger C/O ratio. This result is independent if evaporation is taken into account or not. However, as stated above, the absolute C/O ratio in the outer planets is more extreme if evaporation is taken into account. Namely, the C/O ratio is enhanced for planets forming in the outer disk due to the evaporation of carbon-rich pebbles, while the C/O ratio of planets forming in the inner disk region is very low due to the evaporation of water-rich pebbles (Fig. 3.3).

The heavy element content of the planets in the outer regions of the protoplanetary disk is smaller compared to planets in the inner regions of the protoplanetary disk (bottom in Fig. 3.15) in the case evaporation is taken into account. This is caused by the larger enrichment of heavy elements in the gas phase in the inner disk compared to the outer disk (Fig. 3.4). If no evaporation is taken into account, the heavy element content is larger for planets in the outer regions because the heavy element content is mostly set by the core mass, which is determined by the pebble isolation mass, which is increasing with orbital distance due to its dependence on the disk's aspect ratio (Lambrechts et al., 2014; Bitsch et al., 2018).

If hot Jupiters indeed have super-stellar C/O ratios (Brewer et al., 2017), our model predicts that these planets form in the outer disk and are then scattered inward. Furthermore, our model then predict that these planets have a lower

heavy element content compared to Jupiter type planets with low C/O ratios (Fig. 3.15), giving testable predictions to observations of giant planets.

3.5 DISCUSSION

3.5.1 *Dependence on disk parameters*

As shown in Sect. 3.3, the results strongly depend on the disk parameters. In this section we qualitatively discuss some of the parameters that we have not investigated in detail in this work but will be investigated in future works.

Fragmentation velocities

The fragmentation velocity sets how fast pebbles can become before a collision will lead to fragmentation instead of coagulation. Fragmentation velocities are determined by laboratory experiments (e.g., Blum & Wurm, 2008; Gundlach & Blum, 2015; Musiolik & Wurm, 2019) because the collision properties of dust aggregates are otherwise difficult to quantify. Typical laboratory experiments give fragmentation velocities in the range of $1\,\mathrm{m\,s^{-1}}$ to $10\,\mathrm{m\,s^{-1}}$.

High values of fragmentation velocity lead to large Stokes numbers and high radial pebble velocities. This means that pebble accretion will generally be more efficient but planets need to form their core on shorter timescales, otherwise pebbles will have drifted inward and pebble accretion will not be efficient. This implies that the formation of gas giants requires early planetary embryo formation, in line with evidence from the Solar System, where an early formation of Jupiter could explain the separation between carbonaceous and non-carbonaceous chondrites (Kruijer et al., 2017).

Lower fragmentation velocities will reduce the maximal grain size and, as such, reduce the radial drift of pebbles. As pebble accretion is size dependent (Eq. 3.32), lower fragmentation velocities might hinder pebble accretion (e.g., Venturini et al., 2020). Changes in the fragmentation velocity at the water ice line might also lead to a pressure bump in this region (Müller et al., 2021).

In our simulations we use a constant fragmentation velocity throughout the disk, also motivated by recent laboratory experiments that find no difference in the fragmentation velocity between silicates and water (Musiolik & Wurm, 2019). Other simulations (e.g., Izidoro et al., 2021b; Guilera et al., 2020; Venturini et al., 2020) have used different pebble sizes at ice lines (motivated by water ice evaporation) or implemented viscosity transitions (e.g., at the dead zone edge) resulting in different pebble sizes. Smaller pebbles in the inner regions of the disk can slow down the formation of super-Earths via

pebble accretion (Izidoro et al., 2021b; Venturini et al., 2020). Within our model, a change in pebble sizes at the water ice line would mainly influence the inner regions of the disk, but the heavy element content in the inner disk region (Fig. 3.4) is mainly determined by the water content, which is unaffected by a change of pebble sizes at the water ice line. Regarding planetary compositions, we expect that higher fragmentation velocities will increase the heavy element content of early forming planets because the gas is polluted faster by the evaporation of the larger pebble flux.

Disk mass and radius

The disk mass obviously determines how much mass is available for planet formation. High disk masses lead to high dust masses (if the solid to gas ratio stays the same). Accretion rates of pebbles and gas linearly depend on the amount of matter available. However, type I migration rates also linearly depend on the gas surface density. Planet formation will therefore be accelerated for high disk masses. Since pebble accretion fights the decay of the pebble surface density (i.e., planets need to form before pebbles are gone) this can indirectly influences the growth of planets.

Similarly does the disk radius determine the lifetime of the pebble surface density. Large disk radii on the one hand lead to a longer supply of pebbles from the outer disk, while smaller disks will be depleted of pebbles early on. This can lead to the growth of multiple small mass planets instead of a few large bodies (Kretke & Levison, 2014; Levison et al., 2015).

Furthermore, a change of the available pebble mass and how long the pebble supply lasts, influences the heavy element content of forming giant planets. This can be inferred from Fig. 3.13, which shows that planets forming in disks with more pebbles (large ϵ_0) have a larger heavy element content, potentially similar to more massive disks.

Observations of protoplanetary disks indicate a wide spread in disk mass and radii (e.g., Andrews et al., 2013). We will investigate the effects of this in future studies.

3.5.2 *Model extensions*

In this subsection, we discuss how our model can be extended in the future for various aspects. While all these listed additions would improve our model, the general message that pebble evaporation at ice lines increases the heavy element content in the gas phase of the disk and thus also the heavy element content of gas accretion planets, remains.

Planetesimals

In our model, we only include the contributions of pebble and gas accretion, while we do not model the formation of planetesimals (Drążkowska et al., 2016; Drążkowska & Alibert, 2017; Lenz et al., 2019; Voelkel et al., 2020) and the accretion of those onto planetary embryos. The accretion efficiency of planetesimals in itself depends crucially on the planetesimal size (Fortier et al., 2009; Guilera et al., 2011; Fortier et al., 2013; Johansen & Bitsch, 2019), where the planetesimal population in the Solar System was probably dominated by large (100km) planetesimals (Bottke et al., 2005; Morbidelli et al., 2009) in the inner regions, with decreasing sizes (1-10 km) toward the Kuiper belt (Kenyon & Bromley, 2012). The accretion of planetesimals into the planetary atmosphere could prolong the envelope contraction phase (Alibert et al., 2018; Venturini & Helled, 2020; Guilera et al., 2020), delaying gas accretion and thus resulting in large-scale inward migration. Furthermore, growing gas giants can accrete planetesimals into their envelope, which can increase the heavy element mass of the giant planet as well as the atmospheric C/O ratio.

While we do not model planetesimal formation and accretion in our work, our results clearly show that the evaporation of inward drifting pebbles have a profound impact on the heavy element content of the gas phase and thus of gas accreting planets. Future simulations aimed to study the heavy element content of giant planets should thus include the contributions of planetesimals as well as of pebble evaporation at ice lines.

Evaporation of solids

We modeled the evaporation of dust and pebbles by assuming that the evaporation line crossing solid flux of a molecular species is converted to gas within 0.001 AU (see Eq. 3.19). In reality the evaporation of molecular species from solids depends on desorption rates (Hollenbach et al., 2009). Molecular species are to a different extend volatile. For a molecular species to desorb it has to overcome the binding energy that keeps it on the surface of a pebble. A proper treatment of the desorption rates will not change the amount of heavy elements that is evaporated to the gas. It will rather change the location and spatial interval in which the drifting solids sublimate. However, since planets migrate, we do not expect large differences in the results, since the amount of heavy elements in the gas is the deciding factor (see Fig. 3.4).

Opacities

The midplane temperature and migration rate of the planets depends on the opacity of the protoplanetary disk. We used here for simplicity a subset of the opacities from Bitsch & Savvidou (2021), which are only valid for micrometer grains. However, full grain size distributions feature opacities that are not mimicked by a single grain size (Savvidou et al., 2020). In addition, local pile-ups of dust could change the local opacities and thus influence the cooling rates of the disk. As most of the material is in the form of pebbles, which are millimeters to centimeters in size, these piles might only minimally influence the opacity because the opacities are determined by the small grains rather than the large grains (Savvidou et al., 2020; Savvidou & Bitsch, 2021). We expect that a fully self-consistent treatment will mainly vary the position of the evaporation lines, but our results regarding the heavy element content or the C/O ratio will qualitatively remain valid.

The envelope contraction phase during planet formation depends on the envelope opacity. The duration of the envelope contraction phase is direct proportional to the value of the envelope opacity. We used here a value that is consistent with the findings of Movshovitz & Podolak (2008). Planets migrate very fast during the envelope contraction phase. A low envelope opacity will thus allow fast gas accretion and an earlier transition into the slow type-II migration phase, compared to high envelope opacities (Bitsch & Savvidou, 2021). Future simulations should thus include a more self-consistent treatment of the envelope opacity, eventually also accounting for the bombardment of planetesimals (e.g., Alibert et al., 2018).

Multiple planets

From our Solar System and other extra solar planetary systems we know that planetary systems contain on average more than one planet. An N-body integrator can be used to solve the planet-planet interactions and evolution of multiple planetary seeds in a protoplanetary disk that grow by accretion of planetesimals (Alibert et al., 2013) or pebbles (Levison et al., 2015; Matsumura et al., 2017; Chambers, 2018; Lambrechts et al., 2019b; Izidoro et al., 2021b; Bitsch et al., 2019).

The existence of multiple protoplanets will influence the accretion of pebbles, since planets that are large enough to carve a gap in the gas surface density will stop pebbles from drifting toward possible other planets that grow further in (Morbidelli et al., 2015, 2016; Bitsch et al., 2021; Izidoro et al., 2021a). Morbidelli et al. (2015) used this process to explain the dichotomy between the terrestrial planets and gas giants in our Solar System, while (Morbidelli et al.,

2016) speculated that this effect is also responsible to prevent the accretion of water-rich material onto the Earth.

In addition, a giant planet blocking pebbles exterior to its orbit influences the composition of interior planets by preventing them from accreting the material engulfed in the pebbles. Bitsch et al. (2021) used this effect to show how the water content of inner sub-Neptunes could be used to constrain the time and formation location of giant planets relative to the water ice line.

In addition, collisions between the planets could increase the heavy element content of the formed giant planets (Ginzburg & Chiang, 2020; Ogihara et al., 2021), even though collisions between giant planets might be rare (e.g., Bitsch et al., 2020). These effects clearly show the importance of multi-body simulations in the future.

Chemistry

Including grain surface chemistry in disk models can have a large influence on the chemical composition of the dust grains and of the gas (Semenov et al., 2010; Eistrup et al., 2016; Cridland et al., 2019; Krijt et al., 2020; Notsu et al., 2020). However, the surface per mass is much higher for small dust grains than for large dust grains. Booth & Ilee (2019) argue that chemical reactions will be outperformed by evaporation at evaporation lines due to the fast radial transport of large dust grains. We expect that surface reactions on pebbles will therefore be less dominant than surface reactions on micrometer-sized dust grains. The effect of grain surface reactions onto the chemical composition thus depends on the growth and drift of the pebbles. Models combining both processes in detail are thus needed (e.g., Krijt et al. 2020).

The chemical composition of the underlying disk model is solar (Table 3.1 within our models. However, in reality stars have different composition that are not necessarily solar (e.g., Buder et al. 2018). Past studies have related the solar and stellar abundances to the refractory (Marboeuf et al., 2014b; Thiabaud et al., 2014, 2015a; Bitsch & Battistini, 2020) and volatile (Marboeuf et al., 2014a; Thiabaud et al., 2015b) contents of planetary building blocks and used this to predict the composition of formed planets. These simulations, however, did not take pebble drift and evaporation into account and found that the heavy element content in the gas phase is dominated by the accretion of planetesimals. Adibekyan et al. (2021) recently directly linked the stellar abundances to the metal content of well characterized rocky super-Earths, confirming indeed that the stellar abundances directly influence planetary compositions. While these studies differ in their exact approach, they all clearly show that the underlying chemical composition of the protoplanetary

disk has an enormous influence on the final planetary composition in both, refractories and solids and should be investigated in more detail in the future.

Our model results clearly depend on the underlying chemical model. Different compositions result in different significance of individual evaporation lines. We have shown within this paper that the evaporation of methane is important for a large heavy element content and a large C/O ratio. Models that do not include methane or only small fractions of methane might thus show different C/O fractions within the planetary atmospheres (see also Appendix D). Figures 3.19 and 3.20 demonstrate that this influences mostly the C/O ratio rather than the total heavy element content, showing the robustness of the contribution of pebble evaporation for the heavy element content of giant planets.

Interior structure

We have assumed that during pebble accretion 90% of the accreted pebbles are attributed to the core and 10% are attributed to the heavy-element-rich atmosphere during core buildup. However, more detailed models have revealed that less than 50% of the accreted solids contribute to the core, while the remaining pebbles contribute to the high metallicity envelope (e.g., Brouwers & Ormel 2020; Ormel et al. 2021). Taking a larger fraction of heavy elements to be accreted into the early atmosphere rather than the core will not influence the total heavy element content of the planet, because the accreted mass is the same. It will though influence the C/O ratio of the planet. We discuss this implication in Appendix I.

Interior models, however, also determine how the accreted material is distributed inside the planet and its atmosphere (e.g., Vazan et al., 2018; Brouwers & Ormel, 2020). This could strongly influence any quantitative proposal about atmospheric contents like the discussed C/O ratios, where we always assumed a perfect mixing. Therefore, future models need to include consistent interior models, especially during the planetary buildup phase.

Gas accretion

Gas accretion onto planetary cores is an active area of research (Ayliffe & Bate, 2009; Szulágyi et al., 2016; Schulik et al., 2019; Lambrechts et al., 2019a; Bitsch & Savvidou, 2021). While most gas accretion recipes are derived from 1D models (e.g., Ikoma et al. 2000), only very few accretion recipes from 3D simulations (e.g., Machida et al. 2010) exist. Within our model, the gas accretion rates in our simulations (Eq. 3.39) are derived for gas of H-He composition, but the

gas also contains significant amount of heavy elements in vapor form (e.g., Fig. 3.4).

Previous studies show that gas enriched with heavy elements can significantly influence the gas accretion rates (Hori & Ikoma, 2011; Venturini et al., 2015, 2016). Gas enriched in heavy elements seems to allow a more efficient gas contraction rate, even on cores of below a few Earth masses, which in classical simulations are not allowed to accrete gas efficiently. Venturini et al. (2015) shows that already for $Z_{\rm env}$ >0.45 a significant reduction of the critical core mass for gas accretion can be achieved. However, in the models of Brouwers & Ormel (2020) the pebbles evaporating in the planetary atmosphere do not allow such a fast transition into runaway gas accretion, while the study of Ormel et al. (2021) shows that envelope pollution significantly reduces the time at which the planet reaches the cross over mass for runaway gas accretion in line with Venturini et al. (2015). Furthermore, Johansen et al. (2021) shows that water-rich pebbles entering the planetary Hill sphere can evaporate high up in the planetary atmosphere, where recycling flows (Lambrechts & Lega, 2017; Cimerman et al., 2017) could transport the water vapor away from the planet, preventing the buildup of a high Z envelope.

When the core then transitions into a rapid gas accretion mode, gas accretion rates are mostly determined via 1D simulations (e.g., Ikoma et al. 2000). However, 3D simulations are clearly needed to constrain gas accretion rates (Szulágyi et al., 2016; Schulik et al., 2019; Lambrechts et al., 2019a), where complicated flow patterns around the planets can arise, complicating the picture. These different studies clearly show that gas accretion needs to be investigated in much more detail in the future.

The final mass of the gas giants in our model is determined by the lifetime of the protoplanetary disk and by the disk's viscosity, where larger viscosities allow a larger gas flux through the disk and thus result in a larger accretion rate (Eq. 3.39). Longer disk lifetimes results in longer phases of gas accretion and thus larger planetary masses, while shorter disk lifetimes will result in lower planetary masses. In our model, the disk evolves viscously without photoevaporation (see below), keeping the gas disk mass large also at later times, resulting in larger planetary masses.

Within our model, the exact gas accretion rates should have only little influence on the main message of our work. The inward drifting and evaporating pebbles enrich the gas phase of the disk, which allows the accretion of high metallicity gas, resulting in high heavy element contents of planets (Figs. 3.12 to 3.14). Different implementations of gas accretion rates, would of course influence the growth tracks of planets (Fig. 3.11) and the resulting

C/O ratios in the planetary atmospheres, but the general trend that the C/O ratio increases with larger orbital distances would remain.

Photoevaporation

The disk dispersal only via viscous evolution can take a very long time, if the viscosity is low. We model the end of the disk lifetime by an exponential decay of the disk's gas surface density within the last 100 kyr of its fixed lifetime of 3 Myr. In reality, photoevaporation is thought to disperse the disk (for a review see Alexander et al. 2014).

Photoevaporation does not only disperse the disk toward the end of the disk's lifetime (after about 3 Myr), it also alters the disk structure significantly (Owen et al., 2012, 2013). In fact, photoevaporation can carve a hole in the disk beyond 1 AU, dividing the disk in two reservoirs. This behavior could have important implications for the growth and composition of planets forming in the inner regions of the disk. If the pebble supply to the inner disk is cut, the enrichment with vapor from inward drifting pebbles stops, reducing the heavy element content in the gas phase in the inner regions. In fact this process is similar to a giant planet opening a deep gap in the protoplanetary disk and blocking the pebbles in the outer disk (Fig. 3.4). We thus expect that photoevaporation has a similar effect as growing giant planets on the composition of inner growing planets (see also Bitsch et al. 2021).

Furthermore, photoevaporation can significantly reduce the disk's lifetime, which has large consequences on the growth and migration of giant planets (Alexander & Pascucci, 2012; Monsch et al., 2019). Furthermore, shorter disk lifetimes would give the vapor less time to diffuse inward, similar to lower viscosities (Fig. 3.4), potentially reducing the C/O ratio of inner growing planets. Nevertheless, the inclusion of photoevaporation in our model would not influence our main results significantly, because if photoevaporation were to carve a hole in the disk, planets in the inner regions would not only be deprived of inward diffusing vapor, but of gas in general, stopping their accretion, leaving still heavily vapor-enriched planets behind.

3.5.3 *Heavy element content of giant planets*

In this work we have found that a significant contribution to the heavy element content of gas giants originates from the vapor-enriched gas phase. Past simulations have focused on the contribution to the heavy element content via solid accretion, either via planetesimals (Shibata & Ikoma, 2019; Shibata

et al., 2020; Venturini & Helled, 2020) or even via giant impacts with embryos and other giants (Ginzburg & Chiang, 2020; Ogihara et al., 2021).

The bombardment of the planetary envelope with planetesimals might allow an enrichment compatible to Jupiter's heavy element content (Shibata & Ikoma, 2019; Shibata et al., 2020; Venturini & Helled, 2020), depending on the exact planetesimal surface density, planetesimals size as well as on the migration speed of the planet (Tanaka & Ida, 1999). Giant impacts between super-Earths and giant planets or also between giant planets themselves, mostly occurring towards or after the end of the gas disk's lifetime can additionally enrich the heavy element content of giant planets (Ginzburg & Chiang, 2020; Ogihara et al., 2021). Furthermore, giant impacts could additionally explain the structure of the core of Jupiter (Liu et al., 2019).

The main differences of these works to our here presented work is the composition of the heavy elements within the planet. Our work implies that most of the heavy elements are in volatile form, while a bombardment with planetesimals would imply a significant refractory content. We discuss this implication in much more detail in an accompanying paper.

3.6 SUMMARY AND CONCLUSION

We have performed 1D semi-analytical simulations of the formation of planets in protoplanetary disks. These simulations traced the chemical composition of the accreted pebbles and gas. Pebbles grow from small dust grains by coagulation and drift inward due to gas drag. We compare two main model approaches, where we either include the evaporation and condensation of pebbles at ice lines or not.

Planets build their core from a planetary seed by accreting pebbles while migrating through the disk. Core accretion stops when the planet has grown large enough to create a pressure bump in the surrounding gas, which will trap pebbles and hinder them from reaching the planet. The planet then starts to accrete gas and becomes a gas giant.

Our simulations show that the evaporation of pebbles at evaporation lines largely pollutes the gas with heavy elements (Fig. 3.4), in line with observations of protoplanetary disks (Banzatti et al., 2020; Zhang et al., 2020). Gas giants can therefore accrete large amounts of heavy elements by the accretion of volatile-enriched gas, with the heavy element fraction increasing as the disk viscosity decreases (Fig. 3.12). However, larger viscosities allow the growth of more massive planets due to the more efficient gas delivery from the disk to the planet. Furthermore, our simulations indicate that the heavy element content of giant planets is lower for planets forming farther away from the

host star because the gas is less enriched in heavy elements in the outer disk compared to the inner disk (Fig. 3.15).

Our simulations also indicate that the atmospheric C/O ratio of giant planets increases for planets formed farther away from the host star, especially if the planets form exterior to the water ice line, thus avoiding the accretion of water vapor, which ultimately decreases the atmospheric C/O ratio (Fig. 3.15). Our simulations show that the planetary C/O ratio increases with the formation distance of the giant planet, but at the same time the total heavy element content of the giant planet decreases. Our simulations thus predict that the C/O ratios of giant planets with large heavy element contents should be low, while the C/O ratios of giant planets with low heavy element content should be high. These predictions will be testable with large observation programs such as JWST and ARIEL.

Furthermore, our simulations clearly indicate that the heavy element content of giant planets is largely influenced by the enrichment of gas by pebble evaporation. Future simulations that aim to study the heavy element content and composition of planets should take these effects into account.

ACKNOWLEDGEMENTS

A.D.S and B.B. thank the European Research Council (ERC Starting Grant 757448-PAMDORA) for their financial support. A.D.S. acknowledges funding from the European Union H2020-MSCA-ITN-2019 under Grant no. 860470 (CHAMELEON) and from the Novo Nordisk Foundation Interdisciplinary Synergy Program grant no. NNF19OC0057374. We thank Cornelis Dullemond for discussions about pebble condensation. We also thank the anonymous referees for their comments that helped to improve the manuscript.

APPENDIX

A PARAMETERS IN OUR MODEL

We list in this subsection all the variables and their meaning used in this work.

B TEMPERATURE

The temperature of the disk (see Fig. 3.16) is mainly dependent on two physical processes: Heating through viscous accretion and irradiation by the central star. Irradiation can be described by the simplified assumption that a fraction φ (e.g., a certain solid angle) of the flux $F = \frac{L_\star}{4\pi r^2}$ from the central star heats the surface of the protoplanetary disk (Armitage, 2013; Dullemond, 2013). Here $L_\star$ denotes the Luminosity of the host star. If we assume that the irradiation accounts for the effective temperature T_{eff} of the disk (the emission temperature), we get the heat flux on the disk surface

$$Q_{\text{irr}} = \frac{L_\star}{4\pi r^2}\varphi \qquad \Rightarrow T_{\text{eff}} = \left(\frac{Q_{\text{irr}}}{2\sigma_{\text{SB}}}\right)^{1/4}, \tag{3.56}$$

where σ_{SB} stands for the Stefan–Boltzmann constant. We use a constant value of $\varphi = 0.05$ and $L_\star = L_\odot$ throughout this paper. The heat flux due to viscous accretion heats the midplane. This heat flux can be described by (Pringle, 1981)

$$Q_+ = \frac{9}{4}\Sigma_{\text{gas}}\nu{\Omega_K}^2. \tag{3.57}$$

Using the definition for the optical depth τ_d

$$\tau_d = \frac{1}{2}\Sigma_{\text{gas}}\epsilon_0\kappa_d, \tag{3.58}$$

we get the midplane temperature

$$T_{\text{mid}}^4 = T_{\text{visc}}^4 + T_{\text{eff}}^4 = \frac{3}{8}\frac{\tau_d Q_+}{\sigma_{\text{SB}}} + \frac{Q_{\text{irr}}}{2\sigma_{\text{SB}}}. \tag{3.59}$$

In order to find the midplane temperature, we applied the Brent method (Brent, 1973; Press et al., 1992) that uses the sign change in an interval in

Parameter	Explanation
ν	alpha viscosity parameter
c_s	sound speed
Ω_K	Kepler angular velocity
G	Gravitational constant
$M_\star$	Mass of central star
r	radius coordinate of the disk
k_B	Boltzmann constant
T_{mid}	Temperature of the midplane
μ	mean molecular weight
m_p	proton mass
Δv	sub-Keplerian azimuthal speed
v_K	Keplerian velocity
v_φ	azimuthal velocity of the gas
P	Gas pressure
H_{gas}	scale height of the disk
St	Stokes number of a particle
τ_f	stopping time of a particle
a	particle size
$\rho_\bullet$	density of a dust and pebble particle
Σ_{gas}	Gas surface density
u_Z	general pebble/dust drift velocity
u_{gas}	gas diffusion velocity
ϵ	solid to gas ratio
Σ_Z	total dust surface density (pebbles and dust)
f_m	mass fraction of pebbles
Σ_{peb}	surface density of pebbles
Σ_{dust}	surface density of dust
$\hat{u}_Z$	mass averaged dust drift velocity (dust and pebbles)
u_{peb}	pebble drift velocity
u_{dust}	dust drift velocity
Y	molecular species

Table 3.6: Explanations of variables related to the disk used in our model (part I)

Parameter	Explanation
t	time
$\dot{\Sigma}$	source/sink term for viscous evolution
M_0	initial disk mass
R_0	scaling radius of the disk
ψ	logarithmic gradient of the viscosity at the inner edge
r_{in}	radius at the inner edge of the disk
ξ	normed time
t_ν	viscous time
$\dot{\Sigma}_Y^{evap}$	evaporation source term
$\dot{\Sigma}_Y^{cond}$	condensation source term
$\dot{\Sigma}_Y^{acc,peb}$	source term due to the discount of accreted pebbles
$r_{ice,Y}$	position of the evaporation line of species Y
a_{dust}	dust size
a_{peb}	pebble size
ϵ_p	pebble sticking efficiency
μ_Y	mass of species Y (in proton masses)
$\dot{\Sigma}_{gas,Y}^W$	photoevaporation source term
t_{evap}	start of photoevaporation
τ_{decay}	decay timescale of the disk
$\dot{M}_{disk}$	disk accretion rate

Table 3.7: Explanations of variables related to the disk used in our model (part II)

Parameter	Explanation
J_p	angular momentum of the planet
M	Mass of the planet
a_p	distance of planet to the star
τ_M	Migration timescale
Γ	Torque that acts on the planet
L	accretion luminosity of the planet
$\dot{M}_{peb}$	accretion rates of pebbles onto the planet
Θ	numerical parameter used for the dynamical torque
$\mathcal{P}$	numerical gap parameter
$\mathcal{R}$	Reynolds number
R_H	Hill radius
q	mass ratio of planet to host star
f_{gap}	relative Depth of surface density gap caused by planet
$f(\mathcal{P})$	gravitational gap depth
f_A	gap depth caused by accretion
τ_{II}	Migration timescale for type II migration
M_t	transition mass, where pebble accretion becomes efficient
M_{iso}	pebble isolation mass
M_a	mass of planetary envelope
R_{acc}	impact radius of pebble accretion
ρ_{peb}	density of pebbles in the disk
δv	approach speed of pebbles
H_{peb}	pebble scale hight
$_z$	vertical mixing of pebbles
$\dot{M}_{gas,Ikoma}$	Ikoma gas accretion rate
$\dot{\tau}_{KH}$	Kelvin-Helmholtz contraction rate

Table 3.8: Explanations of variables related to the planet used in our model (part I).

Parameter	Explanation
M_c	Core mass of the planet
κ_{env}	envelope opacity
$\dot{M}_{gas,low}$	low branch of the Machida gas accretion rate
$\dot{M}_{gas,high}$	high branch of the Machida gas accretion rate
$\dot{M}_{HS}$	horseshoe depletion rate
T_{HS}	synodic period at the border of the horseshoe region
Ω_{HS}	synodic orbital frequency at the border of the horseshoe region
r_{HS}	half width of the horseshoe region
x_s	half width of the horseshoe region normed to planetary position
h	aspect ratio at the planetary position
Δt	numerical time step
Σ_{HS}	surface density of the horseshoe region
$\aleph$	gap profile
σ	std. deviation of gap profile
$F_\star$	stellar insulation at planetary position
γ_a, γ_b	Fit parameter for heavy element content
M_Z	mass of heavy elements in planet

Table 3.9: Explanations of variables related to the planet used in our model (part II).

Parameter	Explanation
$L_\star$	stellar luminosity
Q_{irr}	heat flux on the disk surface
F	stellar Flux
φ	fraction of the stellar light that heats the disk
T_{eff}	effective temperature of the disk
Q_+	viscous heat flux due to accretion
τ_d	optical depth
κ_d	dust opacity
T_{mid}	midplane temperature
T_{visc}	temperature caused by viscous heating
α_Σ	slope of the radial gas surface density profile
Σ_{tot}	total surface density (gas and solids)
Σ_{bg}	surface density of the H+He background gas
Σ_v	surface density of the heavy molecular species in the gas phase
$\epsilon_{0,chem}$	intrinsic heavy to gas ratio of the chemical model
m	mass of a dust grain
n_Y	number density of gaseous molecules of species Y
$v_{th,Y}$	mean thermal velocity projected onto a surface

Table 3.10: Explanations of variables used in our model related to the appendix.

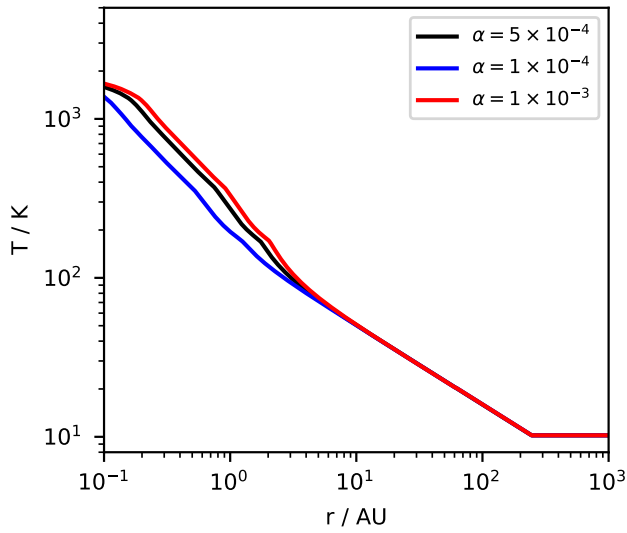

Figure 3.16: Midplane temperature profile (black line) of the protoplanetary disk model. The temperature depends on two constituents: viscous heating (dominant in the inner part) and irradiation from the central star (dominant in the outer part). The different colors show the disk's temperature for different viscosities. Larger viscosities result in more viscous heating and thus higher disk temperatures. The other disk parameters can be found in Table 3.3.

order to determine the root of an equation. We applied the Brent root finding method to solve the equation

$$0 = \frac{3}{8}\frac{\tau_d Q_+}{\sigma_{SB}} + \frac{Q_{irr}}{2\sigma_{SB}} - T_{mid}^4 \tag{3.60}$$

for every grid cell individually. We used a sign change interval of $\left[T_{eff}, 1.5 \times 10^5 K\right]$. Protoplanetary disks likely have a background temperature due to the effects of irradiation from heavy stars that form nearby. We therefore used a minimum value of 10 K for the effective temperature.

When a good solution to Eq. 3.59 has been found we interpolate the temperature to a linear spaced grid by increasing the resolution drastically, apply a Savitzky–Golay filter (Savitzky & Golay, 1964) that smoothes the radial temperature profile and then interpolate back. As the disk evolves in time, the temperature in the inner regions decreases, due to the reduced gas surface density. However, the evolution of the gas surface density is quite minimal, especially for low viscosities (Fig. 3.3). Therefore, we do not evolve the temperature profile of our disk in time for simplicity.

C COMPARISON OF THE DYNAMICAL CORE OF twopoppy WITH chemcomp

We show in this section the comparison of `chemcomp` with `TwoPopPy`[5] (Birnstiel et al., 2012) regarding the evolution of the disk's gas surface density and the pebble surface density for our standard disk model with different viscosities (Table 3.3). However, for this test we use the same temperature profile as in Birnstiel et al. (2012), which is just a power-law compared to our temperature profile corresponding to viscous and stellar heating (Appendix B). Furthermore, we only include one solid and one gas species (hydrogen-helium) for the code comparison, in contrast to the several species we included in our main work (Table 3.2).

We show in Fig. 3.17 the evolution of the gas surface density in time for the two codes for different viscosities. The evolution of the gas surface density is practically identical. The comparison of the evolution of the dust surface density in time (Fig. 3.18) also reveals a very similar evolution. At around 1 Myr, the dust seems to evolve slightly faster in `chemcomp`, especially for higher viscosities. However, after 2 Myr, the differences in the dust surface density between the two codes is minimal, verifying our approach.

5 The version of `TwoPopPy` used for the comparison has the git-hash: `6ac432718bffc3cf197a9e3d78fca492847c36f4`

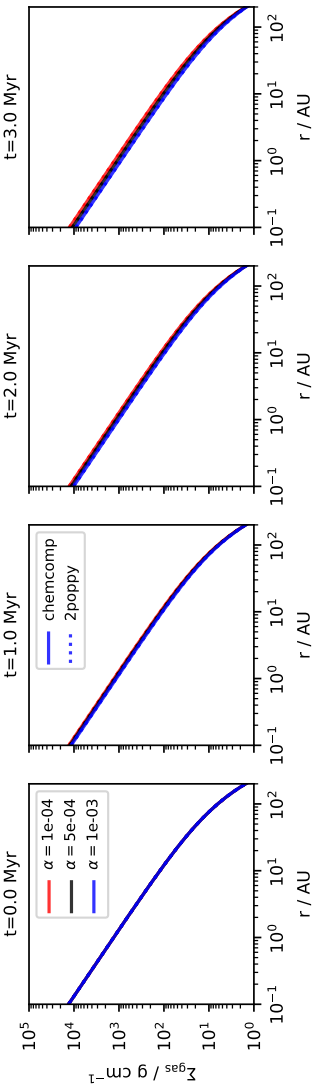

Figure 3.17: Comparison of the gas surface density evolution for different values of α for TwoPopPy with chemcomp for different times.

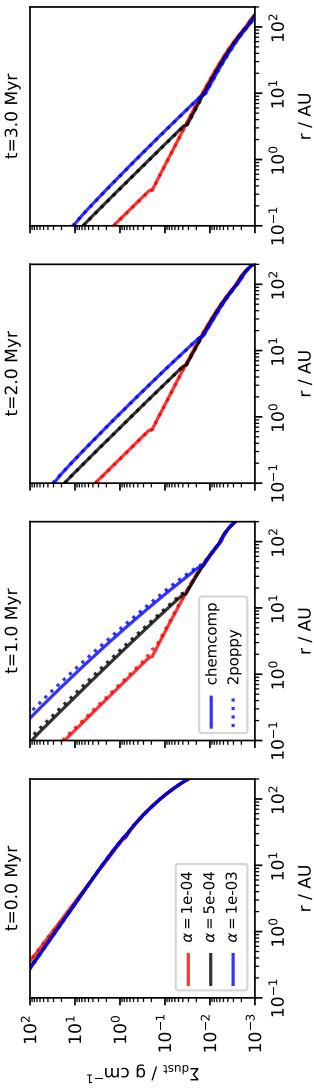

Figure 3.18: Comparison of the dust surface density evolution for different values of α for TwoPopPy with chemcomp for different times.

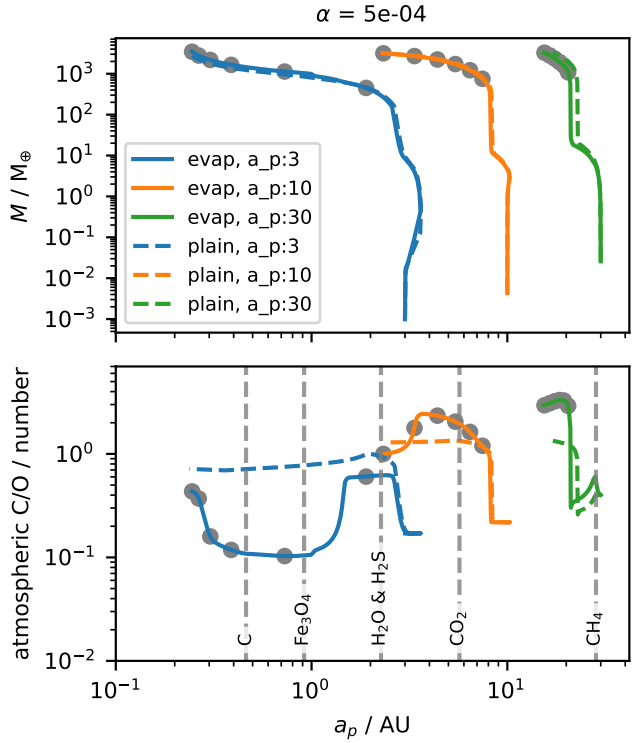

Figure 3.19: Like Fig. 3.11, using the same model parameters, but using the carbon grain model. Model parameters can be found in Table 3.3.

D MODEL WITH CARBON

The results shown in the main part of this work use chemical compositions that do not include carbon grains (see Table 3.2, $\nu_{Y,noC}$). The inclusion of carbon grains will mainly influence the C/O ratio, since it shifts the sublimation of carbon containing material from the methane evaporation line to the carbon evaporation front in the inner disk regions. Figure 3.19 shows how this influences the atmospheric C/O content of planets that grow in a protoplanetary disk with carbon grains, where the same parameters as in Fig. 3.11 have been used. Clearly, the planets forming in the outer regions of the disk now harbor a smaller C/O ratio due to the lack of methane. The inner planet (blue line), though, is mostly unaffected by the inclusion of carbon grains because once the planet crosses the carbon grain evaporation front, water vapor has already diffused inward and diluted the effects of the evaporating carbon grains on

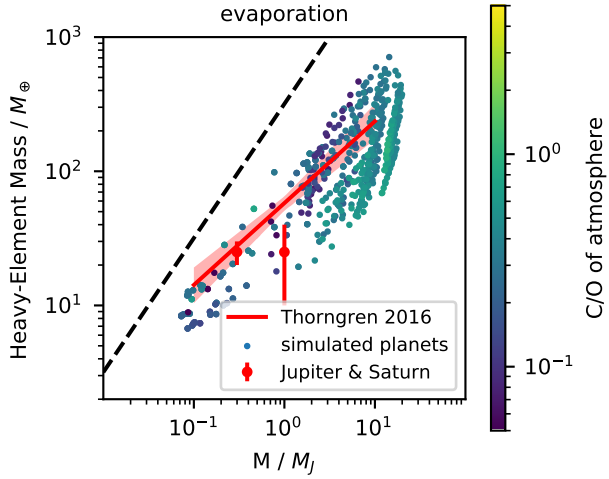

Figure 3.20: Like Fig. 3.14 but using the carbon grain model. The plot shows the model with evaporation.

the C/O ratio. At late times, the inward diffusing carbon-rich gas from the outer disk results in an increase in the planetary C/O ratio, as for the model without carbon grains (Fig. 3.11).

Figure 3.20 shows that the C/O ratio of inner gas giants is slightly smaller in the model without carbon grains. Planets migrating across the carbon grain evaporation front early on can increase their carbon content slightly compared to planets in the model without carbon grains. However, the C/O ratio is only slightly affected because the carbon grain abundance is low compared to the water abundance, which dominates the C/O ratio of the planets accreting gas in the inner disk. However, the total heavy element contents of the planets remain unaffected because the planets accrete most of the gas at a few AU, where most of the volatiles have already evaporated, thus enriching the gas phase.

E COMPOSITION

E.1 *Surface densities*

The total surface density of gas and dust is given as

$$\Sigma_{\text{tot}}(r) = \Sigma_{\text{gas}}(r) + \Sigma_Z(r), \tag{3.61}$$

where Σ_{gas} is initialized from the disk mass via Eq. 3.13. We initialize the dust surface density by forcing a constant (in radius) initial heavy molecular species content (ϵ_0) on the disk.

We can write

$$\Sigma_{gas}(r) = \Sigma_{bg}(r) + \Sigma_v(r), \tag{3.62}$$

where $\Sigma_{bg}(r)$ is the contribution of the background gas (consisting out of Hydrogen and Helium) and $\Sigma_v(r)$ is the contribution from molecular species (see Table 3.2). We can thus write

$$\Sigma_{tot}(r) = \Sigma_{bg}(r) + \Sigma_v(r) + \Sigma_Z(r) \ . \tag{3.63}$$

The intrinsic fraction of heavy molecular species $\epsilon_{0,chem}$ relative to the hydrogen abundance in our chemical model is given by the sum over all molecular volume mixing ratios

$$\epsilon_{0,chem} = \sum_Y \mu_Y \times (Y/H) = 0.0179. \tag{3.64}$$

It should be noted that we want to rescale our chemical model to a heavy molecular species content of ϵ_0 (e.g., $\epsilon_0 = 2\%$). This heavy molecular species content can be thought of as the dust-to-gas ratio, when all molecular species are frozen out.

The dust-to-gas ratio $\epsilon(T)$ is the fraction of heavy molecular species in solids given by the rescaling of the chemical model as

$$\text{›}(T) = \frac{\epsilon_0}{\epsilon_{0,chem}} \times \sum_{Y \in \{dust\}} \mu_Y \times (Y/H). \tag{3.65}$$

Using the surface density of the background gas $\Sigma_{bg}(r)$ we can now reformulate Eq. 3.61 as

$$\begin{aligned} \Sigma_{tot}(r) &= \Sigma_{bg}(r) + (\epsilon_0 - \epsilon(r))\Sigma_{bg}(r) + \epsilon(r)\Sigma_{bg}(r) \\ &= \Sigma_{bg}(r)(1 + \epsilon_0), \end{aligned} \tag{3.66}$$

where ϵ_0 is the mass fraction of heavy molecular species in the disk (i.e., also given by Eq. 3.65 when all species are part of the dust). The background gas surface density can therefore be calculated as

$$\Sigma_{bg}(r) = \Sigma_{gas} \times (1 + (\epsilon_0 - \epsilon))^{-1} \ . \tag{3.67}$$

The dust is then initialized as

$$\Sigma_Z = \epsilon(T) \times \Sigma_{bg}. \tag{3.68}$$

E.2 *Dust composition*

For every molecular species available in dust we used

$$\frac{\Sigma_{Z,Y}}{\Sigma_Z} = \frac{\mu_Y \times (Y/H)}{\sum_{i\in\{dust\}} \mu_i}. \tag{3.69}$$

E.3 *Gas composition*

The molecular weight of the hydrogen-helium mixture in a protoplanetary disk is given by (Gárate et al., 2020)

$$\mu_{H+He} = 2.3. \tag{3.70}$$

For the heavy molecular species available in gas we can use

$$\frac{\Sigma_{gas,Y}}{\Sigma_v} = \frac{\mu_Y \times (Y/H)}{\sum_{i\in\{gas\}} \mu_i}, \tag{3.71}$$

which yields the individual mass fractions of the heavy molecular species Y in the vapor. Using this equation we can now calculate

$$\frac{\Sigma_{gas,Y}}{\Sigma_{gas}} = \frac{\Sigma_{gas,Y}}{\Sigma_v} \times \frac{\Sigma_v}{\Sigma_{gas}} = \frac{\mu_Y \times (Y/H)}{\sum_{i\in\{gas\}} \mu_i} \times \frac{\epsilon_0 - \epsilon}{1 + (\epsilon_0 - \epsilon)}, \tag{3.72}$$

while the background gas species (H+He) is simply given by Eq. 3.67. We note that the sum of the individual gas surface densities of the different molecular species must be the total gas surface density (the same also applies for the dust surface density).

We can now calculate the mean molecular weight from the sum over all molecular species (including the background gas):

$$\mu = \Sigma_{gas} \times \left(\sum_{Y\in\{gas\}} \frac{\Sigma_{gas,Y}}{\mu_Y} \right)^{-1}. \tag{3.73}$$

F GAS, DUST, AND PLANETARY VELOCITIES

The accretion of vapor-enriched gas onto planetary atmospheres depends on the relative speed of the gas to the planet. As the planet accretes gas that is provided by viscous evolution, the gas only reach the planet if the gas moves faster than the planet.

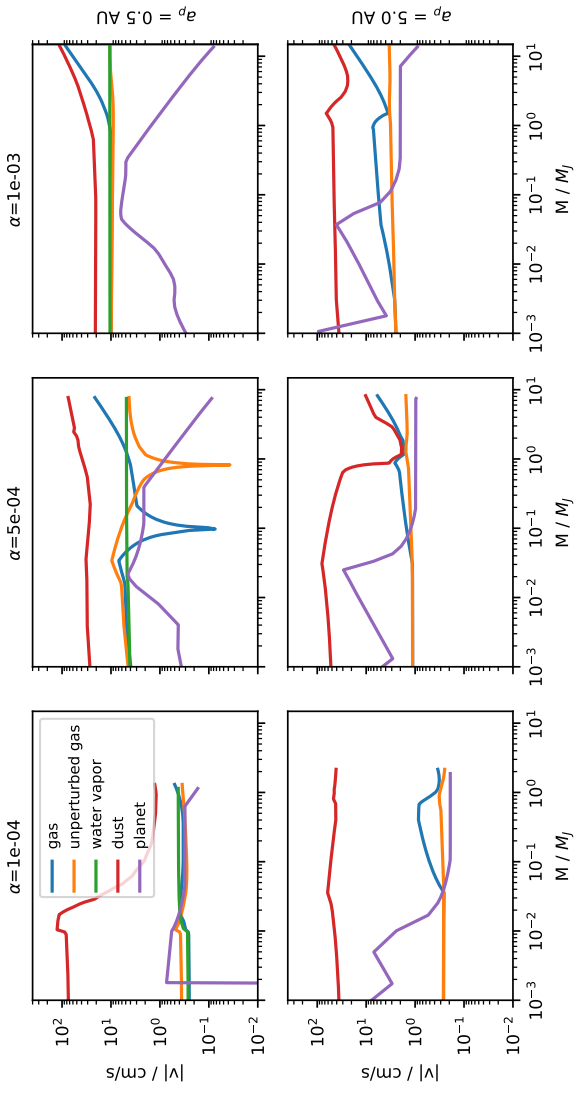

Figure 3.21: Radial velocities of dust, water vapor, perturbed and unperturbed gas, and the planet as a function of the planetary mass for non-migrating planets at 0.5 AU (top) and 5.0 AU (bottom). From left to right the disk's viscosity is increasing. The curves stop once the disk's lifetime reaches 3 Myr.

In Fig. 3.21 we show the radial velocities of the dust, the perturbed and unperturbed gas and planets as a function of the planetary mass. We note that the change of the planetary mass corresponds to the growth of the planet in the simulations, showing effectively a time evolution. The curves stop once the disk has reached its lifetime of 3 Myr. The different velocities are extracted from the same simulations used in Figs. 3.5, 3.6, and 3.7. The unperturbed velocities are extracted from simulations without planets.

The dust velocities originate from Eq. 3.5 and clearly show that dust moves fastest, allowing the enrichment of vapor in the inner disk by volatile transporting pebbles. The dust velocities change in time, due to the evolution of the dust and gas profile of the protoplanetary disk.

The unperturbed gas velocities (where there is no planet embedded in the disk) show some slight variations in time. This effect is caused by slight changes of the gas surface density in time due to evaporation, which influence the gas velocities (Eq. 3.12).

The velocities of the water vapor (only displayed at 0.5 AU because there is no water vapor at 5.0 AU) of simulations without planets are larger than the velocities of the unperturbed gas. This is caused by the lower vapor surface density compared to the total gas surface density, resulting in faster velocities (Eq. 3.12).

The perturbed gas velocities (blue line in Fig. 3.21) correspond to simulations with embedded planets. The main changes in the perturbed gas velocities are caused by the gap opening of the growing planet, which we mimic by changing the disk's viscosity at the planetary position. As the planet growth, the gap becomes deeper, mimicked by increasing the disk's viscosity at the planetary position. An increase in the disk's viscosity automatically increases the velocities of the perturbed gas profile. This approach is designed to keep the radial mass flux across the gap constant. The additional variations in the perturbed gas profile are caused by the further changes of the gas surface density profile due to evaporation of the inward drifting pebbles.

The velocities of the planet reflect the different migration prescriptions. Initially the planet is in type-I migration, which increases with planetary mass. As soon as the planet becomes massive and opens a partial gap, the migration speed decreases toward the initially constant type-II migration rate. Once the planet becomes very massive, its migration speed further decreases due to the inertia, which scales linearly with planetary mass, resulting in a further decrease in the planet's migration rate. This effect is clearly more important for higher viscosities, where the planet can grow faster.

The planetary migration rate of the planet, once it starts to open a partial gap, is always lower than the gas velocity. This effect can also be seen by

comparing the viscous type-II migration rate ($\tau_{visc} = a_p^2/\nu$, e.g., Baruteau et al. 2014) with the gas velocities in a viscously evolving disk

$$v_{r,gas} = -3\alpha\frac{c_s^2}{v_K}\left(\frac{3}{2} - \alpha_\Sigma\right) \tag{3.74}$$

analytically (Takeuchi & Lin, 2002). Here α_Σ denotes the slope of the radial gas surface density profile. This allows the planet to accrete volatile-enriched material brought by inward drifting pebbles in gas form.

G ICE CONDENSATION ONTO DUST GRAINS

The mass increase per grain (with mass $m = \frac{4}{3}\pi\rho_\bullet a^3$) per second due to the condensation (with sticking efficiency $\epsilon_p = 0.5$) of gaseous molecules of species Y with number density

$$n_Y = \frac{\Sigma_{gas,Y}}{\sqrt{2\pi}H_{gas}m_Y} \tag{3.75}$$

and mass $m_Y = \mu_Y m_p$ (e.g., CO: $m_Y = (12+16)m_p$) is given by

$$\frac{dm}{dt} = 4\pi a^2 n_Y v_{th,Y}\epsilon_p m_Y, \tag{3.76}$$

where $v_{th,Y}$ is the mean thermal velocity projected onto a surface given by

$$v_{th,Y} = \sqrt{\frac{k_B T}{2\pi m_Y}}. \tag{3.77}$$

This per grain increase translates to an increase in the solid surface density by

$$\dot{\Sigma}_Y^{cond} = \Sigma_{peb}\frac{1}{m_{peb}}\frac{dm_{peb}}{dt} + \Sigma_{dust}\frac{1}{m_{dust}}\frac{dm_{dust}}{dt}. \tag{3.78}$$

Inserting Eq. 3.76 into Eq. 3.78 yields:

$$\dot{\Sigma}_Y^{cond} = \frac{3}{\rho_\bullet}\left(\frac{\Sigma_{peb}}{a_{peb}} + \frac{\Sigma_{dust}}{a_{dust}}\right) n_Y v_{th,Y}\epsilon_p m_Y. \tag{3.79}$$

If we eliminate $v_{th,Y}$ and n_Y we get

$$\dot{\Sigma}_Y^{cond} = \frac{3\epsilon_p}{2\pi\rho_\bullet}\Sigma_{gas,Y}\left(\frac{\Sigma_{dust}}{a_{dust}} + \frac{\Sigma_{peb}}{a_{peb}}\right)\Omega_k\sqrt{\frac{\mu}{\mu_Y}}. \tag{3.80}$$

H WATER ICE CONTENT IN THE PEBBLES

The efficiency of evaporation of inward drifting pebbles depends crucially on the pebble size and their velocities (e.g., Piso et al. 2015; Drążkowska & Alibert 2017), where larger pebbles drift inward faster (e.g., Brauer et al. 2008). In our model the size of the pebbles is determined by a coagulation/fragmentation equilibrium, where the exact pebble size depends on the viscosity of the disk (Birnstiel et al., 2012). Lower viscosities result in larger pebble sizes, allowing them to drift inward further compared to smaller pebbles before they evaporate.

We show in Fig. 3.22 the ratio of the water ice surface density to the total pebble surface density for different disk viscosities and times. As soon as the pebbles cross the water ice line, they start to evaporate and the water ice fraction decreases. In the cases of lower viscosities, water-ice-rich particles can penetrate farther into the inner disk compared to higher viscosities because of the increased particles size and thus increased particle speed (Eq. 3.19). This result is in line with the simulations of Piso et al. (2015), who also showed that larger particles can penetrate deeper into the disk before they evaporate compared to smaller particles.

Figure 3.22 also reveals an increase in the water ice content in the solids close to the water ice line, which is caused by condensation of outward diffusing water vapor. Furthermore, we also see a dip in the water ice content at around 3-4 AU (depending on the disk's viscosity). This dip is caused by the condensation of CO_2 vapor, which increases the CO_2 content in the solids and consequently decreases the fraction of all other species, including water ice.

The pebbles close to the water ice line have Stokes numbers around 10^{-2} to 0.1 (low viscosity) or 10^{-3} to 10^{-2} (high viscosities), corresponding to particles sizes of ~10 cm (low viscosities) or ~1 cm (high viscosities). The resulting inward drift velocities are in the range of meters per second. Consequently pebbles evaporate within a close distance to the water ice line, in line with the simulations of Drążkowska & Alibert (2017).

I CORE MIXING IN THE ATMOSPHERE

In our main paper, we have shown the atmospheric C/O ratios, where our model initially contributes 10% of the accreted solids during the core buildup phase into the early planetary atmosphere until pebble isolation mass is reached. However, more detailed simulations indicate that the planetary atmosphere buildup might already start before the pebble isolation mass is

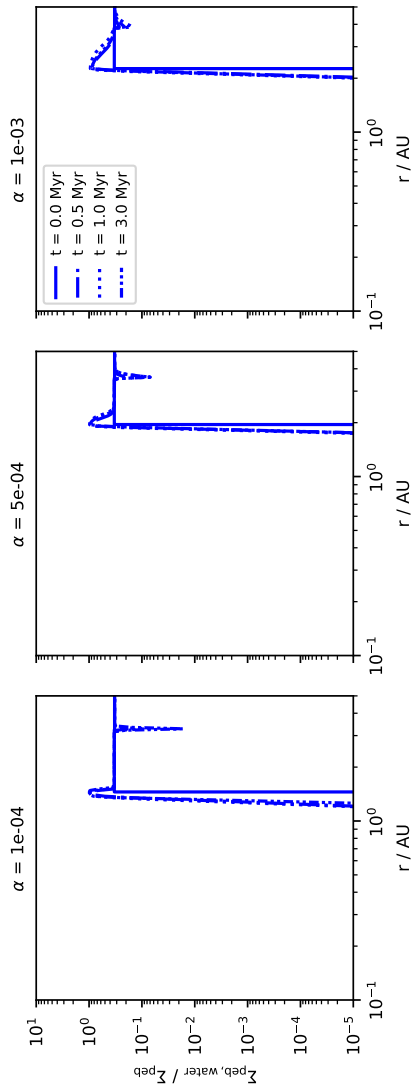

Figure 3.22: Ratio of the water ice surface density in pebbles compared to the total pebble surface density for different viscosities (left to right) as a function of time. The peak around the water ice line is caused by the condensation of water vapor, while the dip around 3-4 AU is caused by the condensation of CO_2, which consequently decreases the fraction of all solids at this position, including water ice.

simulation	$\epsilon_0 = 1 \times 10^{-2}$	$\epsilon_0 = 1.5 \times 10^{-2}$	$\epsilon_0 = 2 \times 10^{-2}$	$\epsilon_0 = 2.5 \times 10^{-2}$
plain	6.5 ± 0.3	7.4 ± 0.3	9.7 ± 0.3	11.6 ± 0.4
evap	29.2 ± 1.9	52.3 ± 3.8	73.4 ± 7.7	84.6 ± 11.0

(a) Fit parameter γ_a

simulation	$\epsilon_0 = 1 \times 10^{-2}$	$\epsilon_0 = 1.5 \times 10^{-2}$	$\epsilon_0 = 2 \times 10^{-2}$	$\epsilon_0 = 2.5 \times 10^{-2}$
plain	0.63 ± 0.02	0.69 ± 0.02	0.68 ± 0.01	0.68 ± 0.01
evap	0.52 ± 0.03	0.46 ± 0.03	0.49 ± 0.04	0.55 ± 0.05

(b) Fit parameter γ_b

Table 3.11: Fit results for Fig. 3.13.

Notes: The total heavy element content is related to the final mass by the power law $M_Z = \gamma_a \cdot M^{\gamma_b}$.

reached and that a larger fraction of the solids might be accreted into the planetary atmosphere (Brouwers & Ormel, 2020; Valletta & Helled, 2020). Nevertheless, a change in the amount of solids that can be accreted in the early atmosphere buildup will not change the total heavy element content of the planet, but would rather change the atmospheric C/O ratio.

We show in Fig. 3.23 the total C/O ratio under the assumption that the whole planetary core is mixed evenly into the planetary atmosphere. The situation shown here is clearly an extreme assumption; however, the total C/O ratio of the planetary atmosphere in reality might thus be in between a complete mixture of the core in the atmosphere and the situation shown in Fig. 3.15, where core and atmosphere are completely separated. While the exact C/O ratio is reduced for the mixing scenario, the general trend that planets forming farther away from the central star should harbor a larger C/O remains intact for both models with and without evaporation of pebbles.

J FIT PARAMETER

The solid to gas ratio fit parameters from Fig. 3.13 can be found in Table 3.11. Thorngren et al. (2016) found $\gamma_a = 57.9 \pm 7.03$ and $\gamma_b = 0.61 \pm 0.08$ for his fit on observed exoplanets. This is best matched with our simulations by $\epsilon_0 = 2.5\%$ in the evaporation model.

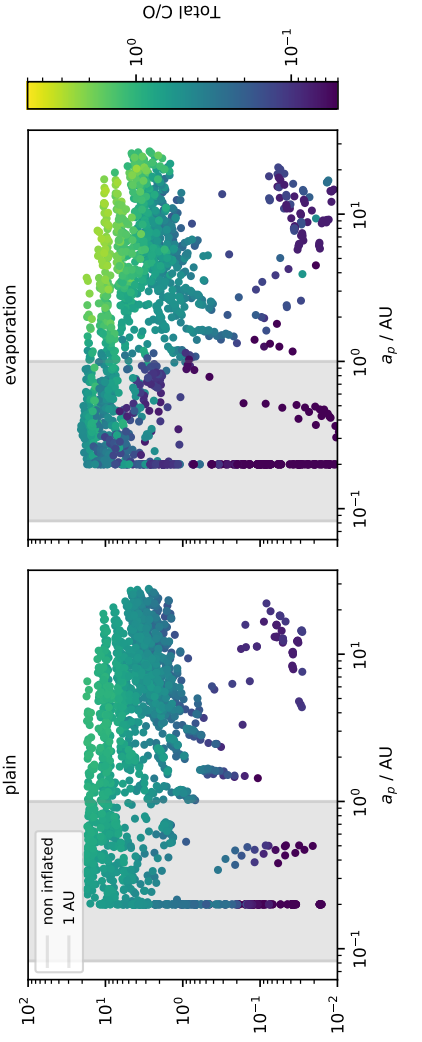

Figure 3.23: Like Fig. 3.15, but the color coding shows the total C/O ratio of core and atmosphere mixed together.

4

HOW DRIFTING AND EVAPORATING PEBBLES SHAPE GIANT PLANETS II: VOLATILES AND REFRACTORIES IN ATMOSPHERES

Aaron David Schneider & Bertram Bitsch

Published in Astronomy & Astrophysics, Volume 654, id.A72, October 2021

Author contributions:
Aaron Schneider conducted the research, developed the numerical model, and wrote most of the paper. Bertram Bitsch supervised the project and contributed significantly to the writing of the manuscript, the interpretation, and discussion of the results.

Notes:
The published version of Schneider & Bitsch (2021a) and Schneider & Bitsch (2021b) made use of a chemical partitioning model that did not conserve the nitrogen abundance. Subsequent corrections to Schneider & Bitsch (2021b), that have been published in a corrigendum (Schneider & Bitsch, 2022) are applied to this version of Schneider & Bitsch (2021b).

Original Abstract
Upcoming studies of extrasolar gas giants will give precise insights into the composition of planetary atmospheres, with the ultimate goal of linking it to the formation history of the planet. Here, we investigate how drifting and evaporating pebbles that enrich the gas phase of the disk influence the chemical composition of growing and migrating gas giants. To achieve this goal, we perform semi-analytical 1D models of protoplanetary disks, including viscous evolution, pebble drift, and evaporation, to simulate the growth of planets from planetary embryos to Jupiter-mass objects by the accretion of pebbles and gas while they migrate through the disk. The gas phase of the protoplanetary disk is enriched due to the evaporation of inward drifting pebbles crossing evaporation lines, leading to the accretion of large amounts of volatiles into the planetary atmosphere. As a consequence, gas-accreting planets are enriched in volatiles (C, O, N) compared to refractories (e.g., Mg, Si, Fe) by up to a factor of 100, depending on the chemical species, its exact abundance and volatility, and the disk's viscosity. A simplified model for the formation of Jupiter reveals that its nitrogen content can be explained by inward diffusing nitrogen-rich vapor, implying that Jupiter did not need to form close to the N_2 evaporation front as indicated by previous simulations. However, our model predicts an excessively low oxygen abundance for Jupiter, implying either Jupiter's migration across the water ice line (as in the grand tack scenario) or an additional accretion of solids into the atmosphere (which can also increase Jupiter's carbon abundance, ultimately changing the planetary C/O ratio). The accretion of solids, on the other hand, will increase the refractory-to-volatile ratio in planetary atmospheres substantially. We thus conclude that the volatile-to-refractory ratio in planetary atmospheres can place a strong constraint on planet formation theories (in addition to elemental ratios), especially on the amount of solids accreted into atmospheres, making it an important target for future observations.

1 INTRODUCTION

Even though more than 4000 exoplanets have been discovered so far (Akeson et al., 2013), it is still unclear how exactly these planets formed. In the core accretion scenario, the planetary core is built by the accretion of planetesimals (Ida & Lin, 2004; Alibert et al., 2005; Ida & Lin, 2008a,b, 2010; Mordasini et al.,

2012; Alibert et al., 2013; Emsenhuber et al., 2021) or pebbles (Lambrechts & Johansen, 2012, 2014; Bitsch et al., 2015b; Ali-Dib, 2017; Ndugu et al., 2018; Brügger et al., 2018; Lambrechts et al., 2019b; Bitsch et al., 2019). While the underlying mechanisms of pebble and planetesimal accretion are fundamentally different, both models require a sufficiently fast formation of a planetary core of a few Earth masses before gas accretion can begin (Pollack et al., 1996; Ikoma et al., 2000).

Hope to constrain the planet formation pathway is based on the detailed characterizations of the planetary atmosphere, especially the C/O ratio (e.g., Öberg et al., 2011). Previous observations of planetary C/O ratios have revealed super-solar C/O values (Brewer et al., 2017), indicating that these planets might originate from beyond the water ice line, where the C/O ratio in the disk is larger (Öberg et al., 2011; Madhusudhan et al., 2017; Booth et al., 2017; Notsu et al., 2020; Schneider & Bitsch, 2021a). Furthermore, current spectroscopic observations of WASP-121b have revealed the absence of VO and TiO (Merritt et al., 2020) and the presence of neutral transition metals such as vanadium (Ben-Yami et al., 2020), providing further constraints on planet formation. The upcoming *James Webb Space Telescope* (JWST) and the *Atmospheric Remote-sensing Infrared Exoplanet Large-survey* (ARIEL) missions are expect to constrain planetary C/O ratios and other atmospheric elemental abundances for many more targets, building a large sample that can be used to constrain planet formation theories.

In Schneider & Bitsch (2021a) we investigate the origin of the total heavy element content of giant planets, where the evaporation of drifting pebbles that pollute the disk gas with heavy elements (see also Banzatti et al. 2020; Zhang et al. 2020) can account for the large fraction of heavy elements inside the giant planets (Thorngren et al., 2016). As a consequence, this process would significantly enrich the planetary atmosphere with volatile elements (e.g., C, O, N) but leave the planetary atmosphere devoid of refractory elements (e.g., Mg, Si, Fe).

On the other hand, Owen et al. (1999) and Atreya et al. (2016) proposed that the super-solar abundances of carbon, nitrogen, and sulfur in the atmosphere of Jupiter could be explained by the accretion of planetesimals. Furthermore, Öberg & Wordsworth (2019) and Bosman et al. (2019) suggest that Jupiter's nitrogen abundance is most likely explained by the formation of Jupiter beyond the N_2 evaporation line, allowing the accretion of nitrogen-rich solids. However, planetesimals and comets are, to a very large fraction, made out of refractory elements. Accreting planetesimals into planetary atmospheres would thus result in a large fraction of refractory elements inside these atmospheres as well.

It is clear that the enrichment of gas giant atmospheres via vapor-enriched gas and planetesimals is fundamentally different and would also lead to different atmospheric compositions. In this work we use our previous model of pebble drift and evaporation (Schneider & Bitsch, 2021a) to study the detailed chemical composition of gas giants, with a special emphasis on volatile and refractory elements as well as on the planetary C/O ratio. We first focus on exoplanet formation and then show results of a simplified model for the inferred composition of Jupiter and Saturn.

2 METHODS

We modeled the formation of gas giant planets by the accretion of pebbles and gas in viscously evolving disks while tracing the chemical composition of the migrating planet. The newly developed code `chemcomp` used in these simulations is explained in detail in Schneider & Bitsch (2021a). These simulations include the evaporation of inward drifting pebbles and the condensation of outward diffusing gas at evaporation lines. Within these models we simulated the growth and migration of single planetary embryos all the way to gas giants.

The initial solid surface density was

$$\Sigma_Z = \epsilon_0 \Sigma_{\rm gas}, \tag{4.1}$$

where ϵ_0 is the solid-to-gas ratio and $\Sigma_{\rm gas}$ is the gas surface density. The solid-to-gas ratio depends on the position in the disk, where a higher solid-to-gas ratio is used when volatile species are frozen out (see Schneider & Bitsch, 2021a, for more details). For all our simulations, we set $\epsilon_0 = 1.5\%$ in the outer disk. The gas surface density can be calculated from the disk mass (M_0) and disk radius (R_0). We utilized here the alpha-viscosity (Shakura & Sunyaev, 1973) prescription, which relates the viscosity to the numerical parameter (α) that describes the turbulent strength. The viscosity is then given by

$$\nu = \alpha \frac{c_s^2}{\Omega_K}, \tag{4.2}$$

where c_s is the isothermal sound speed and Ω_K the orbital period.

Our pebble growth and evolution model is based on that in Birnstiel et al. (2012), where the maximal grain size in the fragmentation-limited regime is determined by the disk viscosity as well as by the dust fragmentation velocity, which we set to $u_{\rm frag} = 5$m/s, following laboratory constraints (Gundlach & Blum, 2015). We used a variable pebble density, $\rho_\bullet$, where the pebble density depends on the volatile-to-refractory ratio in the solid surface

density (Drążkowska & Alibert, 2017). The disk model was calculated on a logarithmically spaced grid of $N_{Grid} = 500$ grid cells in between $r_{in} = 0.1$ AU and $r_{out} = 1000$ AU.

We assumed that the initial chemical composition of the protoplanetary disk is similar to the composition of the host star, for which we used the solar abundances (denoted as [Fe/H]=0) from Asplund et al. (2009). We followed here the chemical compositions as outlined in Schneider & Bitsch (2021a).

The Solar System provides evidence for the initial abundances not only from the solar photosphere, but also from meteorites. In particular, CI chondrites should have accreted refractory carbon grains. By calculating the ratio of carbon inside CI chondrites to carbon in the solar photosphere, we can roughly determine the amount of refractory carbon for our chemical models. Using the data from Lodders (2003), we find that roughly 10% of the carbon should be in refractory components and the remaining carbon in volatile form. Using data from comets (Altwegg et al., 2020) results in a slightly higher refractory carbon content of around 20%. Our standard chemical model therefore contains 20% in refractory carbon, but we also investigated a situation where 60% of all carbon is in refractory form (Table 4.1), representing the refractory carbon fraction in the interstellar medium (ISM; e.g., Bergin et al. 2015)[1]. As more carbon grains are bound in refractories, less oxygen is bound in CO and CO_2, leaving more oxygen available to form water, in turn increasing the water abundance within our model (see Appendix A).

Applying the same argument for sulfur and nitrogen reveals that nearly all sulfur should be in refractory form, while nearly all nitrogen should be in volatile form (Lodders, 2003), in line with our chemical model (Schneider & Bitsch, 2021a). Of course, this argument is based on the assumption that CI chondrites accreted the full refractory component of the corresponding species.

The growth of the planets is divided into two phases. First, the planet accretes pebbles (e.g., Johansen & Lambrechts, 2017) until it reaches the pebble isolation mass (e.g., Lambrechts & Johansen, 2014; Bitsch et al., 2018), where pebble accretion stops. During the solid accretion phase, we attributed 90% of the solids to the core and 10% of the solids to a primordial planetary atmosphere during core buildup, following the idea that pebbles evaporate during accretion (Hori & Ikoma, 2011; Brouwers & Ormel, 2020). The pebble isolation mass is smaller in the inner regions of the disk, due to the flaring disk structure (e.g., Chiang & Goldreich, 1997; Bitsch et al., 2015a), resulting

1 A lot of studies try to link the ISM refractory carbon abundances to the carbon abundance on Earth (e.g., Klarmann et al. 2018; van 't Hoff et al. 2020; Li et al. 2021), showing that there is clearly some uncertainty regarding the incorporation of carbon into solids.

Table 4.1: Condensation temperatures and volume mixing ratios.

Species (Y)	T_{cond} [K]	$\nu_{Y,\,20\%\,C}$	$\nu_{Y,\,60\%\,C}$
CO	20	$0.45 \times C/H$	$0.2 \times C/H$
CH_4	30	$0.25 \times C/H$	$0.1 \times C/H$
CO_2	70	$0.1 \times C/H$	$0.1 \times C/H$
C (carbon grains)	631	$0.2 \times C/H$	$0.6 \times C/H$

Notes: The table displays only the carbon-bearing species used in our work. The full condensation sequence of our chemical model is shown in Schneider & Bitsch (2021a).

in smaller core masses of inner forming planets. The planet then starts to accrete gas from the protoplanetary disk, via a slow gas contraction followed by rapid runaway gas accretion, which is limited by the disk's supply rate, determined by viscosity. For gas accretion, we followed the approach outlined in Ndugu et al. (2021), where the envelope contraction rate is modeled via Ikoma et al. (2000), which depends not only on the planetary core mass, but also on the envelope opacity, κ_{env}. For κ_{env} we used a constant value of 0.05 cm^2/g (Movshovitz & Podolak, 2008).

We used the same set of parameters (see Table 4.2) as that used in Schneider & Bitsch (2021a) and only varied the initial position, $a_{p,o}$, of the planet and the viscous α parameter. Throughout this work we compare the formation of planets in different disks that harbor different viscosities for the disk evolution and pebble growth (see Table 4.2). However, the vertical distribution of the pebbles is assumed to happen with low turbulence ($\alpha_z = 10^{-4}$ for all simulations).

Calculating the atmospheric composition within our model is mainly influenced by the initial assumption that once the planet reaches the pebble isolation mass, it exerts a pressure bump, blocking all available solids exterior to planet. As a consequence, the planets in our model can, at this stage, only accrete evaporated material (also known as vapor), not solids. This is further discussed in Sect. 4.

3 PLANET FORMATION

During the planetary growth, the planet migrates first in type-I migration and then in type-II migration once it opens a gap in the protoplanetary disk. The migration speed during type-II is directly proportional to the disk's

Table 4.2: Parameters used throughout this paper.

Quantity	Value
$a_{p,0}$	$(3, 10, 30)$ AU
t_0	0.05 Myr
κ_{env}	$0.05\,cm^2\,g^{-1}$

(a) Planet

Quantity	Value
r_{in}	0.1 AU
r_{out}	1000 AU
N_{Grid}	500

(b) Grid

Quantity	Value
α	$(1, 5, 10) \times 10^{-4}$
α_z	1×10^{-4}
M_0	$0.128\,M_\odot$
R_0	137 AU
[Fe/H]	0
t_{evap}	3 Myr
ϵ_0	1.5%
u_{frag}	$5\,m\,s^{-1}$

(c) Disk

Notes: Parameters used for the initialization of `chemcomp` that are used throughout this paper, divided into planetary, numerical, and disk parameters. The detailed explanation of these parameters can be found in Schneider & Bitsch (2021a).

viscosity, allowing planets forming in disks with high viscosities to migrate farther inward compared to planets forming in disks with low viscosities (Baruteau et al., 2014). We implanted the planet at t=0.05 Myr and stopped the integration either at the end of the disk's lifetime (at $t_{evap} = 3$ Myr) or when the planet reaches 0.2 AU.

Planetary embryos that start to grow at 3 AU initially first migrate outward due to the effects of the heating torque (Benítez-Llambay et al., 2015; Masset, 2017; Baumann & Bitsch, 2020) but then migrate rapidly inward before they open deep gaps. This is caused by the relatively long envelope contraction phase for these small cores. In fact, the planet forming in a disk with $\alpha = 10^{-3}$ migrates down to the disk's inner edge before 1 Myr of evolution because it is unable to open a deep gap, in contrast to the planets forming in lower viscosity environments.

The planetary embryos starting at 10 and 30 AU evolve in a very similar way. Namely, the planets forming in disks with higher viscosities migrate inward more efficiently due to the delayed gap opening, and they grow to larger masses because the disk's gas supply rate is larger due to the larger viscosity. In fact, the planets forming in very low viscosity environments ($\alpha = 10^{-4}$) only migrate inward for a few AU relative to their starting position.

The inward migration speed of the gas giants reduces as the planets grow (upward shift in the growth tracks toward their end; Fig. 4.1). This is caused by the fact that the type-II migration rate also scales with the planetary mass, resulting in slower migration for more massive planets (Baruteau et al., 2014).

4 VOLATILES VERSUS REFRACTORIES

In this section we discuss the elemental abundances in the planetary atmospheres of the planets formed in our model (see Fig. 4.1). Our planetary model does not include an atmospheric structure model, which would be needed for accurate simulations of the atmospheric composition gradients (e.g., Vazan et al., 2018). We thus assumed a perfectly mixed atmosphere, either with or without a complete mix of the planetary core into the atmosphere, showing the most extreme elemental abundances possible within our model. In the scope of this work, we define the volatile-to-refractory ratio as the ratio of volatile molecules (evaporation temperature below 150 K) to refractory molecules (evaporation temperature above 150 K).

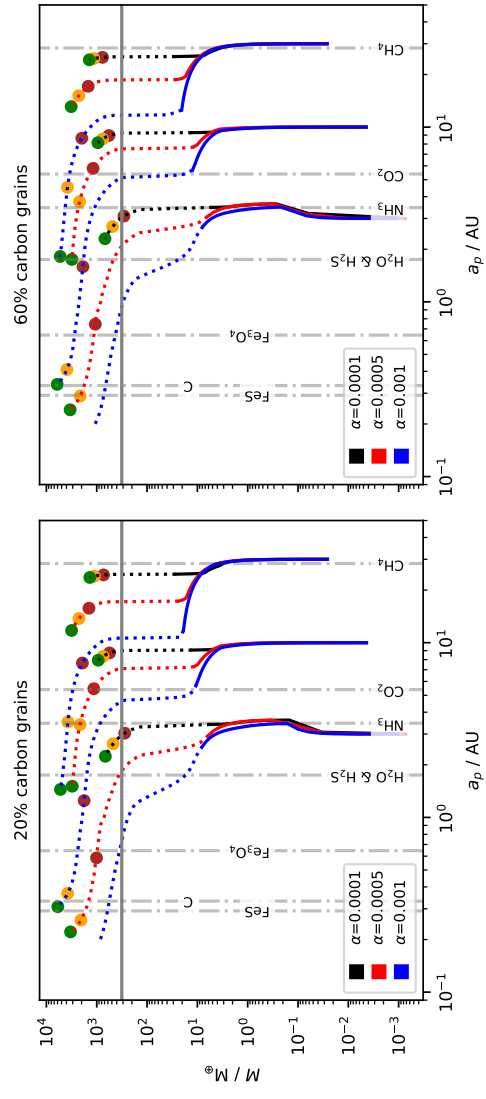

Figure 4.1: Growth tracks of planets that accrete pebbles (solid lines) and gas (dashed lines) starting at different initial positions in disks with different values for α (indicated by color). The dashed gray lines mark the positions of evaporation lines for $\alpha = 5 \times 10^{-4}$. The solid gray horizontal line marks the mass of Jupiter. The brown, yellow, and green dots mark an evolution time of $t = 1$ Myr, $t = 2$ Myr, and $t = 3$ Myr, respectively. The planet starting at 3 AU in a disk with $\alpha = 0.001$ reaches the inner edge of the disk before 1 Myr of evolution. The left panels display models with 20% of the carbon abundance locked in refractory carbon grains, whereas the right panels show models with 60% locked in carbon grains. Model parameters can be found in Table 4.2.

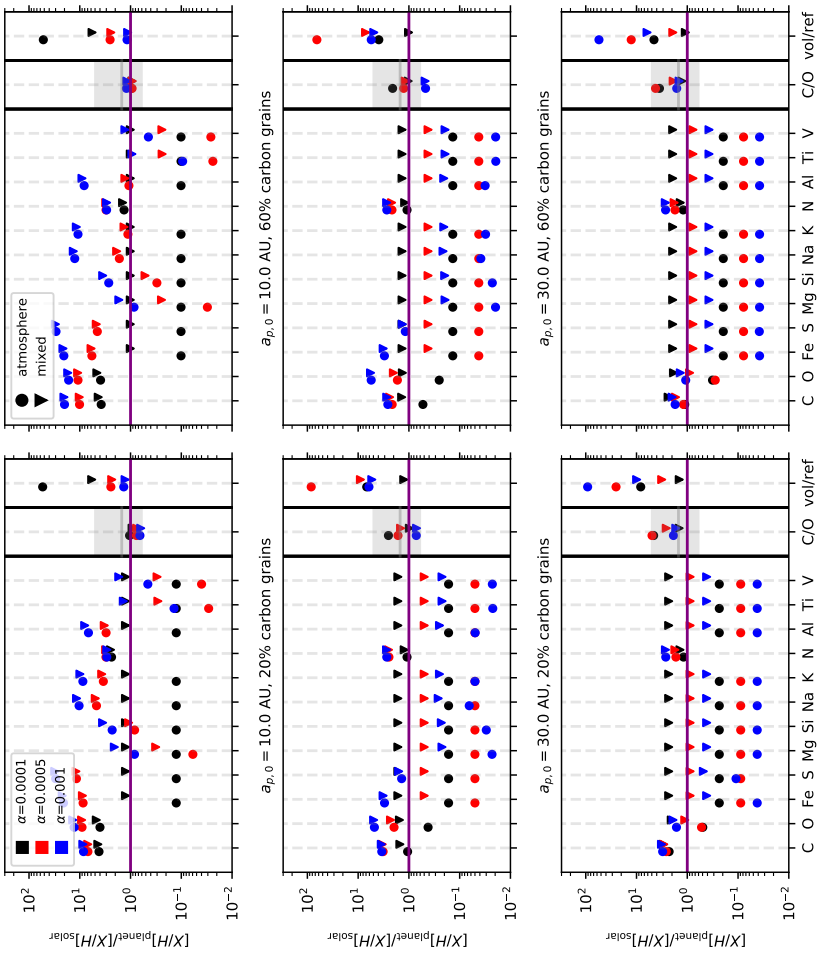

Figure 4.2: Final atmospheric compositions of the planets shown in Fig. 4.1 normalized to the solar composition. We also show the C/O ratio normalized to the solar value on the right of each panel, with Jupiter's C/O ratio marked in gray (Atreya et al., 2016; Li et al., 2020), as well as the volatile-to-refractory ratio, which we calculate as the ratio of volatile to refractory molecules in the atmosphere. The left panels display models with 20% of the carbon abundance locked in refractory carbon grains, whereas the right panels show models with 60% locked in carbon grains. The circles mark the composition of the pure atmosphere, while the triangles mark the composition if the core were completely mixed into the atmosphere.

4.1 *Effects of pebble evaporation*

We show in Fig. 4.2 the elemental ratios inside the planetary atmosphere normalized to the solar composition for the pure atmosphere (circles) or when the core is completely mixed into the atmosphere (triangles). The advantage of this approach is that it shows the maximal (triangles) and minimal (circles) values of the atmospheric composition within our model.

Figure 4.2 clearly shows an enrichment of volatile species (C, O, N) in the planetary atmospheres compared to refractory elements (e.g., Al, Mg, Si), leading to a high volatile-to-refractory ratio, as displayed. This is naturally explained by gas accretion, which allows the accretion of volatile-rich vapor (e.g., H_2O, CO_2, NH_3, CH_4, CO) but not of refractory elements, which are bound in pebbles blocked exterior to the planet. This potentially explains the absence of VO and TiO in WASP-121b (Merritt et al., 2020), although atmospheric effects such as transport and thermal evolution can also reduce the VO and TiO abundances (e.g., Parmentier et al., 2016; Beatty et al., 2017). This effect is also reflected by the decrease in the refractory content in the planetary atmosphere with increasing α values, where larger α values result in faster gas accretion and more massive planets. The accreted gas is refractory poor due to the blockage of refractory-rich pebbles exterior to the planet, which is caused by the pressure bump of the planet that can block pebbles from drifting inward. This dilutes the initially high refractory abundance in the atmosphere during core buildup[2].

One exception is the accretion of the FeS vapor of the planets migrating into the very inner, hot regions of the disk, where FeS evaporates and can be accreted in gaseous form. This results in super-solar Fe/H and S/H values in the atmospheres of the planets starting at 3 AU in disks with $\alpha > 1 \times 10^{-4}$. Our model assumes that a large fraction of sulfur is bound in FeS and only a small amount in H_2S (Kama et al., 2019). In contrast, comets in the Solar System seem to have a large H_2S abundance (Flynn et al., 2006; Mumma & Charnley, 2011), hinting at a different sulfur distribution compared to our nominal model. On the other hand, recondensation of H_2S vapor at the H_2S evaporation front can locally increase the S/H ratio in the solids, potentially explaining the large H_2S abundance in comets. A similar effect at carbon-bearing evaporation fronts is invoked in Mousis et al. (2021) to explain the composition of the comet C/2016 R2. The other refractory species show different abundances for the planets migrating all the way to the inner disks

2 The planet forming at 3 AU in the disk with $\alpha = 10^{-3}$ is an exception because it migrates to the inner edge of the disk before the end of the disk lifetime, where we stop accretion, resulting in the relatively high refractory abundance compared to the counterparts formed in low viscosity disks.

because the different evaporation fronts are crossed at different times. In contrast, the refractory contents of the planets formed in the outer disk are similar for all elements because there the refractories are only in solid form and cannot be accreted with the gas in our model.

The inward drifting and evaporating pebbles enrich the gas in volatiles to super-solar values (C, O, N), explaining the super-solar values of volatile species in the planetary atmospheres. The exception here is oxygen, which can be subsolar for gas-accreting planets forming in the outer regions of the disk if they do not migrate across the CO_2 evaporation front, which would allow an efficient accretion of oxygen with the gas. This effect is clearly visible for the planets forming at 30 AU when comparing the oxygen abundance of the planet forming in a disk with $\alpha = 10^{-3}$ and the planets forming in disks with lower viscosities (Fig. 4.2).

Our simulations also show a clear trend regarding the planetary C/O ratio with increasing initial planetary position. Planets forming farther out have a larger C/O ratio compared to planets forming closer to the host star. This is a direct consequence of the C/O ratio in the gas phase of the protoplanetary disk, which increases with orbital distance due to the evaporation of carbon-bearing species (Schneider & Bitsch, 2021a).

If the planetary core is completely mixed into the planetary atmosphere, the atmosphere is enriched with the material from the core. In our simulations, this implies an enrichment with refractory species, which is clearly visible for all our simulations. Naturally, larger cores lead to more enrichment, where the core mass increases toward larger radii due to the flaring nature of the disk, increasing the pebble isolation mass. Volatile species, on the other hand, are only marginally increased, with only oxygen showing a major increase for the planets forming in the outer disk regions (due to the oxygen bound in CO_2 and water ice). As a consequence, the atmospheric C/O ratio is relatively unchanged, except for the planets forming in the outer disk, which show a drop in the C/O ratio due to the large oxygen content of the core.

The model with 60% carbon grains shows that the gas phase of the disk interior to the carbon grain evaporation line is enriched in carbon compared to the model with only 20% carbon grains, while it is depleted beyond the carbon grain evaporation line. This means that planets that accrete most of the gas beyond the carbon grain evaporation line host atmospheres that have less carbon in a model with more carbon grains (see the right panels of Fig. 4.2) than those in the model with fewer carbon grains (see the left panels of Fig. 4.2). Contrary, planets that migrate all the way to the inner disk have enhanced carbon abundances in a model with more carbon grains. This clearly shows that a detailed chemical model is of crucial importance if the planet

Table 4.4: Additional solid enrichment.

	20% carbon grains	60% carbon grains
Fig. 4.3	$30\,M_\odot$	$30\,M_\odot$
Jupiter	$7\,M_\odot$	$9\,M_\odot$
Saturn	$9\,M_\odot$	$11\,M_\odot$

Notes: Additional solid enrichment for Figs. 4.3 and 4.5.

formation pathway is supposed to be constrained by C/O alone (e.g., Notsu et al., 2020). Nevertheless, the overall planetary C/O ratio is quite similar for planets formed within the two different chemical models.

Including more carbon grains in the chemical model (see Table 4.1) redistributes the carbon-rich evaporation fronts inward because of the reduced amount of CH_4 (see Appendix A). The enhanced evaporation front at 631 K ($r \approx 0.2\,AU$) near the FeS evaporation line raises the C/O ratio of the gas phase C/O in the inner disk (see Fig. 4.6), while lowering the pebble pileup and the pollution due to methane evaporation at the methane evaporation line. The other chemical elements are not affected by the change in the carbon distribution, and the planet formation (growth and migration times) remains largely unaffected as well.

Similar changes in the planetary composition are expected for other elements that can exist in volatile or refractory form (e.g., sulfur).

4.2 *Effects of additional solids*

Planetary atmospheres can also be enriched via collisions (Ogihara et al., 2021) or via the accretion of planetesimals. This can happen either during the buildup of the planetary atmosphere itself (Pollack et al., 1996), which might even delay runaway gas accretion (Alibert et al., 2018; Venturini & Helled, 2020; Guilera et al., 2020), or when a large gaseous envelope has already formed (Shibata & Ikoma, 2019; Shibata et al., 2020). The accretion efficiency depends crucially on the size of the planetesimals (Levison et al., 2010; Fortier et al., 2013; Johansen & Bitsch, 2019) and the migration speed of the planet (Tanaka & Ida, 1999). Furthermore, small pebbles beyond the planetary orbit are subject to turbulent motions caused by the spiral arms of the giant planet; this can transport the pebbles to upper layers of the disk, where they can then subsequently be accreted by the giant planet (Bi et al., 2021; Szulágyi et al., 2022) through a meridional flow around the planet (Morbidelli et al., 2014).

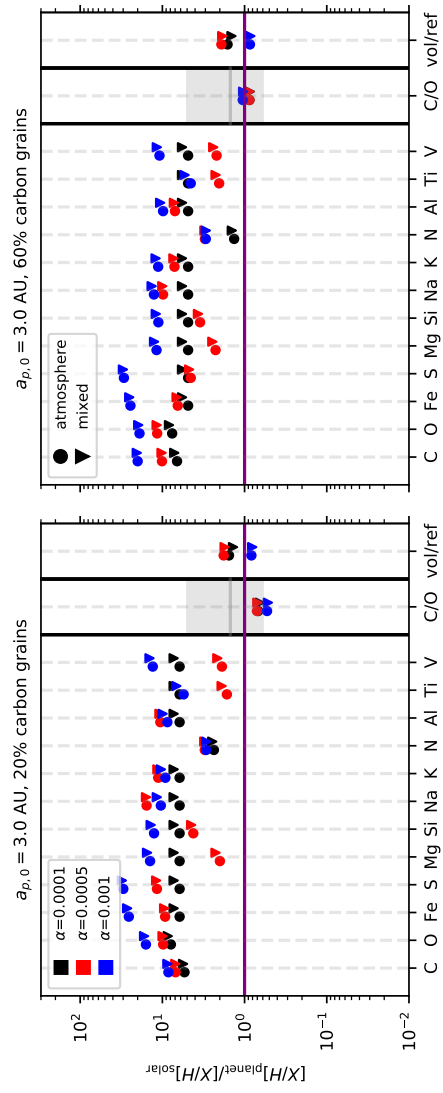

Figure 4.3: As Fig. 4.2, but with the addition of 30 Earth masses of solids into the atmosphere. We only show the results of the planets starting at 3.0 AU because the addition of extra solids into the atmospheres results in the same trends for planets starting farther away from the star.

A detailed modeling of further solid accretion is beyond the scope of this work, and we only artificially added 30 Earth masses (Table 4.4) of solids into the planetary atmospheres of our planets formed via pebble and gas accretion (Fig. 4.1). For simplicity, we used the solid composition at the final orbital position of the planet for the composition of the added material. While this approach is clearly simplified, it illustrates a very important effect: a change in the refractory content in the planetary atmosphere due to solid accretion.

In Fig. 4.3 we show the atmospheric composition of the same planets as in Fig. 4.1, but with 30 Earth masses of solids added into the atmosphere. It is clear that the addition of solids into the atmosphere increases the refractory-to-volatile ratio in the atmosphere for all the different planets formed in our simulations[3]. Furthermore, the planetary C/O ratio decreases as well because of the oxygen bound in the refractory materials.

We additionally note that the nitrogen abundance is not affected by the addition of further solids for the planets shown in Fig. 4.3. This is related to the fact that no nitrogen is in solid form at the planetary position and can thus not be added by the accretion of further solids into the planetary atmosphere. This effect clearly illustrates the implications of our model: The volatile-to-refractory content in planetary atmospheres could give important constraints if solid accretion into atmospheres is efficient.

5 JUPITER AND SATURN

To illustrate the effects of the accretion of vapor-rich material on the atmospheric composition of Jupiter and Saturn, we employed a simplified formation scenario in which the planets do not migrate from their current positions. We only modeled gas accretion onto the planetary cores, which we assumed to be fully formed at 1 Myr, in line with suggestions from cosmochemical studies (Kruijer et al., 2017).

5.1 *Simple growth model for Jupiter and Saturn*

We present here the ingredients for a simplified growth model of Jupiter and Saturn. We started under the assumption that the planetary core has already fully formed at 1 Myr, consistent with constraints from cosmochemistry (Kruijer et al., 2017). The planetary core mass corresponds to the pebble isolation mass at the current orbital positions of Jupiter and Saturn, and

3 The planet starting at 3 AU in the disk with $\alpha = 10^{-4}$ shows mostly an increase in oxygen, which is caused by the final position of the planet close to the water ice line, where the solid composition is dominated by water ice.

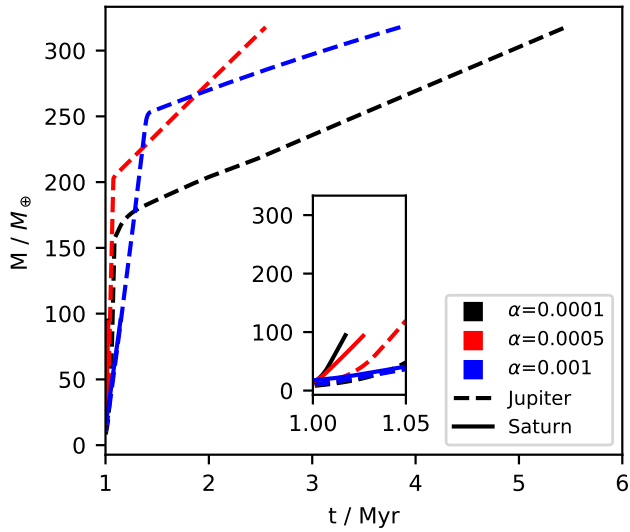

Figure 4.4: Mass growth of the gaseous components of Jupiter and Saturn as a function of time. We start our simulations with an already fully formed core at 1 Myr.

the planet is thus already in the gas accretion phase. We further took the very simplified approach that Jupiter and Saturn do not migrate during their evolution to illustrate the effects of vapor-enriched gas accretion on the atmospheric composition of these planets.

As the gas accretion rates in our nominal model are quite high (Fig. 4.1), we modeled the formation of Jupiter and Saturn in environments with a lower gas surface density because the gas surface density sets, alongside the viscosity, the gas accretion rate in the disk-limited regime (Ndugu et al., 2021). The gas disk masses are 0.0256, 0.0128, and 0.00256 $M_\odot$ for $\alpha = 10^{-4}$, 5×10^{-4}, and 10^{-3}, respectively, allowing the same gas delivery through the disk's accretion rate ($\dot{M}_{gas} \propto \Sigma_g \nu$) for all models. We stopped the integration once the masses of Jupiter and Saturn are reached. We show the growth of Jupiter and Saturn in Fig. 4.4.

Initially, as the planets start to accrete gas, they can feed off the material inside the planet's horseshoe region (Crida & Bitsch, 2017; Bergez-Casalou et al., 2020), allowing initially fast accretion. In fact, the amount of gas close to Saturn's position allows that Saturn accretes its gaseous envelope in less than 100 kyr. Jupiter, on the other hand, after it accretes all the material in its horseshoe region, feeds off the disk's gas supply. Due to the reduced gas

surface density compared to our nominal model, Jupiter accretes gas for a few megayears after its core formation before it reaches its final mass. The time Jupiter needs to reach its final mass is nearly independent of the disk's viscosity, especially in the final stages of gas accretion, because the gas flow through the disk is the same in all three simulations. We note that the gas accretion time for Jupiter seems to be in line with the lifetime of the protosolar nebular (e.g., Wang et al., 2017), but obviously Saturn grows too quickly. We will address the combined growth (and migration) of Jupiter and Saturn in a future work.

5.2 *Implications for the formation of Jupiter and Saturn*

Some elemental abundances have been constrained from previous missions to Jupiter (for a recent review, see Atreya et al. 2016), and the recent Juno mission revealed the oxygen abundance around Jupiter's equator (Li et al., 2020). Under the assumption that the oxygen abundance around Jupiter's equator corresponds to the bulk composition, we determined Jupiter's C/O, as marked in Fig. 4.5, which shows a super-solar C/O. We discuss now the implications of our model on the C, O, N, and refractory abundances of Jupiter.

In order to achieve a super-solar C/O, the planet needs to accrete gas enriched with carbon, which is easiest to achieve beyond the water ice line (Öberg et al., 2011; Schneider & Bitsch, 2021a). While the C/O ratio is matched quite well, the actual O/H values are too low compared to that of Jupiter (Jupiter's O/H is $2.7^{+2.4}_{-1.7}$ solar; Li et al. 2020) because Jupiter stays beyond the water ice line at all times in our model. The addition of oxygen-rich solids (e.g., planetesimals, comets) could provide more oxygen to Jupiter, or an inward migration followed by an outward migration, as in the grand tack scenario (Walsh et al., 2011), could allow the accretion of more oxygen from the gas phase of the protoplanetary disk (see also Fig. 4.2). The measured C/H of Jupiter is larger than in our simulations, which could also be increased by the accretion of further carbon-containing solids or by gas accretion close to evaporation fronts of carbon species.

Recent studies (Ali-Dib, 2017; Öberg & Wordsworth, 2019; Bosman et al., 2019) put forward the idea that Jupiter formed in the outer regions of the disk and then migrated inward (Bitsch et al., 2015b) due to the nitrogen and noble gas abundances in Jupiter's atmosphere, which are enriched by a factor of of two to four compared to the Sun (Owen et al., 1999). The underlying idea of these works is that nitrogen and the noble gases were frozen out and, as such, could be accreted in solid form. This idea is also based on the large abundance

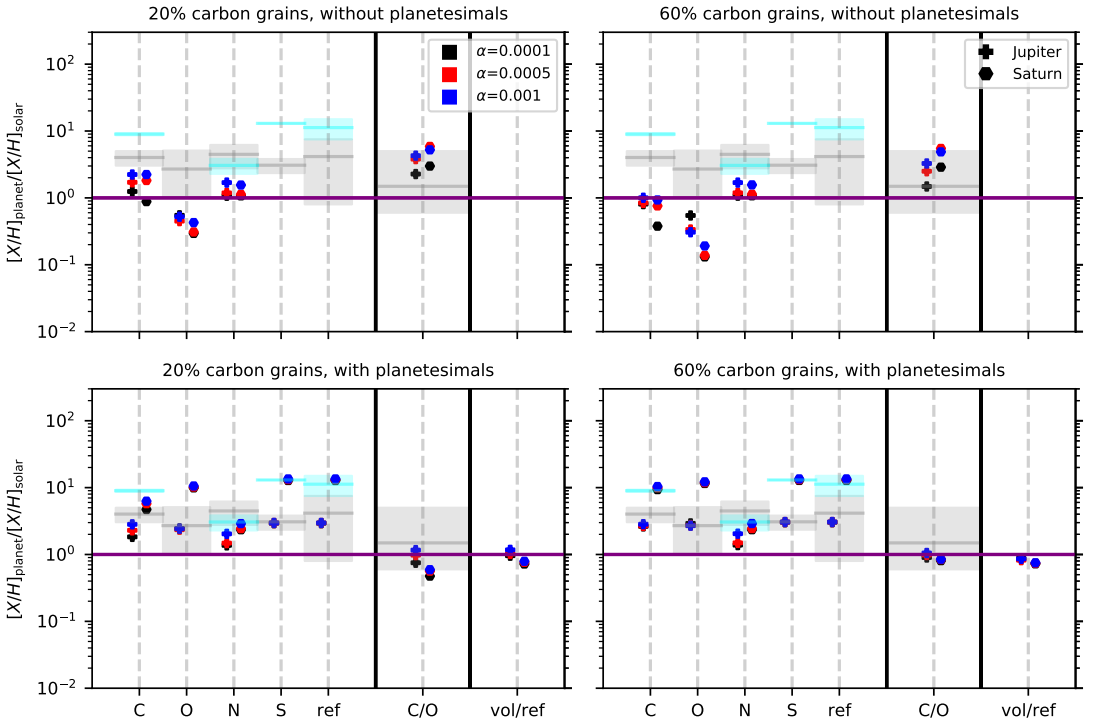

Figure 4.5: Atmospheric compositions of Jupiter and Saturn from our model and the corresponding observations (Atreya et al., 2016; Li et al., 2020). The left panels display models with 20% of the carbon abundance locked in refractory carbon grains, whereas the right panels show models with 60% locked in carbon grains. The bottom panels display the effect of additional solids added to the atmosphere (see Table 4.4). The gray bands correspond to measurements in Jupiter's atmosphere, while the horizontal light blue line marks the measurements for Saturn. We show here only the atmospheric abundances without mixing of the planetary core into the atmosphere because Jupiter has a core (Wahl et al., 2017). The refractory content is zero if we do not add any additional solids because our model does not allow the accretion of solids during the gas accretion phase.

of N_2 compared to NH_3 (Boogert et al., 2015; Cleeves et al., 2018; Pontoppidan et al., 2019). However, NH_3 ices could be locked in salts (Altwegg et al., 2020), allowing an accretion of nitrogen via solids even closer to the host star.

Within our model, we observe super-solar nitrogen abundances for Jupiter and Saturn (Fig. 4.5). This is caused by the evaporation of inward drifting nitrogen-rich pebbles, which enriches the gas phase and consequently the planetary atmosphere. The same should apply for noble gases with very low evaporation temperatures. Our model thus implies that Jupiter did not necessarily need to form close to the N_2 evaporation front.

For Saturn, only constraints for the C/H ratio are available (Atreya et al., 2016). Our solid-free model clearly underproduces the C/H ratio of Saturn, implying that pebble evaporation alone can probably not explain Saturn's composition. On the other hand, our simulations are very simplistic regarding the interior distribution of material. Studies of Jupiter have clearly revealed a diffused core and metallicity gradient inside the planet (Wahl et al., 2017; Vazan et al., 2018; Debras & Chabrier, 2019), which could enhance the elemental abundances compared to our simple model (see the mixing of the core in Fig. 4.2).

In Fig. 4.5 we also show the refractory content in the planetary atmospheres, which is by construction zero for the models without additional solids because our model does not allow the accretion of solids during the gas accretion phase. The refractory content of Jupiter is still unknown for most elements; only the sulfur and phosphor abundances are measured ($\approx 4 \times$ solar; Atreya et al. 2016). However, a small sulfur fraction is in volatile form as H_2S, which could allow sulfur accretion via the gas phase if the planet migrates into the inner disk (Fig. 4.2), as proposed in the grand tack scenario (Walsh et al., 2011). On the other hand, most of the phosphor is locked in refractories (e.g., Lodders, 2003), making this scenario very unlikely.

We also demonstrate how the accretion of additional solids (see Table 4.4) would enrich the planetary atmosphere with refractories (see the bottom panels of Fig. 4.5), as discussed in Sect. 4.2. We calibrated the amount of additionally accreted solids to match the measure sulfur abundance in the atmospheres of Jupiter and Saturn. This corresponds to an additional amount of 7-11 Earth masses of solids that needs to be accreted. However, it is clear from our simplified model that pebble drift and evaporation is an important ingredient for the volatile content of the atmospheres of Jupiter and Saturn, especially for the nitrogen (and noble gas) content.

6 CONCLUSION

We have studied the influence of pebble evaporation on the atmospheric composition of giant planets. In particular, our simulations show that pebble evaporation results in a significant enhancement of the volatile content in the planetary atmospheres compared to the refractory contents. This is caused by accretion of gas enriched in volatiles due to pebble evaporation, which could also explain the C/H and C/O ratios of τ Boo b (Pelletier et al., 2021). Our exact results depend crucially on the underlying chemical model, which determines how much of a given element is in volatile or refractory form (see Sect. 2); however, independently of the exact chemical model, pebble evaporation plays a crucial role in determining the volatile content in a giant planet's atmosphere.

Our simulations show that the C/O ratio alone might not be enough to constrain the formation history of giant planets, and additional constraints, either from other elements (see also Turrini et al., 2021) or from direct abundances (see also Notsu et al., 2020), are needed. Furthermore, our simulations show that Jupiter's nitrogen enrichment could be caused by the accretion of nitrogen-rich gas, implying that Jupiter did not need to form in the very outer regions of the Solar System as proposed (Öberg & Wordsworth, 2019; Bosman et al., 2019).

If additional solids are added to the planetary atmosphere, the refractory content in the planetary atmosphere increases, reducing the volatile-to-refractory fraction. Our simple model also indicates that the addition of refractory material into Jupiter's atmosphere is needed to match the observational constraints. We note, however, that this is also influenced by our model assumption that does not allow the accretion of refractories during the gas accretion phase. Therefore, our study suggests that a large refractory content in planetary atmospheres might be a sign of additional solid pollution (via planetesimals, giant impacts, or dust transported through meridional flows during the gas-disk phase), as also speculated in (Lothringer et al., 2021). Future observations of giant planet atmospheres could thus help to constrain the efficiency of solid accretion into atmospheres.

ACKNOWLEDGEMENTS

A.D.S and B.B. thank the European Research Council (ERC Starting Grant 757448-PAMDORA) for their financial support. A.D.S. acknowledges funding from the European Union H2020-MSCA-ITN-2019 under Grant no. 860470 (CHAMELEON) and from the Novo Nordisk Foundation Interdisciplinary

Synergy Program grant no. NNF19OC0057374. We thank the anonymous referee for the useful remarks that helped improve the manuscript.

APPENDIX

A DISK

In Fig. 4.6 we show the evolution of a disk with $\alpha = 5 \times 10^{-4}$ and the corresponding C/O ratios for the two different refractory carbon contents used in our model. The overall evolution of the gas and pebble surface densities is very similar compared to our nominal model (Schneider & Bitsch, 2021a), the main difference being the reduction in the pebble pileups at the CO, CH_4, and CO_2 evaporation fronts due to less available CO, CH_4, and CO_2 (Table 4.1). On the other hand, we now observe a larger pebble pileup around the carbon grain evaporation front in the inner disk regions as well as an increased pileup around the water ice line because less oxygen is bound in CO and CO_2, increasing the water abundance.

Comparing the two models, the corresponding C/O ratios in the pebbles and gas phase differ mostly in the inner disk regions. In fact, the C/O of the solids and the gas interior to the water ice line (up until the carbon grains evaporate) is now super-solar and subsolar, respectively, opposite to the nominal model (Schneider & Bitsch, 2021a). This is caused by the fact that now large amounts of carbon grains can exist in the inner disk regions. Furthermore, the large spike in the solid C/O ratio at the methane ice line is significantly reduced due to the lower methane fraction. The evolution of the C/O ratio in time shows the effects described in Schneider & Bitsch (2021a), namely the competition between fast inward drifting pebbles and slow vapor diffusion, resulting in a change in the C/O ratio of solids and gas in time.

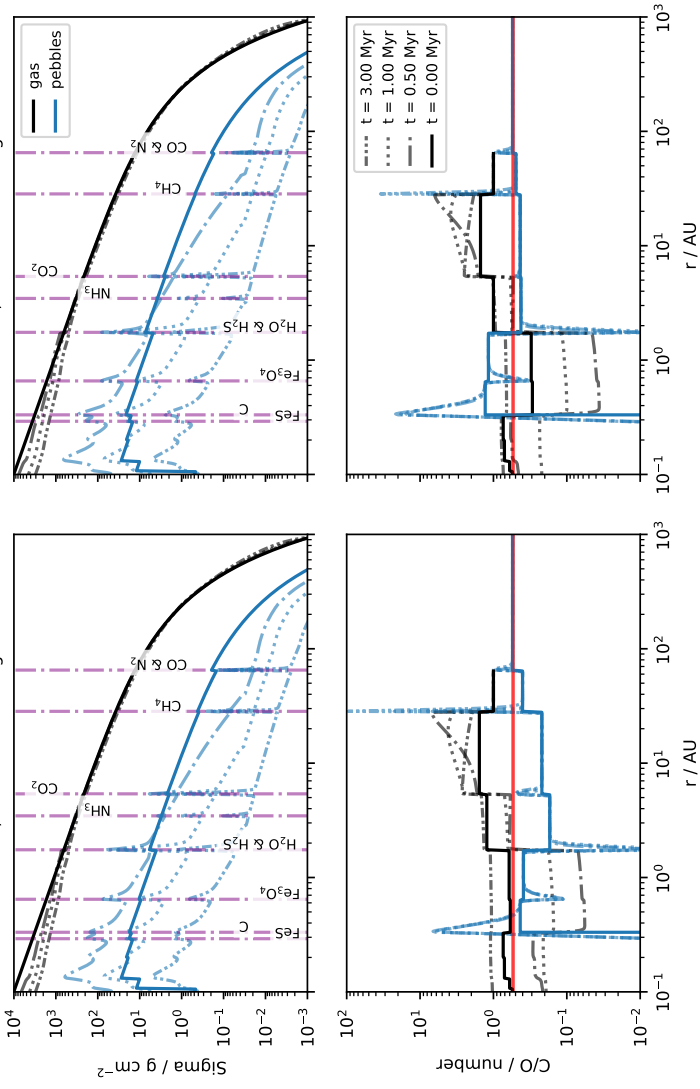

Figure 4.6: Disk evolution (top) for $\alpha = 5 \times 10^{-4}$ and the corresponding C/O ratio in gas and pebbles (bottom). The left panels display models with 20% of the carbon abundance locked in refractory carbon grains, whereas the right panels show models with 60% locked in carbon grains. The red line in the bottom panel marks the solar C/O.

5

HOW DRIFTING AND EVAPORATING PEBBLES SHAPE GIANT PLANETS III: THE FORMATION OF WASP-77A B AND τ BOÖTIS B

Bertram Bitsch, Aaron David Schneider & Laura Kreidberg

Published in Astronomy & Astrophysics, Volume 665, id.A138, September 2022

Author contributions:
Bertram Bitsch designed and lead the study and wrote the manuscript. Aaron Schneider ran the numerical models and created the figures, which are part of the paper. Furthermore, Aaron Schneider contributed to the discussion of the results. Laura Kreidberg contributed to the discussion of the results and the design of the study.

Original Abstract
Atmospheric abundances of exoplanets are thought to constrain the planet formation pathway, because different species evaporate at different temperatures and thus radii in the protoplanetary disc, leaving distinct signatures inside the accreted planetary atmosphere. In particular the planetary C/O ratio is thought to constrain the planet formation pathway, because of the condensation sequence of H_2O, CO_2, CH_4, and CO, resulting in an increase of the gas phase C/O ratio with increasing distance to the host star. Here we use a disc evolution model including pebble growth, drift and evaporation coupled with a planet formation model that includes pebble and gas accretion as well as planet migration to compute the atmospheric compositions of giant planets. We compare our results to the recent observational constraints of the hot Jupiters WASP-77A b and τ Boötis b. WASP-77A b's atmosphere features sub-solar C/H, O/H, H_2O/H with slightly super-solar C/O, while τ Boötis b's atmosphere features super-solar C/H, O/H and C/O with sub-solar H_2O/H. Our simulations qualitatively reproduce these measurements and show that giants like WASP-77A b should start to form beyond the CO_2 evaporation front, while giants like τ Boötis b should originate from beyond the water ice line. Our model allows the formation of sub- and super-solar atmospheric compositions within the same framework. On the other hand, simulations without pebble evaporation, as used in classical models, can not reproduce the super-solar C/H and O/H ratios of τ Boötis b's atmosphere without the additional accretion of solids. Furthermore, we identify the α viscosity parameter of the disc as a key ingredient regarding planetary composition, because the viscosity drives the inward motion of volatile enriched vapor, responsible for the accretion of gaseous carbon and oxygen. Depending on the planet's migration history through the disc across different evaporation fronts, order-of-magnitude differences in atmospheric carbon and oxygen abundance should be expected. Our simulations additionally predict super-solar N/H for τ Boötis b and solar N/H for WASP-77A b. We conclude thus that pebble evaporation is a key ingredient to explain the variety of exoplanet atmospheres, because it can explain both, sub- and super-solar atmospheric abundances.

1 INTRODUCTION

Planet formation models are mostly constrained by the observed mass, radius and orbital distance distributions of exoplanets and their corresponding occurrence rates (e.g. Ida & Lin 2008a; Mordasini et al. 2009; Guilera et al. 2014; Bitsch & Johansen 2017; Ndugu et al. 2018; Mulders et al. 2018; Alessi et al. 2020). However, current and future observations will expand on the constraints on planet formation by adding atmospheric abundances to the data. The link of atmospheric abundances to planet formation models are mostly discussed via the planetary C/O ratio (e.g. Öberg et al. 2011; Madhusudhan et al. 2017; Booth et al. 2017; Cridland et al. 2020; Schneider & Bitsch 2021a; Mollière et al. 2022), which changes with distance to the host star due to condensation of different carbon and oxygen bearing species at different disc temperatures (e.g. H_2O, CO_2, CH_4, CO). Additionally, nitrogen has been discussed as a potential tracer for the formation location of exoplanets (Brogi & Line, 2019; Turrini et al., 2021), but also for Jupiter (Bosman et al., 2019; Öberg & Wordsworth, 2019; Schneider & Bitsch, 2021b).

Detailed observation of atmospheric abundances of exoplanets are still quite rare compared to the bulk of observed exoplanets, but with increasing measurement precision we are beginning to see a diversity in atmospheric properties. Some planets appear to have sub-solar abundances of water (e.g. MacDonald & Madhusudhan 2017; Colón et al. 2020), whereas others are metal-rich (e.g. Wakeford et al. 2018). Even though there is substantial scatter in the mass-atmospheric metallicity relation, there may be an overall tendency for hot Jupiters to be water-poor (Welbanks et al., 2019). On the other hand, it was suggested that the super-stellar alkali metal abundance of some of these hot Jupiters (Welbanks et al., 2019) might be consistent with inward migration and accretion of planetesimals rich in refractories but poor in water ice (Hands & Helled, 2022). However, this process ignores that large amounts of volatiles and even evaporated refractories could be accreted via the gas phase, depending on the migration history of the giant planet (Booth et al., 2017; Schneider & Bitsch, 2021a,b). Additionally Guillot & Hueso (2006) suggested that a large fraction of the heavy element content of giant planets could be accreted at the late stages of the disc evolution, where photoevaporation mainly removes hydrogen and helium from the disc, leading to a natural enrichment of heavy elements. However, a general application of this theory would have difficulties explaining sub-solar compositions. Furthermore, outer giant planets could block inward flowing pebbles, depleting the inner discs of volatiles and pebbles (Morbidelli et al., 2016; Bitsch et al., 2021; Schneider

& Bitsch, 2021a) and thus altering the composition of growing planets (e.g. Bitsch et al. 2021).

Recent observations of exoplanet atmospheres were able to not only constrain single molecules precisely, but also derive C/H, O/H, C/O and H_2O/H within the planetary atmospheres with great precision. Line et al. (2021) observed sub-solar C/H, O/H and H_2O/H with a slightly super-solar C/O in the atmosphere of the 1.8 M_{Jup} inflated (1.2R_{Jup}) hot Jupiter WASP-77A b, orbiting its host star in 1.36 days. In contrast, Pelletier et al. (2021) using SPIRou/CFHT reported super-solar C/H and O/H with slightly super-solar C/O in combination with a sub-solar water abundance in the atmosphere of the 6 Jupiter mass hot Jupiter τ Boötis b, which orbits its host star in 3.3 days. Observing the same planet, Webb et al. (2022) reported a near solar water abundances of the same planet using observations via NIR CARMENES, clearly indicating that the water abundance of τ Boötis b is still debated. We note that these observations pertain to the day side of these planets, implying that the abundances may be affected by disequilibrium processes linked to zonal flows and strong day/night side temperature variations (e.g. Showman & Guillot 2002). Furthermore, interior processes and chemical reactions in the planetary atmosphere might influence the water abundance in the upper atmosphere (e.g. Mollière et al. 2015; Baeyens et al. 2021). As a consequence, it is difficult to draw definite conclusions on planet formation just from the water abundance alone, which is why we mostly rely on C/H and O/H to derive conclusions for our planet formation model.

Even though evidence seems to indicate that the atmospheric abundance is not a tracer of the bulk abundances (e.g Helled et al. 2022; Guillot et al. 2022), also considering recent constraints from Jupiter (Wahl et al., 2017; Vazan et al., 2018; Debras & Chabrier, 2019; Miguel et al., 2022) and Saturn (Mankovich & Fuller, 2021), we nevertheless adopt, for simplicity, the assumption that the atmospheric abundance is a tracer of the bulk abundances. In this work we focus on planet formation simulations in discs governed by pebble growth, drift and evaporation to study the atmospheric abundances of growing and migrating planets. In addition to the orbital parameters and planetary masses, we focus specifically to match the atmospheric constraints of WASP-77A b (Line et al., 2021) and τ Boötis b (Pelletier et al., 2021), because these planets represent the two extreme ends of the exoplanet population: sub- and super-solar abundances, where both extremes have to be matched within the same planet formation scenario. Furthermore their formation is not only constrained through the C/O ratio, but also through C/H, and O/H, not available for most other observed exoplanets, giving the highest level of constraints to planet formation models. In the following we present a planet formation model that

can explain sub- and super-solar atmospheric abundances without invoking the additional accretion of solids into planetary atmospheres, as required by classical models where pebble evaporation is not taken into account (Öberg et al., 2011).

2 PLANETARY GROWTH MODEL

The planet formation model we use is described in detail in Schneider & Bitsch (2021a). In particular the model includes pebble growth and drift (Birnstiel et al., 2012), pebble evaporation and condensation at ice lines (Schneider & Bitsch, 2021a), planet growth via pebble (Johansen & Lambrechts, 2017) and gas accretion (Ndugu et al., 2021) as well as planet migration (Paardekooper et al., 2011; Benítez-Llambay et al., 2015). The initial planetary mass is set by the pebble transition mass, at which the planet starts to accrete efficiently from the Hill regime (Lambrechts & Johansen, 2012). During the build up of the planetary core we attribute 10% of the accreted pebbles to a primordial heavy element atmosphere. The planet switches to gas accretion once it has reached its pebble isolation mass (Lambrechts et al., 2014; Bitsch et al., 2018), at which the planet opens a small gap in the protoplanetary disc, preventing further pebble drift interior to the planet. At this stage the planet can only accrete a gaseous component (incl. H, He and volatiles), but is unable to accrete any solids. This accretion picture is fundamentally different to an accretion scenario including planetesimals, which could still be accreted into planetary atmospheres once the planet starts to accrete an envelope (e.g. Alibert et al. 2018), giving rise to abundance differences in refractories and volatiles in planetary atmospheres (Schneider & Bitsch, 2021b).

In contrast to the classical step-function picture of the gas phase C/O (Öberg et al., 2011), the evaporation of inward drifting pebbles allows more extreme C/O ratios in the gas phase of the disc (e.g. Schneider & Bitsch 2021a), where the C/O ratio over the whole disc radius can vary over a few orders of magnitude depending which carbon or oxygen rich materials evaporate (e.g. the C/O ratio is strongly sub-solar just interior of the water ice line due to the evaporation of water ice) and how fast the vapor moves through the disc. Furthermore, this effect allows super-solar abundances of oxygen and carbon in the gas phase, unachievable in a model without pebble evaporation.

We investigate here the growth and migration of planetary embryos starting at three different locations (3.5, 10 and 30 au) in discs with three different α viscosity parameters ($\alpha = 10^{-4}, 5 \times 10^{-4}, 10^{-3}$). We change the initial planetary positions and α viscosity parameters in section 4. We further assume a solar composition for the different chemical elements (Asplund et al.,

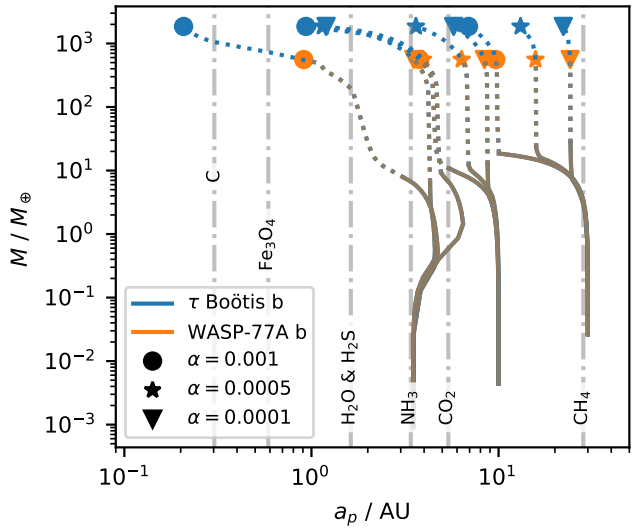

Figure 5.1: Growth tracks of planets starting at different orbital positions in discs with different viscosities (marked by different symbols). The solid lines mark solid accretion, while the dashed lines mark gas accretion. The dots mark the final masses of WASP-77A b (orange) and τ Boötis b (blue). The evaporation lines for different species are shown for $\alpha = 5 \times 10^{-4}$ and their distance to the host star increases with increasing α parameter, but do not evolve in time in our model for simplicity. We note that the growth of the τ Boötis b analogues are a continuation of the growths of the planets resembling WASP-77A b, indicated by a change in color for the corresponding growth tracks. The planetary growth is then stopped once the mass of WASP-77A b or τ Boötis b is reached.

2009) with a solar dust-to-gas ratio ($\epsilon_0 = 0.0124$), motivated by the measured near solar abundances of WASP-77A, (Kolecki & Wang, 2022).

Here we follow a model where 60% of all carbon is locked in refractories (Schneider & Bitsch, 2021b), motivated by ISM carbon abundances (Bergin et al., 2015). As a consequence, 20% of all carbon grains contribute to CO, 10% to CH_4 and 10% to CO_2. We do not include a chemical evolution model because the drift time-scales are shorter than the chemical reaction time-scales (Booth & Ilee, 2019). We note that the chemical composition of the material that the planet accretes depends strongly on the composition of the material in the disc, which is normally assumed to be linked to the stellar abundances. We will investigate the effects of varying stellar abundances on planetary compositions in a future work. We use the standard disc parameters from our previous simulations (Schneider & Bitsch, 2021a,b), shown in Table 5.1 and discussed in appendix A.

In Fig. 5.1 we show the growth tracks of nine planets in their corresponding discs with varying α and initial orbital position. The planetary growth and migration is strongly influenced by the disc's viscosity, because the viscosity sets the migration rate and when the planets are able to open gaps[1] (Crida & Morbidelli, 2007). Additionally the viscosity sets the gas accretion rates once the gap is opened and the planet can only accrete what the disc can provide (Bergez-Casalou et al., 2020; Ndugu et al., 2021). As a result planets in discs with higher viscosities grow larger and migrate more compared to their counterparts in discs with lower viscosities. The initial outward migration of the planets starting at 3.5 au is driven by the heating torque, which acts efficiently due to the fast accretion of pebbles (Benítez-Llambay et al., 2015; Baumann & Bitsch, 2020). During their migration, the planets cross different evaporation fronts and can then start to accrete the corresponding evaporated material with the gas.

Starting from a given orbtial position we integrate until the final planetary masses of WASP-77A b and τ Boötis b have been reached. We make the assumption that the protoplanetary disc dissipates once the final planetary mass has been reached. This implies that the formation of τ Boötis b takes longer than the formation of WASP-77A b, because τ Boötis b needs to accrete more material. This results in typical disc lifetimes between 1.5 to 4 Myr, depending on the planet and on the disc's viscosity (see above).

1 Lower viscosities allow early gap opening, resulting in an earlier transition to the viscously driven type-II migration regime.

3 ATMOSPHERIC ABUNDANCES OF GIANT PLANETS

In Fig. 5.2 we show the atmospheric abundances of the planets shown in Fig. 5.1. In particular we focus on C, O, N as well as on the C/O and the water abundance in the planetary atmospheres, even though our simulations also track other elements (Schneider & Bitsch, 2021a,b). We particularly include the water abundances, because observations seems to indicate that hot Jupiters harbor tendentially a sub-solar water abundance (Welbanks et al., 2019). The water abundance in Fig. 5.2 has been calculated using the chemical equilibrium interpolator of petitRADTRANS (Mollière et al., 2020), which determines the chemical abundances assuming that the atmosphere is in chemical equilibrium. The water abundance in such a model is then only dependent on the temperature, the pressure and the elemental composition of the planet. We calculate the water abundances of τ Boötis b and WASP-77A b by using an average over a pressure range from 10^{-4} to 10 bar. For the temperature, we assume that both planets are on tidally locked orbits with a_p = 0.024 au and a_p = 0.046 au for WASP-77A b and τ Boötis b respectively, leading to equilibrium temperatures of 2366K and 2314K respectively. Using the double gray analytical pressure-temperature profile of Guillot (2010) with an interior temperature of T_{int} = 200K, an infrared opacity of $\kappa_{IR} = 0.01$ cm^2/g and an optical opacity of $\kappa_{vis} = 0.004$ cm^2/g, we obtain (for reference) a temperature at 10^{-3} bar of 2145K and 2097K for WASP-77b and τ Boötis b respectively. The elemental composition which is used to calculate the water abundance with the chemical equilibrium code is consistently inferred from the C/O ratio and the heavy element content of the atmospheres in our planet formation models. We discuss how the lack of pebble evaporation would influence the planetary compositions in Appendix B.

Within our simulations, some very clear trends emerge. Planets accreting most of their material in the inner disc region, have super-solar C/H and O/H values, mostly due to the accretion of water and carbon grain vapor, which enriches the gas to super-solar values (in contrast to simulations without pebble evaporation, see Appendix B). Planets migrating interior to the water ice line feature super-solar water abundances, explaining the large water abundances of some observed giant exoplanets without any problems (Wakeford et al., 2018). However further inward migration across the carbon grain evaporation line increases the planetary C/O, preventing efficient water formation in the atmosphere. The increase of the planetary C/H in the inner disc, strongly depends on the amount of carbon grains in the disc.

Planets staying mostly in the outer disc harbor lower C/H and O/H values, which can even be sub-solar, especially if the planets do not migrate across

the CO_2 or H_2O ice lines[2]. As a consequence, these planets accrete mostly CO and CH_4 gas (besides N_2), resulting in super-solar C/O ratios. Only once the planets migrate across the CO_2 ice line is a sub-solar C/O ratio possible. Additionally, these outer planets all feature a sub-solar water abundance in their atmosphere, in line with observed exoplanets (Welbanks et al., 2019). These exoplanets could form in the outer disc and then be scattered inwards, where they are observed now.

Our simulations predict solar to super-solar nitrogen contents in the giant planets, where the nitrogen content is larger if planets migrate across the NH_3 evaporation front. The simulation that matches the C/H and O/H for τ Boötis b best ($a_P = 3.5$ au, $\alpha = 10^{-4}$), features an N/H content with a similar level of enrichment. In contrast, the simulations that matches C/H and O/H of WASP-77A b best ($a_P = 10$ au, $\alpha = 10^{-4}$ or $\alpha = 5 \times 10^{-4}$), feature solar N/H. The results for the simulations with different viscosities are similar because both WASP-77A b analogues do not migrate across the CO_2 evaporation front.

4 INFLUENCE OF THE DISC'S VISCOSITY

The viscosity in the protoplanetary disc determines the disc's evolution (Lynden-Bell & Pringle, 1974), but it is also important for the composition of planetary atmospheres, because the viscosity sets how fast the vapor, originating from evaporating pebbles, can move inwards. For example, at low viscosity, the CO and CH_4 vapor released at their specific evaporation front will only reach the inner edge of the disc at very late times, while this vapor will reach the inner disc regions within a Myr at high viscosity (Schneider & Bitsch, 2021a).

To stress the importance of the viscosity on the atmospheric abundances, we show in Fig. 5.3 the atmospheric abundances of planets growing in our model at different initial positions in disc's with different α-viscosity parameter, ranging from 5×10^{-5} to 5×10^{-3}. We show the atmospheric C/O, C/H and O/H of these planets after 3 Myr of disc evolution. As the final planetary masses of the planets in these simulations do not match those of WASP-77A b and τ Boötis b, we do not mark the atmospheric constraints for these planets in Fig. 5.3.

Our simulations clearly show a dependency of the atmospheric composition on the disc's viscosity, in contrast to earlier models without pebble evaporation

2 Migration across the water evaporation front does not immediately imply an efficient accretion of water vapor, because the pebbles are trapped in the pressure bump exterior to the planet and can only evaporate once the planet migrated far enough that the pebbles in the pressure bump can evaporate.

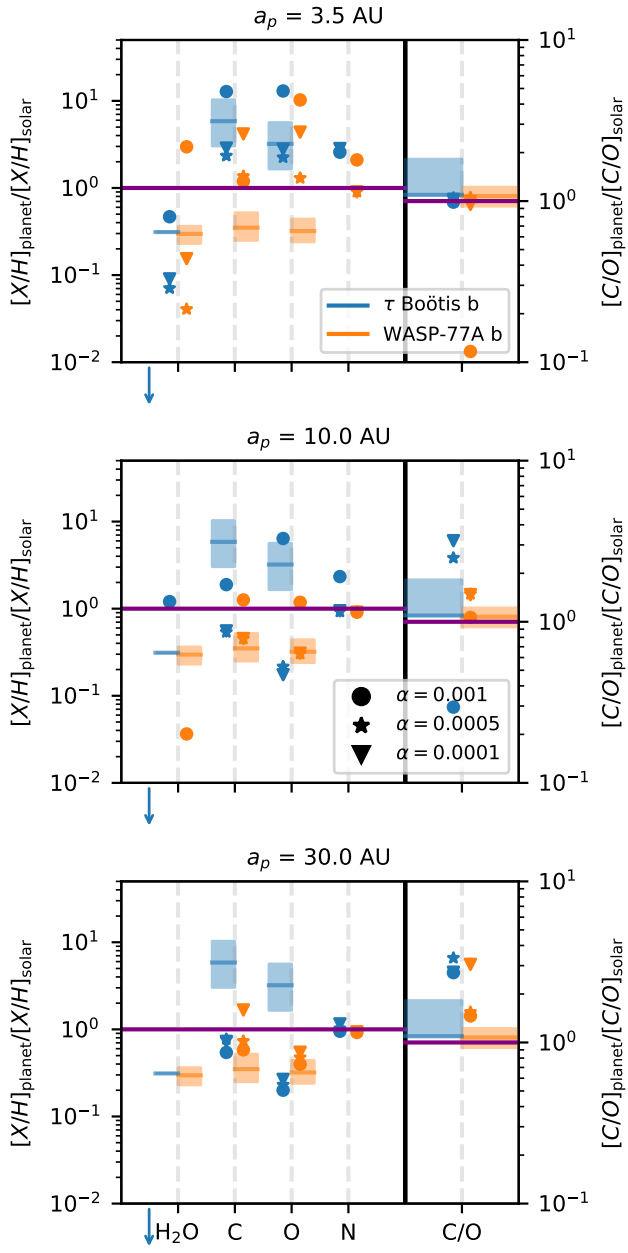

Figure 5.2: Atmospheric abundances of volatiles normed to solar for the different planets shown in Fig. 5.1 at the end of their evolution. The initial planetary position increases from top to bottom. The colors mark the different planets, while the different symbols mark the different levels of viscosity. The orange bands mark the measured atmospheric abundances of WASP-77A b (Line et al., 2021), while the blue band marks the constraints for τ Boötis b, where H_2O/H is less than 10^{-2} (Pelletier et al., 2021), as indicated by the blue arrow. The slightly sub-solar water measurements of Webb et al. (2022) are marked with the horizontal blue bar. Some of our simulations feature water abundances below 10^{-2} and are thus not shown in the figure. Please note the different scale for C/O.

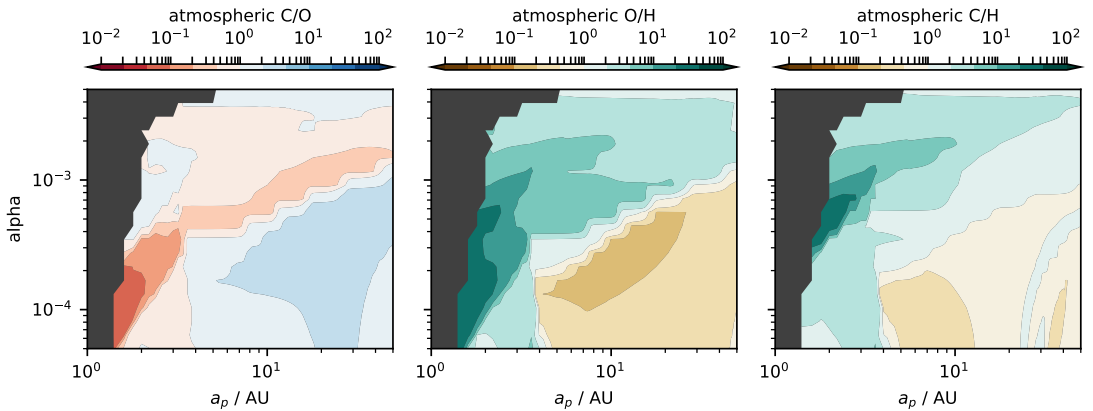

Figure 5.3: Atmospheric C/O, O/H and C/H of planets forming in discs with different α-viscosity at different initial positions after 3 Myr of evolution. The dark regions correspond to planets that have not reached masses above 100 Earth masses. We note that planets growing in discs with higher viscosities migrate farther and are generally more massive than planets growing in discs with lower viscosities (Schneider & Bitsch, 2021a).

(Öberg et al., 2011)). In particular sub-solar O/H and C/H atmospheric values are only possible in the outer disc regions at low viscosities ($\alpha \leqslant 10^{-3}$). On the other hand, super solar C/H and O/H ratios are possible in the outer disc at higher viscosities due to the more efficient inward diffusion of CO and CH_4 gas. In the inner disc regions, super-solar values of C/H and O/H are easily possible, especially interior to the CO_2 and H_2O evaporation fronts. Here the exact value of the C/H and O/H ratio also depends on the disc's viscosity, where larger O/H values are possible at lower viscosity, because the smaller viscosity prevents efficient removal of the water vapor (see Schneider & Bitsch 2021a for a discussion on the disc's water content).

The atmospheric C/O ratio reveals the already established trends from simpler models without evaporation (Öberg et al., 2011; Madhusudhan et al., 2017) that the atmospheric C/O increases with increasing distance to the central star at low viscosity. However, the evaporation of inward drifting pebbles allows more extreme C/O ratios compared to the simple model (see also Appendix B), where C/O ratios below 0.1 and above 4-5 are possible if evaporation is included. However the parameter space for these extreme values is limited to low viscosities, where the initial pile-up of vapor is larger (Schneider & Bitsch, 2021a).

5 MODEL LIMITATIONS

Recent advances in high resolution observations have enabled precise constraints on the abundances of both carbon- and oxygen-bearing molecules (e.g. Brewer et al. 2017; Welbanks et al. 2019; Giacobbe et al. 2021; Pelletier et al. 2021; Line et al. 2021). Here we explore the success of our model in explaining the measured abundances for two case studies: WASP-77A b (Line et al., 2021) and τ Boötis b (Pelletier et al., 2021). In Fig. 5.2 we show the abundances constraints from WASP-77A b and τ Boötis b, where our model is able to qualitatively reproduce these very different abundance measurements, especially in low viscosity environments.

Our model is able to produce sub-solar C/H and O/H ratios with a nearly solar C/O ratio for planets forming completely exterior to the CO_2 evaporation front in line with the observed abundances of WASP-77A b (Line et al., 2021). The inferred super-solar abundances of τ Boötis b (Pelletier et al., 2021) are also reproduced in our model, but they require a formation/migration interior to the CO_2 evaporation line, indicating a formation closer to the host star. We stress that our formation scenario is only based on the constraints of C/H, O/H and C/O and not on the water abundances itself, because it is not very

well constraint at this point (Pelletier et al., 2021; Webb et al., 2022) and can also be influenced by interior processes.

The main assumption of our model is that we can use the atmospheric abundances as a trace of the bulk abundances of the giant planets. However, this assumption is certainly under debate (Helled et al., 2022; Guillot et al., 2022). If compositional gradients inside of the planet exist, then the atmospheric abundances only represent the minimum abundance of a specific chemical element. Future simulations dedicated to link atmospheric abundances to planet formation need to take detailed interior models into account.

Our planet formation model is of course simplified in many aspects that can influence the planetary abundances, e.g. scattering of small dust grains from the outer gap edges into the planetary feeding zone (Bi et al., 2021; Binkert et al., 2021) or the accretion of smaller pebble sizes once the core has reached the pebble isolation mass for the dominant pebble size (Andama et al., 2022), as well as further planetesimal bombardment (e.g. Hands & Helled 2022). We also do not include a realistic photoevaporation procedure, which could allow the enhancement of the heavy elements in the disc midplane due to the loss of hydrogen and helium from the disc's upper layers, consequently enriching the gaseous component accreted by the planet resulting in super-solar abundances (Guillot & Hueso, 2006). In our model, we also do not include the chemical evolution of the gas disc, which can transform the main oxygen and carbon carriers, which also depend on the C/O ratio of the disc (Eistrup et al., 2016), emphasizing the need to constrain stellar abundances to constrain planet formation (Reggiani et al., 2022). For a detailed discussion about limitations of planet formation simulations with respect to atmospheric constraints, see also Mollière et al. 2022.

Our model implicitly implies that WASP-77A b and τ Boötis b formed further away from their host star and were then scattered inwards. While these scattering events are possible (e.g. Jurić & Tremaine 2008; Ford & Rasio 2008; Raymond et al. 2009a; Sotiriadis et al. 2017; Bitsch et al. 2020), it implies that other perturbers in the disc are present. These perturbers could either block inward drifting pebbles, thus influencing planetary growth (e.g. Morbidelli et al. 2015; Bitsch et al. 2019), and can also have dramatic consequences for the composition of the available solids (e.g. Morbidelli et al. 2016) and gases (Bitsch et al., 2021; Schneider & Bitsch, 2021a), requiring a combination of N-body simulations with our here presented planet formation framework to further constrain the formation pathway.

6 SUMMARY AND CONCLUSIONS

In this study we simulated the growth and migration of planetary embryos to gas giants in discs with different α-viscosities to derive their atmospheric abundances. The atmospheric abundances are crucially influenced by the planet's formation location and migration history (e.g. Öberg et al. 2011; Madhusudhan et al. 2017; Schneider & Bitsch 2021a). In line with these studies, our model shows that the atmospheric C/O increases and the corresponding C/H and O/H decrease with increasing planetary formation location. Our results and conclusions apply under the assumption that the atmospheric composition is a tracer of the bulk composition (but see Helled et al. 2022; Guillot et al. 2022).

Our simulations can explain the observed sub-solar water content of giant planets[3], if the planets form exterior to the water ice line or only migrate across the water ice line very late. On the other hand, planets migrating across the water ice line early feature super-solar water contents, in line with some observed exoplanets as well (Wakeford et al., 2018). The water content of exoplanets, however, needs to be constrainted much better in the future via observations, which show a large range in the water abundance of τ Boötis b (Pelletier et al., 2021; Webb et al., 2022). If planets form exterior to the CO_2 evaporation front and only cross the CO_2 evaporation front very late in their evolution, our model can reproduce the measured sub-solar C/H and O/H in combination with around solar C/O ratios of WASP-77A b (Line et al., 2021).

Furthermore our model shows that super-solar C/H and O/H ratios are possible when pebble evaporation is taken into account, allowing a match to the atmospheric measurements of τ Boötis b (Pelletier et al., 2021), if the planet formed exterior to the water evaporation front. This is in contrast to models without pebble evaporation (see appendix B), changing the picture put forward by Öberg et al. (2011), where super-solar C/H and O/H ratios in planetary atmospheres are only possible with additional solid accretion[4].

The effect of pebble evaporation thus allows the formation of planetary atmospheres with sub- and super-solar C/H and O/H. Consequently, our model can match the sub-solar abundances of WASP-77A b (Line et al., 2021) and the super-solar abundances of τ Boötis b (Pelletier et al., 2021), without invoking additional solid accretion for only one of the planets, making our model more general applicable.

3 Other planets can also influence the water abundance in the disc, see Bitsch et al. (2021) and Schneider & Bitsch (2021a).

4 This would also enhance the refractory content of giant planet atmospheres, leaving observable signatures (Schneider & Bitsch, 2021b).

Our study further emphasizes that nitrogen could be used as a tracer for the planet formation location (Turrini et al., 2021; Schneider & Bitsch, 2021b). This is mostly related to its different chemistry and that most of the nitrogen is stored in the super-volatile N_2 component ($T_{evap} = 20K$), reducing the complexity compared to carbon and oxygen bearing molecules. Our model predicts that τ Boötis b should harbor a super-solar nitrogen abundance, while WASP-77A b's atmosphere should be around solar in nitrogen (Fig. 5.2).

Our simulations also show that the effect of pebble evaporation on the composition of planetary atmospheres crucially depends on the disc's viscosity (Fig. 5.3). Especially at low viscosities more extreme sub- and super-solar C/H and O/H ratios are possible, due to the pile-up of evaporated material close to the evaporation fronts (Schneider & Bitsch, 2021a), which is diluted faster at higher viscosity. This clearly shows that the α viscosity does not only play a crucial role for planet formation in itself, but also for the atmospheric abundances of planets and allows for a wide range of atmospheric abundances. Furthermore our model implies that a great diversity in atmospheric compositions of hot Jupiters should be expected naturally from their different formation pathways.

ACKNOWLEDGEMENTS

B.B., acknowledges the support of the European Research Council (ERC Starting Grant 757448-PAMDORA) and of the DFG priority program SPP 1992 "Exploring the Diversity of Extrasolar Planets (BI 1880/3-1). A.D.S. acknowledges funding from the European Union H2020-MSCA-ITN-2019 under Grant no. 860470 (CHAMELEON). We thank the referee Tristan Guillot for his comments that helped to improve our manuscript.

APPENDIX

A MODEL PARAMETERS

We show in Table 5.1 the model parameters used in our study. While we vary the initial planet position and disc viscosity in Section 4, we keep the other parameters the same. Our model assumes a solar composition of the different initial elemental ratios. We integrate the disc's lifetime until the growing planets have reached the planetary masses of WASP-77A b and τ Boötis b. This approach implies that the disc conveniently disappears when the final planetary masses are reached and implies a varying disc lifetime depending on the planetary mass that needs to be reached and on the disc's viscosity, because giants grow faster in high viscosity environments. The disc's lifetimes thus vary between 1.5 Myr to 4 Myr. For Fig. 5.3 we use a fixed lifetime of 3 Myr.

B MODELS WITHOUT PEBBLE EVAPORATION

Our main model includes the evaporation of inward drifting pebbles that cross ice lines. Here we investigate how the atmospheric composition of planets changes, if the evaporation of inward drifting pebbles is not taken into account. We note that this does not influence the growth and migration of the growing planets (Schneider & Bitsch, 2021a).

In Fig. 5.4 we present the atmospheric composition of planets starting at 3.5, 10 and 30 au in discs with different viscosities without taking the evaporation of pebbles into account (compared to Fig. 5.2, where evaporation is taken into account). As expected from previous models (Öberg et al., 2011), super-solar C/H, O/H and N/H ratios can not be achieved by gas accretion alone, failing to reproduce the atmospheric constraints of τ Boötis b (Pelletier et al., 2021). Without the contribution of pebble evaporation, super-solar C/H and O/H values can only be achieved if the planet further accretes solids (e.g. planetesimals). This implies that τ Boötis b would need to accrete further solids to explain its super-solar abundance in contrast to WASP-77A b, opening the question why planetesimal accretion should only be efficient in certain cases. We observe the same effect for the nitrogen abundance, where all planets feature around solar N/H, because the planets migrate

Table 5.1: Parameters used throughout this paper.

Quantity	Value
$a_{p,0}$	(3.5,10,30) au
t_0	0.05 Myr
κ_{env}	$0.05 cm^2/g$

(a) Planet

Quantity	Value
r_{in}	0.1 au
r_{out}	1000 au
N_{Grid}	500

(b) Grid

Quantity	Value
α	$(1, 5, 10) \times 10^{-4}$
α_z	10^{-4}
M_0	0.128 $M_\odot$
R_0	137 au
[Fe/H]	0.0
t_{evap}	3 Myr
ϵ_0	1.24%
u_{frag}	5 m/s

(c) Disc

Notes: Parameters used for the initialization of `chemcomp` that are used throughout this paper, divided into planetary, numerical and disc parameters. The detailed explanation of these parameters can be found in Schneider & Bitsch (2021a).

across the NH_3 evaporation front (where then all nitrogen is in a gaseous component), except if they form in outer regions in low viscosity discs, where 90% of the nitrogen is in gaseous form. All planets formed in this scenario feature extremely sub-solar water abundances, which could be in line with the measurements of Pelletier et al. (2021) for τ Boötis b, but are in disagreement with the measurements of Webb et al. (2022) for the same planet. However, our formation constraints are derived only from C/H, O/H and C/O, because the water abundances is also heavily influenced by interior processes, not studied in detail in this work.

In contrast, the C/O ratio of the planets can become super-solar, if the planets form exterior to the water ice line. In fact, the model without evaporation allows a match to the atmospheric constraints of WASP-77A b, which feature sub-solar C/H and O/H ratios (Line et al., 2021), leading already to the conclusion that WASP-77A b formed exterior to the water ice line. However, from this model it is unclear how far away from the water ice line WASP-77A b should have formed, giving limited constraints to planet formation (Fig. 5.4). The recent study by Reggiani et al. (2022) concluded also that WASP-77A b should form beyond the water ice line, but their model does not include pebble evaporation as well. In contrast, if pebble evaporation is included a formation beyond the CO_2 snow line is needed, because otherwise too much carbon might be accreted (see Fig. 5.2 and Fig. 5.3).

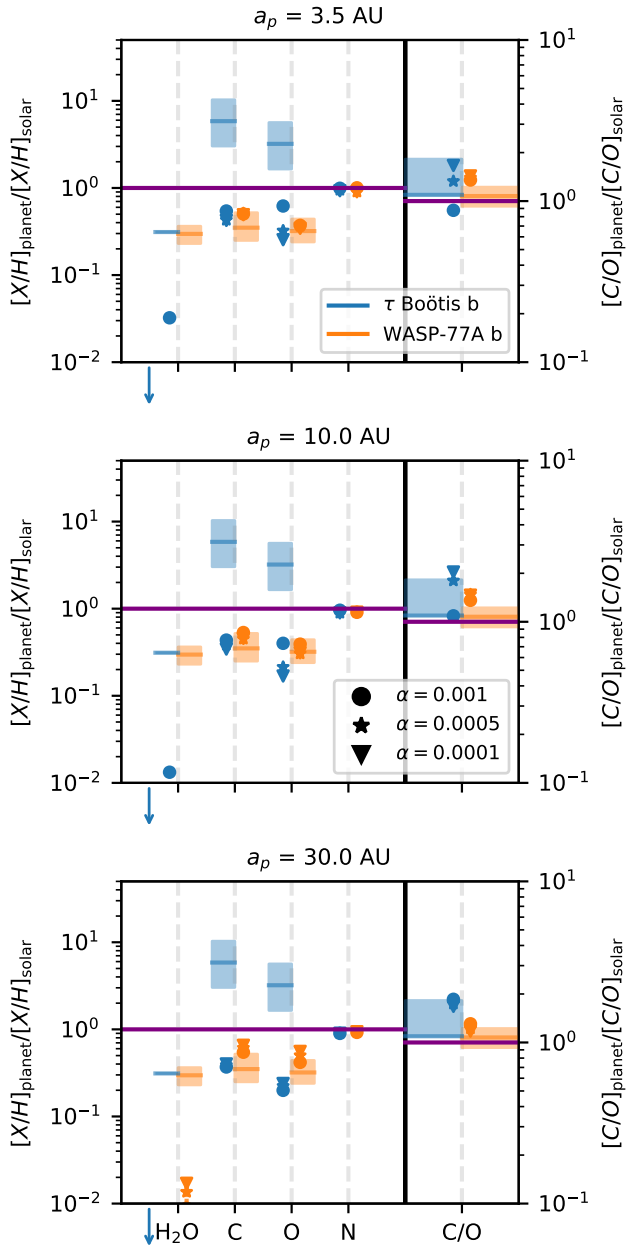

Figure 5.4: Atmospheric C/H, O/H, N/H, C/O and H_2O/H content of planets forming at 3.5, 10 and 30 au in discs with different viscosities. Symbols and color codings are as in Fig. 5.2. We do not take evaporation of inward drifting pebbles into account, in contrast to Fig. 5.2, resulting in generally sub-solar abundances.

6

EXPLORING THE DEEP ATMOSPHERES OF HD 209458B AND WASP-43B USING A NON-GRAY GENERAL CIRCULATION MODEL

Aaron David Schneider, Ludmila Carone, Leen Decin, Uffe Gråe Jørgensen, Paul Mollière, Robin Baeyens, Sven Kiefer & Christiane Helling

Published in Astronomy & Astrophysics, Volume 664, id.A56, August 2022

Author contributions:
Aaron Schneider wrote the manuscript, developed the extensions to the climate model as described in the paper. Ludmila Carone, Leen Decin and Uffe Gråe Jørgensen supervised Aaron Schneider and contributed to the manuscript and discussion of the results. Paul Mollière developed the radiative transfer tools, on which the radiative transfer extension to the climate model bases. Furthermore, Paul Mollière supervised the development of the extension. Robin Baeyens performed comparisons between the full radiative forcing and a simplified forcing and wrote Appendix D. Sven Kiefer contributed to the discussion of the results and helped in particular with Appendix A. Christiane Helling supplied feedback to the manuscript.

Original Abstract
Simulations with a 3D general circulation model (GCM) suggest that one potential driver behind the observed radius inflation in hot Jupiters may be the downward advection of energy from the highly irradiated photosphere into the deeper layers. Here, we compare dynamical heat transport within the non-inflated hot Jupiter WASP-43b and the canonical inflated hot Jupiter HD 209458b, with similar effective temperatures. We investigate to what extent the radiatively driven heating and cooling in the photosphere (at pressures smaller than 1 bar) influence the deeper temperature profile (at pressures between 1 to 700 bar). Our simulations with the new non-gray 3D radiation-hydrodynamical model `expeRT/MITgcm` show that the deep temperature profile of WASP-43b is associated with a relatively cold adiabat. The deep layers of HD 209458b, however, do not converge and remain nearly unchanged regardless of whether a cold or a hot initial state is used. Furthermore, we show that different flow structures in the deep atmospheric layers arise. There, we find that WASP-43b exhibits a deep equatorial jet, driven by the relatively fast tidally locked rotation of this planet (0.81 days), as compared to HD 209458b (3.47 days). However, by comparing simulations with different rotation periods, we find that the resulting flow structures only marginally influence the temperature evolution in the deep atmosphere, which is almost completely dominated by radiative heating and cooling. Furthermore, we find that the evolution of deeper layers can influence the 3D temperature structure in the photosphere of WASP-43b. Thus, dayside emission spectra of WASP-43b may shed more light onto the dynamical processes occurring at greater depths.

1 INTRODUCTION

The *James Webb Space Telescope* (JWST) is set to reveal data of unprecedented quality for several hot to ultra-hot Jupiters. Thanks to their inflated structure and hotter emission temperatures, these bodies are the easiest to observe, making them prime targets for further characterization. Furthermore, JWST observations may even yield insights into one of the long-standing mysteries in exoplanet science, which asks why many of the hot to ultra-hot Jupiters have large radii of $1.5 R_{Jup}$ (inflated), while others have compact atmospheres (not inflated).

A number of processes have been proposed to explain hot Jupiter inflation, including a reduction in the cooling efficiency or injection of additional energy into the interior. However, mechanisms that reduce the cooling of exoplanets fail to maintain inflated radii over timescales of billion years (see the reviews of Zhang, 2020; Fortney et al., 2021). Recent studies have disfavored the reduced cooling hypothesis and point, rather, to the injection of stellar energy into the interior as a viable explanation. Examples include evidence of re-inflation in two close-in hot Jupiters as a result of their receiving more irradiation from their host stars during the course of their evolution (Hartman et al., 2016) as well as a correlation between the amount of radius inflation and incident stellar flux (Thorngren & Fortney, 2018; Thorngren et al., 2019).

There are currently two favored processes for energy injection as an explanation for hot Jupiter inflation: a) Ohmic dissipation as initially proposed by Batygin & Stevenson (2010), where partially ionized wind flows are coupled with the planetary magnetic field, releasing heat in the interior; and b) dynamical downward energy transport from the irradiated atmosphere into deeper layers (Tremblin et al., 2017; Sainsbury-Martinez et al., 2019, 2021). In this study, we focus on the latter mechanism.

Understanding the vertical transport of stellar energy from irradiated atmospheres into deeper layers is computationally challenging as it requires investigating the temperature and the dynamical evolution of atmospheric layers below the observable photosphere (pressures much larger than 1 bar) with large runtimes of $\gg$ 10000 simulation days (Mayne et al., 2019; Mendonça, 2020; Wang & Wordsworth, 2020). Recent studies have tried to tackle this computational issue by invoking additional assumptions at greater depths or by using a simplified radiative transfer treatment (e.g., Tremblin et al., 2017; Mayne et al., 2017; Mendonça, 2020; Carone et al., 2020; Sainsbury-Martinez et al., 2019, 2021).

Mendonça (2020) performed a detailed analysis of angular momentum and heat transport using a Fourier decomposition of the angular momentum transport. The author found that the mean circulation deposits heat from the upper atmosphere into the deeper layers, where he concludes that additional energy sources are needed to explain the radius inflation. Using much longer integration times and a parametric radiative transfer scheme without heating in the deep atmosphere, Sainsbury-Martinez et al. (2019) instead found that radius inflation can be explained by dynamical heat transport if the deep atmosphere is not heated by irradiation. Both of these studies, along with that of Showman et al. (2020), offer the conclusion that a self-consistent radiative transfer treatment is needed for the investigation of the deep layers to further quantify the coupling of the upper and lower atmospheres. Thus, there is

a clear need for an efficient coupling mechanism between hydrodynamics and radiative transfer that is capable of monitoring deep processes over long simulation runtimes. We thus present `expeRT/MITgcm`[1], a fast and versatile radiative transfer scheme coupled with the 3D hydrodynamical code `MITgcm`.

The implementation of `expeRT/MITgcm` is described in Sect. 2. We apply the model to the exoplanets HD 209458b and WASP-43b in Section 3 and we explore the influence of layers deeper than 1 bar on the 3D thermal structure. HD 209458b is a well-observed and frequently modeled hot Jupiter, and WASP-43b is a JWST early release science target (ERS) (Venot et al., 2020; Bean et al., 2018). More crucially, despite having similar effective temperatures between $1400 - 1500$ K, the first planet is inflated, whereas the latter is not (e.g., Helling et al., 2021a, Table 1 and Figure 1). We compare the behavior of the temperature convergence of WASP-43b and HD 209458b in the deep atmosphere in Sect. 4. We show the emission and transmission spectra for WASP-43b and HD 209458b in Sect. 5. We discuss in Sect. 6 the need for GCMs that are capable of tackling different complex processes in hot Jupiters. Finally, we provide a summary and conclusion in Sect. 7.

2 METHODS

In this section, we describe the implementation of radiative transfer into `expeRT/MITgcm`. We first describe the general circulation model in Sect. 2.1 which is followed by a description of the radiative transfer extension introduced in this work (Sect. 2.2). The initialization of our simulations is discussed in Sect. 2.3.

2.1 *Dynamical core set-up*

General circulation models (GCMs) are numerical frameworks that solve a (sub)set of the 3D equations of hydrodynamics on a rotating sphere. We integrated `expeRT/MITgcm` with the deep wind GCM framework introduced in Carone et al. (2020), which uses the dynamical core of the `MITgcm` (Adcroft et al., 2004). The `MITgcm` uses an Arakawa C type cubedsphere grid with resolution C32[2] to solve the 3D hydrostatic primitive equations (see e.g., Showman et al., 2009, Eqs. 1-5) assuming an ideal gas. We used the C32 grid with 24 cores in MPI multiprocessing, resulting in four 16x16 tiles for each of the six cubedsphere faces. As in Showman et al. (2009), we applied a fourth-order Shapiro filter with $\tau_{\rm shap} = 25$ s to smooth horizontal grid-scale

1 `expeRT/MITgcm` is an extension of the `exorad/MITgcm` scheme established in Carone et al. (2020).
2 C32 is comparable to a resolution of 128 x 64 in longitude and latitude.

noise. The use of such smoothing schemes is common in GCMs, but may have a severe impact on atmospheric flows. We refer to Heng et al. (2011b); Skinner & Cho (2021) for a discussion on the impact of smoothing schemes. Our vertical grid uses 41 logarithmically spaced grid cells between 1×10^{-5} bar and 100 bar. We extended the logarithmic domain by six linearly spaced grid cells between 100 bar and 700 bar in order to avoid a large spacing in the deep atmosphere.

We stabilized our model against nonphysical gravity waves by using a "soft" sponge layer that is similar to the one used in THOR (Mendonça et al., 2018b; Deitrick et al., 2020). The zonal horizontal velocity u [m s^{-1}] is damped by a Rayleigh friction term towards its longitudinal mean $\bar{u}$ [m s^{-1}] via:

$$\frac{du}{dt} = -\tilde{k}_{top}(u - \bar{u}), \tag{6.1}$$

where t [s] is the time and $\tilde{k}_{top}$ [s^{-1}] is the strength of the opposed friction and is calculated as a function of pressure p [Pa] by

$$\tilde{k}_{top}(p) = k_{top} \cdot \max\left[0, 1 - \left(\frac{p}{p_{sponge}}\right)^2\right]^2. \tag{6.2}$$

The fudge parameters p_{sponge} [Pa] and k_{top} [s^{-1}] are used to control the position and the strength of the opposed Rayleigh friction. Throughout this paper, we use $k_{top} = 20\,\mathrm{d}^{-1}$ and $p_{sponge} = 1 \times 10^{-4}$ bar, which results in a friction term that slowly increases in strength for $p \leqslant 1 \times 10^{-4}$ bar. We want to note here that we calculate Eq. 6.1 by deprojecting the cubed sphere grid onto its geographic direction, averaging the deprojected u over 20 latitudinal bins and projecting the resulting $\bar{u}$ on the cubedsphere grid.

To parametrize the deep magnetic drag and to stabilize the lower boundary, we followed Carone et al. (2020). We imposed additional Rayleigh friction to the winds in the deep layers ($p \geqslant 490$ bar). Within these layers we damp the zonal velocity u [m s^{-1}] and meridional velocity v [m s^{-1}] by

$$\frac{du}{dt} = -\frac{u}{\tilde{\tau}_{deep}}, \quad \frac{dv}{dt} = -\frac{v}{\tilde{\tau}_{deep}}, \tag{6.3}$$

where we set the strength of the drag $\tilde{\tau}_{deep}$ [s] as

$$\tilde{\tau}_{deep} = \tau_{deep} \max\left(0, \frac{p - 490\,\mathrm{bar}}{700\,\mathrm{bar} - 490\,\mathrm{bar}}\right). \tag{6.4}$$

We used the same parameters as in Carone et al. (2020) and set $\tau_{deep} = 1$ d. Carone et al. (2020) showed that these measures are important for maintaining

numerical stability and to prevent nonphysical boundary effects for WASP-43b. These authors found that models with and without the deep drag yield small differences and only in the temperature and dynamics.

We did not use a convective adjustment scheme to model convection on a subgrid scale (e.g., Deitrick et al., 2020; Lee et al., 2021) because we are explicitly interested in the formation and stability of a deep adiabat by vertical heat-transport. Sainsbury-Martinez et al. (2019) argued that such a deep adiabat should form due to the absence of radiative heating and cooling at layers higher up in the atmosphere compared to layers where the atmosphere would become unstable to convection according to the Schwarzschild criterion.

The gas temperature T [K] of an ideal gas relates the density with the pressure and therefore ultimately determines the dynamics. `MITgcm` treats the temperature by means of the potential temperature, Θ [K], which is given by

$$\Theta = T \left(\frac{p_0}{p} \right)^{R/c_p}, \tag{6.5}$$

where c_p [$J\,kg^{-1}\,K^{-1}$] is the heat capacity at constant pressure, p_0 [Pa] is the pressure at the bottom of the computational domain, and R [$J\,kg^{-1}\,K^{-1}$] is the specific gas constant. The potential temperature Θ is then forced using the thermodynamic energy equation (e.g., Showman et al., 2009):

$$\frac{d\Theta}{dt} = \frac{\Theta}{T} \frac{q}{c_p}, \tag{6.6}$$

where q [$W\,kg^{-1}$] is the heating rate. The heating rate q is given by

$$q = g \frac{\partial F^{net}}{\partial p}, \tag{6.7}$$

where g [$m\,s^{-2}$] is the gravity and F^{net} [$W\,m^{-2}$] is the net radiative flux. We note that this approach towards radiative heating and cooling is not necessarily flux conserving, yielding the possibility of net cooling or heating of the planet.

2.2 *Radiative transfer*

We used the Feautrier method (Feautrier, 1964) in combination with lambda iteration in order to solve the radiative transfer equation. These schemes are frequently used in works on stellar atmospheres (e.g., Gustafsson et al., 1975, 2008), protoplanetary disks (Dullemond et al., 2002) and have been applied in some 1D models of exoplanetary atmospheres (Mollière et al., 2015, 2017, 2019, 2020; Piette & Madhusudhan, 2020). Our implementation of radiative transfer adopts the radiative transfer scheme used in the 1D planet atmosphere model `petitRADTRANS` (Mollière et al., 2019, 2020).

Fluxes

The change of intensity I_ν $[W\,m^{-2}\,sr^{-1}\,Hz^{-1}]$ along a ray passing through a planetary atmosphere in the direction of the unit vector, $\mathbf{n}$, may be described by the radiative transfer equation

$$\mathbf{n}\cdot\nabla I_\nu = \alpha_\nu^{tot}\,(S_\nu - I_\nu)\,, \tag{6.8}$$

where ν [Hz] is the frequency, S_ν $[W\,m^{-2}\,sr^{-1}\,Hz^{-1}]$ is the source function and α_ν^{tot} $[m^{-1}]$ is the inverse mean-free path of the light ray. We solve this equation for photons originating within the planetary atmosphere or scattered out of the incoming stellar ray. The extinction of the incoming stellar intensity is separately modeled using an exponential decay. This is not an approximation; such a separate treatment is allowed given to the linear nature of the equation of radiative transfer. The full solution is then obtained from adding the two intensities (planetary and scattered stellar photons along with extincted stellar intensity). The inverse mean free path α_ν^{tot} is given by the sum of absorption and scattering inverse mean free paths and may be written as

$$\alpha_\nu^{tot} = \alpha_\nu^{abs} + \alpha_\nu^{scat}. \tag{6.9}$$

The mean intensity J_ν $[W\,m^{-2}\,sr^{-1}\,Hz^{-1}]$ is the zeroth order radiative momentum and is given by angle integration (e.g., Gaussian quadrature) of the intensity field. The zeroth and first order radiative moments in plane-parallel are given by

$$[J_\nu, H_\nu] = \frac{1}{2}\int_{-1}^{1} [1,\mu]\, I_\nu(z,\mu)\mathrm{d}\mu, \tag{6.10}$$

where $\mu = \cos\theta$ is the angle between the atmospheric normal and the ray and H_ν $[W\,m^{-2}\,Hz^{-1}]$ is related to the flux (see below).

We use the source function in the coherent isotropic scattering approximation for the planetary and scattered stellar photon field, given by

$$S_\nu = \epsilon_\nu B_\nu(T) + (1-\epsilon_\nu)(J_\nu^{pla} + J_\nu^{\star}), \tag{6.11}$$

where $B_\nu(T)$ $[W\,m^{-2}\,sr^{-1}\,Hz^{-1}]$ is the Planck function at temperature T [K], while J_ν^{pla} $[W\,m^{-2}\,sr^{-1}\,Hz^{-1}]$ and $J_\nu^{\star}$ $[W\,m^{-2}\,sr^{-1}\,Hz^{-1}]$ are the mean intensity of the planetary atmosphere and the stellar attenuated radiation field respectively, and ϵ_ν is the photon destruction probability given by

$$\epsilon_\nu = \frac{\alpha_\nu^{abs}}{\alpha_\nu^{tot}}. \tag{6.12}$$

The mean intensity of the stellar attenuated radiation field in a plane-parallel atmosphere $J_\nu^\star$ [$W\,m^{-2}\,sr^{-1}\,Hz^{-1}$] (Mollière et al., 2015) is given by

$$J_\nu^\star = \frac{I_\nu^\star(p=0)}{4\pi}\exp\left(-\tau_\nu/\mu_*\right), \tag{6.13}$$

where $I_\nu^\star(p=0)$ [$W\,m^{-2}\,sr^{-1}\,Hz^{-1}$] is the stellar intensity field at the top of the planetary atmosphere. Here, `expeRT/MITgcm` uses the PHOENIX stellar model spectrum (Husser et al., 2013) that is part of `petitRADTRANS` to calculate the stellar attenuated radiation field. The angle between the atmospheric normal and the incoming stellar light $\mu_\star$ for a tidally locked exoplanet is given by

$$\mu_\star = \cos\vartheta\cos\varphi, \tag{6.14}$$

where ϑ is the latitude and φ is the longitude. We note that we do not extend the plane-parallel assumption by including a geometric depth dependence in $\mu_\star$, which would improve the treatment of the poles (see Appendix A). The optical depth, τ_ν, in a hydrostatic atmosphere that is parallel to the atmospheric normal is given by

$$\tau_\nu = \int \frac{\kappa_\nu^{tot}}{g}dp, \tag{6.15}$$

where κ_ν^{tot} [$m^2\,kg^{-1}$] is the cross-section per unit mass (opacity) and depends on the gas density, ρ [$kg\,m^{-3}$], as:

$$\kappa_\nu^{tot} = \frac{\alpha_\nu^{tot}}{\rho}. \tag{6.16}$$

We can express the received bolometric stellar flux $F^\star$ [$W\,m^{-2}$] using Eqs. 6.10 and 6.13 as

$$F^\star = -4\pi\int_\nu H_\nu^\star\,d\nu = 4\pi\mu_\star\int_\nu J_\nu^\star\,d\nu. \tag{6.17}$$

We solved Eq. 6.8 using the well established Feautrier method (Feautrier, 1964) with ALI (Olson et al., 1986) in order to get the planetary flux. Once a converged solution (see Sect. 2.2) of the planetary intensity field has been found, we can calculate the emerging bolometric fluxes from the integration of the planetary radiation field F^{pla} [$W\,m^{-2}$] using Eq. 6.10:

$$F^{pla} = \int_\nu F_\nu^{pla}d\nu = -4\pi\int_\nu H_\nu^{pla}d\nu. \tag{6.18}$$

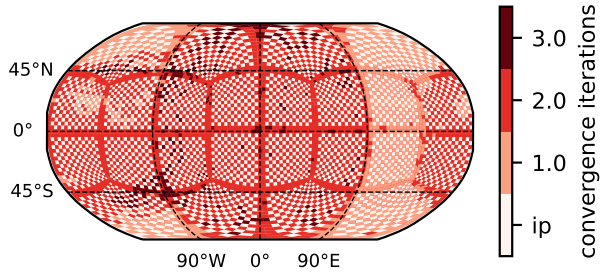

Figure 6.1: Horizontal map displaying the number of iterations to converge the source function (Eq. 6.11) during runtime (at t = 12 000 d) for the HD 209458b simulation. The interpolated cells (ip) are staggered to each other. The C32 grid divides the horizontal domain into 24 individual computational domains, as seen by the line structure.

The total bolometric flux F^{net} $[W\,m^{-2}]$ can now be calculated by

$$F^{net} = F^{pla} + F^{\star}. \tag{6.19}$$

Since Eq. 6.7 requires finite differencing of F^{net}, we followed the approach of Showman et al. (2009) and evaluated the fluxes on the vertically staggered cell interfaces. Lee et al. (2022) find that the use of a quadratic Bezier interpolation scheme for the interpolation of the temperature to the vertical interfaces greatly improves the accuracy and stability of the radiative transfer routine. Our tests confirm this finding and we therefore chose to also use this interpolation scheme.

We calculated Eq. 6.19 for every second grid column and linearly interpolate the fluxes in between (see e.g., Showman et al., 2009). The placement of the interpolated cells is shown in Fig. 6.1, where the bright cells indicate the interpolated cells. We note that the C32 geometry prohibits a strict interpolation of every second column. This is caused by the tiling of the horizontal domain into individual computational domains. It is therefore necessary to calculate the radiative transfer at the tile borders, as seen in Fig.

6.1. We test the interpolation scheme in Appendix B.3 and find that the error introduced by the interpolation is below 2%.

Convergence of the source function

There are two modes that `expeRT/MITgcm` can operate in: with scattering and without scattering. We set $\epsilon_\nu = 1$ if scattering is neglected, in which case Eq. 6.11 can be reduced to the LTE source function $S_\nu = B_\nu(T)$. We iterate over the radiative transfer solution (so-called lambda iteration) if $\epsilon_\nu < 1$ (i.e., scattering is included), since S_ν depends on I_ν (see Eqs. 6.10 and 6.11). We note that the Feautrier method has an exact solution in the isotropic scattering case. However, its solution would require a full matrix inversion (see e.g., Hubeny, 2017), which is computationally expensive. Here we chose to solve the Feautrier equation by inverting a tridiagonal matrix instead, which requires iterating on the source function. For this, we use ALI (Olson et al., 1986) instead to speed up the convergence of the source function. We choose to call the source function converged if the relative change of the source function is smaller than 2% of the reciprocal local lambda approximator (Olson et al., 1986; Rutten, 2003). We performed numerical experiments, which confirmed that 2% yields a good tradeoff between accuracy and model performance, in agreement with Auer (1991); Rutten (2003). We use the knowledge of the source function of the previous radiative time-step as an initial guess for the current time-step. The number of iterations that are needed to converge the source function depends on the amplitude of structural changes in the temperature with time. During the first radiative time-step (see Table 6.5) we find that 50-100 iterations are needed to converge the source function, while later time-steps reduce the amount of necessary iterations significantly to orders of one to three iterations per time-step (see Fig. 6.1).

Our numerical implementation of the ALI method in `expeRT/MITgcm` is an optimized version of the flux routine (with scattering) in `petitRADTRANS` (Mollière et al., 2020), which has been tested and benchmarked (Baudino et al., 2017). The major difference between the implementation in `petitRADTRANS` and `expeRT/MITgcm` is that we chose to not include Ng acceleration (Ng, 1974) since the inclusion of Ng acceleration would only help within the first few time steps, whereas convergence of the source function is reached within a few iterations at later time steps (usually less than 2, see also Fig. 6.1).

The flexibility of our radiative transfer approach combined with its accuracy yields no drawback in terms of performance. When using the 24 core model setup, we report fast model runtimes of approximately 600 or 1000 simulated days per day of model runtime for a radiative time-step of 100 s or 300 s, respectively. We note that we take a different approach than e.g., Rauscher

& Menou (2012); Lee et al. (2021), who developed a less complex radiative treatment to shorten the model run-time. Instead, our approach uses a full radiative transfer treatment, but with a different implementation than the one used in previous GCMs (e.g., Showman et al., 2009; Amundsen et al., 2016).

Opacities

Generally, `expeRT/MITgcm` operates on a precalculated grid of correlated-k opacities. The opacity in each correlated-k (e.g., Goody et al., 1989) wavelength bin is sorted in size and its distribution is sampled by a 16 point subgrid. Opacities are precalculated offline on a grid of 1000 logarithmically spaced temperature points between 100 K and 4000 K for every vertical layer. An overview of the used opacity sources can be found in Table 6.1. Opacities were obtained from the `ExoMolOP` database (Chubb et al., 2021) where available.

Opacities are precalculated and combined using a wrapper around the low-resolution mode of `petitRADTRANS`. Molecular abundances, the value for the specific gas constant $R = 3590\,J\,kg^{-1}\,K^{-1}$ and the specific heat capacity at constant pressure, $c_p = 12\,766\,J\,kg^{-1}\,K^{-1}$, are inferred using the equilibrium chemistry package of `petitRADTRANS`. We used solar metallicity and solar C/O ratios, however, formation models for hot gas giants may hint towards sub-solar C/O ratios and super-solar metallicities (e.g., Mordasini et al., 2016; Schneider & Bitsch, 2021a,b). We note that our approach to the chemical composition of the gas is computationally fast, but implies a fixed chemical composition during runtime. Additionally, this treatment neglects a physically correct treatment of cold traps, where certain species would condense out and not be available at altitudes above, which could prohibit a stratosphere caused by TiO and VO.

We used `expeRT/MITgcm` with three different wavelength grids (see Tables 6.2 and 6.3). The default resolution S0 uses $N_{bins} = 6$ wavelength bins from 0.26 µm to 300 µm. We used finer grids with 11 or 30 bins (S1 and S2 hereafter) to benchmark our model to the wavelength grids used in `SPARC/MITgcm` (Kataria et al., 2013). Those tests are shown in Appendix B.

2.3 *Model initialization*

We followed the suggestion of Lee et al. (2021) and homogeneously initialize the upper layers (pressures below 1 bar) of our models with the analytic temperature profile of Parmentier et al. (2015). We calculated the substellar irradiation temperature T_{irr} of HD 209458b and WASP-43b using the stellar

Table 6.1: Opacity table

Type	Species	source
Gas	H_2O	Polyansky et al. (2018)
	CO_2	Yurchenko et al. (2020)
	CH_4	Yurchenko et al. (2017)
	NH_3	Coles et al. (2019)
	CO	Li et al. (2015)
	H_2S	Azzam et al. (2016)
	HCN	Barber et al. (2014)
	PH_3	Sousa-Silva et al. (2015)
	TiO	McKemmish et al. (2019)
	VO	McKemmish et al. (2016)
	FeH	Wende et al. (2010)
	Na	Piskunov et al. (1995)
	K	Piskunov et al. (1995)
Rayleigh scattering	H_2	Dalgarno & Williams (1962)
	He	Chan & Dalgarno (1965)
CIA	H_2-H_2	BR, RG12
	H_2-He	BR, RG12
	H^-	Gray (2008)

Notes: CIA is short for collision induced absorption. BR stands for Borysow et al. (1988, 1989); Borysow & Frommhold (1989); Borysow et al. (2001); Borysow (2002) and RG12 stands for Richard et al. (2012). Potassium and sodium are broadened with the coefficients of Allard et al. (2019).

Table 6.2: Low-resolution wavelength grid (S0)

Left border wavelength [μm]	Right border wavelength [μm]
0.26	0.42
0.42	0.85
0.85	2.02
2.02	3.50
3.50	8.70
8.70	300.00

Notes: Low-resolution wavelength grid (S0) used throughout this work. Rows represent one wavelength bin.

Table 6.3: Wavelength resolutions

Abbreviation	N_{bins}	Reference
S0	6	Table 6.2
S1	11	Kataria et al. (2013)
S2	30	Showman et al. (2009)

Notes: Wavelength resolutions used in `expeRT/MITgcm`. We note that the upper wavelength edge of all methods (including S1 and S2) is set to 300 μm. The accuracy of these different binning methods has been benchmarked in Appendix B.

radius, $R_\star$ [m], semi major axis, a_p [m], and stellar effective temperature, $T_\star$ [K], as

$$T_{irr} = T_\star \sqrt{\frac{R_\star}{2a_p}}, \tag{6.20}$$

where we use an effective stellar temperature, $T_\star$, and a stellar radius, $R_\star$, of $T_\star^{\text{HD 209458}} = 6092\,\text{K}$ and $R_\star^{\text{HD 209458}} = 1.203\,R_\odot$(Boyajian et al. (2015)) for HD 209458b and then $T_\star^{\text{WASP}-43} = 4520\,\text{K}$ and $R_\star^{\text{WASP}-43} = 0.667\,R_\odot$ for WASP-43b (Gillon et al., 2012). We assumed both planets to be tidally locked on a circular orbit. We set the rotation period of HD 209458b to $P_{rot}^{\text{HD 209458b}} = 3.47\,\text{d}$ and the orbital separation to $a_p^{\text{HD 209458b}} = 0.047\,47\,\text{AU}$ (Southworth, 2008, 2010) and for WASP-43b to $P_{rot}^{\text{WASP}-43\text{b}} = 0.8135\,\text{d}$ and $a_p^{\text{WASP}-43\text{b}} = 0.015\,26\,\text{AU}$ (Gillon et al., 2012). Using Eq. 6.20, we estimated $T_{irr}^{\text{HD 209458b}} = 1479\,\text{K}$ and $T_{irr}^{\text{WASP}-43\text{b}} = 1441\,\text{K}$ for HD 209458b and WASP-43b, respectively. We used the fit from Thorngren et al. (2019) with these irradiation temperatures to estimate the interior temperature resulting from radiation of the planetary interior. This procedure yields interior temperatures of 575 K and 549 K, respectively. These irradiation and interior temperatures are then used to calculate the analytic temperature profile of Parmentier et al. (2015). We note that these interior temperatures were only used to initialize the temperature of our simulations, since we do not enforce radiative (-convective) equilibrium in the atmosphere of our GCM models during runtime.

The deep layers (pressures above 10 bar) are homogeneously set to a hot adiabatic temperature profile of the form

$$T(p > 10\,\text{bar}) = \Theta_{ad} \cdot \left(\frac{p}{1\,\text{bar}}\right)^{\eta}, \tag{6.21}$$

where we follow Sainsbury-Martinez et al. (2019) to guess high values of $\Theta_{ad}^{\text{HD 209458b}} = 1800\,\text{K}$ and $\Theta_{ad}^{\text{WASP}-43\text{b}} = 1400\,\text{K}$ as the temperature of the adiabat at 1 bar. The slope of the adiabat η is given by

$$\eta = \frac{R}{c_p} \approx 3.56. \tag{6.22}$$

The intermediate pressure ($1\,\text{bar} \leqslant p \leqslant 10\,\text{bar}$) levels are linearly interpolated between the adiabat and the analytic model of Parmentier et al. (2015). This procedure allows for a hot initial state in the deep layers, as proposed in Sainsbury-Martinez et al. (2019). We assume a value of $g^{\text{HD 209458b}} = 8.98\,\text{m s}^{-2}$ (e.g., Lee et al., 2021) and $g^{\text{WASP}-43\text{b}} = 46.9\,\text{m s}^{-2}$

(Gillon et al., 2012) for the surface gravity, respectively. Differences in the model setup of WASP-43b compared to HD 209458b (see Table 6.4) only occur in the surface gravity, rotation period and radiative time-step (see Table 6.5).

We ran the model for 12 000 days with a dynamical time-step of $\Delta t = 25$ s.[3] Since the temperature in the upper layers might change significantly during the first 500 days, we recalculate the radiative fluxes in every fourth dynamical time-step, which we do by defining a radiative time-step, Δt_{rad}, which we set to $\Delta t_{rad} = 100$ s (see Table 6.5). In the case of WASP-43b, we continue the simulation with the same radiative time-step, whereas we use a longer radiative time-step for the rest of the HD 209458b simulation of 300 s. A shorter radiative time-step is needed for the simulations of WASP-43b, since WASP-43b undergoes large structural changes throughout the model runtime, whereas HD 209458b reaches a steady state in the observable atmosphere within the first few hundred days (see Sect. 4).

3 STATE OF THE UPPER ATMOSPHERE

The number of planets modelled with fully coupled GCMs has increased a great deal since Showman et al. (2009) first introduced a fully coupled GCM for hot Jupiters. We chose to focus on HD 209458b and WASP-43b in this work. HD 209458b has been modeled by many of the relevant fully coupled hot Jupiter GCMs (Showman et al., 2009; Amundsen et al., 2016; Lee et al., 2021), making it a suitable target for comparisons between our model and previous works. Our non-gray 3D GCM WASP-43b simulations will be compared to simulations, at a similar level of complexity, of the same planet by Kataria et al. (2015). Comparisons with Baeyens et al. (2021), where a simpler radiative transfer scheme is used, are shown in Appendix D.

3.1 *HD 209458b*

We show the time-averaged temperature for different pressure layers in Fig. 6.2. The temperature has been time-averaged over the last 100 d. The temperature maps demonstrate the typical features of a tidally locked hot Jupiter climate: The strongly irradiated dayside transports heat to the nightside via a superrotating jet (e.g., Showman & Polvani, 2011), while shifting the hottest point eastwards. The upper layers ($p < 1 \times 10^{-3}$ bar) are strongly influenced by stellar irradiation, whereas advection is negligible (Fig. 6.2, top left panel). In contrast, the deeper layers ($p > 1 \times 10^{-2}$ bar) are more efficient in redistributing heat by advection (Fig. 6.2, bottom left panel).

3 Day refers to 24 h or 1 earth day.

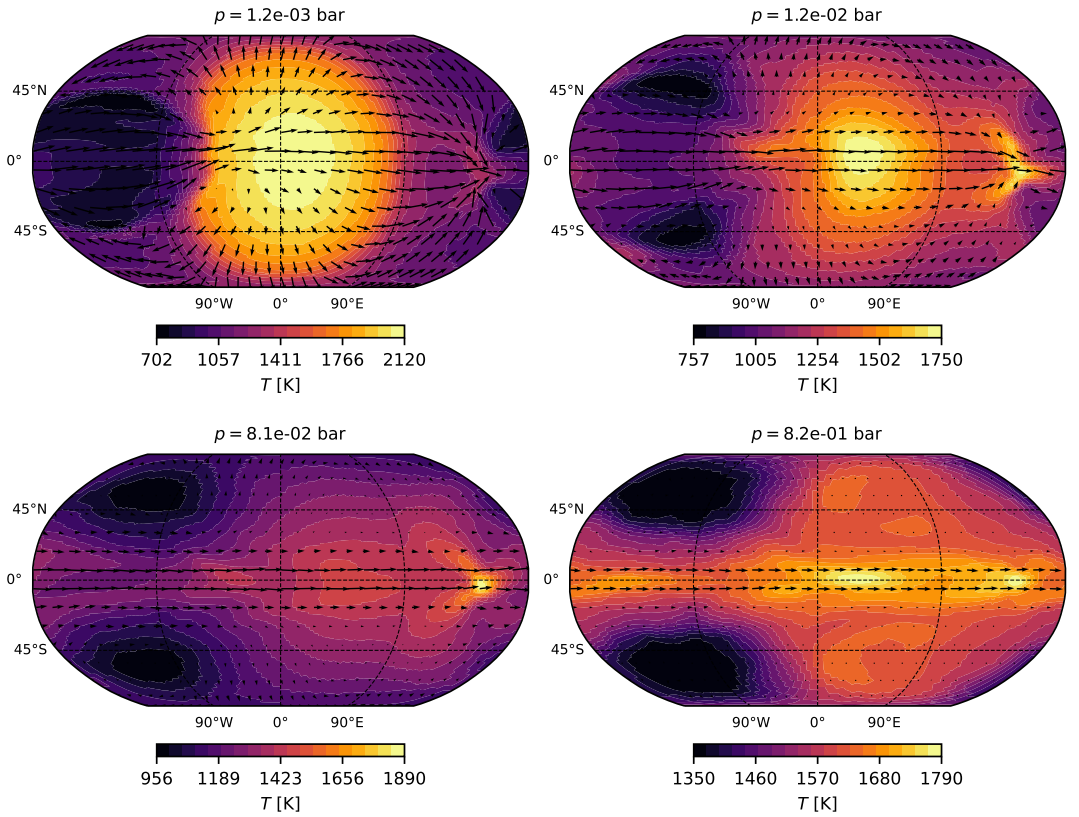

Figure 6.2: Maps of HD 209458b displaying the color coded temperature at different pressure levels (as indicated above the maps). The substellar point is located at (0°,0°).

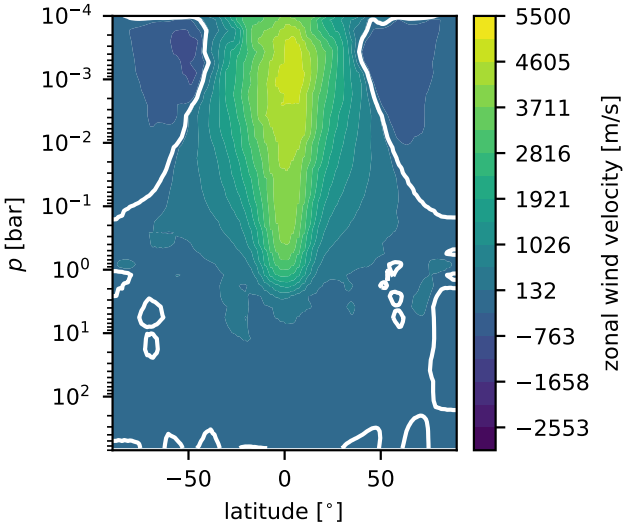

Figure 6.3: Zonally averaged zonal wind velocities for HD 209458b. Positive values correspond to prograde flow. The white line depicts the change of sign.

The zonal mean wind velocities are shown in Fig. 6.3. The superrotating jet of HD 209458b as seen in Kataria et al. (2016); Amundsen et al. (2016); Lee et al. (2021) is reproduced with `expeRT/MITgcm`. The magnitude of the jet ($\approx 5000\,\mathrm{m\,s^{-1}}$) agrees best with Kataria et al. (2016); Lee et al. (2021) and is lower than the value reported by Amundsen et al. (2016) of $7000\,\mathrm{m\,s^{-1}}$.

The temperature maps of the HD 209458b simulations (Fig. 6.2) qualitatively match those of Lee et al. (2021, Fig. 5) showing that the general flow pattern as well as the day to night temperature difference are similar. Small asymmetric features in the temperature map highlight that the model has not yet equillibriated, even though the model was run for 12000 days. We note that our simulations are initialized with a hot deep adiabat that is maintained throughout the runtime (see Sect. 4) while other simulations of HD 209458b (e.g., Amundsen et al., 2016; Showman et al., 2009) did not use such a hot interior.

The simulations of Showman et al. (2009); Lee et al. (2021) exhibit a temperature inversion due to the presence of TiO and VO around the substellar point, which results in an enhanced absorption of incoming stellar light. Our simulation of HD 209458b reproduces this temperature inversion, since we also include contributions of TiO and VO to the gas opacities that we use in our models (see Table 6.1). Small uncertainties in temperature and opacities

may result in slightly hotter or cooler gas temperatures, which could result in the presence or absence of TiO and VO, since the dayside temperature of HD 209458b is very close to the TiO and VO condensation curves. This further highlights the importance of accurate interpolation schemes, such as the Bezier interpolation for the temperature (see Sect. 2.2), as well as the fine grained opacity grid with 1000 logarithmically spaced temperature points.

3.2 *WASP-43b*

Similarly to Fig. 6.2 for HD 209458b, the temperature maps for WASP-43b are shown in Fig. 6.4. The results are well in line with the `SPARC/MITgcm` results for WASP-43b (Kataria et al., 2015) with TiO and VO. The day-to-night temperature differences as well as the flow patterns are comparable.

Unlike the case of Carone et al. (2020), our simulations do not exhibit a retrograde flow. As noted in Carone et al. (2020), the retrograde flow in their simulation was embedded in strong superrotation. Thus, both tendencies - the one of the prograde flow and that of the retrograde flow - were engaged in a "tug of war". The main difference between the simulations of Carone et al. (2020) and this work is, however, that this work does not require artificial temperature forcing in deep layers. Our simulations therefore capture the full feedback between dynamics and radiation that was missing in Carone et al. (2020). This feedback seems to strengthen superrotation, apparently allowing for full superrotation to win the "tug of war" over the tendency for retrograde flow. Carone et al. (2020) found that the tendency toward retrograde flow is associated with a deep jet that can transport zonal momentum upwards. The transport of zonal momentum has been analyzed in several studies (e.g., Showman et al., 2015; Mendonça, 2020; Wang & Wordsworth, 2020; Carone et al., 2020), but it is still not clear what conditions would lead a deep equatorial jet toward retrograde flow. We will investigate the transport of zonal momentum in more detail in a follow-up publication and instead focus on the temperature evolution at greater depths in this work.

Carone et al. (2020) find that the depth of the equatorial jet of WASP-43b is likely linked to the rotation period. Their argumentation bases on two simulations of WASP-43b. Their nominal WASP-43b simulation with a rotation period of 0.81 days shows signs of a deep equatorial jet, which is not found in a simulation of WASP-43b with a rotation period of 3.5 days (as for HD 209458b). Our non-gray model of WASP-43b confirms this finding of Carone et al. (2020). WASP-43b indeed exhibits a deeper equatorial jet compared to HD 209458b, which can be seen in the zonal mean of the wind flow (see Fig. 6.5). We note that the simulations of Kataria et al. (2015) do not

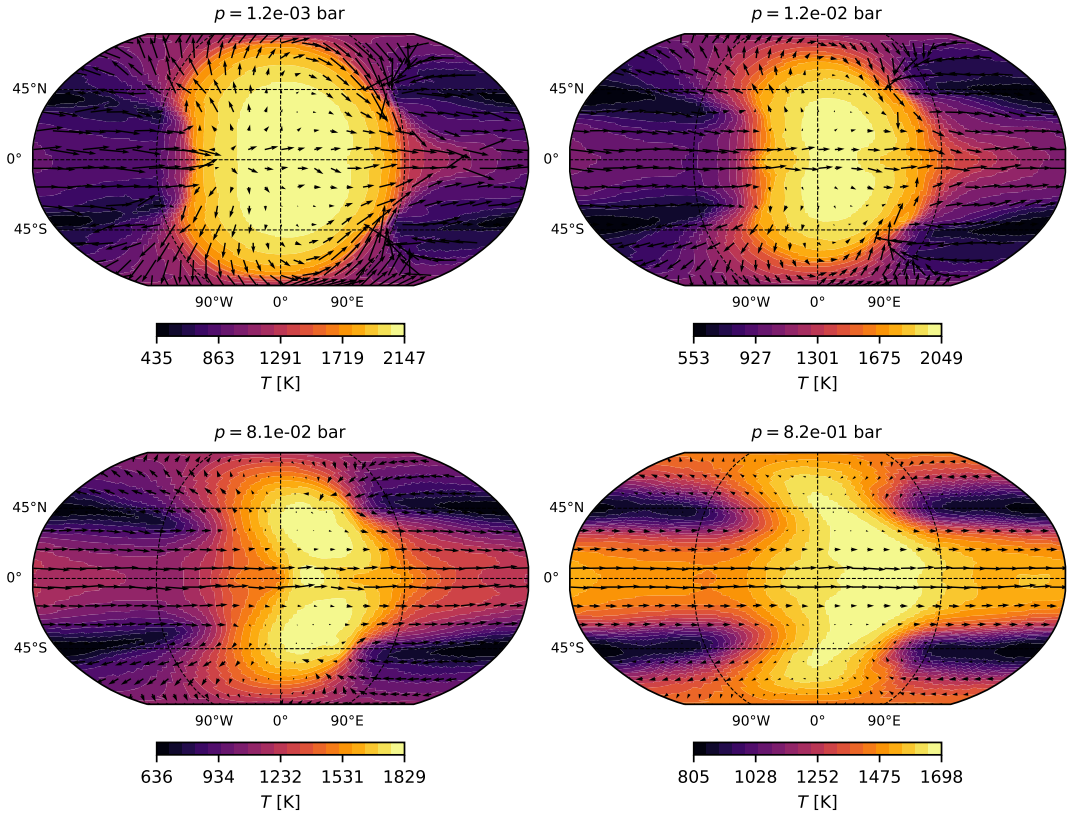

Figure 6.4: Maps of WASP-43b displaying the color coded temperature at different pressure levels (like Fig. 6.2).

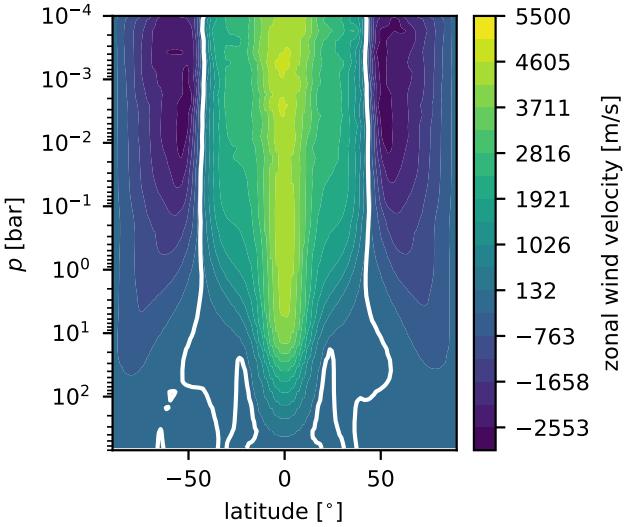

Figure 6.5: Zonally averaged zonal wind velocities (like Fig. 6.3) for WASP-43b.

exhibit such a deep jet, which is likely caused by the short runtime of 50 d compared to the 12 000 d used here. Future works are warranted to unveil the physical reasons behind the depth of the equatorial jet.

4 TEMPERATURE CONVERGENCE OF THE DEEP LAYERS

The GCM experiments of Sainsbury-Martinez et al. (2019) indicate that hot Jupiters might pump the energy input from irradiation into the deep atmosphere ($p > 1\,\mathrm{bar}$) by means of dynamic heat transport, leading to hot temperatures in their deep atmosphere. The equation of entropy conservation in steady state can be written as (e.g., Tremblin et al., 2017; Sainsbury-Martinez et al., 2019)

$$\frac{d\Theta}{dt} - \mathbf{u} \cdot \nabla\Theta = 0, \tag{6.23}$$

where $\mathbf{u}$ is the velocity vector, $\nabla\Theta$ is the spatial gradient of the potential temperature, Θ, and $\frac{d\Theta}{dt}$ encapsulates dissipative process that cool or heat the atmosphere[4]. If we only consider irradiation, $\frac{d\Theta}{dt}$ becomes very small in the deep layers of the atmosphere because most of the stellar light is absorbed in

4 $\frac{d\Theta}{dt}$ is given by Eq. 6.6 in this work, but other processes such as Ohmic dissipation could also play a role.

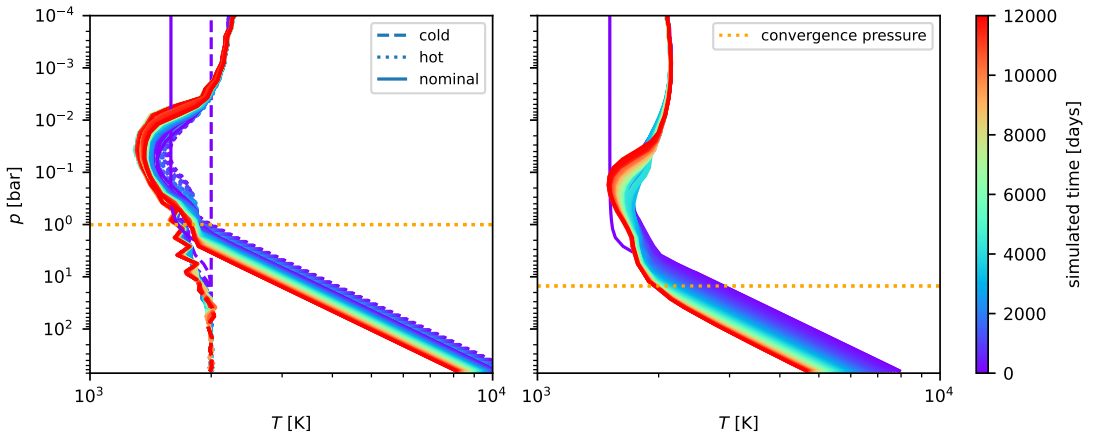

Figure 6.6: Evolution of the temperature profile at the substellar point for HD 209458b (left) and WASP-43b (right). The left panel includes the evolution of two additional HD 209458b simulations with a colder and a hotter initial temperature profile. The right panel includes one additional WASP-43b simulation with a cooler initial temperature profile. The additional simulations initialized with an adiabat ran for 3000 days, whereas the cool HD 209458b ran for 5000 days. The temperature time averaging and output interval is set to 100 days, therefore not resolving the fast semi-convergence of the temperature in the photosphere during the first 100 days. The horizontal orange dashed line illustrates the approximate altitude at which radiative heating or cooling becomes very small.

the upper atmosphere. However, this requires that either $\mathbf{u}$ or $\nabla\Theta$ become very small. To fulfill the latter, the potential temperature must be close to constant and therefore follow an adiabat ($T \propto p^{\eta}$).

The potential temperature of such an adiabat would therefore be mainly determined by the temperature of the convergence pressure, which is defined as the region where heating and cooling by radiation becomes very small. Furthermore, the convergence pressure lies higher up in the atmosphere compared to the pressure at which the atmosphere would be convective.

The weakness of radiative cooling and heating in the deep layers of the atmosphere requires long model runtimes. We can utilize the fast runtime of `expeRT/MITgcm` of 600-1000 simulated days per day of model runtime to study the temperature convergence in the deeper layers of the atmosphere. We investigate the temperature evolution of HD 209458b and WASP-43b in Fig. 6.6, where we show the temperature profile at the substellar point as a function of time. For HD 209458b, we show two additional simulations with different initial temperature profiles. The first one is identical to the nominal model, but uses $\Theta_{ad} = 2000\,\mathrm{K}$ for the initial deep adiabat, instead of $\Theta_{ad} = 1800\,\mathrm{K}$ for the nominal model (see Sect. 2.3); whereas the second simulation was initialized with a globally isothermal temperature of $T = 2000\,\mathrm{K}$. We performed a similar test for WASP-43b, where we ran a model of WASP-43b that has been initialized, with $\Theta_{ad} = 900\,\mathrm{K}$, instead of the nominal $\Theta_{ad} = 1400\,\mathrm{K}$. We chose to stop the extra HD 209458b and WASP-43b simulations with an adiabatic interior at $t = 3000\,\mathrm{d}$, since the only purpose of these simulations is to gain information about the dependence of the temperature convergence behavior on initial conditions. However, it is important to note that the convergence time needed to cool down the deep atmosphere from a hot state to a colder state is shorter than the time needed to heat the deep atmosphere from a cold state to a hotter state (Sainsbury-Martinez et al., 2019).

We find that for WASP-43b, the temperature in the deep layers is steadily evolving during the full 12 000 d simulation. The rate of temperature change drops from approximately $1.5\,\mathrm{K\,d^{-1}}$ to approximately $0.05\,\mathrm{K\,d^{-1}}$ at the end of the simulation, while slowly converging. This process of cooling results in an almost isothermal temperature profile in the photosphere of WASP-43b, which is subsequently changing into a more pronounced temperature inversion once the deep cooling becomes less efficient (see Fig. 6.6, right panel). The decaying rate of cooling in the deep layers forecasts a final cool adiabat of $\Theta_{ad} \approx 700\,\mathrm{K}$.

The temperature evolution of the initially cool WASP-43b simulation overlaps with the temperature evolution of the nominal simulation. However, the later states of the nominal WASP-43b including the thermal inversion matches the initially cold simulation fairly well. We therefore find that the evolution

of the temperature of the initially cold WASP-43b simulation confirms the independence of the final state of the deeper atmosphere of WASP-43b on initial conditions.

HD 209458b, on the other hand, appears to maintain its initial temperature profile in the deep layers (see Fig. 6.6, left panel). The temperature constantly decreases with a rate varying around $(0.1 \pm 0.1)\,\mathrm{K\,d^{-1}}$. Furthermore, we see that the deep temperature evolution is similar for the hot initial temperature profile, yielding very low values for the temperature decay in time. A perfect initial guess by chance is therefore impossible. We therefore conclude that we could not reach temperature convergence in the deep layers of HD 209458b within 12000 days. This outcome, while "negative," is of significance for other studies that have already published temperature maps of HD 209458b.

The temperature in the isothermally initialized HD 209458b simulation does not evolve towards a hotter state in the deep layers. It is not possible to predict whether the final state of the temperature in the deep layers of these simulations will indeed be adiabatic. We can thus not confirm Sainsbury-Martinez et al. (2019) in that the deep layers of this simulation heat up towards such a state. Additionally, the temperature exhibits a shaky pattern that is likely linked to the deeper parts of the atmosphere. This pattern arises at the convergence pressure and could be explained by upward propagating gravity waves; a process that has also been postulated for the atmospheres of brown dwarfs (e.g., Freytag et al., 2010; Showman & Kaspi, 2013). We therefore postulate that this pattern is linked to the strength of the dynamic processes in the deeper parts of the atmosphere. It remains an open question if this pattern disappears when convergence is reached or if it could be forced to a stably stratified temperature profile with the use of a convective adjustment scheme (e.g., Deitrick et al., 2020; Lee et al., 2021), which we do not use within this work. We plan to examine these gravity waves and the effect of a convective adjustment scheme in detail in an upcoming work.

In the following, we investigate the effect of surface gravity and planetary rotation on the convergence behavior of the temperature in the deep atmosphere. Radiative timescales scale reciprocally with the surface gravity (see e.g., Showman et al., 2020), leading to longer radiative timescales in HD 209458b at similar pressure levels compared to WASP-43b, even though both planets receive a similar amount of energy from their host star. The pressure level where the radiative heating and cooling becomes irrelevant is therefore different for both planets, where irradiation is penetrating into deeper pressure layers in the atmosphere of WASP-43b compared to HD 209458b. This will then influence the pressure level and temperature at which a deep adiabat could couple to the radiatively dominated part of the atmosphere (according

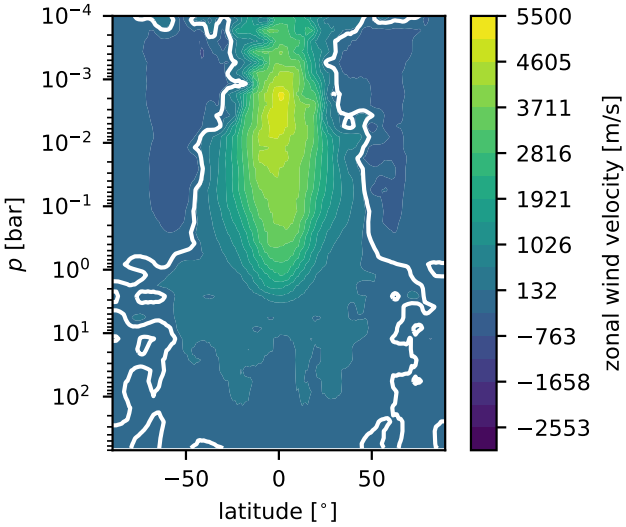

Figure 6.7: Zonally averaged wind velocities (like Fig. 6.5) for a model of WASP-43b with a rotation period equal to the rotation period of HD 209458b.

to the explanations of Tremblin et al., 2017; Sainsbury-Martinez et al., 2019). Hence, we think that a colder interior of WASP-43b in our simulations is a natural consequence of the assumption of the value of the surface gravity.

We performed an additional simulation of a WASP-43b-like planet with a rotation period equal to the rotation period of HD 209458b ($P_{rot} = 3.47$ d), instead of the nominal short rotation period of $P_{rot} = 0.8135$ d. The goal of this additional simulation is to consider the dependence of the temperature evolution on rotation. The zonal wind velocity in the case of slow rotation is significantly different to our nominal model of WASP-43b, where we find that unlike the nominal simulation (Fig. 6.5), the slowly rotating WASP-43b simulation does not exhibit a deep equatorial jet. This finding agrees well with the work of Carone et al. (2020), who predicted that WASP-43b exhibits a deep superrotating jet, which is linked to the fast rotation of WASP-43b.

Recently, Sainsbury-Martinez et al. (2021) proposed that the efficiency of downward heat transport of energy depends on the presence or absence of rotational dynamics over advective dynamics. If rotational dynamics dominate over advective dynamics, which is the case for a deep equatorial jet, we would expect a lower efficiency for the downward heat transport of energy. We therefore compared the temperature in the model of WASP-43b with a deep jet (nominal) to the model without a deep jet ($P_{rot} = 3.5$ d). We show the resulting

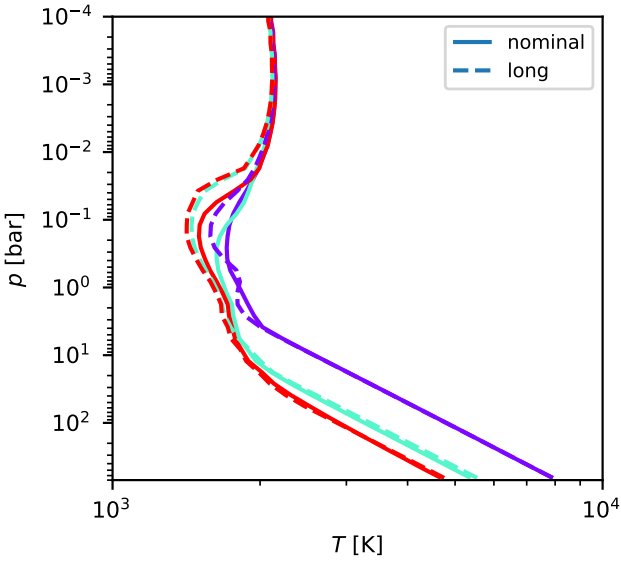

Figure 6.8: Evolution of the temperature profile at the substellar point (like Fig. 6.6). Three time steps (100 d, 5000 d and 12 000 d) of the nominal model of WASP-43b are compared to a model of WASP-43b with a rotation period equal to the rotation period of HD 209458b. The color scale is the same as in Fig. 6.6.

substellar point temperature profiles in Fig. 6.8, where we find that both simulations exhibit a similar temperature evolution in the deep atmosphere. The independence of the deep temperature profile on the rotation period leads us to the conclusion that the fast temperature convergence of WASP-43b can be almost exclusively explained by the continuously strong radiative heating and cooling in the deep atmosphere caused by the high value of surface gravity.

The requirement of zero radiative heating and cooling (see Eq. 6.23) for the theory of downward transport of energy (Sainsbury-Martinez et al., 2019) can only be monitored with a climate model that includes radiative feedback. Using our model, we find that radiative heating and cooling can still be important at greater depths, bringing on the question of how the requirements for the formation of a hot deep adiabat might be matched. However, we do note that our simulations demonstrate that our non-gray GCM succeeds in maintaining an adiabatic deep atmosphere, without the need for a convective adjustment scheme. We propose that a further detailed analysis is needed to settle the question of whether a downward transport of energy is possible.

5 SYNTHETIC SPECTRA

We post-processed our GCM results using `petitRADTRANS` to obtain emission and transmission spectra. We followed Baeyens et al. (2021) and calculated the transmission spectrum using the average temperature in latitude $\pm 20°$ around the west and east terminators ($\varphi = -90°$ and $\varphi = 90°$). Such an isothermal treatment of the terminator region is possible since temperature variations in the terminator region are very small for pressure layers below 1×10^{-2} bar, which are most relevant to the transmission spectrum. The transmission spectrum is then calculated using the radius and gravity values of Table 6.4 for a reference pressure of 0.01 bar. As in Baeyens et al. (2021), we determined the final transit spectrum by quadratically averaging the east and west terminators. For WASP-43b, we show the Kreidberg et al. (2014) HST/WFC3 data around the $\approx 1.4\,\mu m$ H_2O feature, whereas for HD 209458b, we show the data of Crossfield et al. (2012); Sing et al. (2016); Evans et al. (2015). We calculate the mean of the observed values of the wavelength dependent radius as well as of the calculated transmission spectra for each observed spectral window to determine the offset in radius between observations and our model. We then corrected the observed radius by subtracting this offset. The offset correction is necessary due to differences in the normalization of the radius (see e.g., Lee et al., 2021).

For the emission spectrum, we chose to regrid our GCM output onto a low resolution rectangular grid with a 15° longitude-latitude resolution (288

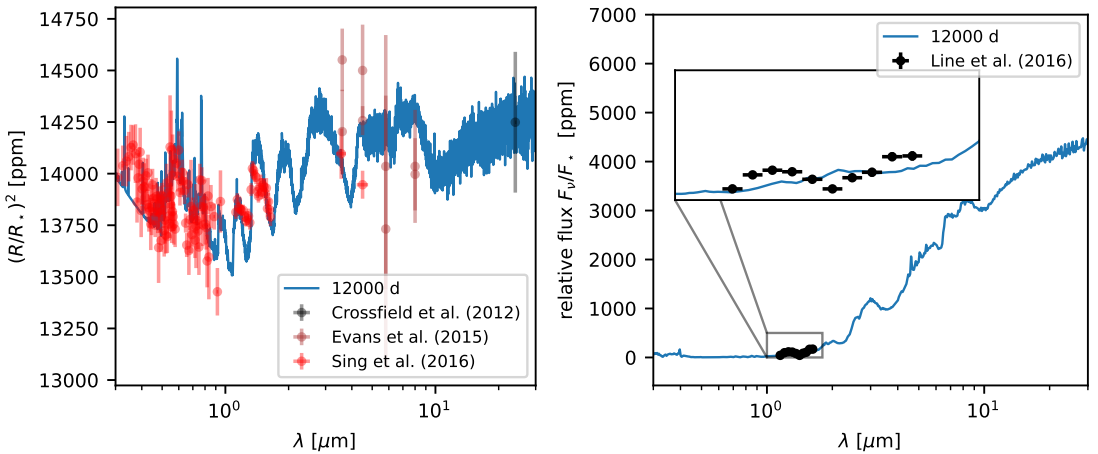

Figure 6.9: Synthetic transmission spectrum (top) and dayside emission spectrum (bottom) for HD 209458b calculated from simulation results after 12000 days, compared to the observations. The thermal inversion, caused by the TiO and VO opacities, overcasts the observed water feature at ≈1.4 µm.

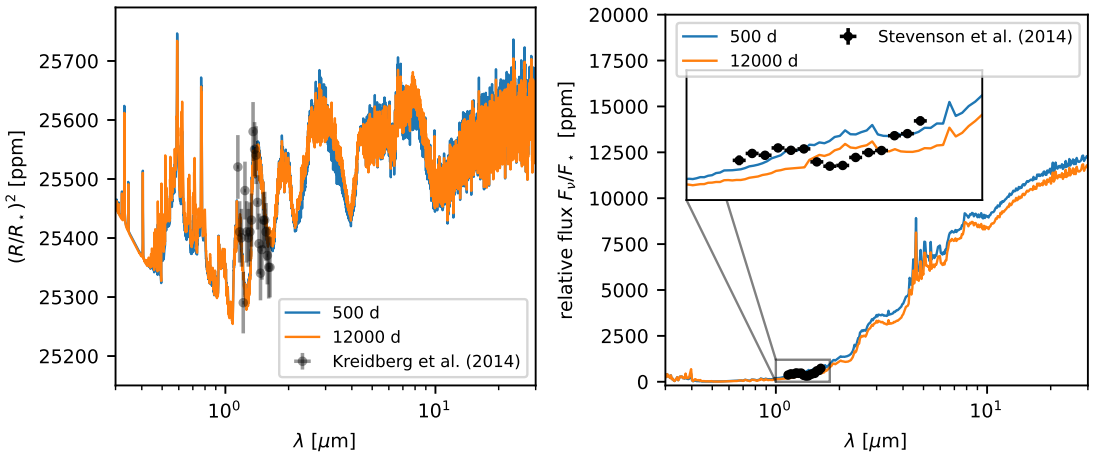

Figure 6.10: Synthetic transmission spectra (top) and dayside emission spectra (bottom) for WASP-43b calculated from simulation results after 500 and 12000 days, compared to the observations. The thermal inversion, caused by the TiO and VO opacities, overcasts the observed water feature at ≈1.4 µm.

horizontal grid cells). We then calculated the angle dependent planetary intensity at the top of each vertical column using a derivative of the flux routine of `petitRADTRANS` for 20 Gaussian μ quadrature points. We then integrated the intensity field over the solid angle to obtain the flux in the direction of the observer (see e.g., Seager, 2010; Amundsen et al., 2016). The general procedure is identical to the one used in Carone et al. (2020) and only differs in its numerical implementation, where we use `petitRADTRANS` instead of `petitCODE` to obtain the intensity.[5] We tested the impact of the low-resolution spatial grid on the resulting emission spectrum by testing an even lower spatial resolution of 30° (72 grid cells) and found that only minimal differences occur, validating the 288 grid cells approach outlined above. We chose to plot the data of Stevenson et al. (2014) for WASP-43b and the data of Line et al. (2016) for HD 209458b. We note that we do not correct the observed emission spectrum for systematic errors, but instead plot the published values.

We investigate whether the difference in the magnitude of the temperature inversion caused by the ongoing convergence of the deeper atmosphere of our WASP-43b simulation would impact predictions for observables. The resulting transmission spectra for HD 209458b in Fig. 6.9 and WASP-43b in Fig. 6.10 show good agreement with the observed values. However, we find that the pressure region between around 1 bar contributes most to the spectrum for wavelengths between 0.4 µm and 2 µm, whereas the pressure range between 0.1 bar and 0.001 bar dominates the infrared spectrum. This would explain, why we only see a (very small) difference between the transmission spectra for WASP-43b at 500 d and 12 000 d in the infrared but not in the optical (see Fig. 6.9).

In examining the dayside emission spectra, we find that the shape of the water line feature of WASP-43b and HD 209458b does not seem to agree between the observed water feature and the model spectra. The reason for the difference in the shape of the water feature is found in the inclusion of TiO and VO opacities, which cause a temperature inversion (Showman et al., 2009). A similar trend can be found in Lee et al. (2021, Fig. 7, right panel), where the authors show the spectral differences of a semi-gray model without temperature inversion compared to more advanced models that include the temperature inversion. A model without TiO and VO in the upper atmosphere would therefore clearly fit the observed spectra much better. Further, the lack of clouds and the assumption of solar metallicity in our model affects the emitted flux and also effect the strength of superrotation (e.g., Kataria et al., 2015; Drummond et al., 2018a; Parmentier et al., 2021).

5 The python package used to obtain and integrate the emission spectrum has been made publicly available and can be found at `https://prt-phasecurve.readthedocs.io/`.

Moreover, we find that the 500 d and 12 000 d emission spectra of the WASP-43b model are clearly impacted by the state of the deep atmosphere (see Fig. 6.6). The flux differences in the emission spectrum thus highlight the effect of deep temperature convergence on the observable atmosphere. These differences are not seen for HD 209458b because the observable atmosphere seems to be unaffected by the state of the deep atmosphere (see Fig. 6.6).

6 DISCUSSION

In this work, we employ `expeRT/MITgcm`, a new 3D GCM with non-gray radiative transfer specifically built to investigate the processes at work in greater depths in more detail. The first application of this model to WASP-43b and HD209458b shows interesting results in flow and temperature at such depths and may thus shed light onto the unsolved question of hot Jupiter inflation.

6.1 *Versatile fast 3D GCM with non-gray radiative transfer*

There are currently several 3D exoplanet atmosphere models available, which vary in their complexity of radiative transfer (Showman et al., 2009; Rauscher & Menou, 2012; Dobbs-Dixon & Agol, 2013; Amundsen et al., 2016; Mendonça et al., 2018b; Lee et al., 2021) and even in the basic implementation of the Navier Stokes equation to treat fluid dynamics, ranging from hydrostatic primitive equations (e.g., Showman et al., 2009) to full (e.g., Mayne et al., 2014; Mendonça et al., 2018b; Deitrick et al., 2020). In addition, several 3D climate models include additional physical processes, which are thought to be important for the understanding of exoplanet atmospheres: clouds (Lee et al., 2016; Lines et al., 2019; Parmentier et al., 2021; Roman et al., 2021), photochemical hazes (Steinrueck et al., 2021), disequilibrium chemistry (Agúndez et al., 2014a; Drummond et al., 2018b; Mendonça et al., 2018a; Baeyens et al., 2021), and magnetic fields (Rogers & Showman, 2014). Cloud modeling in 3D climate models ranges from detailed kinetic modeling (e.g., Lee et al., 2016) to simple but efficient parametrization (e.g., Roman et al., 2021; Christie et al., 2021).

In addition to cloud modeling, disequilibrium chemistry, and magnetic field interaction, there is a need for GCMs that are capable of investigating processes at greater depths such as deep wind flow and deep energy transport. In this work, we introduce a new non-gray GCM formalism that is numerically efficient and thus ideally suited to tackle the challenging processes at greater depths. The main reason for these advances is the use of the Feautrier

method in combination with accelerated lambda iteration to solve the radiative transfer equation (Sects. 2.2 and 2.2). We find that these methods allow us to run non-gray GCM models for 1000 simulation days within just a single day of run time and using 24 cores. Applying the code to WASP-43b and HD 209458b shows that the upper atmosphere agrees well with the results of other non-gray GCMs (Sect. 3) for these planets (Kataria et al., 2015; Showman et al., 2009; Amundsen et al., 2016; Lee et al., 2021). The differences with Newtonian cooling as used in Carone et al. (2020) are shown in Appendix. D. The computational efficiency of `expeRT/MITgcm` allows extending the work of Sainsbury-Martinez et al. (2019) to investigate temperature convergence for very long simulation times at deeper layers without artificial external forcing mechanisms (Sect. 4).

6.2 *Importance of the temperatures in the deep atmosphere*

The temperature in layers below 10 bar can influence the observable chemistry in several ways: for instance, iron and magnesium could condense in these layers and consequently would not be present in the gas phase of the upper atmosphere, where they would be observable via high-resolution spectroscopy (Sing et al., 2019, Fig. 13). Other possibilities include the quenching of methane via disequilibrium chemistry (Agúndez et al., 2014b; Baeyens et al., 2021) and the thickness of clouds also depends on the temperature at deeper layers (Fortney et al., 2020). Silicate cloud formation can remove or inject oxygen-bearing molecules from the gas phase (Helling et al., 2019b, 2021a). Therefore, deep cloud condensation might affect local C/O ratios in cloud forming regions even more than thinner clouds. At the same time, the condensation of important cloud particles such as magnesium at greater depths may affect the composition of clouds higher up, as pointed out by Helling et al. (2021a).

In this work, we focused on energy transport and thermal evolution at greater depths, because it is still an open question whether energy can be injected via 3D circulation from the irradiated photosphere into deeper layers in hot to ultra-hot Jupiters that could at least partly explain hot Jupiter inflation (Mayne et al., 2014; Tremblin et al., 2017; Mayne et al., 2017). For WASP-43b, we find that higher surface gravities compared to HD 209458b already naturally lead to a deeper convergence pressure. Thus, setting the surface gravity and assuming long-enough run times drives the simulation at greater depths naturally to a colder state. The surface gravity of WASP-43b, however, is higher because it is not inflated. In other words: the state of inflation sets the surface gravity, which, in turn, strongly affects the convergence behavior towards the final state. This dependence of the convergence behavior on the state

of inflation is obviously not optimal, since it creates a "chicken-and-the-egg problem" when investigating energy transport at greater depths. However, we stress that our numerical efficient non-gray GCM has the potential to explore this problem in more detail, where we will also take additional dissipative processes at greater depths into account in the future.

6.3 *Effect of deep dynamics on the observable atmosphere*

Only a few GCM studies of hot Jupiters have been conducted thus far with the aim to explore dynamical effects at greater depths owing to the computational challenges that need to be resolved in the deeper atmosphere. Mayne et al. (2017) explored the possibility of deep wind flow when horizontal temperature differences at greater depths are imposed. Carone et al. (2020) showed that fast rotators like WASP-43b (orbital periods less than 1.5 d) naturally evolve equatorial jets that can extend very deep into the interior. In the Solar System, the fast-rotating gas giants are also shown to have deep jets (Kaspi et al., 2018; Iess et al., 2019). In this work, the deep equatorial jets in WASP-43b and shallow equatorial jets in HD 209458b are reproduced. Thus, we stress, as does Carone et al. (2020), that some extrasolar planets like the JWST ERS target WASP-43b (Venot et al., 2020; Bean et al., 2018) can be dynamically active at greater depth greater than 200 bar, which is the typical lower boundary assumed for hot Jupiter GCMs (e.g., Showman et al., 2009; Amundsen et al., 2016; Deitrick et al., 2020; Parmentier et al., 2021; Lee et al., 2021). More importantly, we find in this work that resolving dynamics at greater depths is important to allow the deep atmosphere of WASP-43b to self-consistently evolve towards cool adiabat ($\Theta_{\mathrm{ad}} \approx 700$ K).

It is not only the energy transport at greater depths that is influenced by deep dynamics. Previous works indicate that the presence of a deep flow may impact the observable wind and temperature structure of hot Jupiters. Mayne et al. (2017) showed that the deep wind flow can greatly diminish superrotation in the observable atmosphere. Wang & Wordsworth (2020) found that the simulated wind flow structure in their mini-Neptune simulation can abruptly change from two jets to one jet, which could be observable via changes in the hotspot location. This change happens without forced conversion after 50000 simulation days. Furthermore, Carone et al. (2020) find that in their simulations, superrotation can be completely disrupted at the dayside, leading to a local retrograde flow. In this work, we do not find this retrograde flow, but instead unperturbed superrotation. This can partly be attributed to the fact that our models do not rely on artificial temperature forcing in the deep atmosphere, but instead, they can capture the feedback between dynamics

and irradiation that tends to strengthen superrotation. Carone et al. (2020) also noted that superrotation is never completely removed, and that there are apparently two tendencies at play in the upper atmosphere: one leading to superrotation and one leading to other flows.

Parmentier et al. (2021) noted that the strength of superrotation in the observable atmosphere at the dayside can be diminished by nightside cloud coverage. Beltz et al. (2022b); Hindle et al. (2021) indicated that magnetic field interaction can completely suppress superrotation. Observationally, it was found that CoRoT-2b appears to have a retrograde flow at the dayside (Dang et al., 2018) and HAT-P-7b may even have a dynamically shifting hot spot (Armstrong et al., 2016). Thus, future works that includes large-scale flow at greater depths is warranted in order to investigate the interplay among more complex physics and its effect on the observable atmosphere.

It has been further hypothesized that shocks, mechanical dissipation of strong winds, and turbulent vertical mixing at greater depths may also inject energy into the interior and contribute to inflation (Li & Goodman, 2010; Heng, 2012; Perna et al., 2012; Fromang et al., 2016; Menou, 2019). It is, however, unclear whether shear flow instabilities at greater depths (Menou & Rauscher, 2009; Rauscher & Menou, 2010; Liu & Showman, 2013; Carone et al., 2020) may affect the vertical heat flow. Tackling these processes requires higher resolution non-hydrostatic 3D atmosphere simulations (Menou, 2019; Fortney et al., 2021).

We note that the question of the importance of dynamical processes at greater depths in atmospheres is neither new nor solely constrained to hot Jupiters. There are clear parallels between the dynamics and the heat transport at greater depths in brown dwarfs (Sainsbury-Martinez et al., 2021). Considerable work has also been done in understanding such processes both for the Earth's climate and for stellar atmospheres. Such examples are clumpy dust formation triggered by shock waves via large scale convective flows at greater depths in AGB stars (Fleischer et al., 1992; Woitke & Niccolini, 2005; Höfner & Freytag, 2019) and the need to resolve downdrafts reaching deep into the interior (Freytag et al., 2017, 2019) or "convective overshooting" at the boundary of convective and stably stratified regions in stars (e.g., Hanasoge et al., 2015; Bressan et al., 1981). The issue of "convective overshooting" seems to resemble the boundary problem between a convective interior and a stably stratified irradiated atmosphere in hot Jupiters. Similar processes are also relevant in Earth GCMs: the importance of dry and moist convection in the Earth's atmosphere and surface friction was identified early on (Manabe et al., 1965; Peixóto & Oort, 1984). The importance of convection and surface friction was also identified in GCMs of tidally locked exo-Earths (Carone et al., 2016;

Koll & Abbot, 2016; Sergeev et al., 2020) and for brown dwarfs (Tremblin et al., 2019). Thus, it comes as no surprise that processes at greater depths matter in hot Jupiters as well. More importantly, deep dynamical processes impact the large-scale circulation higher up and can potentially yield important insights into the evolution of exoplanets.

7 SUMMARY AND CONCLUSIONS

Here, we introduce and explain `expeRT/MITgcm`, which extends the deep wind framework `exorad/MITgcm` of Carone et al. (2020) with full gaseous radiative transfer, including scattering. We demonstrate that the Feautrier method with accelerated lambda iteration and correlated-k is a fast and accurate approach to model the non-gray radiative transfer while still achieving model runtimes of hundreds of simulation days in a single runtime day.

We simulated the two hot Jupiters HD 209458b and WASP-43b which are almost equally irradiated, but which have different orbital periods ($P_{rot}^{HD\ 209458b} = 3.47\,d$ and $P_{rot}^{WASP-43b} = 0.8135\,d$) and surface gravities ($g^{HD\ 209458b} = 8.98\,m\,s^{-2}$ and $g^{WASP-43b} = 46.9\,m\,s^{-2}$).

We find that our results for the observable atmosphere of HD 209458b and WASP-43b agree well with the findings of previous works. Our WASP-43b models were able to confirm a deep equatorial jet as well as a dependency of the temperature in the observable atmosphere on the state of the deep atmosphere as predicted by Carone et al. (2020). However, we did not find the retrograde equatorial flow. Future work is needed to investigate the reason for these differences.

We investigated the deep atmosphere (pressures between 1 and 700 bar) of WASP-43b and HD 209458b and found a difference in the temperature evolution. WASP-43b cools down to a cold temperature in the deep atmosphere, whereas HD 209458b successfully maintains its initial temperature profile within the runtime. This difference in the temperature evolution can be linked to the different values of the surface gravity, where we find that due to the high surface gravity of our WASP-43b simulations, radiative heating and cooling are very important at greater depths. We looked at the dependency of the temperature evolution on the rotation period and found that the difference in temperature evolution is not significantly enhanced by the presence or absence of a deep equatorial jet.

Last but not least, we caution that longer convergence time scales of at least 10000 simulation days are needed to properly resolve the observable atmosphere temperature structure of non-inflated exoplanets such as WASP-43b. The observable atmosphere of inflated hot Jupiters such as HD 209458b

seems to be decoupled from the deep atmosphere and, therefore, it can be expected to be resolved after 1000 days of simulation time.

More work is warranted to identify whether and how energy transport from the irradiated atmosphere into the interior contributes to inflation. The computationally efficient non-gray GCM `expeRT/MITgcm` that we introduce here is an ideal tool to self-consistently tackle deep wind flow and energy transport.

ACKNOWLEDGEMENTS

A.D.S., L.D., U.G.J, S.K. and C.H. acknowledge funding from the European Union H2020-MSCA-ITN-2019 under Grant no. 860470 (CHAMELEON). L.C. acknowledges support from the DFG Priority Programme SP1833 Grant CA 1795/3. L.D. acknowledges support from the KU LEUVEN interdisciplinary IDN grant IDN/19/028 and the FWO research grant G086217N. U.G.J acknowledges funding from the Novo Nordisk Foundation Interdisciplinary Synergy Program grant no. NNF19OC0057374. P.M. acknowledges support from the European Research Council under the European Union's Horizon 2020 research and innovation program under grant agreement No. 832428-Origins. R.B. acknowledges support from a PhD fellowship of the Research Foundation – Flanders (FWO). The computational resources and services used in this work were provided by the VSC (Flemish Supercomputer Center), funded by the Research Foundation Flanders (FWO) and the Flemish Government – department EWI. We also thank an anonymous referee for their very useful comments that helped a lot in the interpretation of the obtained results.

APPENDIX

A IMPORTANCE OF SPHERICITY IN STELLAR ATTENUATION

The incident angle for the stellar light onto the planetary atmosphere is accounted by the factor $\mu_\star$. In Eq. 6.14, $\mu_\star$ is derived assuming plane-parallel geometry, which is a broadly used approximation (see e.g., Showman et al., 2009; Amundsen et al., 2016; Lee et al., 2021). Because this paper is meant to benchmark the radiative transfer implementation by comparing it with previous work, we used plane-parallel atmospheres and did not account for the sphericity of the model atmospheres.

While the incident angle in the substellar region is independent of depth and agrees well with the plane-parallel assumption, substantial differences are expected at the polar regions, where the effective solar path length deviates significantly from the solar path length in plane-parallel, ultimately altering the angle of incidence. The expected deviation in $\mu_\star$ between a spherical and a plane-parallel approximation increases with pressure (and, therefore, optical depth) and is potentially more important at greater depths. On the other hand, we note that the stellar component of the flux $F^\star$ decreases with optical depth.

A correct treatment of sphericity would involve rewriting Eqs. 6.13 and 6.15, which would lead to a double integral over the solid angle. Since this is not computationally feasible, some authors (Li & Shibata, 2006; Mendonça et al., 2018a) who account for sphericity in the environment of a GCM have expanded the plane-parallel assumption with the correction of the effective path-length. The resulting incident angle $\mu_{\star,\mathrm{eff}}(z)$ would then be dependent on the height z and the planetary radius R_p and is in its simplest approximation given by (Li & Shibata, 2006):

$$\mu_{\star,\mathrm{eff}}(z) = \sqrt{1 - \left(\frac{R_p}{R_p + z}\right)^2 (1 - \mu_\star^2)}. \tag{6.24}$$

In conclusion, the plane-parallel assumption is suitable if only the uppermost part of the atmosphere is probed or if the error of the optical depth within the polar regions causes only negligible effects. If the atmosphere is to be probed deeper, an additional treatment of the sphericity is vital (e.g., Li & Shibata, 2006). We plan to incorporate this aspect in an upcoming work.

B VERIFICATION OF THE RADIATIVE TRANSFER

It has been shown in previous works (Showman et al., 2009; Amundsen et al., 2016; Lee et al., 2021) as well as in this work that the inclusion of a full gaseous radiative transfer in GCMs is vital to obtain a full understanding of the atmospheric dynamics of hot Jupiters. However, a correct treatment of radiative transfer in the framework of a GCM is computationally very expensive and simplifications need to be well understood and justified. The correlated-k approximation and the assumption of equilibrium chemistry both lead to significant simplifications.

We tested the validity of radiative transfer in our model in a three-step process. We first show a comparison of the fluxes and heating rates obtained with `petitRADTRANS` and `expeRT/MITgcm` in Sect. B.1 and then our testing of the wavelength binning, done by comparing the resulting temperature profile in Sect. B.2. We finally show our testing of the influence of the horizontal interpolation of fluxes on the temperature profile in Sect. B.3.

B.1 *Verification of fluxes and heating rates*

We follow the suggestion of Amundsen et al. (2014) and implement their dayside test for a cloud-free atmosphere in `expeRT/MITgcm`. We show the fluxes and heating rates in Fig. 6.11, where we compare the results obtained with `expeRT/MITgcm` in different wavelength resolutions with scattering turned on and off to results obtained with `petitRADTRANS`, which has been benchmarked in Baudino et al. (2017).

We find that our results agree well with `petitRADTRANS`, which uses a much higher wavelength resolution of approximately 1000 times more correlated-k wavelength bins compared to the nominal resolution of our models (see Table 6.3). We note that the employed method of random sampling to combine opacities of individual species is prone to errors in the order of a few percent. On top of that, there is a general loss of accuracy when using low-resolution opacities (e.g., Leconte, 2021), which is also in the order of a few percent.

The differences in the bolometric stellar flux ($F^{\star}_{\nu}$) can be explained by the numerical accuracy of the integration, which depends on the amount of frequency bins used to integrate the spectral flux (see Eq. 6.17). Reducing this error would require calculations of the stellar bolometric flux for a high wavelength resolution and a normalization of the stellar spectral flux to the high-resolution bolometric flux. The current low-resolution implementation of `petitRADTRANS` does not include such a normalization, so any future implementation of `expeRT/MITgcm` might improve on that.

Overall, there seems to be a general good agreement between Fig. 6.11 and the simulations shown in Amundsen et al. (2014). We note that Amundsen et al. (2014) used the Kurucz stellar spectrum[6], while we used the PHOENIX stellar spectrum (Husser et al., 2013) that is part of `petitRADTRANS`. Differences might also occur due to the different opacities, where we used the same species as mentioned in Amundsen et al. (2014), but from updated opacity sources (see Table 6.1). Furthermore, we used the equilibrium chemistry of Mollière et al. (2019), while Amundsen et al. (2014) used the analytic abundances of Burrows & Sharp (1999).

B.2 *So vs S1*

We perform an additional simulation of HD 209458b using the S1 resolution in order to benchmark the So resolution used in the model (see Table 6.3). The wavelength resolution S1 is introduced in Kataria et al. (2013). This additional simulation is initialized with the results of the So simulation, shown in Sect. 3.1 at 10000 days. We then run the model for 2000 days and compare the resulting temperature profile in Fig. 6.12.

We find that differences between the two wavelength resolutions are on the order of a few percent in the observable part of the atmosphere, while the relative error decreases with pressure. The hotter temperature of the upper layers in the So simulation can partly be accounted for by the stronger incoming flux, as discussed above. We note that the smaller error in the deeper layers of the atmosphere demonstrates that the deep layers are not radiatively driven, and can only be driven by other mechanisms such as dynamics at greater depths.

B.3 *Performance of the interpolation scheme*

We performed an additional short term simulation (run for 100 days) without the horizontal interpolation of fluxes, where we solved the radiative transfer equation in every grid cell instead of every second grid cell (see Fig. 6.1). These models are identically to the cold HD 209458b model presented in Sect. 4, where we use a globally isothermal temperature of 2000 K to initialize the model. We show the resulting time averaged temperature after 100 days of the model with and without interpolation in Fig. 6.13 and find that both agree within 2%. We can therefore conclude that the small wavelength resolution introduces a larger error compared to the error introduced by the horizontal interpolation of the fluxes.

6 see `http://kurucz.harvard.edu/stars/hd209458/`

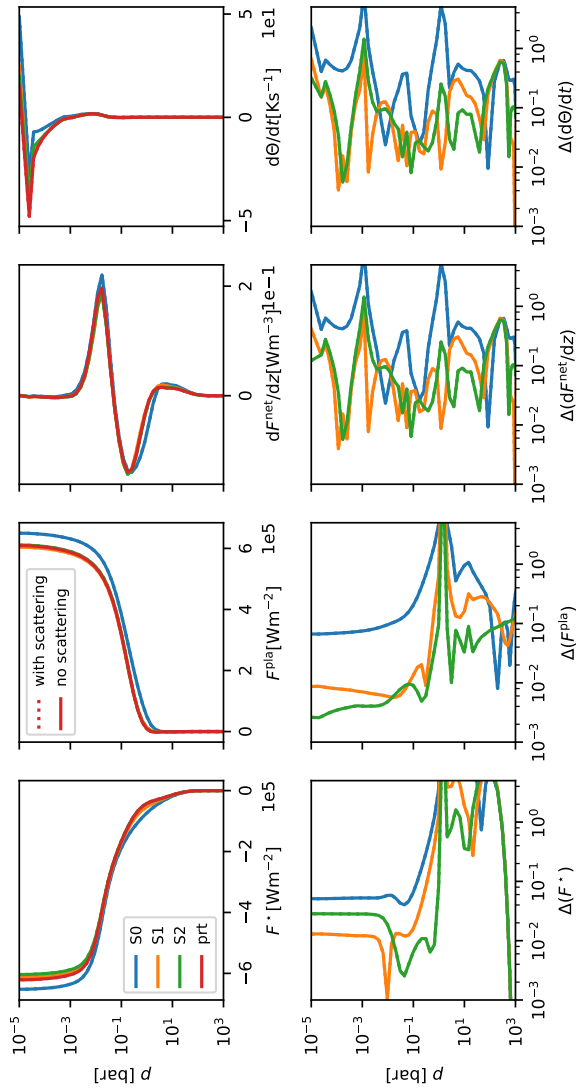

Figure 6.11: Test 3 of Amundsen et al. (2014) for a mixed dayside hot Jupiter atmosphere, where we compare fluxes and heating rates for different wavelength resolutions (see Table 6.3) in `expeRT/MITgcm` (S0, S1, S2) to `petitRADTRANS` (prt). The bottom panels display the residuals of the above panels. From left to right, we show the incoming stellar flux, the emitting planetary flux, the gradient of the net flux, and the resulting change of potential temperature.

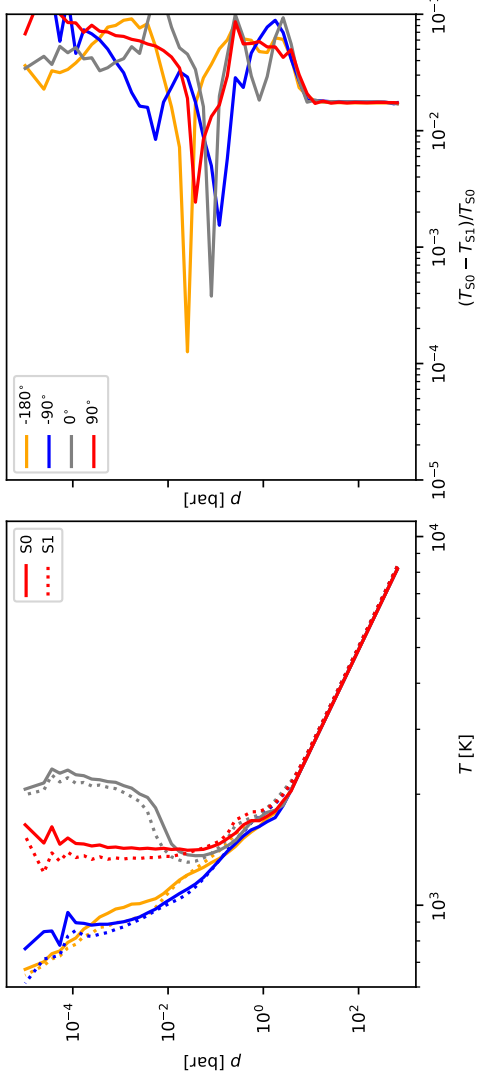

Figure 6.12: Additional test demonstrating the performance of S0 vs S1 by looking at the final temperature differences (at 12000 days) for several longitudes. The S1 simulation is initialized at 10000 days using the state of the nominal S0 simulation.

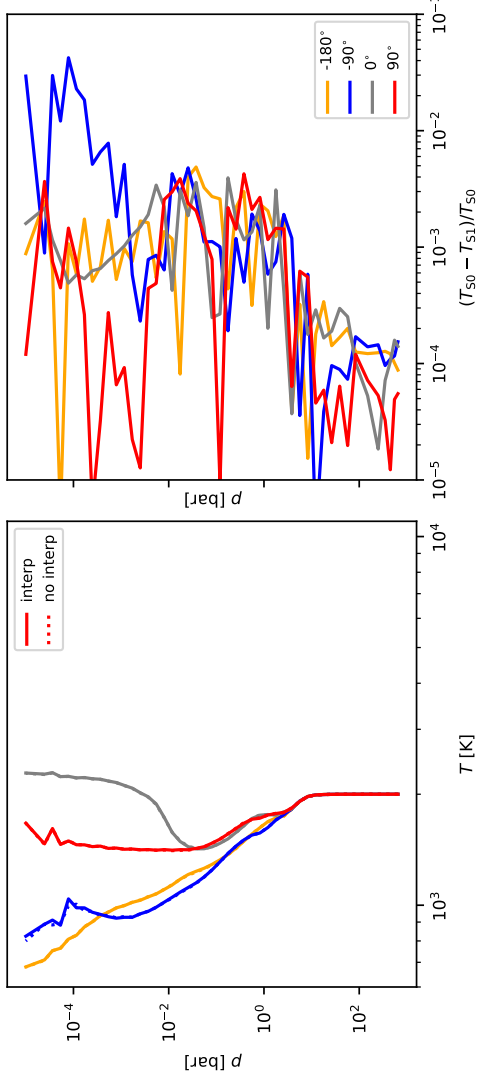

Figure 6.13: Additional test demonstrating the performance of the flux interpolation scheme (see Fig. 6.1 and Sect. 2.2) by looking at an isothermally (T=2000 K) initialized HD 209458b simulation with and without the horizontal interpolation of fluxes.

C PARAMETERS

Table 6.4: Parameters

Parameter	Meaning	HD 209458b	WASP-43b
Δt	dynamical time-step	25 s	25 s
$T_\star$	stellar temperature	6092 K	4520 K
$R_\star$	stellar radius	$1.203\,R_\odot$	$0.667\,R_\odot$
a_p	semi-major axis	0.047 47 AU	0.015 26 AU
T_{irr}	substellar irradiation temperature	1479 K	1441 K
Θ_{ad}	initial temperature at 1 bar	1800 K	1400 K
R_p	planetary radius	$1.38\,R_{Jup}$	$1.036\,R_{Jup}$
c_p	specific heat capacity at const. p	$12\,766\,J\,kg^{-1}\,K^{-1}$	$12\,766\,J\,kg^{-1}\,K^{-1}$
R	specific gas constant	$3590\,J\,kg^{-1}\,K^{-1}$	$3590\,J\,kg^{-1}\,K^{-1}$
P_{rot}	rotation period	3.47 d	0.8135 d
g	surface gravity	$8.98\,m\,s^{-2}$	$46.9\,m\,s^{-2}$
k_{top}	sponge layer Rayleigh friction	$20\,d^{-1}$	$20\,d^{-1}$
τ_{deep}	timescale for Rayleigh friction in deep layers	1 d	1 d
p_{top}	lowest pressure level	1×10^{-5} bar	1×10^{-5} bar
p_{bottom}	highest pressure level	700 bar	700 bar
N_{layers}	vertical resolution	47	47

Notes: Parameters used in simulations throughout this work.

Table 6.5: Radiative time-steps

time [days]	$\Delta t^{rad}_{HD_2}$ [s]	Δt^{rad}_{W43b} [s]
0-500	100	100
500-12 000	300	100

Notes: Radiative time-steps $\Delta t^{rad}_{HD_2}$ and Δt^{rad}_{W43b} for the simulations shown in Sect. 3.1 and 3.2 respectively. The radiative time-step is increased stepwise, since temperature tendencies decrease with time.

We show the parameters that we employ in our models of HD 209458b and WASP-43b in Table 6.4. We update the radiative fluxes of WASP-43b more often than we do for HD 209458b, since our models of WASP-43b keep evolving in temperature even after hundreds of days, whereas our model of HD 209458b shows no sign of temperature evolution after a few hundred days. The corresponding numerical flux update rates (radiative time-steps) are shown in Table 6.5.

D SIMPLIFIED FORCING VS FULL RADIATIVE TRANSFER

Our simulations of HD 209458b and WASP-43b with fully coupled radiative feedback are compared to similar simulations from a grid of 3D GCM models taken from Baeyens et al. (2021) with different parameters. The grid models are forced using the Newtonian cooling formalism and use the same model as in Carone et al. (2020). Specifically, to match the climate properties of HD 209458b a model with $T_{eff} = 1400\,K$, $g = 10\,m\,s^{-2}$ and host star type G5 is selected (Figs 6.14 and 6.15). For the WASP-43b-like case, we compare our simulation to a model with $T_{eff} = 1400\,K$, $g = 100\,m\,s^{-2}$ and host star type K5 (Figs 6.16 and 6.17). Additional information about these grid models can be found in Baeyens et al. (2021). Because the Newtonian-cooled grid models and the fully coupled models in this work make use of the same dynamical core (`MITgcm`) and similar radiative transfer module (`petitRADTRANS`), their comparison highlights the important role of radiative feedback in hot Jupiter climates. We note that the grid models do not use TiO and VO opacities, while the fully coupled models do include TiO and VO, leading to a temperature inversion in the fully coupled models, which is not to be expected in the Newtonian-cooled models.

In general, the Newtonian-cooled grid models show qualitative agreement with the simulations presented in this work, but quantitative differences are

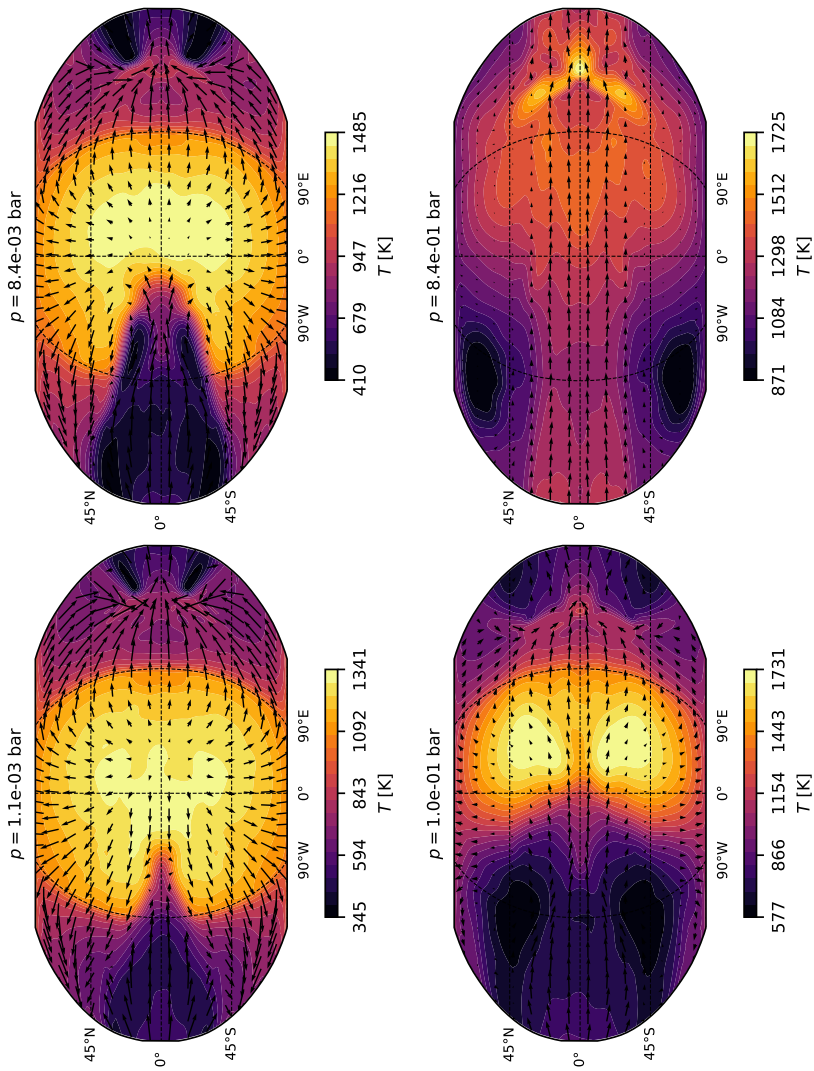

Figure 6.14: Maps of a model of HD 209458b with Newtonian cooling displaying the color coded temperature at different pressure levels (like Fig. 6.2).

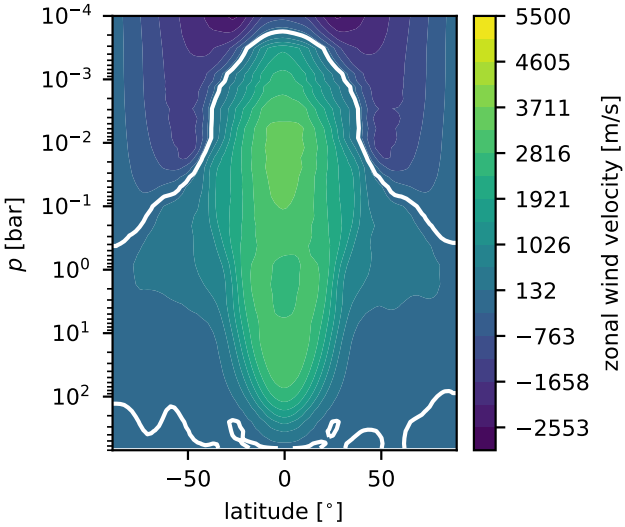

Figure 6.15: Zonally averaged zonal wind velocities (like Fig. 6.3) for the model of HD 209458b with Newtonian cooling.

present. For the case of HD 209458b, the grid model (Fig. 6.14) appears to be cooler than the fully coupled model (Fig. 6.2), in particular regarding the nightside of the planet, owing to the colder effective temperature of the grid model. The equatorial jet is not as fast in the grid model as in the fully coupled simulation. In the former, it reaches wind speeds up to $5.0\,\mathrm{km\,s^{-1}}$, whereas in the latter, wind speeds up to $7.2\,\mathrm{km\,s^{-1}}$ are attained (see Figs 6.15 and 6.3). Finally, the jet persists up to the lowest pressures in the fully coupled simulation, whereas in the Newtonian-cooled model, the low-pressure regime is characterized by a thermally direct day-to-night circulation. The transition between a shallow and a deep jet seems to be for rotation periods between two and three days (e.g, compare first two columns of Fig. 3 from Baeyens et al., 2021), and because the grid model is not a perfect match to HD 209458b, it falls on the different side of this transition.

The disappearance of cold nightsides with a reduced day-night temperature contrast and a thermally direct wind flow at high altitudes, when full radiative feedback is taken into account, can also be seen in Amundsen et al. (2016). A more efficient day-night heat redistribution, when radiative feedback is taken into account, was also noted by Showman et al. (2009). In the models of Amundsen et al. (2016), however, the wind speed of the zonal jet stream is slightly slower in the fully coupled GCM than in the Newtonian-cooled GCM.

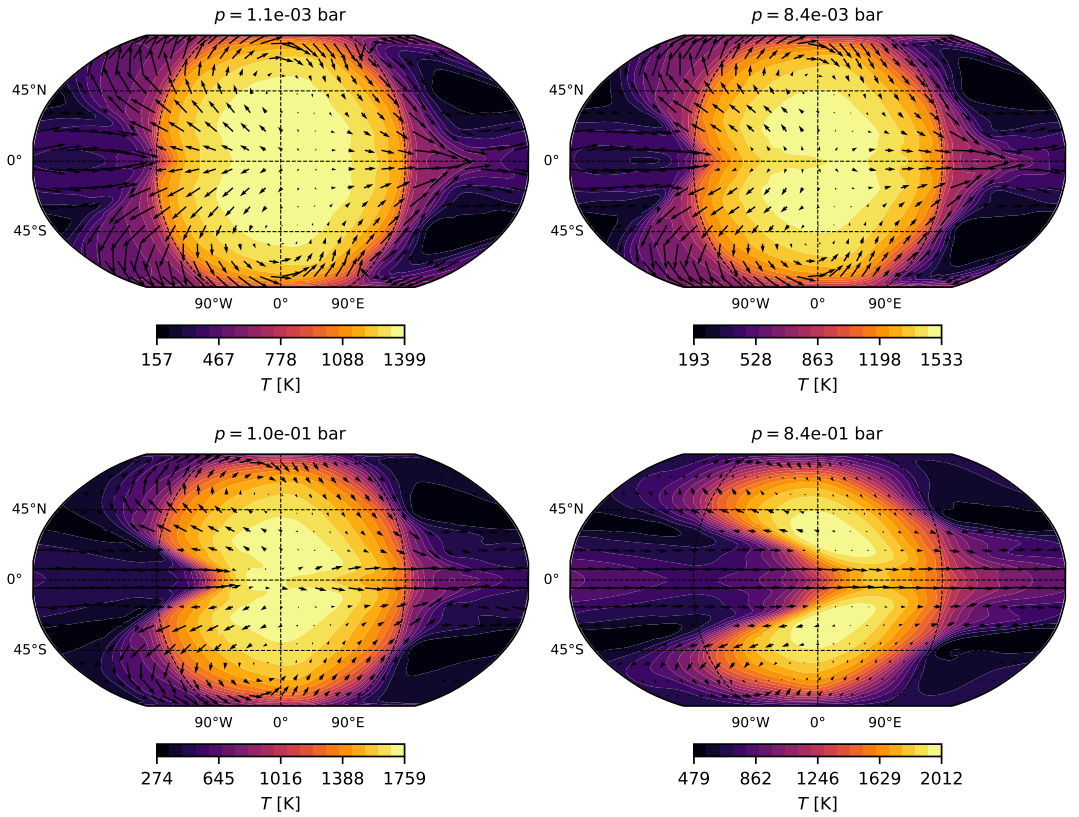

Figure 6.16: Maps of WASP-43b with Newtonian cooling displaying the color coded temperature at different pressure levels (like Fig. 6.4).

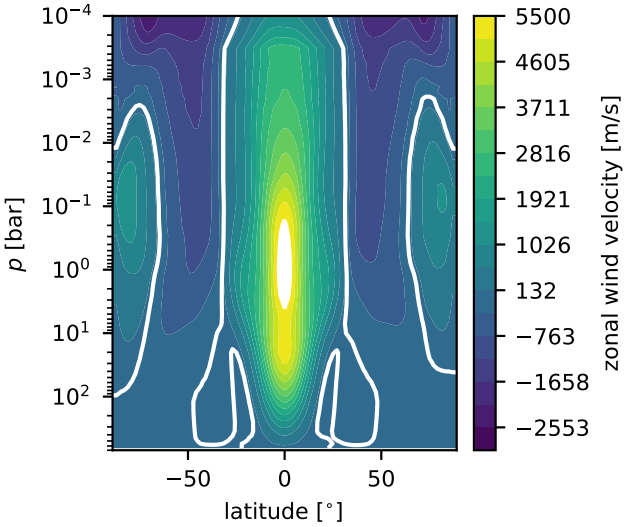

Figure 6.17: Zonally averaged zonal wind velocities (like Fig. 6.5) for the model of WASP-43b with Newtonian cooling.

In contrast, we find that the full radiative feedback yields a zonal jet stream that is slightly faster than the Newtonian-cooled case. Hence, further detailed comparisons between the two forcing mechanisms are necessary to establish their impact on the jet stream speed.

Finally, for the case of WASP-43b, the same quantitative changes discussed above can be observed when a Newtonian-cooled and fully coupled model are compared. Additionally, a climate transition is observed, in which the Newtonian-cooled model yields equatorial retrograde flow (Fig. 6.16), but the fully coupled model does not (Fig. 6.4). A possible explanation for the disappearance of retrograde flow in the latter case could be that retrograde and superrotating equatorial flow are competing tendencies (Carone et al., 2020). The increase in jet strength in the fully coupled model, as established in the HD 209458b comparison in the previous paragraph, would then become the dominant tendency in WASP-43b. Given that the fully coupled model should be the more realistic of the two forcing mechanisms, future investigations will be needed to investigate whether retrograde equatorial wind flow can also be elicited in models with radiative feedback.

7

NO EVIDENCE FOR RADIUS INFLATION IN HOT JUPITERS FROM VERTICAL ADVECTION OF HEAT

Aaron David Schneider, Ludmila Carone, Leen Decin, Uffe Gråe Jørgensen & Christiane Helling

Published in Astronomy & Astrophysics, Volume 666, id.L11, October 2022

Author contributions:
Aaron Schneider designed the study, ran the simulations, which are part of the study and wrote the manuscript. Ludmila Carone, Leen Decin and Uffe Gråe Jørgensen supervised Aaron Schneider and contributed to the manuscript and discussion of the results. Christiane Helling supplied feedback to the manuscript.

Original Abstract
Elucidating the radiative-dynamical coupling between the upper photosphere and deeper atmosphere may be key to our understanding of the abnormally large radii of hot Jupiters. Very long integration times of 3D general circulation models (GCMs) with self-consistent radiative transfer are needed to obtain a more comprehensive picture of the feedback processes between dynamics and radiation. Here, we present the longest 3D nongray GCM study to date (86 000 d) of an ultra-hot Jupiter (WASP-76 b) that has reached a final converged state. Furthermore, we present a method that can be used to accelerate the path toward temperature convergence in the deep atmospheric layers. We find that the final converged temperature profile is cold in the deep atmospheric layers, lacking any sign of vertical transport of potential temperature by large-scale atmospheric motions. We therefore conclude that coupling between radiation and dynamics alone is not sufficient to explain the abnormally large radii of inflated hot gas giants.

1 INTRODUCTION

Characterizing and understanding the atmospheres of exoplanets is now more within reach than ever before thanks to the recent launch of the *James Webb Space Telescope* (JWST). Many of the observed hot gas giants exhibit very large radii and therefore low bulk densities. One of the long-standing questions in the field of hot and ultra-hot Jupiters (UHJs) pertains to the mechanism that inflates those planets. Interior models of the observed exoplanet population reveal that the state of inflation links the incident flux with the temperature in the deep atmosphere (Thorngren & Fortney, 2018; Thorngren et al., 2019; Sarkis et al., 2021). These studies find that the intrinsic temperatures increase with instellation and peak at an instellation of $\approx 2 \times 10^9$ erg/s/cm^2 (Thorngren et al., 2019). Different explanations have been proposed to understand the mechanisms that lead to these hot intrinsic temperatures. There are two hypotheses that could explain inflation (Fortney et al., 2021). The first proposes that planets are heated by tidal interactions (e.g., Bodenheimer et al., 2001; Arras & Socrates, 2010; Socrates, 2013), whereas the second claims that incident stellar flux is deposited into the deep atmosphere.

A prominent theory that fits with the latter hypothesis is Ohmic dissipation (Perna et al., 2010a; Batygin & Stevenson, 2010; Menou, 2012; Rauscher & Menou, 2013; Helling et al., 2021b; Knierim et al., 2022), which proposes that magnetic fields should couple to ionized flows in the upper atmosphere,

slowing down zonal winds and therefore depositing heat by friction. However, it is unclear whether or not this mechanism is sufficiently active at sufficiently deep layers to heat the deep atmosphere (Rauscher & Menou, 2013). Using a 2D model with parameterized vertical transport, Tremblin et al. (2017) find that heat would be transported downwards by means of vertical transport of potential temperature without the need of magnetic fields. The authors claim that incident energy input from stellar instellation is self-consistently advected downwards. Idealized 3D general circulation models (GCM) with parametrized thermal forcing seem to reproduce this mechanism (Sainsbury-Martinez et al., 2019, 2021).

In recent work, we introduced `expeRT/MITgcm`, a 3D GCM with self-consistent radiative transfer for hot Jupiters without the limitations of the above-mentioned models (Schneider et al., 2022b). In this latter paper, we focussed on the effects of surface gravity and rotation rate on the temperature evolution. Here, we extend this work to the final state of the converged atmosphere, using the same 3D nongray GCM and integrating for long enough to converge the temperature in the deep atmosphere.

In order to find a planet that is suitable for studying the issue of temperature convergence in the deep layers of the atmosphere, we decided to go to the temperature extremes and simulate the ultra-hot Jupiter WASP-76 b. WASP-76 b has been observed with radial velocity (West et al., 2016) and transit spectroscopy (Seidel et al., 2019) and has both a Spitzer phase curve (May et al., 2021) and winds characterized by high-resolution spectroscopy (Ehrenreich et al., 2020; Kesseli & Snellen, 2021; Kesseli et al., 2022). Additionally, the climate of WASP-76 b was recently modeled (Wardenier et al., 2021; Savel et al., 2022; Beltz et al., 2022a). WASP-76 b has a very low bulk density and can therefore be considered to be inflated, while we also know that it receives a high incident stellar flux. We therefore expect there to be a mechanism at play that inflates the radius of this giant planet by transporting potential energy downwards.

We begin by describing the methods used in this paper (Sect. 2). We then explain how we reached temperature convergence in our models (Sect. 3) before discussing the limitations of our methods (Sect. 4). Finally, we present our conclusions in Sect. 5.

2 METHODS

2.1 *General circulation model*

This work utilizes `expeRT/MITgcm` described in detail in Schneider et al. (2022b) and Carone et al. (2020). In particular, `expeRT/MITgcm` builds on the dynamical core of the general circulation model (GCM) `MITgcm` (Adcroft et al., 2004) and solves the 3D hydrostatic primitive equations of fluid dynamics (e.g., Showman et al., 2009, Eq. 1-4) on an Arakawa C-type cubed-sphere grid with a resolution of C32 assuming an ideal gas. The vertical grid contains 41 logarithmically spaced layers from 1×10^{-5} bar to 100 bar, extended by six linearly spaced layers between 100 bar and 700 bar. The model includes Rayleigh friction at the bottom of the computational domain (below 490 bar), a sponge layer at the top of the atmosphere (above 1×10^{-4} bar), and a fourth-order Shapiro filter. We caution that the choice of numerical methods, such as the choice of the dynamical core, often has a significant influence on the circulation and the temperature (Heng et al., 2011b; Polichtchouk et al., 2014; Skinner & Cho, 2021; Carone et al., 2021). For the scope of this work, we identify the use of deep drag as having possible repercussions for our findings, and therefore discuss the influence of the drag on the results of this work in Appendix A.

The temperature in the atmosphere is forced by radiative heating and cooling using a multi-wavelength radiative transfer scheme that operates during the runtime of the climate model. More specifically, the radiation field is updated with a radiative time step of $\Delta t_{rad} = 100$ s, which is four times the dynamical time step $\Delta t_{dyn} = 25$ s. The radiative transfer includes scattering and uses five correlated-k wavelength bins with 16 Gaussian quadrature points per wavelength bin. The implementation of radiative transfer in `expeRT/MITgcm` is based on `petitRADTRANS` (Mollière et al., 2019, 2020). One advantage of using `expeRT/MITgcm` is its flexibility and performance, which enable long integration times while maintaining the accuracy of a multi-wavelength radiation scheme (Schneider et al., 2022b).

We use opacities on a pre-calculated grid of pressure and temperature, assuming local chemical equilibrium. Most opacities are obtained from exomol[1], and we use H_2O (Polyansky et al., 2018), CO_2 (Yurchenko et al., 2020), CH_4 (Yurchenko et al., 2017), NH_3 (Coles et al., 2019), CO (Li et al., 2015), H_2S (Azzam et al., 2016), HCN (Barber et al., 2014), PH_3 (Sousa-Silva et al., 2015), TiO (McKemmish et al., 2019), VO (McKemmish et al., 2016), FeH (Wende et al., 2010), Na (Piskunov et al., 1995), and K (Piskunov et al., 1995) opacities for the gas absorbers. Furthermore, we include Rayleigh scattering with H_2 (Dalgarno & Williams, 1962) and He (Chan & Dalgarno, 1965) and collision-induced absorption (CIA) with H_2–H_2 and H_2–He (Borysow et al.,

1 https://www.exomol.com/

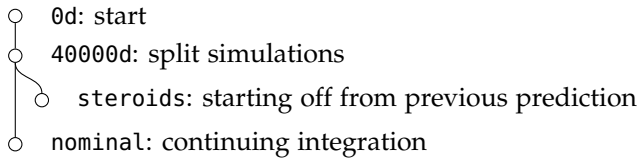

Figure 7.1: Overview of the simulations in this work. The `steroids` model starts at $t = 40\,000$ d from the `nominal` model with the guess of the final state obtained via the method outlined in Appendix B.

1988, 1989; Borysow & Frommhold, 1989; Borysow et al., 2001; Richard et al., 2012; Borysow, 2002) and H^- (Gray, 2008).

As the goal of this paper is to look at the conservation of energy and the interplay between dynamical energy transport and radiative energy transport, we updated `expeRT/MITgcm` to conserve energy lost by friction at the bottom boundary. Kinetic energy lost due to friction on the horizontal velocity $\vec{u}$ [$m\,s^{-1}$] is converted to thermal energy using the following equation (Rauscher & Menou, 2013):

$$\frac{dT}{dt} = \frac{u^2}{c_p \tau_{deep}}, \tag{7.1}$$

where $\frac{dT}{dt}$ [$K\,s^{-1}$] is the change in the temperature T [K], τ_{deep} is the friction timescale (as described in Schneider et al., 2022b; Carone et al., 2020), and c_p [$J\,kg^{-1}\,K^{-1}$] is the heat capacity at constant pressure. Otherwise, we use the same parameters as in Schneider et al. (2022b).

2.2 *Setup of WASP-76 b simulations*

We use `expeRT/MITgcm` to model WASP-76 b, an ultra-hot Jupiter orbiting WASP-76, where we assume $T_\star = 6250\,K$ and $R_\star = 1.73\,R_\odot$ as the stellar temperature and radius of WASP-76 (West et al., 2016). We model WASP-76 b on a tidally locked orbit of 0.033 AU with an orbital period of 1.8 d (West et al., 2016). The planetary radius and mass are taken as $1.83 R_{jup}$ and $0.92 M_{jup}$ respectively (West et al., 2016), resulting in a low gravity of $g = 6.81\,m\,s^{-2}$. We use $c_p = 13\,784\,J\,kg^{-1}\,K^{-1}$ and $R = 3707\,J\,kg^{-1}\,K^{-1}$ as the specific heat capacity at constant pressure and the specific gas constant, respectively.

We set up two models in this paper (Fig. 7.1). The `nominal` model is a model of WASP-76 b, which has been initialized with a particularly hot initial state. We use the same method to initialize the temperature profile that was used in

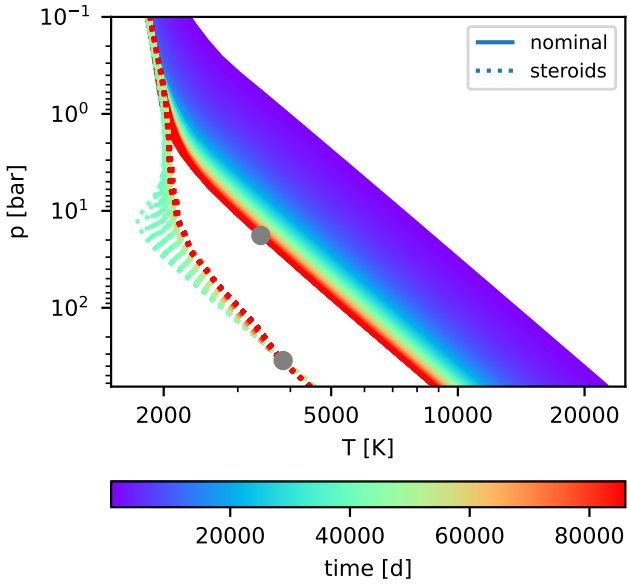

Figure 7.2: Temperature evolution (color coded) of the horizontally averaged temperature in the deep layers of the atmosphere for the `nominal` model (solid lines) and the `steroids` model (dotted lines). A gray dot displays the position of the radiative convective boundary (RCB) at the final state.

Schneider et al. (2022b), incorporating an adiabatic temperature profile below 10 bar with $\Theta_{ad} = 4000\,\mathrm{K}$ as the temperature that the adiabat would have at 1 bar. We chose such a hot initial state because planets are thought to form in hot conditions (e.g., Fortney et al., 2021).

The `steroids` model has been initialized from the `nominal` model at $t = 40\,000$ d. The initialization of the `steroids` model is done by extrapolating the temperature evolution of the `nominal` model using log-linear regression. The extrapolation to find the `steroids` model resembles a hotter limit on the prediction from the temperature evolution of the `nominal` model up until $t = 40\,000$ d, while we take over the dynamical state (e.g., the velocity field). We explain the details of the fit and initialization in Appendix B.

3 RESULTS FROM A NONGRAY 3D GCM

Utilizing the performance of `expeRT/MITgcm`, we monitor the temperature convergence of WASP-76 b up to $t = 86\,000$ d. We show the final atmospheric

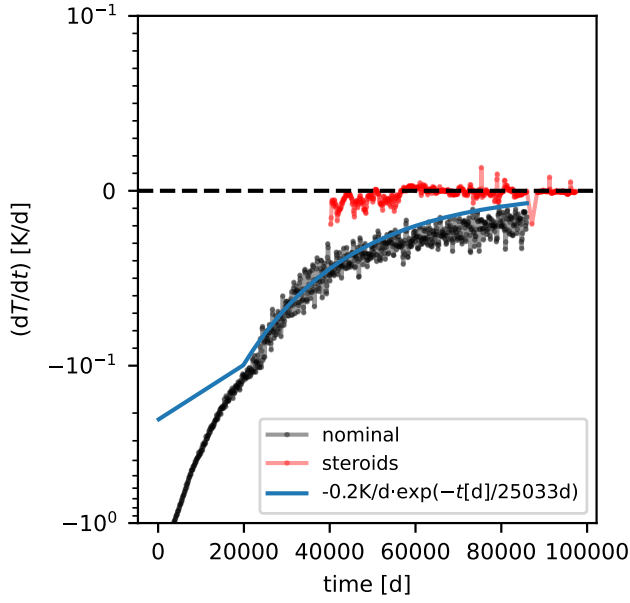

Figure 7.3: Evolution of the rate of temperature change at 650 bar with time of the `nominal` (black) and the `steroids` (red) model. We note that the y-axis is linear between −0.01 and 0.01 and logarithmic elsewhere. The fit on the rate of temperature change by an exponential decay around t = 40 000 d is shown in blue.

state and observables in Appendix C. The horizontally averaged thermal profile for pressures above $p = 0.1\,\mathrm{bar}$ is shown in Fig. 7.2. The `nominal` model cools down from an initially hot state to an almost stable solution within 30 000 d, where the temperature changes at the bottom boundary become smaller than $0.1\,\mathrm{K\,d^{-1}}$, as shown in Fig. 7.3. However, the temperature of the model continues to decrease further and will reach a much colder state within reasonable timescales. Structure models such as those of Thorngren et al. (2019) and Sarkis et al. (2021) often give predictions about the location of the radiative convective boundary (RCB), defined as the first pressure layer from the bottom upwards, where the temperature becomes subadiabatic (Thorngren et al., 2019). For better comparison of our model to those predictions, we calculate the RCB in the same way, and show this as gray dots in Fig. 7.2.

We fitted the temperature evolution around 40 000 d in order to estimate how much colder the final state would be. Assuming an exponential decay of the temperature changes with time, we estimated the final temperature at $p = 650\,\mathrm{bar}$ to be $T = 4567\,\mathrm{K}$ (Appendix B). We performed a second simulation (dubbed `steroids`) using this final state as an initial condition to monitor the stability of such a model. The resulting temperature evolution of this model is shown as dotted lines in Fig. 7.2. The new initial state seems to be a good initial guess in the deep layers, whereas some adjustment happens in intermediate layers between 0.1 bar and 100 bar. Looking at the temperature change rates (Fig. 7.3), we find that the temperature reaches a steady state, where the temperature stops changing, and the temperature changes start to swap signs in an oscillating manner with $\approx 5 \times 10^{-3}\,\mathrm{K\,d^{-1}}$. We therefore claim that temperature convergence has been reached in the `steroids` model, implying that the temperature of our WASP-76 b models self-consistently converges to a cold interior.

The planet gains energy from stellar irradiation and loses energy by thermal radiation. We can therefore formulate the energy balance as an integral over the net radiative flux F_{tot} as

$$\int F_{tot}(\varphi, \vartheta) dA = \int (F_\star + F_{pla}) dA = 4\pi R_{pla}^2 \sigma_{SB} T_{int}^4, \tag{7.2}$$

where ϑ and φ are latitude and longitude respectively, $T_{int}[\mathrm{K}]$ is the intrinsic temperature and R_{pla} is the planetary radius. Here, F_{pla} and $F_\star$ are the planetary and stellar fluxes, respectively. In radiative equilibrium, without an internal energy source, it should hold that

$$\int F_\star dA = -\int F_{pla} dA, \tag{7.3}$$

and subsequently $T_{int} = 0\,K$ from Eq. 7.2. We note that we do not impose a nonzero flux as the boundary condition of the radiative transfer in our GCM. Instead, the boundary condition for the thermal flux at the deepest layer of the atmosphere is zero, which corresponds to $T_{int} = 0\,K$.

We display the effect of the intrinsic temperature on the temperature profile in Fig. 7.4, where we show temperature profiles with three different intrinsic temperatures (500 K, 600 K, and 700 K) along with the final time steps of the `steroids` and `nominal` model from Fig. 7.2. The temperature profiles for the different intrinsic temperatures have been calculated from the temperature evolution of the `nominal` model (Fig. 7.2) using Eq. 7.2 with bolometric fluxes, which was computed during the runtime of the climate simulations. The `steroids` model has a negative total net flux, rendering it impossible to calculate a physical meaningful intrinsic temperature.

Combining the predictions from Thorngren et al. (2019) and Sarkis et al. (2021), we find that the intrinsic temperature of WASP-76 b should be approximately $(600 \pm 100)\,K$ and the RCB location should be $(1 \pm 1)\,bar$ according to structure models. Thus, we can compare the intrinsic temperature to the predictions and find that the intrinsic temperature of the final `nominal` model is 434 K, which is significantly below the predicted value of 600 K from structure models.

The right plot in Fig. 7.4 displays the RCB location for the same models. Comparing the RCB location of the final globally averaged `nominal` and `steroids` model to the predictions from the above-mentioned 1D structure models, we find that the locations of the RCB in our models are much deeper than 10 bar, and therefore not in line with predictions. Rauscher & Showman (2014) showed that the RCB location varies horizontally, because the equatorial regions have higher stellar fluxes than the polar regions. We therefore performed additional calculations of the RCB with temperature averages of the polar ($|\vartheta| > 45°$) and equatorial ($|\vartheta| < 45°$) regions. We can confirm the findings of Rauscher & Showman (2014), namely that the RCB location seems to vary horizontally, where we find higher and deeper levels for polar and equatorial regions, respectively. The different values of the RCB for different horizontal regions is caused by the fact that the temperature becomes horizontally homogeneous only at deeper levels in the atmosphere. We therefore conclude that the intrinsic model differences of 1D and 3D models make the comparison of RCB locations more difficult.

We show the evolution of the area-integrated radiative fluxes ($F_\star$ and F_{pla}) along with the total energy of the `steroids` and `nominal` in Fig. 7.5. We follow

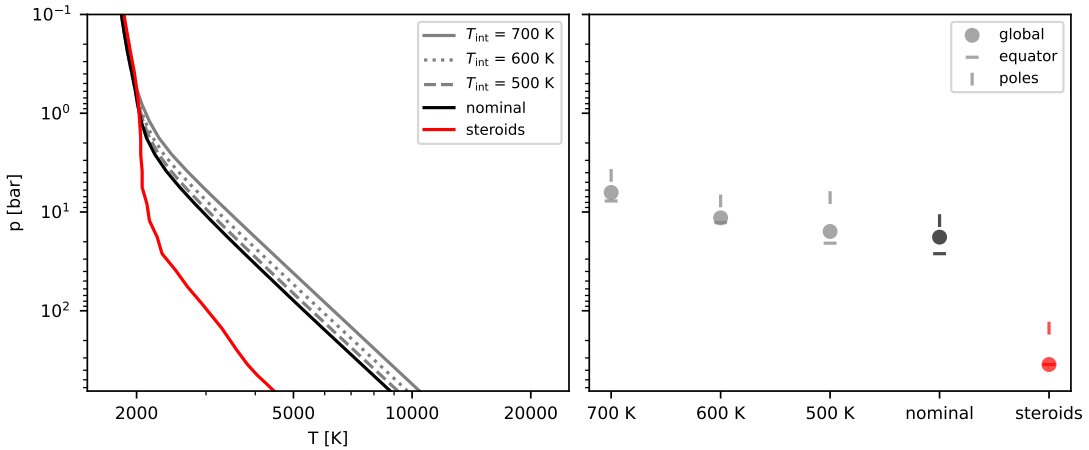

Figure 7.4: Temperature profiles and RCB locations. Left: Temperature profiles for different intrinsic temperatures (gray) and final temperature profiles of the `nominal` ($T_{int} \approx 434$ K) and `steroids` simulation. Right: Calculated RCB for the different temperature profiles of the left panel. Additional markers display the RCB calculated for the equatorial and the polar region. The gray profiles are calculated from the temperature evolution of the `nominal` model. We note that the `steroids` model loses energy due to dissipation and therefore has no physical intrinsic temperature.

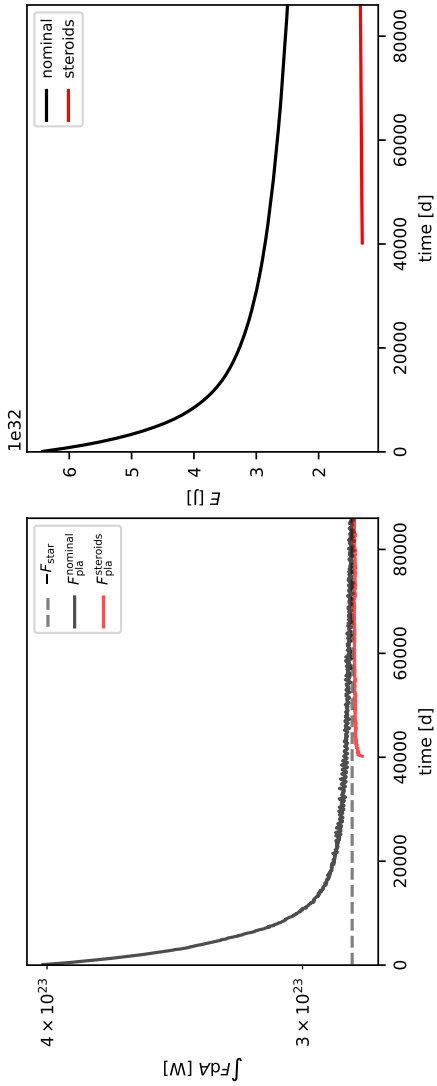

Figure 7.5: Energy budget of the `nominal` and `steroids` simulations. Left: Radiative energy budget ($\int F dA$). Right: Evolution of the total energy. Both simulations converge toward radiative equilibrium with approximately 0.1% accuracy.

Polichtchouk et al. (2014) and calculate the total energy (TE) as a sum of the potential, kinetic, and internal energy by

$$\mathrm{TE} = \int_V \left(\frac{u^2 + v^2}{2} + c_p T + gZ \right) \rho dV, \tag{7.4}$$

where Z is the geometric height. The plot shows that the high temperatures in the deep atmosphere do not lead to large flux differences between the stellar and planetary fluxes, which can be explained by the relation between flux and temperature, which goes with the fourth power of the temperature (Eq. 7.2). Intrinsic temperatures on the order of 1000 K therefore become insignificant against the temperature of the thermal emission, which is on the order of 2000 K. The `nominal` model loses energy during its evolution as the planet cools down, whereas the `steroids` model heats up again slightly. These trends manifest themselves in the right panel of Fig. 7.5, showing that the `steroids` model conserves the total energy, whereas the `nominal` model is still losing energy through radiation to space.

Our model conserves the radiative energy to roughly 99.9%. Deitrick et al. (2022) recently reported that in practice their `THOR` GCM always tends toward a negative radiative flux balance, with discrepancies of as large as a few percent. The authors claim that the reason for that can be found in the numerical dissipation processes in their model such as sponge layers and hyper-diffusion.[2] Similarly, Rauscher & Menou (2012) report that their total radiative heating rate is always positive, balancing a loss of kinetic energy due to numerics. The conservation of energy and angular momentum in `MITgcm` was benchmarked by Polichtchouk et al. (2014), revealing that `MITgcm` is particularly poor at conserving angular momentum, whereas it performs well at conserving energy, which can be confirmed for the `steroids` model in the right panel of Fig. 7.5. We therefore think that conservation of the radiative energy with an accuracy of 99.9% is already very good. It is therefore perfectly reasonable that the `steroids` model is indeed losing more energy than it is gaining, while still being in equilibrium.

4 DISCUSSION

We conclude that we cannot find large-scale atmospheric motions able to inflate a planet significantly. Instead, we find that heating and cooling by radiation dominate the temperature evolution even in deep layers, forcing our

2 We note that all GCMs need some form of dissipation for numerical reasons (Jablonowski & Williamson, 2011).

nongray simulations toward a cool final state. We therefore propose that hydrodynamical models of hot gas giants need extra physics or parameterization (such as dissipative drag or diffusion) to recreate an inflated interior.

Youdin & Mitchell (2010) and Tremblin et al. (2017) showed that vertical heat transport by turbulent mixing could possibly inflate the interior. However, their models do not model vertical mixing self-consistently, instead relying on a parameter that sets the mixing strength. Using idealized GCM simulations, Sainsbury-Martinez et al. (2019) claimed that large-scale atmospheric motions could be a reason for a tendency toward a hot adiabatic interior in their simulations. There are two major differences between the model used in this work and the GCM used in the work of these latter authors that need to be considered when questioning the lack of a hot interior in our models in comparison to their work. One of the obvious differences is the treatment of radiation: whereas Sainsbury-Martinez et al. (2019) do not include radiative cooling and heating in the deep atmosphere, we apply a nongray radiative transfer scheme.

Perhaps equally as important, the second difference is the use of numerical dissipation, where Sainsbury-Martinez et al. (2019) use a hyper-diffusion scheme to stabilize their model, whereas we use a fourth-order Shapiro filter. Previous studies showed that in general, both dissipation schemes (filtering and diffusion) have a profound influence on the temperature and dynamics of a GCM (e.g., Polichtchouk et al., 2014; Koll & Komacek, 2018; Hammond & Abbot, 2022). Sainsbury-Martinez et al. (2019) showed that the strength of numerical diffusion in their model critically impacts the timescale of the tendency toward the hot adiabat, where a strong numerical diffusion relates to a faster evolution toward a hot interior. It could therefore be possible that their finding might have been caused by heat diffusion from their numerical dissipation scheme.

It is still unclear how the interior of hot and ultra-hot Jupiters interact with the upper atmosphere. There are currently few studies that link the convective interior with the photosphere dynamics (Showman et al., 2020). The first steps toward this goal were made by Lian et al. (2022), who model the effect of convective forcing on the circulation patterns of hot irradiated planets with a combination of Newtonian forcing in the upper atmosphere and perturbations in the deep atmosphere. A model able to combine 1D interior models with realistic 3D atmospheric models including radiative transfer would also be desirable and would reveal insights into the connection between the convection in the deep interior and the atmosphere. Similar approaches, connecting convective interiors with upper radiative atmospheres, exist in the stellar community (e.g., Skartlien et al., 2000; Freytag et al., 2010, 2017, 2019).

The present work is the most complete GCM study to date, which is aimed at understanding the coupling of the upper and the deeper atmosphere in hot Jupiters. However, we note that we are so far omitting important effects for ultra-hot Jupiters: Ohmic dissipation, dissociation of H_2 and clouds. The upper atmospheres of ultra-hot Jupiters like WASP-76b are highly ionized due to their high temperatures (e.g., Helling et al., 2021b). Magnetic fields, if present, would therefore couple strongly to the ionized winds. Rauscher & Menou (2013) and Beltz et al. (2022a) showed that friction induced by magnetic fields acting on ionized winds may alter the dynamical state of the atmosphere and lead to additional heating in the upper atmosphere, where friction is converted to heat. It is still debated and unclear (Rauscher & Menou, 2013; Showman et al., 2020) as to whether this extra heat could be sufficient to inflate a planet.

Recent simulations of ultra-hot Jupiters showed that H_2 dissociation can alter their thermal structure (Tan & Komacek, 2019). The energy needed to dissociate molecular hydrogen on the day side cools the atmosphere, while recombination of atomic hydrogen heats the night side, leading to an overall reduced day–night temperature contrast. Similarly, the presence of clouds in a 3D GCM will alter the thermal and dynamical state of hot Jupiters (Roman et al., 2021; Deitrick et al., 2022). Realistic models of ultra-hot Jupiters should therefore take these effects into account, even though it is unlikely that these effects are important for the deeper parts of the atmosphere.

5 SUMMARY AND CONCLUSIONS

In this work, we investigate one of the main hypotheses proposed by Guillot & Showman (2002) and Youdin & Mitchell (2010) to explain the abnormally large radii of inflated hot Jupiters: Energy transport from the irradiated atmosphere into deeper layers. We performed long-term (86 000 d) nongray 3D GCM simulations of WASP-76 b to search for signs of vertical advection of potential temperature from the upper irradiated atmosphere into the interior. Our simulations started from a hot initial state and cooled down toward a colder state. We then used an exponential fit on the temperature convergence to extrapolate the temperature toward a possible final converged state, which was reached soon after for the extrapolated simulation. The final converged simulation exhibits a cold temperature profile, lacking signs of vertical advection of heat from the upper atmosphere into the interior. We find instead that the atmosphere has cooled down to radiative equilibrium, conserving energy with an accuracy of 99.9%.

Our work strongly disfavors vertical downward advection of energy from the irradiated part of the atmosphere by large-scale atmospheric circulation as a possible explanation for inflation. We suggest instead that physical processes other than radiation and dynamics need to be taken into account in order to match the abnormal large radii of inflated hot Jupiters. Such processes could be the interaction between a convective interior and the atmosphere, small-scale turbulent transport, or magnetic field interactions. Future investigations are needed to quantify their effects on the state of radius inflation.

ACKNOWLEDGEMENTS

We thank Xianyu Tan for fruitful discussions on the effect of numerical dissipation on the thermal structure of GCM simulations. We also thank an anonymous referee for their useful comments that improved the quality of the manuscript. A.D.S., L.D., U.G.J and C.H. acknowledge funding from the European Union H2020-MSCA-ITN-2019 under Grant no. 860470 (CHAMELEON). L.C. acknowledges the Royal Society University Fellowship URF R1 211718 hosted by the University of St Andrews. U.G.J acknowledges funding from the Novo Nordisk Foundation Interdisciplinary Synergy Program grant no. NNF19OC0057374. The bibliography of this publication has been typesetted using `bibmanager` (Cubillos, 2020)[3]. The post-processing of GCM data has been performed with `gcm-toolkit` (Schneider et al., 2022) [4]

3 https://bibmanager.readthedocs.io/en/latest/
4 https://gcm-toolkit.readthedocs.io/en/latest/

APPENDIX

A EFFECT OF THE DRAG

Previous studies revealed the enormous impact of the chosen (often unjustified) dissipation schemes (Heng et al., 2011b; Skinner & Cho, 2021). We perform a test simulation with a 1000 times longer friction timescale (τ_{deep}) compared to the `nominal` and `steroids` simulations. This longer friction timescale weakens the strength of the Rayleigh drag applied to the deep atmosphere and makes sure that the prescription of the bottom drag does not affect the conclusions of this work. This additional simulation has been started from the `nominal` model at 40 000 d and has been carried out for 10 000 d.

We compare the temperature evolution of the `nominal` simulation to the simulation with the low drag in Fig. 7.6, where we find that the simulation with the lower drag cools down slower than the `nominal` simulation. The reason for the difference in the temperature evolution can be found in the Fig. 7.7, where we show the temperature maps at 650 bar of the model with low drag and the `nominal` model. Both models start from an average temperature of 10 080 K at 40 000 d and cool down by a few hundred Kelvin. However, we find that the drag stops the equatorial jet, which otherwise descends toward the bottom boundary in the simulation with low drag. Simultaneously, stopping the equatorial jet leads to an efficient north–south redistribution of the temperature at the bottom boundary. Thus, in the model with much smaller drag, we find that the temperature starts diverging between the poles and the equator, where the equator cools down slower than the poles.

Considering this result, it is reasonable to conclude that the final converged solution of a model with lower drag would be hotter than the `steroids` model, possibly reducing the gap between outgoing and incoming radiation in the left panel of Fig. 7.5. Nevertheless, we also find that this simulation continues to cool down, still showing no sign of the vertical advection of heat that would, on the contrary, lead to a warming of the deep layers.

B PREDICTION OF THE FINAL STATE OF THE ATMOSPHERE

Temperature convergence in the deep layers of the atmospheres of hot Jupiters is impossible to reach in reasonable model runtimes. We therefore propose to

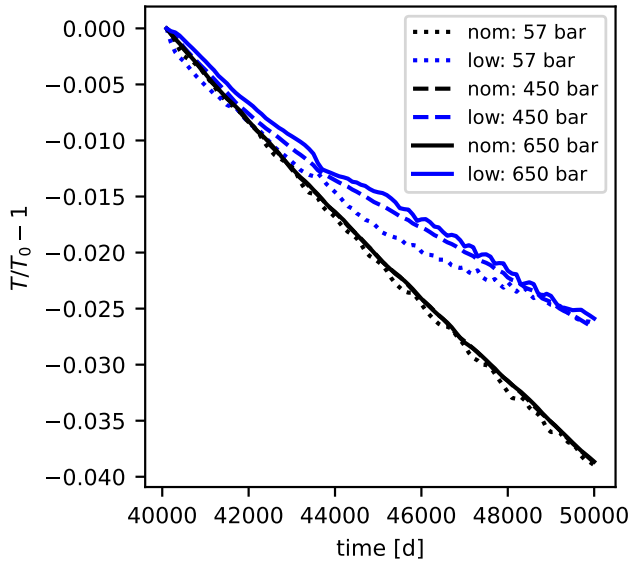

Figure 7.6: Evolution of the temperature in three pressure layers (57 bar, 450 bar, 650 bar) in a simulation with low drag compared to the `nominal` simulation. The temperature in each layer is normed to the respective initial value at 40 000 d.

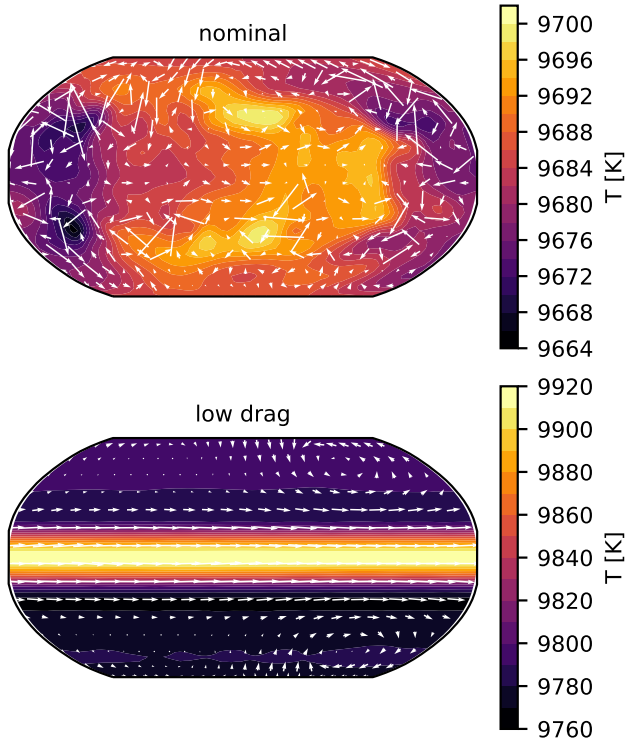

Figure 7.7: Isobaric temperature slices at $t = 50\,000\,\mathrm{d}$ at $p = 650\,\mathrm{bar}$ for the `nominal` and the model with low drag. The temperature has been averaged over the last 100 d. The substellar point is located in the center of the plot.

speed up convergence by predicting the final converged state and extrapolating to this final state, which can then be used to initialize a new model. The method outlined below is one possible approach to doing this. In order to be able to predict the final state of the temperature in the deep atmosphere, we apply three assumptions:

1. The temperature in the deep atmosphere is horizontally isotropic and homogeneous.
2. The temperature decrease can be modeled by an exponential decay.
3. The deep layers are adiabatic: $T = T_{650\,\mathrm{bar}} \left(\frac{p}{650\,\mathrm{bar}}\right)^{R/c_p}$.

We note that these assumptions (especially the second) are rather too simplified to capture the actual cooling of planets, which is not thought to be consistent over time (Ginzburg & Sari, 2015). However, these simplifications do not need to be true, because their only purpose is to predict the initial state of the `steroids` model. Moreover, in order to minimize temporal variations unrelated to the general trend of temperature convergence, we compute the horizontally and temporally averaged temperature over a sampling period of 1000 d. We perform this computation for four sampling periods (e.g., for a total of 4000 d) yielding four values for the potential temperature of four consecutive sampling periods. This computation is done in retrograde at $t = 40\,000$ d with the 100 d time-averaged temperature fields from 36 000 d to 40 000 d.

We then use the least-squares method to fit a linear relation

$$y_i = \log\left(\frac{(dT/dt)_i}{\lambda}\right), \tag{7.5}$$

where λ is a norm that ensures that the value inside log stays positive and unitless. We set

$$\lambda = \sum_j (dT/dt)_j, \tag{7.6}$$

the subscripts $i, j \in \{1, 2, 3, 4\}$ to denote the four support points of the fit. We can now use the least-squares method to solve

$$\begin{pmatrix} y_1 \\ y_2 \\ y_3 \\ y_4 \end{pmatrix} = \begin{pmatrix} t_1 & 1 \\ t_2 & 1 \\ t_3 & 1 \\ t_4 & 1 \end{pmatrix} \cdot \begin{pmatrix} m & c \end{pmatrix}, \tag{7.7}$$

in order to obtain the best-fit values for m and c, which is equivalent to

$$\frac{dT}{dt} = \lambda\tilde{c} \cdot \exp(mt), \tag{7.8}$$

where $\tilde{c} = \exp(c)$. The fit, as displayed in Fig. 7.3, matches the temperature change rates around $t = 40\,000$ d. However, the real temperature change rates for later times are slightly below the fit, meaning that the temperature cools down even faster than predicted by the fit.

We then estimate the final temperature from integrating Eq. 7.8 over time and get

$$T(t) = T_0 + \frac{\lambda\tilde{c}}{m}(\exp(mt) - 1). \tag{7.9}$$

We evaluate this equation at the age of the mother star, which is ≈ 5 Gyr (West et al., 2016), and find that the temperature at 650 bar should be $T_{650\,\mathrm{bar}} = 4567$ K. This temperature at the bottom of the simulation domain is then translated to an adiabatic temperature profile for the atmospheric layers below 10 bar and is used to kick off the `steroids` model.

In order to force the simulation to continue with this new temperature profile for pressure levels below 10 bar, we developed a method that would smoothly force the temperature towards the predicted state during runtime. This method consists of a time-based smoothing, where the temperature is forced towards the final state by splitting the total change of temperature over a period of 10 d. We make sure that the temperature is changed by the expected amount, but still modulate the change rates by a sine function $\frac{dT}{dt} \propto \sin\left(\pi \frac{t}{10\,\mathrm{d}}\right)$ to smoothen the transition. A linear vertical smoothing between 1 bar and 10 bar ensures that the upper atmosphere above 1 bar stays untouched from the artificial forcing, which should only change the temperature in the deep layers. These measures are only used for the period of 10 d, and their only purpose is to force the temperature of the `steroids` model towards its new initial condition. The temperature forcing after 40 010 d is then given by standard radiative heating and cooling as computed self-consistently within the GCM.

C MODELS OF WASP-76B

We found in Schneider et al. (2022b) that the influence of the deep atmospheric state on the temperature profile in the upper atmospheric layers is very limited. As we see in Fig. 7.2, the global average of the temperature in the `steroids` and `nominal` model only diverges for pressures above 1 bar. We show an

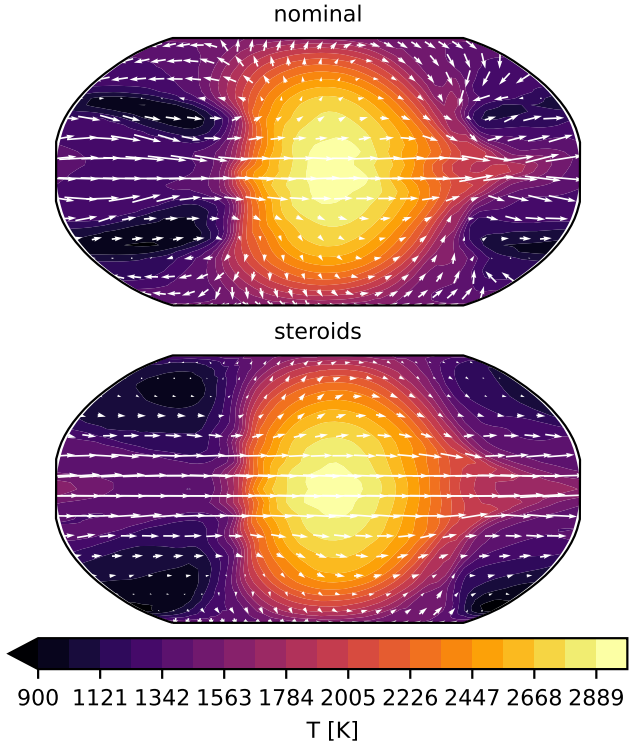

Figure 7.8: Final isobaric temperature-slices at $p \approx 1.2\,\mathrm{bar}$ for the `nominal` and `steroids` model. The temperature has been averaged over the last 100 d. The substellar point is located in the center of the plot.

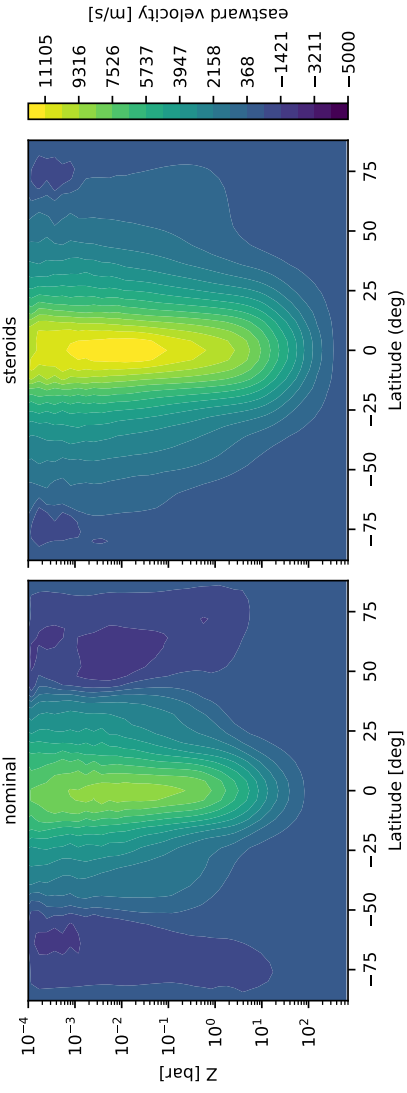

Figure 7.9: Zonal mean eastward velocity for the `nominal` and the `steroids` model.

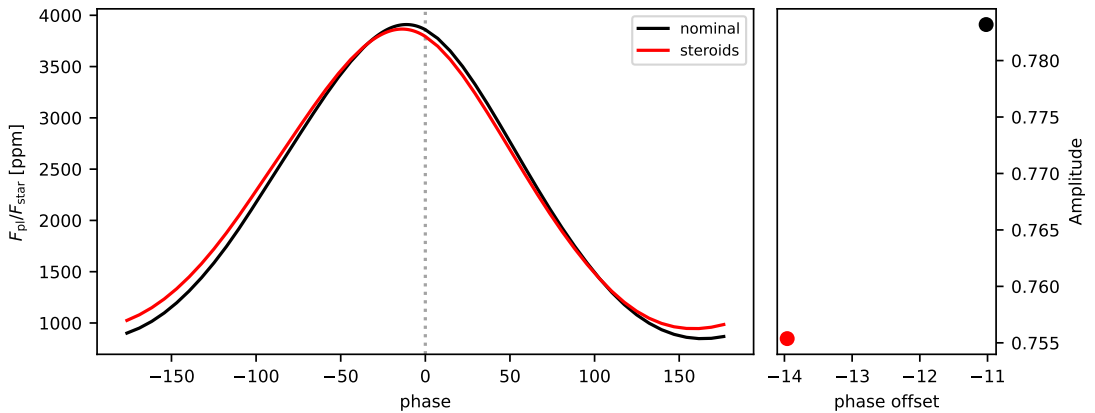

Figure 7.10: Phase curve and phase offset. Left: Phase curve at $\lambda = 4.5\,\mu m$, computed using `prt_phasecurve`. The dashed gray line corresponds to the center of the dayside. Right: Difference between the dayside center and the maximum of the phase curve.

isobaric map of the temperature at 1 bar in Fig. 7.8, where we can see that the steroid and nominal model look similar, yet not identical. This becomes especially apparent in the plots of the zonal mean of the zonal wind velocity in Fig. 7.9. The winds in the steroids model are much stronger than the winds in the nominal model. This will have an observable impact, resulting in higher hot spot offsets and greatly impacting high-resolution Doppler observations.

These strong differences in wind speed were not observed in the simulations of Schneider et al. (2022b), where we did not compare models with such differences in temperature. The transition to higher wind speeds might be caused by the increase in the weather layer, which is caused by larger (relative) horizontal anisotropies in the deep atmosphere, which affects the jet strength (Mayne et al., 2017). However, we note that the kinetic energy makes up less than 1% of the energy budget in our models. It is therefore also possible that the reason for the differences is simply rooted in the particularly poor conservation of angular momentum in MITgcm (Polichtchouk et al., 2014). Further study is needed to entangle the dynamical differences in models with cold and hot interiors.

To quantify the hot spot offset, we computed phase curves using prt_phasecurve[5]. prt_phasecurve computes 288 intensity fields at the top of the atmosphere using petitRADTRANS (Mollière et al., 2019, 2020) on a longitude latitude grid with 15° resolution and for 20 angles instead of the nominal 3 angles that petitRADTRANS uses. These individual spectra are then integrated by taking the individual angles into account (i.e., without the assumption of isotropic irradiation).

The difference in the offset shift can be seen in the thermal phase curve in Fig. 7.10. The overall shape of the phase curves in the nominal and steroids model is very similar. However, we can see that the day–night contrast is higher in the case of the nominal model, which can be explained by the strong winds in the steroids model that are more efficient in equilibrating the temperature in the steroids model. Similarly, we can see that the hot spot offset is greater in the steroids model, which is another outcome of the strong winds that transport energy further, before it can be reradiated.

5 available at: https://prt-phasecurve.readthedocs.io/en/latest/

8

EVIDENCE OF RADIUS INFLATION IN RADIATIVE GCM MODELS OF WASP-76B DUE TO THE ADVECTION OF POTENTIAL TEMPERATURE

Felix Sainsbury-Martinez, Pascal Tremblin, Aaron David Schneider, Ludmila Carone, Isabelle Baraffe, Gilles Chabrier, Christiane Helling, Leen Decin & Uffe Gråe Jørgensen

Published in Monthly Notices of the Royal Astronomical Society, Volume 524, Issue 1, September 2023

Author contributions:
Felix Sainsbury-Martinez and Pascal Tremblin designed the study together with Aaron Schneider and Ludmila Carone. Felix Sainsbury-Martinez wrote the manuscript and analyzed the output of the climate model simulations. Aaron Schneider contributed to the writing and discussion of the results and provided the numerical model and ran the simulations, which are part of the study. Ludmila Carone, Leen Decin and Uffe Gråe Jørgensen supervised Aaron Schneider and contributed to the manuscript and discussion of the results. Isabelle Baraffe contributed with computations of interior structure models. Gilles Chabrier and Christiane Helling supplied feedback to the manuscript.

Original Abstract
Understanding the discrepancy between the radii of observed hot Jupiters and standard 'radiative-convective' models remains a hotly debated topic in the exoplanet community. One mechanism which has been proposed to bridge this gap, and which has recently come under scrutiny, is the vertical advection of potential temperature from the irradiated outer atmosphere deep into the interior, heating the deep, unirradiated, atmosphere, warming the internal adiabat, and resulting in radius inflation. Specifically, a recent study which explored the atmosphere of WASP-76b using a 3D, non-grey, GCM suggested that their models lacked radius inflation, and hence any vertical enthalpy advection. Here we perform additional analysis of these, and related, models, focusing on an explicit analysis of vertical enthalpy transport and the resulting heating of the deep atmosphere compared with 1D models. Our results indicate that, after any evolution linked with initialisation, all the WASP-76b models considered here exhibit significant vertical enthalpy transport, heating the deep atmosphere significantly when compared with standard 1D models. Furthermore, comparison of a long time-scale (and hence near steady-state) model with a Jupiter-like internal-structure model suggests not only strong radius-inflation, but also that the model radius, $1.98 R_J$, may be comparable with observations ($1.83 \pm 0.06 R_J$). We thus conclude that the vertical advection of potential temperature alone is enough to explain the radius inflation of WASP-76b, and potentially other irradiated gas giants, albeit with the proviso that the exact strength of the vertical advection remains sensitive to model parameters, such as the inclusion of deep atmospheric drag.

1 INTRODUCTION

Observations of hot Jupiters (Laughlin et al., 2011) and hot brown dwarfs (see Fig. 4 of Casewell et al. 2020) have revealed a significant discrepancy between standard 'radiative-convective' single column (1D) atmospheric models and the properties of observed objects: observed radii of highly irradiated objects tend to be significantly larger than 1D atmospheric models suggest (see, for example, Figure 1 of Komacek & Youdin 2017). This indicates that said 1D models are likely failing to capture some key physics or dynamics which drive the observed radius discrepancy (i.e. inflation). In 1D models this discrepancy is 'solved' via the inclusion of an intrinsic/internal temperature,

which essentially acts to heat the deep atmosphere (internal adiabat) to a more physical value, allowing for atmospheric retrievals of transit observations, without actually elucidating on exactly what dynamics drives this heating other than typically claiming that it is linked with thermal escape from the interior (Guillot & Showman, 2002; Baraffe et al., 2003; Sudarsky et al., 2003; Chabrier et al., 2004; Thorngren et al., 2019).

In a collective effort to understand this deep heating/radius inflation problem, a vast array of different physical mechanisms have been suggested as possible causes/solutions (see Baraffe et al. 2010; Fortney & Nettelmann 2010; Baraffe et al. 2014 for a more in-depth overview of many of the proposed mechanisms) including tidal heating and dissipation (Arras & Socrates, 2010; Lee, 2019), the ohmic dissipation of electrical/magnetic energy (Batygin & Stevenson, 2010; Perna et al., 2010a; Rauscher & Menou, 2012; Helling et al., 2021b; Knierim et al., 2022), the deep deposition of kinetic energy (Guillot & Showman, 2002), enhanced opacities which inhibit interior cooling (Burrows et al., 2007), double-diffusive convection which hampers convective heat transport (Chabrier & Baraffe, 2007), or the vertical advection of potential temperature (first proposed and studied in 2D by Tremblin et al. 2017 and studied in 3D by Sainsbury-Martinez et al. 2019, 2021).

Fortunately, observations can help us to narrow down which of the above mechanisms might be responsible for the observed radius inflation. Specifically, observational studies of hot Jupiters and hot brown dwarfs (e.g. Demory & Seager 2011; Laughlin et al. 2011; Lopez & Fortney 2016; Sestovic et al. 2018; Casewell et al. 2020) have revealed a clear trend: a general increase in the observed radius of highly irradiated gaseous planets with stellar irradiation, except in the case of very-highly irradiated objects in very short orbits (e.g. SDSS1411B - Casewell et al. 2018) where little to no inflation is observed. One such mechanism which can explain this trend without the inclusion of model-dependent fine tuning is the vertical advection of potential temperature (i.e. enthalpy).

Briefly this mechanism can be understood as follows: for a tidally locked, gaseous exoplanet, the strong stellar irradiation leads to a very hot outer atmosphere paired with a very strong super-rotating equatorial jet. This driving can be understood via a 2D stationary circulation model, in which, due to mass and angular momentum conservation, significant vertical winds arise (as proposed/seen in Tremblin et al. 2017; Sainsbury-Martinez et al. 2019). Note that such a view is opposed by Showman & Polvani (2011), who assume/propose that only the irradiated layers of the atmosphere are meteorologically active, and that deeper layers are either quiescent or purely convective (not that the latter would have any negative implications for our

mechanism, beyond the temperature of the adiabat). Not only do our results disagree with this view (see Figure 8.2), but other studies, such as Carone et al. (2020); Schneider et al. (2022b) have shown that significant wave activity and zonal/vertical winds can occur in these deep atmospheric layers. If this holds true, and we propose that it does, these aforementioned vertical winds carry high potential temperature fluid parcels from the hot (radiative) outer atmosphere deep into the interior (where radiative effects tend to zero - as shown in Figure 8.3), driving the formation of a non-convective (i.e. advective) adiabat at lower pressures than 1D models (without an artificially increased internal/intrinsic temperature) would predict. Because this adiabat forms at lower pressures , and because the radiative, advective and deep convective (i.e. interior) regions must smoothly connect, the internal adiabats temperature temperature is significantly increased when compared to a model which lacks advection and considers a radiative-convective boundary alone. In turn, this increase in the temperature of the internal adiabat, leads to an increase in the internal entropy, and hence an inflated radius.
This is very similar to what occurs in a 1D model when the internal/intrinsic temperature is increased, although here it is occurring due to fundamental physics. An example of this can be seen in Thorngren et al. (2019), who find a clear link between the pressure of the RCB (radiative-convective boundary), i.e. where the outer atmosphere connects with the interior adiabat, and the intrinsic temperature, i.e. internal heat flux that their models impose. However the heating which drives the formation of this non-convective adiabat has nothing to do with heat transport from the interior. Rather it is heating associated with the irradiated outer atmosphere, which should, at steady-state, balance any outwards heat transport from the interior, stalling any internal cooling and leading to a net zero internal flux (i.e. no heating from the interior), a stable, inflated, radii, and a natural link between radius inflation and surface irradiation.

It is important to note that this mechanism is distinct from the kinetic energy transport and deposition mechanism proposed by Guillot & Showman (2002). In their mechanism, stellar irradiation is converted to kinetic energy in the outer atmosphere (by atmospheric pressure gradients), this energy is then somehow transported down towards the interior (possibly by, for example, Kelvin-Helmholtz instabilities, vertical advection, or waves), where it then dissipates, heating the deep atmosphere and warming the internal adiabat. Rather, the mechanism we (and Tremblin et al. 2017; Sainsbury-Martinez et al. 2019) propose skips these uncertain energy conversion steps, and instead we directly transport hot (high enthalpy) material from from the outer

atmosphere to the deep atmosphere via already present flows and circulations.

Recently, Schneider et al. (2022a), called into question the validity of vertical potential temperature advection as a possible explanation for the radius inflation of the ultra-hot Jupiter WASP-76b (West et al. 2016; Seidel et al. 2019; Ehrenreich et al. 2020; Kesseli et al. 2022), arguing that their (hot-start) 3D atmospheric models, calculated with expeRT/MITgcm, and including a self-consistent, non-grey radiative transfer model (see Schneider et al. 2022b for a detailed discussion of this code), suggested that coupling between radiation and dynamics alone is not sufficient to explain the inflated radii of highly-irradiated, gaseous, exoplanets.

Here, we intend to investigate this claim in more detail, performing additional analysis of the nominal WASP-76b simulation discussed in Schneider et al. (2022a) along with additional, cooler-start (i.e. cooler initial deep adiabats) calculations that were run exclusively for this work. Specifically, we intend to investigate the vertical mass and enthalpy (i.e. potential temperature) transport in these models, confirming if vertical advection plays a significant role in the dynamics, before comparing the steady-state 3D models with internal-structure models based upon the work of Baraffe et al. (2010) in order to confirm how much, if any, of the inflated radius of WASP-76b potential temperature advection alone can explain.
In Section 2, we start with a brief overview of expeRT/MITgcm before introducing the models discussed as part of this work. This is followed, in Section 3 with our analysis, focusing on the vertical transport of potential temperature and its implications for the steady-state deep atmosphere of our WASP-76b models. We finish, in Section 4 by discussing the implications of our results, with a particular focus on the sustainability of potential temperature advection as an explanation for the inflated radii of highly irradiated, tidally locked, gaseous exoplanets.

2 METHODS

The methodology and models used in this work are based on the work of Schneider et al. (2022b) and Schneider et al. (2022a). Here we give a brief overview of the GCM used to calculate the WASP-76b models considered here, before giving a more in depth description of said WASP-76b models setup.

2.1 *expeRT/MITgcm*

Briefly, expeRT/MITgcm (Carone et al., 2020; Schneider et al., 2022b) builds on the dynamical core of the MITgcm (Adcroft et al., 2004), pairing said core with the petitRADTRANS (Mollière et al., 2019) radiative transfer (radiative transfer (RT)) model in order to enable the long model integration times required to explore the steady-state dynamics of the deep atmospheres of hot Jupiters, whilst also maintaining the accuracy of a multi-wavelength radiation scheme. expeRT/MITgcm solves the primitive equations of meteorology (Vallis, 2017; Showman et al., 2009), for an ideal gas, on an Arakawa C-type cubed sphere (designed to avoid numerical issues near the poles which occur due to singularities in the coordinate system; for more details of this grid, see, for example, Miller 1984) with a horizontal resolution C32[1] and a vertical grid that contains a combination of 41 linearly in $\log(P)$ (i.e. log-pressure) spaced layers between 1×10^{-5} and 100 bar, paired with 6 linearly in P spaced layers between 100 and 700 bar. As in Showman et al. (2009); Carone et al. (2020) this model includes a horizontal fourth-order Shapiro filter (with τ = 25 s) in order to smooth grid-scale noise. Additionally, expeRT/MITgcm includes a linear Rayleigh-drag (which is also known as a linear-basel drag scheme - see Carone et al. 2020, particularly Section 2.3 and Appendix A for a discussion of this dynamics preserving approach as well as comparisons with other drag-schemes) at the bottom of the atmosphere (between 490 and 700 bar) and a sponge layer at the top of the atmosphere (for $P < 1 \times 10^{-4}$ bar). We discuss the implications of this Rayleigh-drag on the vertical advection of potential temperature, and hence radius inflation, in more detail in Section 3. Note: we selected 700 bar as the maximum pressure of our simulation domain in-order to balance modelling a sufficient portion of the deep atmosphere with the increasing computational costs of modelling high-pressure regions (due to their increased dynamical timescales).

Radiatively, the outer atmosphere is heated and cooled using a runtime (i.e. coupled), multi-wavelength, RT scheme based upon petitRADTRANS. Specifically, the radiative dynamics are updated every 100 seconds, quadruple the dynamical time step ($\Delta t_{dy} = 25$ s), with the radiative transport calculated using a correlated-k approach that includes 5 wavelength bins each of which contain 16 Gaussian quadrature points (see Goody et al. 1989 for an introduction to the correlated-k approach to RT, and Appendix B of Schneider et al. 2022b for a discussion of the accuracy of the limited wavelength bin approach). Note that opacities for the RT scheme are based on a pre-calculated pressure-temperature grid, assume local chemical equilibrium, and include

1 C32 is comparable to a resolution of 128 × 64 in longitude and latitude

the following gas absorbers (with data taken from the ExoMol[2] database): H_2O, CO_2, CH_4, NH_3, CO, PH_3, H_2S, TiO, VO, HCN, Na, K and FeH. Additionally, the RT model includes Rayleigh-scattering for both H_2 and He, and collision-induced-absorption for $H_2 - H_2$, $He - He$ and H^- (see Schneider et al. 2022a for more details). We do not include equilibrium condensation since, assuming that the latent heat release is low (Woitke & Helling, 2003; Helling, 2019; Helling et al., 2019a), it should have little effect on the photosphere, especially for WASP-76b whose day-side can be assumed to be cloud free, and is simply too hot for condensation to occur.

Finally, the inclusion of an artificial Rayleigh-drag scheme in the deep atmosphere implies that an additional energy source term must be added to the deep atmosphere to account for the conversion of energy lost from drag to heat (Rauscher & Menou 2013; Carone et al. 2020; Schneider et al. 2022b), which is then locally returned to the atmosphere. This takes the form:

$$\frac{dT}{dt} = \frac{u^2}{c_p \tau_{drag}}, \tag{8.1}$$

where T is the local temperature of the atmosphere, u is the horizontal (zonal plus meridional) wind speed, τ_{drag} is the Rayleigh-drag timescale at the bottom of the atmosphere, and c_p is the heat capacity at constant pressure.

2.2 *Models of WASP-76b*

WASP-76b is a tidally locked ultra-hot Jupiter-like planet ($M = 0.92 \pm 0.03 M_J$) that orbits its host star at a distance of 0.033 AU, corresponding to an orbital period of 1.81 Earth days, and which appears to exhibit significant radius inflation, with an observed radius of $1.83 \pm 0.06 R_J$ (West et al., 2016). The host star, WASP-76, is a hot yellow-white (F7V) main-sequence star with an effect temperature of $T_{eff} = 6250 \pm 100$ K and a radius of $R_* = 1.73 \pm 0.04 R_\odot$ (Gaia Collaboration et al., 2018). Further, all our models assume a fixed specific heat capacity, $c_p = 13784\ J\,kg^{-1}K^{-1}$and a fixed specific gas constant, $R = 3707\ J\,kg^{-1}K^{-1}$, which corresponds to a adiabatic index $\gamma \simeq 1.36$ (these values have been extracted from petitRADTRANS). However the Rayleigh-drag timescale does vary, with the majority of our models setting $\tau_{drag} = 1$ day, and a low-drag model setting $\tau_{drag} = 1000$ days. Finally, we include zero heat flux from the interior, meaning that any deep atmospheric heating is purely due to downwards enthalpy advection from the irradiated outer atmosphere.

2 www.exomol.com and Tennyson et al. (2016); Chubb et al. (2021)

Model	Run Time (d)	Peak $F_{\mathcal{H}}$ (erg cm^{-2})	Mean $F_{\mathcal{H}}$ (erg cm^{-2})
Nominal	155,100	-8.40×10^{11}	-6.24×10^{7}
2500 K	57,100	-1.81×10^{12}	-2.35×10^{7}
1800 K	69,200	-8.70×10^{11}	-2.99×10^{7}
1400 K	69,700	-5.09×10^{11}	-6.04×10^{7}
1000 K	69,100	-2.14×10^{11}	-8.59×10^{7}
Low Drag	50,000	-2.46×10^{12}	-3.84×10^{8}

Table 8.1: Peak (downward) and global mean vertical enthalpy flux for five WASP-76b models in which either the temperature of the initial deep adiabat or the strength of the deep drag have been changed, along with the nominal model presented in Schneider et al. (2022a). Note: the Low Drag model has been run for 10,000 additional days using a snapshot of the nominal model after 40,000 days (i.e. the 'evolved' model of Schneider et al. 2022a) of simulation time as an initial condition. Further, the mean vertical enthalpy flux for the nominal model at an equivalent timestep to that of the Low Drag model remains essentially unchanged.

Here we consider 6 models of WASP-76b, five of which only differ in the temperature profile used to initialise them, and one in which the strength of the deep Rayleigh-drag has been reduced (as previously mentioned). For the former models, the initialisation profile is a combination of an isotherm, based upon the stellar irradiation, in the outer atmosphere (i.e. for $P < 1$ bar), and an adiabat, with a reference temperature (θ) taken at 1 bar, throughout the deep atmosphere (i.e. $P > 10$ bar), with a linear interpolation between the two profiles between 1 and 10 bar. Here we consider reference temperatures of $\theta = 4000$ K (i.e. the nominal model which was first presented in Schneider et al. 2022a, but which has been further evolved as part of this work), 2500 K, 1800 K, 1400 K and 1000 K, which range from hotter than the adiabat of the final nominal model of Schneider et al. (2022a) to cooler - thus allowing us to explore models in which the deep atmosphere is both heating and cooling. These initial profiles can be seen in Figure 8.1, where we plot the initial profile of each variable initialisation model as a dashed line. On the other hand, the low-drag model (with $\tau_{drag} = 1000$ days) is initialised from a snapshot of the nominal model (with $\theta = 4000$ K) taken after 40,000 days of simulation time. Note that, other than the nominal model, all the models featured here were performed as part of this work.

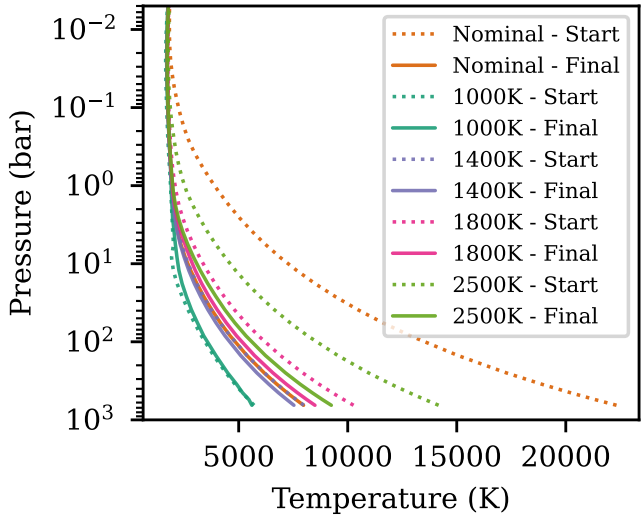

Figure 8.1: Horizontal mean Temperature-Pressure profiles for our five WASP-76b atmospheric models with different initialisation temperatures. For each of the variable initial temperature models considered here, i.e. the nominal (4000 K), 1000 K, 1400 K, 1800 K, and 2500 K start models, we include a profile near initialisation (dotted) and a profile at the end of the models runtime (solid). Note that the nominal model has been run for significantly longer than the other models (Table 8.1), and hence is likely to represent the steady state that all aforementioned models are converging towards.

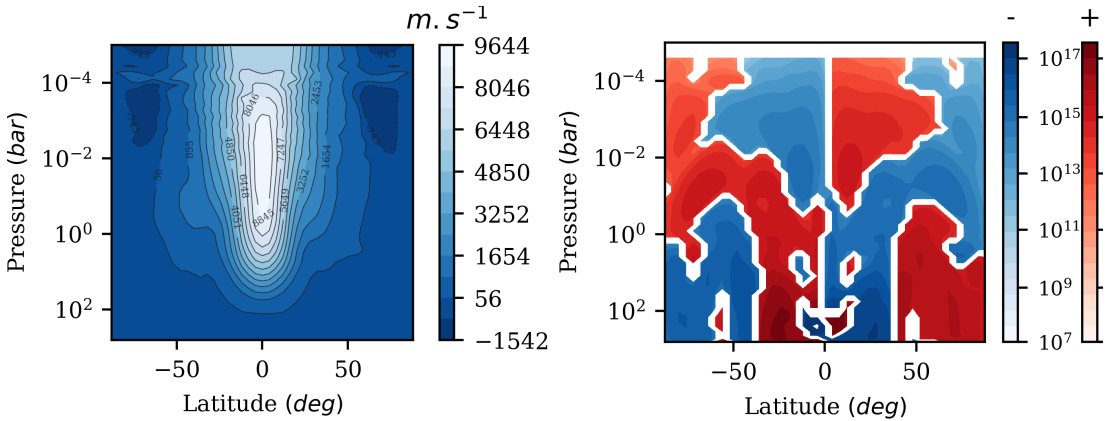

(a) Zonal-Mean Zonal Wind

(b) Meridional Mass Streamfunction

Figure 8.2: The zonal-mean zonal wind (left) and meridional circulation streamfunction (right) for the nominal GCM model of WASP-76b. In the zonal wind profile, easterly winds are positive and westerly winds are negative, whilst in the meridional circulation profile, we plot the streamfunction using a log scale in order to clearly illustrate the full circulation profile, especially in the outer atmosphere. Here, clockwise circulations are shown in red and anti-clockwise in blue - these circulations combine to reveal an equatorial upwelling in the outer atmosphere driven by the strong day-side irradiation, and an equatorial downflow in the deep atmosphere, which is linked with the downward advection of potential temperature.

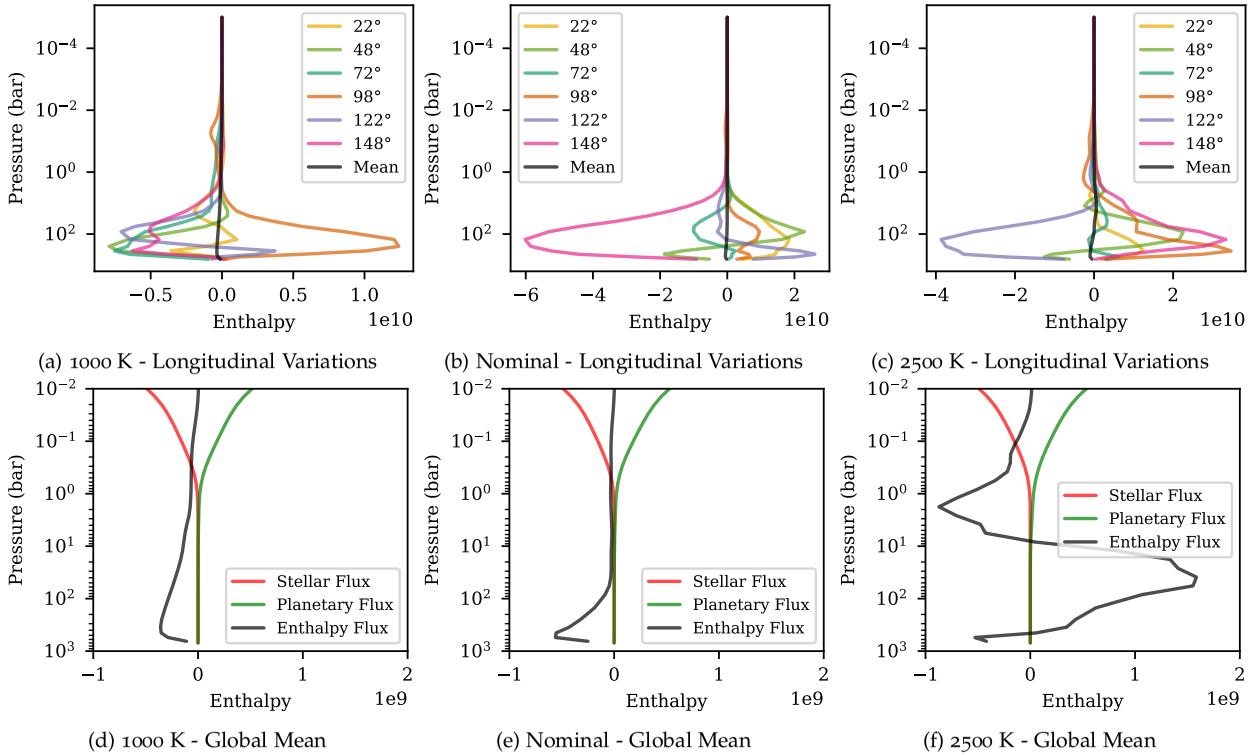

Figure 8.3: Longitudinal variation of the meridional mean (top) and global mean (bottom) vertical enthalpy flux $F_{\mathcal{H}}$ profiles for three WASP-76b GCM models with different initial deep adiabat temperatures; 1000 K - left, nominal (4000 K) - middle, and 2500 K - right. In the top row figures, we plot the vertical enthalpy flux profiles at 6 different longitudes, ranging from just east of the anti-stellar point to just west of the substellar point, as well as the global mean vertical enthalpy flux profile. However, since the mean flux is significantly smaller than the local fluxes, we replot the mean profiles in the bottom row in order to better demonstrate the vertical variations in enthalpy transport, focusing on the advection into the deep atmosphere. Here we also include the horizontal mean stellar (incoming) and planetary (outgoing) fluxes in order to reinforce that the deep atmosphere is radiatively quiescent. Note: the 2500 K profiles are calculated near the start of the simulation when the cooling is strongest - similar results can be found near initialisation for the nominal and other hot-start models.

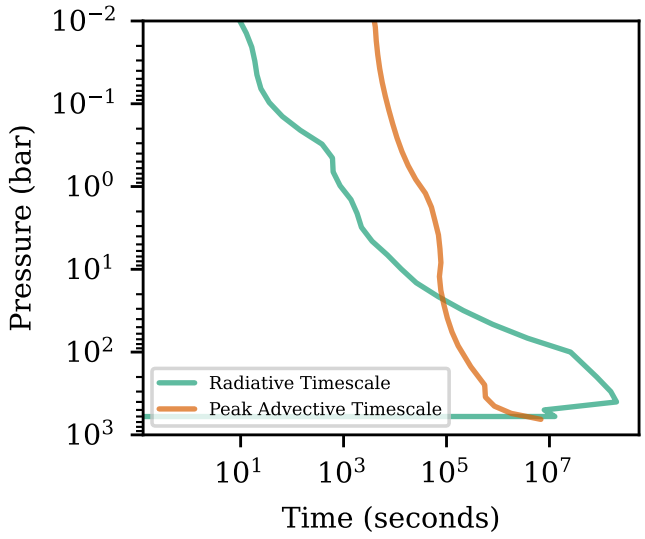

Figure 8.4: Comparison of the peak vertical advective time-scale ($\tau_{adv} = H/u_r$, where H is the atmospheric scale height and u_r is the maximum downward velocity) and the global-mean radiative timescale for the near steady-state nominal model. Note how, despite both timescales increasing with pressure, the rapid increase in optical depth means that advection dominates over radiation in the deep atmosphere.

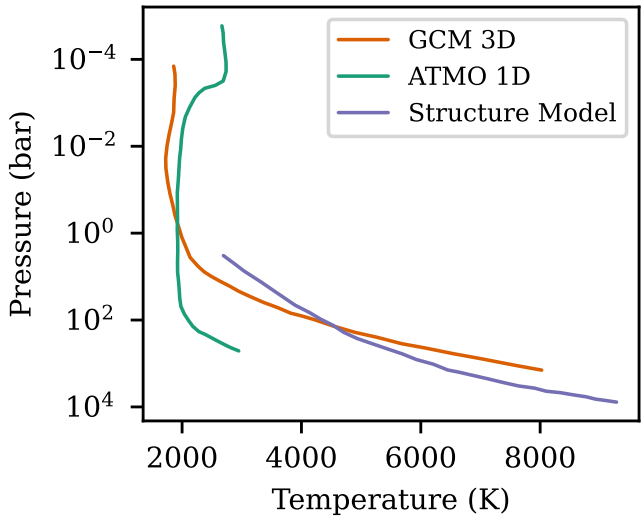

Figure 8.5: Comparison of the horizontal mean Temperature-Pressure profile from the nominal GCM model of WASP-76b (orange) with both a 1D model calculated using ATMO (with $T_{int} = 100$ K - green) and an internal-structure model, based on the work of Baraffe et al. (2003); Chabrier et al. (2004), of a hot Jupiter with a mass of $0.9 M_J$ and an inflated radius of $1.98 R_J$ (purple).

3 RESULTS

A broader analysis of the nominal model, after 86,000 days of runtime, is presented in Schneider et al. (2022a). Instead, here, we focus our analysis on the vertical advection of potential temperature, including what drives this advection, what effect it has on the deep atmosphere, and how much, if any, of WASP-76b radius inflation can be attributed to it.

We start our analysis with the nominal model, which, after over 155,000 days of simulation time (which corresponds to over 10,000 advective turnover timescales in the deep atmosphere - see Figure 8.4), is approaching steady-state at almost all simulated pressures. Here we find that the strong day/night temperature difference associated with the combination of both tidal-locking and a hot host-star has resulted in the formation of a rapid super-rotating jet (see Figure 8.2a, which plots the zonal mean zonal wind at 155,000 days) that extends significantly into the deep atmosphere: at the equator the region in which $u_{zonal} > 1000\ m\,s^{-1}$ extends to pressures greater than 10 bar. Such deep jets were already predicted in Carone et al. (2020) and confirmed in Schneider et al. (2022b,a). Here, we emphasise that these deep jets facilitate the formation of an advective adiabat at the same depths as Sainsbury-Martinez et al. (2019) propose to explain the inflated radius of HD209458b.
In turn, strong latitudinal and vertical flows also develop, as can be seen in the meridional mass streamfunction (i.e. the meridional circulation profile - Equation 16 of Sainsbury-Martinez et al. 2019). In Figure 8.2b we plot the meridional circulation profile for the nominal model at near steady-state, with clockwise circulations shown in red and anticlockwise circulations shown in blue. Here we find that, at the equator, the strong stellar irradiation on the day-side leads to a general upwelling between 10^{-5} and ~ 1 bar - driven by the combination of a clockwise circulation in the northern hemisphere and an anti-clockwise circulation in the south, both of which also drive material away from the substellar point/equator in the outer atmosphere. However, as we move deeper into the atmosphere, where the radiative time-scale is longer and hence advective effects can start to play a more significant role, we find that the sense of the meridional circulations has changed, likely due flows associated with the super-rotating jet taking over the vertical driving, leading to a strong downflow at the equator balanced by mass-conserving upflows at mid-latitudes (i.e. around 45° - i.e. at the edge of the super-rotating jet). A similar circulation pattern was found by Sainsbury-Martinez et al. (2021) for Kepler-13Ab, a hot brown dwarf with a very hot (A-class) host star, and was

shown to be sufficient to drive significant deep heating.

We next explore if this is also the case for our WASP-76b models. Specifically, we start by investigating the vertical transport of enthalpy. We first recall briefly how this quantity impacts the averaged energy transport in the atmosphere. Assuming the density is near steady-state (a similar assumption to the anelastic approximation), the mass and energy conservation equations are given by

$$\begin{aligned} \nabla(\rho\mathbf{u}) &= 0, \\ \partial_t(\rho E) + \nabla\left((\rho e + \rho u^2/2 + P + \rho\phi)\mathbf{u} + \mathbf{F}_{\text{rad}}\right) &= 0. \end{aligned} \tag{8.2}$$

where ρ, p, e, and E are the atmospheric density, pressure, internal, and total energy; $\mathbf{u}$ the velocity of the flow; ϕ the gravitational potential and $\mathbf{F}_{\text{rad}}$ the radiative flux (including the irradiation from the host star). We will assume that the flow is low Mach in the deep atmosphere and therefore neglect the contribution of the kinetic energy. Furthermore we rewrite the energy flux as a function of the enthalpy $\rho e + p = \rho c_p T$, with c_p specific heat capacity at constant pressure and T the temperature. By averaging Equation 8.2 in 2D over the full sphere (Ω), we get

$$\begin{aligned} \frac{1}{4\pi}\int_{4\pi} \rho u_z \, d\Omega &= 0, \\ \partial_t\left(\frac{1}{4\pi}\int_{4\pi} \rho E \, d\Omega\right) + \partial_z\left(\frac{1}{4\pi}\int_{4\pi} (\rho c_p T + \rho\phi)u_z + F_{\text{rad}}) \, d\Omega\right) &= 0. \end{aligned} \tag{8.3}$$

assuming there is no mass flux out of the domain of interest in a plane-parallel approximation. The gravitational potential does not depend on latitude/-longitude, therefore, because of mass conservation, its contribution to the energy flux is zero. Only the contribution of the enthalpy and the radiative flux remain:

$$\partial_t\left(\frac{1}{4\pi}\int_{4\pi} \rho E \, d\Omega\right) + \partial_z\left(\frac{1}{4\pi}\int_{4\pi} (\rho c_p T(z,\theta,\phi)u_z + F_{\text{rad}}) \, d\Omega\right) = 0. \tag{8.4}$$

If the temperature is uniform, e.g. a 1D model, the contribution of the enthalpy is zero similarly to the contribution of the gravitational potential. If not, e.g. a 3D GCM, cold downflows and hot upflows will tend to cool the deep atmosphere whereas hot downflows and cold upflows will tend to warm the deep atmosphere. This is how the circulation can transport energy from the irradiated hot top layers to the deep atmosphere, even in the absence of convective processes.

This split between upflows and downflows can be seen in Figure 8.3, where we plot the longitudinal variation of the latitudinal-mean vertical enthalpy (top) and the horizontal-mean vertical enthalpy (bottom) for three models, two of which are near-steady-state (left - 1000 K initialisation - centre - 4000 K, i.e. nominal, initialisation) and one which was initialised with a hot deep adiabat that is still rapidly cooling at the time of the snapshot (right - 2500 K initialisation after 200 days).
Starting with the longitudinal variations of the latitudinal-mean vertical enthalpy (top - Figure 8.3), it is clear that the direction of enthalpy transport varies significantly across the planetary surface. This was to be expected as tidally-locked thermal and wind dynamics, particularly in the outer atmosphere, are highly spatially inhomogeneous. However, this is further complicated by the effect that the temperature of the initial deep adiabat has on the overall dynamics - when a model is initialised with a deep atmosphere that is hotter than its final steady-state, excess energy must leave the deep atmosphere and, since radiative time-scales in the deep atmosphere are long, this typically occurs via changes in the wind structure and hence vertical enthalpy transport. An example of this effect can be found when comparing the models shown in Figure 8.3: for the hot-start (2500 K) model near initialisation, Figure 8.3c, we find that vertical enthalpy transport is primarily outwards, other than over a limited longitude and latitude range associated with a mass-conserving downflow. Almost the exact opposite scenario is found for a cool (1000 K) initialisation model (throughout its runtime), Figure 8.3a, where we find that the enthalpy flow is directed downwards at most longitudes, albeit, once again, with a mass conserving counter flow. Finally the nominal model, Figure 8.3b, represents a mix of the two regimes, with dynamics that can be linked to a combination of its very hot initialisation, leading to significant initial cooling, and long-run-time, leaving the model close to steady-state (although still warming in the deeper regions of the atmosphere due to the very-long dynamical times required to heat high-pressure regions of a hot Jupiter - see the isothermal model of Knierim et al. (2022)).

This difference in regime is also reflected in the horizontal-mean vertical enthalpy profiles (bottom - Figure 8.3): both the 1000 K and nominal models reveal a net downwards enthalpy flux, extending from the outer atmosphere all the way to the bottom of the simulation domain. Furthermore, this peak in the downwards flux is married with the radiative flux (both outwards and inwards) tending towards zero, as required in the potential temperature advection mechanism (Tremblin et al. 2017). Note that the vertical extent of the enthalpy downflow is reduced in the nominal model when compared with the

1000 K model, which is due to the nominal model being closer to steady-state and hence heating being limited to the deepest regions of the simulation domain (see Figure 7 of Sainsbury-Martinez et al. 2019 for an example of this top-down evolution - similar top down heating can be found in the 1400 K model as it warms back up from the initial cooling that occurred during model initialisation). This effect (i.e. a switch from radiative to advective dynamics) can also be seen when comparing the vertical-advective and global-mean-radiative timescales: as we move deeper into the atmosphere, the dynamics switch from being radiatively dominated to advectively driven, at around the same pressure as the deep adiabat forms. However, it is important to note that this is a 1D view of an inherently 3D problem - between the tidally located nature of the planetary irradiation (i.e. the xied day-side and nigth-side), and the strong longitude and latitude dependence of the vertical winds, the exact pressure at which the atmosphere changes dynamical regimes is likely to be highly localised. Yet it is reassuring to confirm that, on a global scale, the regime transition occurs about where we would expect and as required for our mechanism to work.
On the other hand, early outputs of the 2500 K model reveal, as expected, a strong enthalpy upflow throughout most of the deep atmosphere, although as the simulation evolves and the deep atmosphere finishes cooling, this slowly evolves towards the deep heating seen in the 1000 K and nominal models. Hints of this evolution towards deep heating can be seen around 1 bar where a weaker net downflow has started to develop. As shown in Table 8.1, the global steady-state vertical enthalpy flux is generally independent of the initialisation temperature. That is to say that, given enough time, almost all the models here should settle onto the same steady-state profile, with the initialisation temperature only affecting the time taken to reach that profile. The only exception to this rule is the model in which we have modified the deep Rayleigh-drag.

As shown in Table 8.1, the model with slower deep Rayleigh-drag exhibits a significantly stronger peak and importantly mean vertical enthalpy flux than the models with fast drag ($\tau_{drag} = 1$ day), even when models are compared at the same point in time ($\sim 50,000$ days). This difference in vertical heating rate, and hence the temperature of the steady-state deep atmosphere, can be understood through using the vertical advective timescale ($\tau_{adv} \sim \frac{H}{w_r}$): if we consider the scale height, H, to be on the order of the radius WASP-76b and the velocity to be the global mean vertical velocity ($w_r = 734\ m\,s^{-1}$), we find that $\tau_{adv} \sim 2.06$ days (see Figure 8.4). I.e., for most of the models considered, the advective and drag time-scales in the deep atmosphere are of the same

order of magnitude, leading to a noticeable reduction in the vertical wind speed, and hence vertical enthalpy flux in these models when comparing them with a no/low drag model in which the advective time-scale is significantly shorter than the drag time-scale (see Table 8.1). A similar effect can be seen in the zonal-mean zonal-wind, with the Low Drag model exhibiting a jet that extends significantly deeper into the atmosphere than the nominal model it is based upon. We discuss the implications of this result on the expected level of advective radius inflation in Section 4.

Finally we compare, in Figure 8.5, the near-steady-state temperature-pressure profile of the nominal model with both a 1D model of the outer and deep atmosphere calculated using ATMO (see Tremblin et al. 2015 for an overview of the ATMO model) and an internal-structure model (which extends down to over 10^7 bar), based upon the work of Baraffe et al. (2003); Chabrier et al. (2004), of a hot Jupiter with a mass of $0.9 M_J$. This internal-structure model is rather unique, as it is very difficult to generate a model with such a large radius. In order to do so, a large amount of thermal energy (corresponding to a luminosity of 2×10^{28} erg s^{-1}) must be deposited deep enough into the planetary interior to modify the internal adiabat (i.e. inflate the radius). As a consequence, the radius of the planet becomes essentially constant with time from early ages and the evolution is stalled (see Figure 4 of Chabrier et al. (2004)).
Note that the input physics and equation of state of these internal-structure models differs from that considered in expeRT/MITgcm (typically GCMs use simpler equations of state for computational efficiency reasons, and because they are focused upon relatively low-density dynamics). As such, the adiabatic index of our models and the internal-structure models also differ, complicating a direct comparison between the deep atmospheric temperature-pressure profiles in the two models. Instead, in order to divine which structure-model is the closet match to our steady-state GCM model, and hence calculate the level of radius inflation exhibited, we follow standard practice and perform the model comparison at a fixed pressure of 100 bar (i.e. at a reference-pressure which is sufficiently deep so that the atmosphere is optically thick and hence either convectively or advectively driven).
The result of this comparison is the selection of a internal-structure model with a radius of $R = 1.98 R_J$ being chosen as the best 'match' to our steady-state atmospheric model. This radius is broadly compatible with the observed radius of WASP-76b, $R = 1.83 \pm 0.06 R_J$, suggesting that potential temperature advection alone is enough to explain the radius inflation of WASP-76b. A conclusion that is further reinforced by the partially evolved T-P profiles

found in our alternate initialisation temperature models (see the solid lines in Figure 8.1). Despite the shorter run time of the alternative start models, Figure 8.1 clearly shows that all of the models are converging towards the same, inflated, deep T-P profile found in the nominal model, albeit at different rates due to differences in the efficiency of deep cooling versus heating (see Sainsbury-Martinez et al. 2019), i.e. the slow heating of the 1000 K model in Figure 8.1. This suggests that our conclusion of advection alone being sufficient to explain the radius inflation of WASP-76b is fairly robust.

4 DISCUSSION

In this work, we have performed additional analysis on extended and derivative versions of the WASP-76b models of Schneider et al. (2022a), focusing our analysis on the vertical advection of potential temperature, and its ability to heat the deep atmosphere with respect to 1D atmospheric models, leading to radius inflation with respect to these 1D models (as introduced by Tremblin et al. 2017 and explored, in a parametrised 3D model, by Sainsbury-Martinez et al. 2019, 2021). Importantly, thanks to the inclusion of a robust radiative transfer scheme (based upon petitRADTRANS) in expeRT/MITgcm, these models also allow us to complete the 'wish' of Sainsbury-Martinez et al. (2019): exploring the steady-state atmosphere of a hot Jupiter with a self-consistent radiative transfer scheme (in the outer atmosphere) so that a comparison between a atmospheric model and an internal-structure model can be made, thus quantifying, almost, the exact level of radius inflation that potential temperature advection alone can explain.

We started by exploring the zonal-mean zonal and meridional dynamics (Figure 8.2), with the aim of confirming the presence of a strong super-rotating jet that drives an equatorial downflow between the irradiated outer atmosphere and the advective deep atmosphere. This analysis was performed for six models, five of which have different initial deep adiabat temperatures ranging from significantly hotter to cooler than the expected steady-state deep atmosphere (see the dashed lines in Figure 8.1), and one which extends the nominal model of Schneider et al. (2022a), but with slower deep Rayleigh-drag, and which we include in order to explore the robustness of our results.
For all five WASP-76b models with varying deep initialisation temperatures, we found that, once any deep atmospheric cooling had slowed/stopped, the strong super-rotating jet extends to $P > 1$ bar and drives a meridional circulation profile that includes a zonal-mean downflow that connects the radiative outer atmosphere with the advective deep atmosphere. This implies that high

potential temperature fluid parcels from the outer atmosphere can indeed be transported vertically downwards, potentially heating the deep atmosphere.

Next, we explored if this was indeed the case, investigating how the mean vertical enthalpy advection ($F_{\mathcal{H}r}(r,\theta,\phi) = \rho c_p T U_r(r,\theta,\phi)$) varies with both longitude and pressure (see Figure 8.3 and Table 8.1). This analysis revealed a number of trends which line up with the dynamics of the atmosphere. For example, for models that are initialised with an overly hot deep adiabat, and hence exhibit significant initial, deep cooling, the primary direction of enthalpy transport is from the deep to the outer atmosphere where it can be radiated away. However as such a model evolves, and the deep atmosphere cools towards (and maybe overshoots - an effect seen in the hot initialisation models of Sainsbury-Martinez et al. 2021) steady-state, we find that all of our models exhibit a net downwards flow of enthalpy, with the strength and pressure range of the downwards transport decreasing as the deep atmosphere very slowly equilibrates (a process that can take many hundreds to thousands of Earth years for $P > 100$ bar; Sainsbury-Martinez et al. 2019, 2021). Of course that is not to say that the vertical enthalpy transport lacks horizontal structure. As with the wind that drives it, differences in the vertical enthalpy transport are primarily linked with the differences in the day-side and night-side forcing, leading to a near global overturning circulation pattern that drives upwards vertical enthalpy transport on the day-side and downwards transport on the night-side, where divergent and wave driven circulations converge. We intend to explore the structure of the horizontal and vertical wind and enthalpy flux in more detail as part of a future study, including investigating how rotation impacts the dynamics (and hence may effect which hot Jupiters are inflated and which are not).
Overall we find that, regardless of the initial conditions (i.e. with enough time), all of our fast drag models exhibit comparable peak and mean vertical enthalpy transport into the deep atmosphere. Furthermore this vertical enthalpy transport is also comparable, if not slightly stronger than that found in a reanalysis of the HD209458b models of Sainsbury-Martinez et al. (2019), reinforcing the idea that vertical potential temperature advection alone can explain the inflated radii of highly irradiated, gaseous, exoplanets.

We further confirm that this is the case via a comparison of our nominal WASP-76b models near-steady-state T-P profile (a T-P profile that all WASP-76b models appear to be converging towards - see Figure 8.1 - albeit at varying rates due to differences in the efficiency of cooling versus heating in the deep atmosphere) with an internal-structure model based upon the work of Baraffe

et al. (2003); Chabrier et al. (2004). As shown in Figure 8.5, the closest match to the nominal model is an internal-structure model with a mass of $0.9M_J$ and an inflated radius of $1.98R_J$, which is more than large enough to fully explain the observed radius of WASP-76b ($R = 1.83 \pm 0.06R_J$). Note however that this comparison was performed by only considering the temperature at 100 bar (a fairly standard pressure at which atmospheric and internal-structure model comparisons are performed), a necessary approximation given the rather different adiabatic indexes found in our models and the internal-structure models considered here. Briefly, this difference occurs due to differences in the physics and specifically the equation of state considered in the models, with expeRT/MITgcm using a relatively simplified EOS (for both computational efficiency reasons as well as the GCMs focus upon modelling relatively low-density regions of the atmosphere) in comparison to that used in Baraffe et al. (2003); Chabrier et al. (2004). As such, an exact calculation of the level of radius inflation found in our model is beyond the current generation of GCMs, although work is in the pipeline to develop next-generation GCMs with updated dynamics and physics that will allow for even more robust comparisons with internal-structure models. However this does not mean that our calculation is without value, or that our results are far from the exact radius of our atmospheric model. For example, an internal-structure model with $R = R_J$ is a very poor fit to our atmospheric model with deep temperatures at 100 bar that are a order of magnitude cooler than than found with expeRT/MITgcm, reinforcing our inference that this model exhibits significant, advectively driven, radius inflation.

However this is the not only effect that drives uncertainty in the exact level of radius inflation that advective heating can drive. For example, Mayne et al. (2019), showed that the dynamics of small-Neptunes and super-Earths varied significantly between models which solved the primitive equations of meteorology the the full Navier-Stokes equations. Other model choices can also affect the strength of the deep heating, such as the strength of any grid-scale smoothing (i.e. the inclusion of a Shapiro filter, which can affect the strength of the zonal jet and hence the vertical wind and advection - see Koll & Komacek 2018; Skinner & Cho 2021; Hammond & Abbot 2022), the atmospheric chemistry considered (e.g. equilibrium vs non-equilibrium chemistry), or the sources of opacity included (for example the inclusion of SiO, Fe and FeII opacity may affect atmospheric heating and the depth to which radiation penetrates, changing the T-P profile slightly. See, for example Lothringer et al. 2020). Here we investigate one of these possible sources of uncertainty: the inclusion, and thus strength, of deep Rayleigh-drag.

This uncertainty can be seen by comparing the nominal model, with $\tau_{drag} = 1.0$ days, with a model in which the deep Rayleigh-drag has been significantly slowed, such that $\tau_{drag} = 1000$ days. i.e. a model in which the drag time-scale is significantly slower than the vertical advective timescale, which is of the order of 2 days for WASP-76b. Starting with the zonal-mean zonal-wind, our analysis indicates that the equatorial jet extends significantly deeper than in the nominal model. In turn, this drives stronger vertical mixing which results in a vertical enthalpy flux that is notably enhanced with respect to the nominal model. If we them compare the nominal model after 50,000 days with the low drag model after 40,000+10,000 days, we find that the deep T-P profile in the slow drag model is a little warmer, suggesting a slightly larger inflated radius. Comparing the vertical enthalpy flux at this time, confirms that the low drag model exhibits significantly enhanced deep heating. As such, and without a more complete understanding of how much, if any, Rayleigh-drag should be included in the deep atmosphere of hot Jupiter models, there will always remain an uncertainty on the exact level of radius inflation that vertical advection can drive. However, given that a) the Rayleigh-drag is confined to the highest pressure regions of the atmosphere (allowing for advective heat transport into the outer deep atmosphere, and then adiabatic mixing to carry heat deeper), and b) that the strength of the vertical advective transport is more than enough to explain the observed radius inflation, even in the nominal model with 'strong' drag, we are confident in our conclusion that the vertical advection of potential temperature alone is enough to explain the radius inflation of many hot Jupiters (and hot brown dwarfs), including WASP-76b.

5 CONCLUDING REMARKS

Overall, our analysis of the vertical mixing and vertical transport of potential temperature in an extended sample of the the WASP-76b models of Schneider et al. (2022a) has revealed that, contrary to their conclusions, the vertical advection of potential temperature alone is more than enough to explain the radius inflation of WASP-76b.

This difference in conclusion arises for a number of reasons.

The first is simply that the nominal model of Schneider et al. (2022a) was not run for long enough, and that their approach to avoid the computational expense of evolving a radiative GCM to steady-state in the deep atmosphere (i.e. the steroids model) made a number of assumptions about the deep dynamics which limit the applicability of such a extrapolative approach. Specifically,

when extrapolating the evolution of their nominal models deep P-T profile, they focused on the evolution of the temperature at 650 bar, which, for the time frame they considered, revealed near exponential cooling. However, as shown in the isothermal-start model of Sainsbury-Martinez et al. (2019), advective heating of the deep atmosphere starts in the lower pressure regions of the deep atmosphere (i.e. at the bottom of the radiatively dominated outer atmosphere) and slowly pushes deeper with time, with the time to heat the atmosphere only increasing as the heating moves deeper and the local density increases. Evidence for this top down heating in the steroids models can be seen in Figure 2 of Schneider et al. (2022a), with slow heating occurring between ~ 5 and ~ 100 bar, leaving the region around 650 bar to appear steady and hence evolved. Here, by evolving the nominal model for an additional 69000 days of simulation time, we are approaching a true steady-state that is significantly hotter than the steroids model. Furthermore, when compared with an internal-structure model from Baraffe et al. (2003); Chabrier et al. (2004), this steady-state corresponds to a radius of $1.98R_J$, more than large enough to explain the observed, inflated, radius of WASP-76b ($R = 1.83 \pm 0.06R_J$).

The second reason for our difference in conclusion can be linked to the wide use of intrinsic/internal temperatures in the exoplanetary communities. Briefly, radius inflation is simply the difference between the observed radii of a hot Jupiter and a standard 'radiative-convective' 1D model its outer atmosphere. This difference is believed to occur because 1D atmospheric models lack some fundamental physics that drive deep heating, with suggestion ranging from ohmic dissipation to vertical heat transport, and is 'fixed' (or accounted for) in 1D models by including an artificial, intrinsic/internal temperature meant to represent the heating of the deep atmosphere. Commonly this is linked with excess energy loss from the interior (hence the name internal temperature), however Tremblin et al. (2017) and Sainsbury-Martinez et al. (2019) proposed that this deep heating instead occurs due to vertical heat transport, with no need for any energy transport from the interior to the outer/deep atmosphere (i.e. zero net deep flux). In essence, this intrinsic temperature acts as a 'fudge' factor designed to allow for direct comparisons between observations (such as transmission spectra) and 1D models, and relying upon it outside of those scenarios can lead to either over or under (as was the case in Schneider et al. 2022a) estimation of the level of radius inflation. Instead, as done here, comparisons must be done with internal-structure models, even when the accuracy of those comparisons is limited by the different equations of state used (i.e. by the simplified EOS used in GCMs - although work is in progress to change this).

Of course, many questions remain about the exact level of radius inflation that vertical advection can drive, and if it can fully explain the differences seen in radius inflation for the broader hot Jupiter community, including those unusual objects that are very highly irradiated and yet show little to no sign of inflation (for example WASP-43b or WASP-18b). expeRT/MITgcm now makes a radiatively robust study of these objects possible for the first time, and we look forward to the results of future work with this, and other next-generation, models.

However there is now no doubt that potential temperature advection provides a robust explanation for some if not all of the observed radius inflation of hot Jupiters and hot brown dwarfs, and as such changes to how future GCM studies are performed are recommended. Previously, it has been recommended that future GCM studies of hot Jupiters be initialised with a adiabat at the bottom of their simulation domain and then be allowed to evolve to steady-state (Sainsbury-Martinez et al., 2019). However this remains computationally expensive and can lead to mistakes when models are not allowed to evolve sufficiently. As such, given how well potential temperature advection alone can explain the inflated radii of hot Jupiters, we suggest that future studies should initialise their deep atmosphere with an adiabat based upon the best fitting internal-structure model that corresponds to the inflated radii, albeit modified to match the adiabatic index of the GCM.

ACKNOWLEDGEMENTS

We would like to thank the anonymous referee for their comments and corrections. F. Sainsbury-Martinez would like to thank UK Research and Innovation for support under grant number MR/T040726/1 I.B receives support from the ERC grant No. 787361-COBOM and the consolidated STFC grant ST/R000395/1. A.D.S., L.D., U.G.J and C.H. acknowledge funding from the European Union H2020-MSCA-ITN-2019 under Grant no. 860470 (CHAMELEON). L.C. acknowledges the Royal Society University Fellowship URF R1 211718 hosted by the University of St Andrews. U.G.J acknowledges funding from the Novo Nordisk Foundation Interdisciplinary Synergy Program grant no. NNF19OC0057374.

DATA AVAILABILITY

Data is available upon request.

9

CONCLUSIONS AND FUTURE PROSPECTS

1 SUMMARY

In this thesis, we developed models, which are capable to predict observables of giant planets. Two sets of models were utilized to address two different questions. Firstly, planet formation models were employed to predict the atmospheric composition and bulk composition of gas giant exoplanets formed in disks with pebble evaporation and condensation (Chapters 3, 4, and 5). Secondly, a fast radiative transfer solver was integrated into a climate model to examine how atmospheric dynamics can deposit energy in deep atmospheric layers of hot Jupiters, potentially leading to radius inflation (Chapters 6, 7, and 8).

In Chapter 3, we introduced `chemcomp`, a planet formation model, consisting of a disk model and a model of the growth of a protoplanet. The disk model traces the composition of different chemical species in a 1D viscous gas disk. In the disk, both gas and dust are followed during diffusion and drift for each chemical species individually. Pebbles crossing ice lines are removed from the solid surface density and added to the gas phase to mimic evaporation of inward drifting pebbles. The planet is then birthed into the disk and accretes first solids and later gas from the disk, while migrating through the disk. Using this model, we found that the evaporation of solids contaminates the gas in the protoplanetary disk and thus increases the heavy element content of the gas giants that form in the disk. In this way, planets that form outside the major condensation lines, will have low heavy element content, whereas planets that cross the evaporation lines, in particular the water evaporation line, will have relatively high amounts of metals in their atmosphere. When planets are large enough to carve a gap into the disk, pebbles will be stopped from drifting inwards, which will then stop the pollution of the gas by evaporating pebbles. Furthermore, we found that this process is largely regulated by the viscosity in the disk, where large viscosities

hinder the formation of large pebbles, resulting in a slow pebble drift and consequently slower heavy element enrichment in the inner disk. At the same time, larger viscosities enable the formation of larger planets, because of a more efficient gas accretion onto the planet. Using a population synthesis approach of studying a variety of different parameters, we demonstrated that we could match the heavy element content relation from Thorngren et al. (2016). We found that the C/O ratio in the planetary atmosphere will be larger for planets that form further out, since the evaporation of water will lower the C/O ratio in the gas phase of the inner disk.

In Chapter 4, we used `chemcomp` to explore how individual elemental abundances are affected by the inclusion of pebble drift and evaporation. We found that volatile molecular species, which are loosely defined by having evaporation lines outside the inner disk, such as H_2O, CO_2, CO, NH_3, N_2, pollute the gas in the inner parts of the disk. This results in super solar values for oxygen, carbon, and nitrogen in the gas phase of the inner disk. Thus, giant planets forming in such disks, would harbor supersolar volatile abundances in their atmosphere, whereas they would harbor subsolar refractory abundances. We showed that, unlike the pebble drift and evaporation case, solid pollution, such as planetesimal accretion, would lead to super solar abundances of refractories. Thus, measuring the volatiles and refractories in exoplanet atmospheres can tell something about the formation history of a planet. Furthermore, we demonstrated that we would need additional pollution of extra solids to explain the formation of Saturn and Jupiter.

In Chapter 5, we utilized `chemcomp` to analyze the atmospheric composition measurements of τ-Boötis b and WASP-77A b, aiming to understand their formation pathways. Our model suggests that the formation of WASP-77A b possibly initiated beyond the CO_2 evaporation line, which could account for the sub-solar C/H and O/H values. Regarding τ-Boötis b, our findings indicate a probable formation beyond the water evaporation line, consistent with the super-solar C/H and O/H values. Taking into account the evaporation and condensation of pebbles can account for both sub- and super-solar values in the same model, without the need for an inclusion of additional solids. Furthermore, we find that the α viscosity is a very important parameter in determining the composition of the formed planets in the pebble evaporation and condensation scenario.

In Chapter 6, we introduced `expeRT/MITgcm`, a GCM with correlated-k radiative transfer, which is fast enough to achieve long runtimes. `expeRT/MITgcm` is an upgrade to the Newtonian cooling version `exorad/MITgcm`, as implemented in Carone et al. (2020). The radiative transfer routines build on the 1D radiative transfer code `petitRADTRANS` (Mollière et al., 2019, 2020) and we

have optimized them for speed to match the requirements needed for these long runtimes. Using `expeRT/MITgcm`, we have modeled the atmosphere of HD 209458 b and WASP-43 b for 12,000 simulation days. We find that we can confirm the finding of Carone et al. (2020), that WASP-43 b has a deep wind jet, linked to its short rotation period, whereas we conclude that we do not find evidence for a retrograde jet, as predicted in Carone et al. (2020). Looking at the temperature evolution of both planets, we find that both planets do not converge to a final state, but instead continue to cool from a hot initial state to a cooler state. WASP-43 b cools faster than HD 209458 b, which can be explained by the difference in the assumed value for the surface gravity, where atmospheric paths are shorter for WASP-43 b due to its higher surface gravity, thus leading to a faster cooling. We then looked at the rotation rate of the planet and whether it would affect the temperature evolution of the planet, where we find that the temperature evolution of the planet is not affected by the rotation rate. We finally created synthetic phase curve emission spectra from the models and compared them to observations of HD 209458 b and WASP-43 b, where we found that the state of the deep atmosphere matters for the state of the observable atmosphere, in line with findings of Komacek et al. (2022).

In Chapter 7, we performed simulations of WASP-76 b, an inflated ultra hot Jupiter, covering 86,000 days of simulation time in order to study whether it is possible to find a fully converged end state. We found that we could not converge the simulation from a hot initial state, even with this long runtime. A model that starts from a cooler initial state did not significantly advance during the runtime. In this publication, we looked deeper into the global energy budget of the models and found that the models evolved into a state where the total radiative energy budget is negative, meaning that the intrinsic temperature, which is an often used measure of inflation, would be unphysical. We thus concluded that our models would converge to a final solution that is too cold to explain the inflated radius of WASP-76 b.

After publishing Schneider et al. (2022a) (Chapter 7), we discussed our results with Felix Sainsbury-Martinez and Pascal Tremblin. We decided to extend the simulations from Schneider et al. (2022a) to 155,000 days, because they were not convinced about our conclusion that the final converged solution would be too cold to explain the inflated radius. We also performed extra simulations with different initial starting temperature profiles. In Chapter 8, we compare these new results with interior structure models that assume a hot interior to match the inflated radius of WASP-76 b. We find that the GCM results approximately match. Unlike initially thought in Schneider et al. (2022a) (Chapter 7), a total negative radiative energy budget with an unphysi-

cal intrinsic temperature does not mean that a planet is not inflated. Instead, a negative flux balance just means, that the upper atmosphere is radiatively decoupled from the deep atmosphere. Thus, if the deep atmosphere is still hot, its heating is independent of radiative heating and cooling. We thus concluded in this work, that it must indeed be the atmospheric circulation that deposits warm air in the deep atmosphere and thus heats up the interior. In this paper, we also stressed that numerical choices, such as boundary conditions, affect the temperature evolution in GCMs.

2 GENERAL CONCLUSIONS AND OUTLOOK

Understanding the formation of planets requires formation models that are capable to produce observables such as atmospheric abundances. To this end, we developed `chemcomp`, a planet formation model that traces the chemical composition of the disk and the resulting composition of the planet. We applied the model to study the effect of pebble drift and evaporation. The key findings are

- Drifting pebbles will enrich the gas in the inner disk highly in heavy elements. Therefore, disks, in which pebbles have enough time to sufficiently pollute the gas phase with evaporated pebbles, will form planets with atmospheres rich in heavy elements.
- The C/O ratio in disks is time-dependent, complicating the simple picture of Öberg et al. (2011) (see Fig. 1.4), where atmospheric C/O ratios could be directly linked to the location of formation. However, small C/O ratios can be expected for planets that accrete large parts of their atmosphere inside the water ice line.
- The atmospheric abundances of Jupiter and Saturn can not be explained by pebble drift and evaporation alone, and instead require the accretion of additional solids.
- Jupiters nitrogen content can be explained by pebble evaporation, removing the need for the formation of Jupiter in the outer solar system, as speculated by Öberg & Wordsworth (2019); Bosman et al. (2019).
- The volatile to refractory ratio can give insides into the amount of accreted solids into the planetary atmosphere, as has been also speculated by Lothringer et al. (2021).

Future observations, with high signal-to-noise ratios and better constraints on the abundances of chemical species in the atmosphere, will reveal important constraints on planet formation models. With `chemcomp`, we have

introduced a planet formation framework that is capable to test and link some observables to planet formation processes. Using `chemcomp`, several works have attempted to link planetary abundances to their formation path (Schneider & Bitsch, 2021a; Bitsch et al., 2021; Schneider & Bitsch, 2021b; Bitsch et al., 2022; Mollière et al., 2022; Chatziastros et al., 2024; Danti et al., 2023; Müller et al., in review; Eberlein et al., in prep). Furthermore, `chemcomp` has also been used to understand the influence of stellar abundances on the formation of super Mercuries (Mah & Bitsch, 2023) and to study the influence of planet formation on the abundances of chemical species in the stellar photosphere (Hühn & Bitsch, 2023), as well as to understand other disk and formation processes (Bitsch & Mah, 2023; Savvidou & Bitsch, 2023; Mah et al., 2023; Lienert et al., in prep; Savvidou & Bitsch, in prep; Andama & Bitsch, in prep; Ndugu & Bitsch, in prep).

Many questions remain open, such as how to link the accreted composition with the atmospheric abundances, since chemical processes in the atmosphere and the interior will shuffle chemical species around, rendering it difficult to straight up compare atmospheric abundances to predictions from formation models such as `chemcomp`. Furthermore, planet formation models are very parametric and can therefore accommodate many possible solutions. It will thus be very crucial to constrain some parameters, such as the fragmentation velocity, possible viscous alpha parameters and other microphysical parameters.

In order to tackle the question of hot Jupiter inflation, we have developed a numerical model that is capable to perform long term simulations of hot gas giant exoplanets. The simulations of WASP-76 b were the first full radiative hot Jupiter simulations that track such a long convergence time. Furthermore, we have been proven wrong by Felix Sainsbury-Martinez and Pascal Tremblin about our conclusions in Schneider et al. (2022a). However, by collaborating, we have, using a more sophisticated model, confirmed the findings of Sainsbury-Martinez et al. (2019) that the atmospheric circulation alone might be sufficient to explain the inflated radius of hot gas giants. Our overall conclusions are thus

- The simulation time needed o converge the temperature in the deep atmosphere of hot gas giants is very long and typically infeasible for radiative hot Jupiter GCMs
- Advection of warm air into the deep atmosphere might be indeed able to heat deep layers and thus explain the inflated radii of hot Jupiters.

- GCMs of hot Jupiters have numerical limits, which is important to keep in mind, and which has also been pointed out by a number of other studies (e.g., Polichtchouk et al., 2014; Mayne et al., 2019).
- The intrinsic temperature is not a useful concept for 3D models such as GCMs. Instead, a radiatively decoupled atmosphere and interior might lead to unphysical intrinsic temperatures but still inflated radii.
- A hot initialization is faster to converge than a cool initialization, confirming Sainsbury-Martinez et al. (2019).
- The state of the deep atmosphere is important for the atmospheric circulation and thus influences observables such as phase curve observations and emission spectra of hot gas giants.

We stress, that further future investigation is needed to disentangle effects from numerical choices such as boundary conditions, the equations that are solved (e.g., HPE), and physical processes such as the vertical transport of potential temperature. We thus recommend, that the bottom boundary condition for the temperature in hot Jupiter GCMs, that try to produce observables, is anchored on 1D structure models that match the observed radius of these gas giants. Such an interface could be similar to that of Komacek et al. (2022). Overall, we think that GCM intercomparison projects, such as CAMEMBERT (Christie et al., 2022) and MOCHA, will hopefully help to constrain the limits of the predictive power of such hot Jupiter models.

BIBLIOGRAPHY

Adcroft, A., Campin, J.-M., Hill, C., & Marshall, J. 2004, Monthly Weather Review, 132, 2845

Adcroft, A., Hill, C., & Marshall, J. 1997, Monthly Weather Review, 125, 2293

Adibekyan, V., Dorn, C., Sousa, S. G., et al. 2021, Science, 374, 330

Aguichine, A., Mousis, O., Devouard, B., & Ronnet, T. 2020, ApJ, 901, 97

Agúndez, M., Parmentier, V., Venot, O., Hersant, F., & Selsis, F. 2014a, A&A, 564, A73

Agúndez, M., Venot, O., Selsis, F., & Iro, N. 2014b, ApJ, 781, 68

Akeson, R. L., Chen, X., Ciardi, D., et al. 2013, PASP, 125, 989

Alessi, M., Pudritz, R. E., & Cridland, A. J. 2020, MNRAS, 493, 1013

Alexander, R., Pascucci, I., Andrews, S., Armitage, P., & Cieza, L. 2014, in Protostars and Planets VI, ed. H. Beuther, R. S. Klessen, C. P. Dullemond, & T. Henning, 475–496

Alexander, R. D. & Pascucci, I. 2012, MNRAS, 422, L82

Ali-Dib, M. 2017, MNRAS, 464, 4282

Alibert, Y., Carron, F., Fortier, A., et al. 2013, A&A, 558, A109

Alibert, Y., Mordasini, C., Benz, W., & Winisdoerffer, C. 2005, A&A, 434, 343

Alibert, Y., Venturini, J., Helled, R., et al. 2018, Nature Astronomy, 2, 873

Allard, N. F., Spiegelman, F., Leininger, T., & Molliere, P. 2019, VizieR Online Data Catalog, J/A+A/628/A120

Altwegg, K., Balsiger, H., Hänni, N., et al. 2020, Nature Astronomy, 4, 533

Amundsen, D. S., Baraffe, I., Tremblin, P., et al. 2014, A&A, 564, A59

Amundsen, D. S., Mayne, N. J., Baraffe, I., et al. 2016, A&A, 595, A36

Amundsen, D. S., Tremblin, P., Manners, J., Baraffe, I., & Mayne, N. J. 2017, A&A, 598, A97

Andama, G. & Bitsch, B. in prep

Andama, G., Ndugu, N., Anguma, S. K., & Jurua, E. 2022, MNRAS, 510, 1298

Andrews, S. M., Huang, J., Pérez, L. M., et al. 2018, ApJ, 869, L41

Andrews, S. M., Rosenfeld, K. A., Kraus, A. L., & Wilner, D. J. 2013, ApJ, 771, 129

Armitage, P. J. 2013, Astrophysics of Planet Formation

Armstrong, D. J., de Mooij, E., Barstow, J., et al. 2016, Nature Astronomy, 1, 0004

Arras, P. & Socrates, A. 2010, ApJ, 714, 1

Asplund, M., Grevesse, N., Sauval, A. J., & Scott, P. 2009, ARA&A, 47, 481

Ataiee, S., Baruteau, C., Alibert, Y., & Benz, W. 2018, A&A, 615, A110

Atreya, S. K., Crida, A., Guillot, T., et al. 2016, arXiv e-prints, arXiv:1606.04510

Auer, L. 1991, in NATO Advanced Study Institute (ASI) Series C, Vol. 341, Stellar Atmospheres - Beyond Classical Models, ed. L. Crivellari, I. Hubeny, & D. G. Hummer, 9

Ayliffe, B. A. & Bate, M. R. 2009, MNRAS, 393, 49

Azzam, A. A. A., Tennyson, J., Yurchenko, S. N., & Naumenko, O. V. 2016, MNRAS, 460, 4063

Baeyens, R., Decin, L., Carone, L., et al. 2021, MNRAS, 505, 5603

Baeyens, R., Konings, T., Venot, O., Carone, L., & Decin, L. 2022, MNRAS, 512, 4877

Banzatti, A., Pascucci, I., Bosman, A. D., et al. 2020, ApJ, 903, 124

Baraffe, I., Chabrier, G., & Barman, T. 2010, Reports on Progress in Physics, 73, 016901

Baraffe, I., Chabrier, G., Barman, T. S., Allard, F., & Hauschildt, P. H. 2003, A&A, 402, 701

Baraffe, I., Chabrier, G., Fortney, J., & Sotin, C. 2014, in Protostars and Planets VI, ed. H. Beuther, R. S. Klessen, C. P. Dullemond, & T. Henning, 763–786

Barber, R. J., Strange, J. K., Hill, C., et al. 2014, MNRAS, 437, 1828

Baruteau, C., Crida, A., Paardekooper, S. J., et al. 2014, in Protostars and Planets VI, ed. H. Beuther, R. S. Klessen, C. P. Dullemond, & T. Henning, 667–689

Batygin, K. & Stevenson, D. J. 2010, ApJ, 714, L238

Batygin, K., Stevenson, D. J., & Bodenheimer, P. H. 2011, ApJ, 738, 1

Baudino, J.-L., Mollière, P., Venot, O., et al. 2017, ApJ, 850, 150

Baumann, T. & Bitsch, B. 2020, A&A, 637, A11

Bean, J. L., Stevenson, K. B., Batalha, N. M., et al. 2018, PASP, 130, 114402

Beatty, T. G., Madhusudhan, N., Pogge, R., et al. 2017, AJ, 154, 242

Bell, K. R., Cassen, P. M., Klahr, H. H., & Henning, T. 1997, ApJ, 486, 372

Beltz, H., Rauscher, E., Kempton, E. M. R., et al. 2022a, AJ, 164, 140

Beltz, H., Rauscher, E., Roman, M. T., & Guilliat, A. 2022b, AJ, 163, 35

Ben-Yami, M., Madhusudhan, N., Cabot, S. H. C., et al. 2020, ApJ, 897, L5

Benítez-Llambay, P., Masset, F., Koenigsberger, G., & Szulágyi, J. 2015, Nature, 520, 63

Bergez-Casalou, C., Bitsch, B., Pierens, A., Crida, A., & Raymond, S. N. 2020, A&A, 643, A133

Bergin, E. A., Blake, G. A., Ciesla, F., Hirschmann, M. M., & Li, J. 2015, Proceedings of the National Academy of Science, 112, 8965

Bi, J., Lin, M.-K., & Dong, R. 2021, ApJ, 912, 107

Binkert, F., Szulágyi, J., & Birnstiel, T. 2021, MNRAS, 506, 5969

Birnstiel, T., Andrews, S. M., Pinilla, P., & Kama, M. 2015, ApJ, 813, L14

Birnstiel, T., Dullemond, C. P., & Brauer, F. 2009, A&A, 503, L5

Birnstiel, T., Dullemond, C. P., & Brauer, F. 2010, A&A, 513, A79

Birnstiel, T., Klahr, H., & Ercolano, B. 2012, A&A, 539, A148

Bitsch, B. & Battistini, C. 2020, A&A, 633, A10

Bitsch, B., Izidoro, A., Johansen, A., et al. 2019, A&A, 623, A88

Bitsch, B. & Johansen, A. 2017, in Astrophysics and Space Science Library, Vol. 445, Formation, Evolution, and Dynamics of Young Solar Systems, ed. M. Pessah & O. Gressel, 339

Bitsch, B., Johansen, A., Lambrechts, M., & Morbidelli, A. 2015a, A&A, 575, A28

Bitsch, B., Lambrechts, M., & Johansen, A. 2015b, A&A, 582, A112

Bitsch, B. & Mah, J. 2023, A&A, 679, A11

Bitsch, B., Morbidelli, A., Johansen, A., et al. 2018, A&A, 612, A30

Bitsch, B., Raymond, S. N., Buchhave, L. A., et al. 2021, A&A, 649, L5

Bitsch, B. & Savvidou, S. 2021, A&A, 647, A96

Bitsch, B., Schneider, A. D., & Kreidberg, L. 2022, A&A, 665, A138

Bitsch, B., Trifonov, T., & Izidoro, A. 2020, A&A, 643, A66

Blum, J. & Wurm, G. 2008, ARA&A, 46, 21

Bodenheimer, P., Lin, D. N. C., & Mardling, R. A. 2001, ApJ, 548, 466

Boogert, A. C. A., Gerakines, P. A., & Whittet, D. C. B. 2015, ARA&A, 53, 541

Booth, R. A., Clarke, C. J., Madhusudhan, N., & Ilee, J. D. 2017, MNRAS, 469, 3994

Booth, R. A. & Ilee, J. D. 2019, MNRAS, 487, 3998

Borysow, A. 2002, A&A, 390, 779

Borysow, A. & Frommhold, L. 1989, ApJ, 341, 549

Borysow, A., Frommhold, L., & Moraldi, M. 1989, ApJ, 336, 495

Borysow, A., Jorgensen, U. G., & Fu, Y. 2001, J. Quant. Spectr. Rad. Transf., 68, 235

Borysow, J., Frommhold, L., & Birnbaum, G. 1988, ApJ, 326, 509

Bosman, A. D., Cridland, A. J., & Miguel, Y. 2019, A&A, 632, L11

Bottke, W. F., Durda, D. D., Nesvorný, D., et al. 2005, Icarus, 175, 111

Bouchy, F., Moutou, C., Queloz, D., & CoRoT Exoplanet Science Team. 2009, in Transiting Planets, ed. F. Pont, D. Sasselov, & M. J. Holman, Vol. 253, 129–139

Boyajian, T., von Braun, K., Feiden, G. A., et al. 2015, MNRAS, 447, 846

Brauer, F., Dullemond, C. P., & Henning, T. 2008, A&A, 480, 859

Brent, R. 1973, Algorithms for minimization without derivatives (Prentice-Hall)

Bressan, A. G., Chiosi, C., & Bertelli, G. 1981, A&A, 102, 25

Brewer, J. M., Fischer, D. A., & Madhusudhan, N. 2017, AJ, 153, 83

Brogi, M., de Kok, R. J., Albrecht, S., et al. 2016, ApJ, 817, 106

Brogi, M. & Line, M. R. 2019, AJ, 157, 114

Brogi, M., Snellen, I. A. G., de Kok, R. J., et al. 2012, Nature, 486, 502

Brouwers, M. G. & Ormel, C. W. 2020, A&A, 634, A15

Brown, T. M., Charbonneau, D., Gilliland, R. L., Noyes, R. W., & Burrows, A. 2001, ApJ, 552, 699

Brügger, N., Alibert, Y., Ataiee, S., & Benz, W. 2018, A&A, 619, A174

Buchhave, L. A., Bitsch, B., Johansen, A., et al. 2018, ApJ, 856, 37

Buder, S., Asplund, M., Duong, L., et al. 2018, MNRAS, 478, 4513

Burrows, A., Hubeny, I., Budaj, J., & Hubbard, W. B. 2007, ApJ, 661, 502

Burrows, A. & Sharp, C. M. 1999, ApJ, 512, 843

Carone, L., Baeyens, R., Mollière, P., et al. 2020, MNRAS, 496, 3582

Carone, L., Keppens, R., & Decin, L. 2016, MNRAS, 463, 3114

Carone, L., Mollière, P., Zhou, Y., et al. 2021, A&A, 646, A168

Casewell, S. L., Debes, J., Braker, I. P., et al. 2020, MNRAS, 499, 5318

Casewell, S. L., Littlefair, S. P., Parsons, S. G., et al. 2018, MNRAS, 481, 5216

Chabrier, G. & Baraffe, I. 2007, ApJ, 661, L81

Chabrier, G., Barman, T., Baraffe, I., Allard, F., & Hauschildt, P. H. 2004, ApJ, 603, L53

Chambers, J. 2018, ApJ, 865, 30

Chan, Y. M. & Dalgarno, A. 1965, Proceedings of the Physical Society, 85, 227

Charbonneau, D., Brown, T. M., Latham, D. W., & Mayor, M. 2000, ApJ, 529, L45

Charbonneau, D., Brown, T. M., Noyes, R. W., & Gilliland, R. L. 2002, ApJ, 568, 377

Chatziastros, L., Bitsch, B., & Schneider, A. D. 2024, A&A, 681, A52

Chiang, E. I. & Goldreich, P. 1997, ApJ, 490, 368

Chrenko, O., Brož, M., & Lambrechts, M. 2017, A&A, 606, A114

Christie, D. A., Lee, E. K. H., Innes, H., et al. 2022, PSJ, 3, 261

Christie, D. A., Mayne, N. J., Lines, S., et al. 2021, MNRAS, 506, 4500

Chubb, K. L., Rocchetto, M., Yurchenko, S. N., et al. 2021, A&A, 646, A21

Ciesla, F. J. & Cuzzi, J. N. 2006, Icarus, 181, 178

Cimerman, N. P., Kuiper, R., & Ormel, C. W. 2017, MNRAS, 471, 4662

Cleeves, L. I., Öberg, K. I., Wilner, D. J., et al. 2018, ApJ, 865, 155

Coles, P. A., Yurchenko, S. N., & Tennyson, J. 2019, MNRAS, 490, 4638

Colón, K. D., Kreidberg, L., Welbanks, L., et al. 2020, AJ, 160, 280

Crida, A. & Bitsch, B. 2017, Icarus, 285, 145

Crida, A. & Morbidelli, A. 2007, MNRAS, 377, 1324

Crida, A., Morbidelli, A., & Masset, F. 2006, Icarus, 181, 587

Cridland, A. J., Eistrup, C., & van Dishoeck, E. F. 2019, A&A, 627, A127

Cridland, A. J., van Dishoeck, E. F., Alessi, M., & Pudritz, R. E. 2020, A&A, 642, A229

Crossfield, I. J. M., Knutson, H., Fortney, J., et al. 2012, ApJ, 752, 81

Cubillos, P. E. 2020, bibmanager: A BibTeX manager for LaTeX projects

Currie, T., Biller, B., Lagrange, A., et al. 2023, in Astronomical Society of the Pacific Conference Series, Vol. 534, Protostars and Planets VII, ed. S. Inutsuka, Y. Aikawa, T. Muto, K. Tomida, & M. Tamura, 799

Cuzzi, J. N., Hogan, R. C., & Bottke, W. F. 2010, Icarus, 208, 518

Cuzzi, J. N. & Zahnle, K. J. 2004, ApJ, 614, 490

D'Alessio, P., Cantó, J., Hartmann, L., Calvet, N., & Lizano, S. 1999, ApJ, 511, 896

Dalgarno, A. & Williams, D. A. 1962, ApJ, 136, 690

Dang, L., Cowan, N. B., Schwartz, J. C., et al. 2018, Nature Astronomy, 2, 220

Danti, C., Bitsch, B., & Mah, J. 2023, A&A, 679, L7

Dawson, R. I. & Johnson, J. A. 2018, ARA&A, 56, 175

de Boer, J., Salter, G., Benisty, M., et al. 2016, A&A, 595, A114

Debras, F. & Chabrier, G. 2019, ApJ, 872, 100

Deitrick, R., Heng, K., Schroffenegger, U., et al. 2022, MNRAS, 512, 3759

Deitrick, R., Mendonça, J. M., Schroffenegger, U., et al. 2020, ApJS, 248, 30

Demory, B.-O. & Seager, S. 2011, ApJS, 197, 12

Dittrich, K., Klahr, H., & Johansen, A. 2013, ApJ, 763, 117

Dobbs-Dixon, I. & Agol, E. 2013, MNRAS, 435, 3159

Drążkowska, J. & Alibert, Y. 2017, A&A, 608, A92

Drążkowska, J., Alibert, Y., & Moore, B. 2016, A&A, 594, A105

Drążkowska, J., Stammler, S. M., & Birnstiel, T. 2021, A&A, 647, A15

Drummond, B., Hébrard, E., Mayne, N. J., et al. 2020, A&A, 636, A68

Drummond, B., Mayne, N. J., Baraffe, I., et al. 2018a, A&A, 612, A105

Drummond, B., Mayne, N. J., Manners, J., et al. 2018b, ApJ, 855, L31

Dullemond, C. 2012, Lecture notes on radiative transfer in astrophysics

Dullemond, C. P. 2013, Theoretical Models of the Structure of Protoplanetary Disks - Les Houches 2013

Dullemond, C. P. & Birnstiel, T. 2018, DISKLAB - A protoplanetary disk modeling package in Python

Dullemond, C. P., Birnstiel, T., Huang, J., et al. 2018, ApJ, 869, L46

Dullemond, C. P., van Zadelhoff, G. J., & Natta, A. 2002, A&A, 389, 464

Eberlein, M., Bitsch, B., & Schneider, A. D. in prep

Ehrenreich, D., Lovis, C., Allart, R., et al. 2020, Nature, 580, 597

Eistrup, C., Walsh, C., & van Dishoeck, E. F. 2016, A&A, 595, A83

Emsenhuber, A., Burn, R., Weder, J., et al. 2023, A&A, 673, A78

Emsenhuber, A., Mordasini, C., Burn, R., et al. 2021, A&A, 656, A69

Ercolano, B. & Clarke, C. J. 2010, MNRAS, 402, 2735

Ercolano, B., Clarke, C. J., & Drake, J. J. 2009, ApJ, 699, 1639

Evans, T. M., Aigrain, S., Gibson, N., et al. 2015, MNRAS, 451, 680

Feautrier, P. 1964, Comptes Rendus Academie des Sciences (serie non specifiee), 258, 3189

Flaherty, K. M., Hughes, A. M., Teague, R., et al. 2018, ApJ, 856, 117

Fleischer, A. J., Gauger, A., & Sedlmayr, E. 1992, A&A, 266, 321

Flock, M., Ruge, J. P., Dzyurkevich, N., et al. 2015, A&A, 574, A68

Flynn, G. J., Bleuet, P., Borg, J., et al. 2006, Science, 314, 1731

Ford, E. B. & Rasio, F. A. 2008, ApJ, 686, 621

Fortier, A., Alibert, Y., Carron, F., Benz, W., & Dittkrist, K. M. 2013, A&A, 549, A44

Fortier, A., Benvenuto, O. G., & Brunini, A. 2009, A&A, 500, 1249

Fortney, J. J., Dawson, R. I., & Komacek, T. D. 2021, Journal of Geophysical Research (Planets), 126, e06629

Fortney, J. J., Lodders, K., Marley, M. S., & Freedman, R. S. 2008a, ApJ, 678, 1419

Fortney, J. J., Marley, M. S., & Barnes, J. W. 2007, ApJ, 659, 1661

Fortney, J. J., Marley, M. S., Saumon, D., & Lodders, K. 2008b, ApJ, 683, 1104

Fortney, J. J. & Nettelmann, N. 2010, Space Sci. Rev., 152, 423

Fortney, J. J., Visscher, C., Marley, M. S., et al. 2020, AJ, 160, 288

Freytag, B., Allard, F., Ludwig, H. G., Homeier, D., & Steffen, M. 2010, A&A, 513, A19

Freytag, B., Höfner, S., & Liljegren, S. 2019, IAU Symposium, 343, 9

Freytag, B., Liljegren, S., & Höfner, S. 2017, A&A, 600, A137

Fromang, S., Leconte, J., & Heng, K. 2016, A&A, 591, A144

Gaia Collaboration, Brown, A. G. A., Vallenari, A., et al. 2018, A&A, 616, A1

Gárate, M., Birnstiel, T., Drążkowska, J., & Stammler, S. M. 2020, A&A, 635, A149

Giacobbe, P., Brogi, M., Gandhi, S., et al. 2021, Nature, 592, 205

Gill, A. E. 1980, Quarterly Journal of the Royal Meteorological Society, 106, 447

Gillon, M., Triaud, A. H. M. J., Fortney, J. J., et al. 2012, A&A, 542, A4

Ginzburg, S. & Chiang, E. 2020, MNRAS, 498, 680

Ginzburg, S. & Sari, R. 2015, ApJ, 803, 111

Ginzburg, S. & Sari, R. 2016, ApJ, 819, 116

Goldreich, P. & Tremaine, S. 1979, ApJ, 233, 857

Goldreich, P. & Tremaine, S. 1980, ApJ, 241, 425

Goody, R., West, R., Chen, L., & Crisp, D. 1989, J. Quant. Spectr. Rad. Transf., 42, 539

Gordon, S. & McBride, B. 1994, NASA Reference Publication 1311

GRAVITY Collaboration, Nowak, M., Lacour, S., et al. 2020, A&A, 633, A110

Gray, D. F. 2008, The Observation and Analysis of Stellar Photospheres

Grimm, S. L. & Heng, K. 2015, ApJ, 808, 182

Grimm, S. L., Malik, M., Kitzmann, D., et al. 2021, ApJS, 253, 30

Guilera, O. M., Cuello, N., Montesinos, M., et al. 2019, MNRAS, 486, 5690

Guilera, O. M., de Elía, G. C., Brunini, A., & Santamaría, P. J. 2014, A&A, 565, A96

Guilera, O. M., Fortier, A., Brunini, A., & Benvenuto, O. G. 2011, A&A, 532, A142

Guilera, O. M., Sándor, Z., Ronco, M. P., Venturini, J., & Miller Bertolami, M. M. 2020, A&A, 642, A140

Guillot, T. 2010, A&A, 520, A27

Guillot, T., Burrows, A., Hubbard, W. B., Lunine, J. I., & Saumon, D. 1996, ApJ, 459, L35

Guillot, T., Fletcher, L. N., Helled, R., et al. 2022, arXiv e-prints, arXiv:2205.04100

Guillot, T. & Hueso, R. 2006, MNRAS, 367, L47

Guillot, T. & Showman, A. P. 2002, A&A, 385, 156

Gundlach, B. & Blum, J. 2015, ApJ, 798, 34

Gustafsson, B., Bell, R. A., Eriksson, K., & Nordlund, A. 1975, A&A, 42, 407

Gustafsson, B., Edvardsson, B., Eriksson, K., et al. 2008, A&A, 486, 951

Güttler, C., Blum, J., Zsom, A., Ormel, C. W., & Dullemond, C. P. 2010, A&A, 513, A56

Hammond, M. & Abbot, D. S. 2022, MNRAS, 511, 2313

Hanasoge, S., Miesch, M. S., Roth, M., et al. 2015, Space Sci. Rev., 196, 79

Hands, T. O. & Helled, R. 2022, MNRAS, 509, 894

Hartlep, T. & Cuzzi, J. N. 2020, ApJ, 892, 120

Hartman, J. D., Bakos, G. Á., Bhatti, W., et al. 2016, AJ, 152, 182

Heimbach, P., Hill, C., & Giering, R. 2002, in Computational Science—ICCS 2002: International Conference Amsterdam, The Netherlands, April 21–24, 2002 Proceedings, Part II 2, Springer, 1019–1028

Held, I. M. & Suarez, M. J. 1994, Bulletin of the American Meteorological Society, 75, 1825

Helled, R., Werner, S., Dorn, C., et al. 2022, Experimental Astronomy, 53, 323

Helling, C. 2019, in Journal of Physics Conference Series, Vol. 1322, Journal of Physics Conference Series, 012028

Helling, C., Gourbin, P., Woitke, P., & Parmentier, V. 2019a, A&A, 626, A133

Helling, C., Iro, N., Corrales, L., et al. 2019b, A&A, 631, A79

Helling, C., Lewis, D., Samra, D., et al. 2021a, A&A, 649, A44

Helling, C., Worters, M., Samra, D., Molaverdikhani, K., & Iro, N. 2021b, A&A, 648, A80

Heng, K. 2012, ApJ, 761, L1

Heng, K., Frierson, D. M. W., & Phillipps, P. J. 2011a, MNRAS, 418, 2669

Heng, K., Menou, K., & Phillipps, P. J. 2011b, MNRAS, 413, 2380

Henry, G. W., Marcy, G. W., Butler, R. P., & Vogt, S. S. 2000, ApJ, 529, L41

Hill, C., Adcroft, A., Jamous, D., & Marshall, J. 1999, in Proceedings of Eigth ECMWF Workshop on the Use of Parallel Processors in Meteorology. World Scientific

Hindle, A. W., Bushby, P. J., & Rogers, T. M. 2021, ApJ, 922, 176

Hoeijmakers, H. J., Ehrenreich, D., Heng, K., et al. 2018, Nature, 560, 453

Hoeijmakers, H. J., Ehrenreich, D., Kitzmann, D., et al. 2019, A&A, 627, A165

Höfner, S. & Freytag, B. 2019, A&A, 623, A158

Hollenbach, D., Kaufman, M. J., Bergin, E. A., & Melnick, G. J. 2009, ApJ, 690, 1497

Holton, J. R. 1992, An introduction to dynamic meteorology

Hori, Y. & Ikoma, M. 2011, MNRAS, 416, 1419

Howard, A. W., Marcy, G. W., Bryson, S. T., et al. 2012, ApJS, 201, 15

Hubeny, I. 2017, MNRAS, 469, 841

Hühn, L. A. & Bitsch, B. 2023, A&A, 676, A87

Husser, T. O., Wende-von Berg, S., Dreizler, S., et al. 2013, A&A, 553, A6

Ida, S. & Lin, D. N. C. 2004, ApJ, 604, 388

Ida, S. & Lin, D. N. C. 2008a, ApJ, 673, 487

Ida, S. & Lin, D. N. C. 2008b, ApJ, 685, 584

Ida, S. & Lin, D. N. C. 2010, ApJ, 719, 810

Iess, L., Militzer, B., Kaspi, Y., et al. 2019, Science, 364, aat2965

Ikoma, M., Nakazawa, K., & Emori, H. 2000, ApJ, 537, 1013

Izidoro, A., Bitsch, B., & Dasgupta, R. 2021a, ApJ, 915, 62

Izidoro, A., Bitsch, B., Raymond, S. N., et al. 2021b, A&A, 650, A152

Jablonowski, C. & Williamson, D. L. 2011, The Pros and Cons of Diffusion, Filters and Fixers in Atmospheric General Circulation Models, ed. P. Lauritzen, C. Jablonowski, M. Taylor, & R. Nair (Berlin, Heidelberg: Springer Berlin Heidelberg), 381–493

Johansen, A. & Bitsch, B. 2019, A&A, 631, A70

Johansen, A., Klahr, H., & Henning, T. 2011, A&A, 529, A62

Johansen, A. & Lacerda, P. 2010, MNRAS, 404, 475

Johansen, A. & Lambrechts, M. 2017, Annual Review of Earth and Planetary Sciences, 45, 359

Johansen, A., Ronnet, T., Bizzarro, M., et al. 2021, Science Advances, 7, eabc0444

Johansen, A. & Youdin, A. 2007, ApJ, 662, 627

Johansen, A., Youdin, A., & Mac Low, M.-M. 2009, ApJ, 704, L75

Jurić, M. & Tremaine, S. 2008, ApJ, 686, 603

JWST Transiting Exoplanet Community Early Release Science Team, Ahrer, E.-M., Alderson, L., et al. 2023, Nature, 614, 649

Kalyaan, A., Pinilla, P., Krijt, S., et al. 2023, ApJ, 954, 66

Kalyaan, A., Pinilla, P., Krijt, S., Mulders, G. D., & Banzatti, A. 2021, ApJ, 921, 84

Kama, M., Shorttle, O., Jermyn, A. S., et al. 2019, ApJ, 885, 114

Kaspi, Y., Galanti, E., Hubbard, W. B., et al. 2018, Nature, 555, 223

Kataria, T., Showman, A. P., Fortney, J. J., et al. 2015, ApJ, 801, 86

Kataria, T., Showman, A. P., Lewis, N. K., et al. 2013, ApJ, 767, 76

Kataria, T., Sing, D. K., Lewis, N. K., et al. 2016, ApJ, 821, 9

Kenyon, S. J. & Bromley, B. C. 2012, AJ, 143, 63

Keppler, M., Benisty, M., Müller, A., et al. 2018, A&A, 617, A44

Kesseli, A. Y. & Snellen, I. A. G. 2021, ApJ, 908, L17

Kesseli, A. Y., Snellen, I. A. G., Casasayas-Barris, N., Mollière, P., & Sánchez-López, A. 2022, AJ, 163, 107

Klarmann, L., Ormel, C. W., & Dominik, C. 2018, A&A, 618, L1

Kley, W. & Nelson, R. P. 2012, ARA&A, 50, 211

Knierim, H., Batygin, K., & Bitsch, B. 2022, A&A, 658, L7

Knutson, H. A., Charbonneau, D., Allen, L. E., Burrows, A., & Megeath, S. T. 2008, ApJ, 673, 526

Knutson, H. A., Charbonneau, D., Allen, L. E., et al. 2007, Nature, 447, 183

Kolecki, J. R. & Wang, J. 2022, AJ, 164, 87

Koll, D. D. B. & Abbot, D. S. 2016, ApJ, 825, 99

Koll, D. D. B. & Komacek, T. D. 2018, ApJ, 853, 133

Komacek, T. D., Gao, P., Thorngren, D. P., May, E. M., & Tan, X. 2022, ApJ, 941, L40

Komacek, T. D., Showman, A. P., & Tan, X. 2017, ApJ, 835, 198

Komacek, T. D., Thorngren, D. P., Lopez, E. D., & Ginzburg, S. 2020, ApJ, 893, 36

Komacek, T. D. & Youdin, A. N. 2017, ApJ, 844, 94

Kreidberg, L., Bean, J. L., Désert, J.-M., et al. 2014, ApJ, 793, L27

Kretke, K. A. & Levison, H. F. 2014, AJ, 148, 109

Krijt, S., Bosman, A. D., Zhang, K., et al. 2020, ApJ, 899, 134

Krijt, S., Schwarz, K. R., Bergin, E. A., & Ciesla, F. J. 2018, ApJ, 864, 78

Kruijer, T. S., Burkhardt, C., Budde, G., & Kleine, T. 2017, Proceedings of the National Academy of Science, 114, 6712

Lambrechts, M. & Johansen, A. 2012, A&A, 544, A32

Lambrechts, M. & Johansen, A. 2014, A&A, 572, A107

Lambrechts, M., Johansen, A., & Morbidelli, A. 2014, A&A, 572, A35

Lambrechts, M. & Lega, E. 2017, A&A, 606, A146

Lambrechts, M., Lega, E., Nelson, R. P., Crida, A., & Morbidelli, A. 2019a, A&A, 630, A82

Lambrechts, M., Morbidelli, A., Jacobson, S. A., et al. 2019b, A&A, 627, A83

Laughlin, G., Crismani, M., & Adams, F. C. 2011, ApJ, 729, L7

Leconte, J. 2021, A&A, 645, A20

Lee, E., Dobbs-Dixon, I., Helling, C., Bognar, K., & Woitke, P. 2016, A&A, 594, A48

Lee, E. K. H., Lothringer, J. D., Casewell, S. L., et al. 2022, arXiv e-prints, arXiv:2203.09854

Lee, E. K. H., Parmentier, V., Hammond, M., et al. 2021, MNRAS, 506, 2695

Lee, E. K. H., Tsai, S.-M., Hammond, M., & Tan, X. 2023, A&A, 672, A110

Lee, J.-M., Heng, K., & Irwin, P. G. J. 2013, ApJ, 778, 97

Lee, U. 2019, MNRAS, 484, 5845

Lega, E., Crida, A., Bitsch, B., & Morbidelli, A. 2014, MNRAS, 440, 683

Lenz, C. T., Klahr, H., & Birnstiel, T. 2019, ApJ, 874, 36

Levison, H. F., Kretke, K. A., & Duncan, M. J. 2015, Nature, 524, 322

Levison, H. F., Thommes, E., & Duncan, M. J. 2010, AJ, 139, 1297

Li, C., Ingersoll, A., Bolton, S., et al. 2020, Nature Astronomy, 4, 609

Li, G., Gordon, I. E., Rothman, L. S., et al. 2015, ApJS, 216, 15

Li, J., Bergin, E. A., Blake, G. A., Ciesla, F. J., & Hirschmann, M. M. 2021, Science Advances, 7, eabd3632

Li, J. & Goodman, J. 2010, ApJ, 725, 1146

Li, J. & Shibata, K. 2006, Journal of the Atmospheric Sciences, 63, 1365

Lian, Y., Showman, A. P., Tan, X., & Hu, Y. 2022, ApJ, 928, 166

Lienert, J., Bitsch, B., & Henning, T. in prep

Line, M. R., Brogi, M., Bean, J. L., et al. 2021, Nature, 598, 580

Line, M. R., Stevenson, K. B., Bean, J., et al. 2016, AJ, 152, 203

Lines, S., Mayne, N. J., Manners, J., et al. 2019, MNRAS, 488, 1332

Liu, B. & Showman, A. P. 2013, ApJ, 770, 42

Liu, S.-F., Hori, Y., Müller, S., et al. 2019, Nature, 572, 355

Lodato, G., Scardoni, C. E., Manara, C. F., & Testi, L. 2017, MNRAS, 472, 4700

Lodders, K. 2003, ApJ, 591, 1220

Lodders, K. 2010, in Formation and Evolution of Exoplanets, 157

Lopez, E. D. & Fortney, J. J. 2013, ApJ, 776, 2

Lopez, E. D. & Fortney, J. J. 2016, ApJ, 818, 4

Lorek, S., Lacerda, P., & Blum, J. 2018, A&A, 611, A18

Lothringer, J. D., Fu, G., Sing, D. K., & Barman, T. S. 2020, ApJ, 898, L14

Lothringer, J. D., Rustamkulov, Z., Sing, D. K., et al. 2021, ApJ, 914, 12

Lynden-Bell, D. & Pringle, J. E. 1974, MNRAS, 168, 603

Lyra, W., Raettig, N., & Klahr, H. 2018, Research Notes of the American Astronomical Society, 2, 195

MacDonald, R. J. & Madhusudhan, N. 2017, MNRAS, 469, 1979

Machida, M. N., Kokubo, E., Inutsuka, S.-I., & Matsumoto, T. 2010, MNRAS, 405, 1227

Madhusudhan, N. 2019, ARA&A, 57, 617

Madhusudhan, N., Bitsch, B., Johansen, A., & Eriksson, L. 2017, MNRAS, 469, 4102

Madhusudhan, N., Crouzet, N., McCullough, P. R., Deming, D., & Hedges, C. 2014, ApJ, 791, L9

Madhusudhan, N., Harrington, J., Stevenson, K. B., et al. 2011, Nature, 469, 64

Mah, J. & Bitsch, B. 2023, A&A, 673, A17

Mah, J., Bitsch, B., Pascucci, I., & Henning, T. 2023, A&A, 677, L7

Mamajek, E. E. 2009, in American Institute of Physics Conference Series, Vol. 1158, Exoplanets and Disks: Their Formation and Diversity, ed. T. Usuda, M. Tamura, & M. Ishii, 3–10

Manabe, S., Smagorinsky, J., & Strickler, R. F. 1965, Monthly Weather Review, 93, 769

Mankovich, C. R. & Fuller, J. 2021, Nature Astronomy, 5, 1103

Marboeuf, U., Thiabaud, A., Alibert, Y., Cabral, N., & Benz, W. 2014a, A&A, 570, A36

Marboeuf, U., Thiabaud, A., Alibert, Y., Cabral, N., & Benz, W. 2014b, A&A, 570, A35

Marshall, J., Adcroft, A., Hill, C., Perelman, L., & Heisey, C. 1997a, J. Geophys. Res., 102, 5753

Marshall, J., Hill, C., Perelman, L., & Adcroft, A. 1997b, J. Geophys. Res., 102, 5733

Marshall, J. & Plumb, R. A. 2007, Atmosphere, ocean and climate dynamics (San Diego, CA: Academic Press)

Martinez, C. F., Cunha, K., Ghezzi, L., & Smith, V. V. 2019, ApJ, 875, 29

Masset, F. S. 2017, MNRAS, 472, 4204

Matsumura, S., Brasser, R., & Ida, S. 2017, A&A, 607, A67

Matsuno, T. 1966, Journal of the Meteorological Society of Japan, 44, 25

May, E. M., Komacek, T. D., Stevenson, K. B., et al. 2021, AJ, 162, 158

Mayne, N. J., Baraffe, I., Acreman, D. M., et al. 2014, A&A, 561, A1

Mayne, N. J., Debras, F., Baraffe, I., et al. 2017, A&A, 604, A79

Mayne, N. J., Drummond, B., Debras, F., et al. 2019, ApJ, 871, 56

Mayor, M. & Queloz, D. 1995, Nature, 378, 355

Mazeh, T., Naef, D., Torres, G., et al. 2000, ApJ, 532, L55

McKemmish, L. K., Masseron, T., Hoeijmakers, H. J., et al. 2019, MNRAS, 488, 2836

McKemmish, L. K., Yurchenko, S. N., & Tennyson, J. 2016, MNRAS, 463, 771

Mendonça, J. M. 2020, MNRAS, 491, 1456

Mendonça, J. M., Grimm, S. L., Grosheintz, L., & Heng, K. 2016, ApJ, 829, 115

Mendonça, J. M., Malik, M., Demory, B.-O., & Heng, K. 2018a, AJ, 155, 150

Mendonça, J. M., Tsai, S.-m., Malik, M., Grimm, S. L., & Heng, K. 2018b, ApJ, 869, 107

Menou, K. 2012, ApJ, 745, 138

Menou, K. 2019, MNRAS, 485, L98

Menou, K. & Rauscher, E. 2009, ApJ, 700, 887

Merritt, S. R., Gibson, N. P., Nugroho, S. K., et al. 2020, A&A, 636, A117

Miguel, Y., Bazot, M., Guillot, T., et al. 2022, A&A, 662, A18

Miller, M. J. 1984, Quarterly Journal of the Royal Meteorological Society, 110, 280

Miller, N. & Fortney, J. J. 2011, ApJ, 736, L29

Mollière, P., Molyarova, T., Bitsch, B., et al. 2022, ApJ, 934, 74

Mollière, P., Stolker, T., Lacour, S., et al. 2020, A&A, 640, A131

Mollière, P., van Boekel, R., Bouwman, J., et al. 2017, A&A, 600, A10

Mollière, P., van Boekel, R., Dullemond, C., Henning, T., & Mordasini, C. 2015, ApJ, 813, 47

Mollière, P., Wardenier, J. P., van Boekel, R., et al. 2019, A&A, 627, A67

Monsch, K., Ercolano, B., Picogna, G., Preibisch, T., & Rau, M. M. 2019, MNRAS, 483, 3448

Morbidelli, A., Bitsch, B., Crida, A., et al. 2016, Icarus, 267, 368

Morbidelli, A., Bottke, W. F., Nesvorný, D., & Levison, H. F. 2009, Icarus, 204, 558

Morbidelli, A., Lambrechts, M., Jacobson, S., & Bitsch, B. 2015, Icarus, 258, 418

Morbidelli, A. & Nesvorny, D. 2012, A&A, 546, A18

Morbidelli, A., Szulágyi, J., Crida, A., et al. 2014, Icarus, 232, 266

Mordasini, C., Alibert, Y., & Benz, W. 2009, A&A, 501, 1139

Mordasini, C., Alibert, Y., Georgy, C., et al. 2012, A&A, 547, A112

Mordasini, C., van Boekel, R., Mollière, P., Henning, T., & Benneke, B. 2016, ApJ, 832, 41

Mousis, O., Aguichine, A., Bouquet, A., et al. 2021, arXiv e-prints, arXiv:2103.01793

Movshovitz, N. & Podolak, M. 2008, Icarus, 194, 368

Mulders, G. D., Pascucci, I., Apai, D., & Ciesla, F. J. 2018, AJ, 156, 24

Müller, A., Keppler, M., Henning, T., et al. 2018, A&A, 617, L2

Müller, J., Savvidou, S., & Bitsch, B. 2021, A&A, 650, A185

Müller, S., Ben-Yami, M., & Helled, R. 2020, ApJ, 903, 147

Mumma, M. J. & Charnley, S. B. 2011, ARA&A, 49, 471

Musiolik, G. & Wurm, G. 2019, ApJ, 873, 58

Müller, J., Bitsch, B., & Schneider, A. D. in review

Nakagawa, Y., Sekiya, M., & Hayashi, C. 1986, Icarus, 67, 375

Ndugu, N. & Bitsch, B. in prep

Ndugu, N., Bitsch, B., & Jurua, E. 2018, MNRAS, 474, 886

Ndugu, N., Bitsch, B., Morbidelli, A., Crida, A., & Jurua, E. 2021, MNRAS, 501, 2017

Nelson, R. P., Gressel, O., & Umurhan, O. M. 2013, MNRAS, 435, 2610

Ng, K. C. 1974, J. Chem. Phys., 61, 2680

Noti, P. A., Lee, E. K. H., Deitrick, R., & Hammond, M. 2023, MNRAS, 524, 3396

Notsu, S., Eistrup, C., Walsh, C., & Nomura, H. 2020, MNRAS, 499, 2229

Öberg, K. I., Murray-Clay, R., & Bergin, E. A. 2011, ApJ, 743, L16

Öberg, K. I. & Wordsworth, R. 2019, AJ, 158, 194

Ogihara, M., Hori, Y., Kunitomo, M., & Kurosaki, K. 2021, A&A, 648, L1

Okuzumi, S. 2009, ApJ, 698, 1122

Olson, G. L., Auer, L. H., & Buchler, J. R. 1986, J. Quant. Spectr. Rad. Transf., 35, 431

Ormel, C. W. & Klahr, H. H. 2010, A&A, 520, A43

Ormel, C. W., Shi, J.-M., & Kuiper, R. 2015, MNRAS, 447, 3512

Ormel, C. W., Vazan, A., & Brouwers, M. G. 2021, A&A, 647, A175

Owen, J. E., Clarke, C. J., & Ercolano, B. 2012, MNRAS, 422, 1880

Owen, J. E., Scaife, A. M. M., & Ercolano, B. 2013, MNRAS, 434, 3378

Owen, J. E. & Wu, Y. 2013, ApJ, 775, 105

Owen, T., Mahaffy, P., Niemann, H. B., et al. 1999, Nature, 402, 269

Paardekooper, S. J. 2014, MNRAS, 444, 2031

Paardekooper, S. J., Baruteau, C., & Kley, W. 2011, MNRAS, 410, 293

Parmentier, V., Fortney, J. J., Showman, A. P., Morley, C., & Marley, M. S. 2016, ApJ, 828, 22

Parmentier, V., Guillot, T., Fortney, J. J., & Marley, M. S. 2015, A&A, 574, A35

Parmentier, V., Line, M. R., Bean, J. L., et al. 2018, A&A, 617, A110

Parmentier, V., Showman, A. P., & Fortney, J. J. 2021, MNRAS, 501, 78

Pascucci, I. & Sterzik, M. 2009, ApJ, 702, 724

Peixóto, J. P. & Oort, A. H. 1984, Reviews of Modern Physics, 56, 365

Pelletier, S., Benneke, B., Darveau-Bernier, A., et al. 2021, AJ, 162, 73

Perna, R., Heng, K., & Pont, F. 2012, ApJ, 751, 59

Perna, R., Menou, K., & Rauscher, E. 2010a, ApJ, 719, 1421

Perna, R., Menou, K., & Rauscher, E. 2010b, ApJ, 724, 313

Pierens, A. 2015, MNRAS, 454, 2003

Piette, A. A. A. & Madhusudhan, N. 2020, ApJ, 904, 154

Pinilla, P., Lenz, C. T., & Stammler, S. M. 2021, A&A, 645, A70

Piskunov, N. E., Kupka, F., Ryabchikova, T. A., Weiss, W. W., & Jeffery, C. S. 1995, A&AS, 112, 525

Piso, A.-M. A., Öberg, K. I., Birnstiel, T., & Murray-Clay, R. A. 2015, ApJ, 815, 109

Piso, A.-M. A. & Youdin, A. N. 2014, ApJ, 786, 21

Polichtchouk, I., Cho, J. Y. K., Watkins, C., et al. 2014, Icarus, 229, 355

Pollack, J. B., Hubickyj, O., Bodenheimer, P., et al. 1996, Icarus, 124, 62

Polyansky, O. L., Kyuberis, A. A., Zobov, N. F., et al. 2018, MNRAS, 480, 2597

Pontoppidan, K. M., Salyk, C., Banzatti, A., et al. 2019, ApJ, 874, 92

Press, W. H., Teukolsky, S. A., Vetterling, W. T., & Flannery, B. P. 1992, Numerical recipes in FORTRAN. The art of scientific computing

Pringle, J. E. 1981, ARA&A, 19, 137

Raettig, N., Klahr, H., & Lyra, W. 2015, ApJ, 804, 35

Ramírez, V., Cridland, A. J., & Mollière, P. 2020, A&A, 641, A87

Rasio, F. A., Tout, C. A., Lubow, S. H., & Livio, M. 1996, ApJ, 470, 1187

Rauscher, E. & Menou, K. 2010, ApJ, 714, 1334

Rauscher, E. & Menou, K. 2012, ApJ, 750, 96

Rauscher, E. & Menou, K. 2013, ApJ, 764, 103

Rauscher, E. & Showman, A. P. 2014, ApJ, 784, 160

Raymond, S. N., Armitage, P. J., & Gorelick, N. 2009a, ApJ, 699, L88

Raymond, S. N., O'Brien, D. P., Morbidelli, A., & Kaib, N. A. 2009b, Icarus, 203, 644

Reggiani, H., Schlaufman, K. C., Healy, B. F., Lothringer, J. D., & Sing, D. K. 2022, AJ, 163, 159

Richard, C., Gordon, I. E., Rothman, L. S., et al. 2012, J. Quant. Spectr. Rad. Transf., 113, 1276

Rogers, T. M. & Showman, A. P. 2014, ApJ, 782, L4

Roman, M. & Rauscher, E. 2017, ApJ, 850, 17

Roman, M. T., Kempton, E. M. R., Rauscher, E., et al. 2021, ApJ, 908, 101

Rutten, R. J. 2003, Radiative Transfer in Stellar Atmospheres

Sainsbury-Martinez, F., Casewell, S. L., Lothringer, J. D., Phillips, M. W., & Tremblin, P. 2021, A&A, 656, A128

Sainsbury-Martinez, F., Wang, P., Fromang, S., et al. 2019, A&A, 632, A114

Sarkis, P., Mordasini, C., Henning, T., Marleau, G. D., & Mollière, P. 2021, A&A, 645, A79

Savel, A. B., Kempton, E. M. R., Malik, M., et al. 2022, ApJ, 926, 85

Savitzky, A. & Golay, M. J. E. 1964, Analytical Chemistry, 36, 1627

Savvidou, S. & Bitsch, B. 2021, A&A, 650, A132

Savvidou, S. & Bitsch, B. 2023, A&A, 679, A42

Savvidou, S. & Bitsch, B. in prep

Savvidou, S., Bitsch, B., & Lambrechts, M. 2020, A&A, 640, A63

Schäfer, U., Yang, C.-C., & Johansen, A. 2017, A&A, 597, A69

Schneider, A. D., Baeyens, R., & Kiefer, S. 2022, gcm_toolkit, tools for GCM postprocessing

Schneider, A. D. & Bitsch, B. 2021a, A&A, 654, A71

Schneider, A. D. & Bitsch, B. 2021b, A&A, 654, A72

Schneider, A. D. & Bitsch, B. 2022, How drifting and evaporating pebbles shape giant planets (Corrigendum), Astronomy & Astrophysics, Volume 659, id.C3, 3 pp.

Schneider, A. D., Carone, L., Decin, L., Jørgensen, U. G., & Helling, C. 2022a, A&A, 666, L11

Schneider, A. D., Carone, L., Decin, L., et al. 2022b, A&A, 664, A56

Schneider, A. D., Dullemond, C. P., & Bitsch, B. 2018, A&A, 617, L7

Schneider, A. D., Mollière, P., Louppe, G., et al. 2024, A&A, 682, A79

Schulik, M., Johansen, A., Bitsch, B., & Lega, E. 2019, A&A, 632, A118

Seager, S. 2010, Exoplanet Atmospheres: Physical Processes

Seager, S. & Sasselov, D. D. 2000, ApJ, 537, 916

Seidel, J. V., Ehrenreich, D., Pino, L., et al. 2020, A&A, 633, A86

Seidel, J. V., Ehrenreich, D., Wyttenbach, A., et al. 2019, A&A, 623, A166

Semenov, D., Hersant, F., Wakelam, V., et al. 2010, A&A, 522, A42

Sergeev, D. E., Lambert, F. H., Mayne, N. J., et al. 2020, ApJ, 894, 84

Sestovic, M., Demory, B.-O., & Queloz, D. 2018, A&A, 616, A76

Shakura, N. I. & Sunyaev, R. A. 1973, A&A, 24, 337

Shapiro, R. 1970, Reviews of Geophysics and Space Physics, 8, 359

Shibata, S., Helled, R., & Ikoma, M. 2020, A&A, 633, A33

Shibata, S. & Ikoma, M. 2019, MNRAS, 487, 4510

Showman, A. P., Cooper, C. S., Fortney, J. J., & Marley, M. S. 2008, ApJ, 682, 559

Showman, A. P., Fortney, J. J., Lian, Y., et al. 2009, ApJ, 699, 564

Showman, A. P. & Guillot, T. 2002, A&A, 385, 166

Showman, A. P. & Kaspi, Y. 2013, ApJ, 776, 85

Showman, A. P., Lewis, N. K., & Fortney, J. J. 2015, ApJ, 801, 95

Showman, A. P. & Polvani, L. M. 2011, ApJ, 738, 71

Showman, A. P., Tan, X., & Parmentier, V. 2020, Space Sci. Rev., 216, 139

Sing, D. K. 2018, arXiv e-prints, arXiv:1804.07357

Sing, D. K., Fortney, J. J., Nikolov, N., et al. 2016, Nature, 529, 59

Sing, D. K., Lavvas, P., Ballester, G. E., et al. 2019, AJ, 158, 91

Skartlien, R., Stein, R. F., & Nordlund, Å. 2000, ApJ, 541, 468

Skinner, J. W. & Cho, J. Y. K. 2021, MNRAS, 504, 5172

Snellen, I., de Kok, R., Birkby, J. L., et al. 2015, A&A, 576, A59

Snellen, I. A. G., de Kok, R. J., de Mooij, E. J. W., & Albrecht, S. 2010, Nature, 465, 1049

Socrates, A. 2013, arXiv e-prints, arXiv:1304.4121

Sotiriadis, S., Libert, A.-S., Bitsch, B., & Crida, A. 2017, A&A, 598, A70

Sousa-Silva, C., Al-Refaie, A. F., Tennyson, J., & Yurchenko, S. N. 2015, MNRAS, 446, 2337

Southworth, J. 2008, MNRAS, 386, 1644

Southworth, J. 2010, MNRAS, 408, 1689

Spiegel, D. S., Burrows, A., & Milsom, J. A. 2011, ApJ, 727, 57

Stammler, S. M., Birnstiel, T., Panić, O., Dullemond, C. P., & Dominik, C. 2017, A&A, 600, A140

Steinrueck, M. E., Showman, A. P., Lavvas, P., et al. 2021, MNRAS, 504, 2783

Stevenson, K. B., Désert, J.-M., Line, M. R., et al. 2014, Science, 346, 838

Stevenson, K. B., Line, M. R., Bean, J. L., et al. 2017, AJ, 153, 68

Struve, O. 1952, The Observatory, 72, 199

Sudarsky, D., Burrows, A., & Hubeny, I. 2003, ApJ, 588, 1121

Szulágyi, J., Binkert, F., & Surville, C. 2022, ApJ, 924, 1

Szulágyi, J., Masset, F., Lega, E., et al. 2016, MNRAS, 460, 2853

Takeuchi, T. & Lin, D. N. C. 2002, ApJ, 581, 1344

Tan, X. & Komacek, T. D. 2019, ApJ, 886, 26

Tanaka, H. & Ida, S. 1999, Icarus, 139, 350

Tennyson, J., Yurchenko, S. N., Al-Refaie, A. F., et al. 2016, Journal of Molecular Spectroscopy, 327, 73

Thiabaud, A., Marboeuf, U., Alibert, Y., et al. 2014, A&A, 562, A27

Thiabaud, A., Marboeuf, U., Alibert, Y., Leya, I., & Mezger, K. 2015a, A&A, 580, A30

Thiabaud, A., Marboeuf, U., Alibert, Y., Leya, I., & Mezger, K. 2015b, A&A, 574, A138

Thorngren, D. & Fortney, J. J. 2019, ApJ, 874, L31

Thorngren, D., Gao, P., & Fortney, J. J. 2019, ApJ, 884, L6

Thorngren, D. P. & Fortney, J. J. 2018, AJ, 155, 214

Thorngren, D. P., Fortney, J. J., Murray-Clay, R. A., & Lopez, E. D. 2016, ApJ, 831, 64

Tremblin, P., Amundsen, D. S., Mourier, P., et al. 2015, ApJ, 804, L17

Tremblin, P., Chabrier, G., Mayne, N. J., et al. 2017, ApJ, 841, 30

Tremblin, P., Padioleau, T., Phillips, M. W., et al. 2019, ApJ, 876, 144

Turner, N. J., Fromang, S., Gammie, C., et al. 2014, in Protostars and Planets VI, ed. H. Beuther, R. S. Klessen, C. P. Dullemond, & T. Henning, 411–432

Turrini, D., Schisano, E., Fonte, S., et al. 2021, ApJ, 909, 40

Valletta, C. & Helled, R. 2020, ApJ, 900, 133

Vallis, G. K. 2017, Atmospheric and Oceanic Fluid Dynamics: Fundamentals and Large-Scale Circulation

Van Eylen, V., Agentoft, C., Lundkvist, M. S., et al. 2018, MNRAS, 479, 4786

van 't Hoff, M. L. R., Bergin, E. A., Jørgensen, J. K., & Blake, G. A. 2020, ApJ, 897, L38

Vazan, A., Helled, R., & Guillot, T. 2018, A&A, 610, L14

Venot, O., Parmentier, V., Blecic, J., et al. 2020, ApJ, 890, 176

Venturini, J., Alibert, Y., & Benz, W. 2016, A&A, 596, A90

Venturini, J., Alibert, Y., Benz, W., & Ikoma, M. 2015, A&A, 576, A114

Venturini, J., Guilera, O. M., Ronco, M. P., & Mordasini, C. 2020, A&A, 644, A174

Venturini, J. & Helled, R. 2020, A&A, 634, A31

Voelkel, O., Deienno, R., Kretke, K., & Klahr, H. 2021a, A&A, 645, A131

Voelkel, O., Deienno, R., Kretke, K., & Klahr, H. 2021b, A&A, 645, A132

Voelkel, O., Klahr, H., Mordasini, C., & Emsenhuber, A. 2022, A&A, 666, A90

Voelkel, O., Klahr, H., Mordasini, C., Emsenhuber, A., & Lenz, C. 2020, A&A, 642, A75

Wahl, S. M., Hubbard, W. B., Militzer, B., et al. 2017, Geophys. Res. Lett., 44, 4649

Wakeford, H. R., Sing, D. K., Deming, D., et al. 2018, AJ, 155, 29

Walsh, K. J., Morbidelli, A., Raymond, S. N., O'Brien, D. P., & Mandell, A. M. 2011, Nature, 475, 206

Wang, H., Weiss, B. P., Bai, X.-N., et al. 2017, Science, 355, 623

Wang, H. & Wordsworth, R. 2020, ApJ, 891, 7

Wardenier, J. P., Parmentier, V., Lee, E. K. H., Line, M. R., & Gharib-Nezhad, E. 2021, MNRAS, 506, 1258

Wardenier, J. P., Parmentier, V., Line, M. R., & Lee, E. K. H. 2023, MNRAS, 525, 4942

Webb, R. K., Gandhi, S., Brogi, M., et al. 2022, MNRAS, 514, 4160

Weber, P., Benítez-Llambay, P., Gressel, O., Krapp, L., & Pessah, M. E. 2018, ApJ, 854, 153

Weidenschilling, S. J. 1977, MNRAS, 180, 57

Welbanks, L., Madhusudhan, N., Allard, N. F., et al. 2019, ApJ, 887, L20

Wende, S., Reiners, A., Seifahrt, A., & Bernath, P. F. 2010, A&A, 523, A58

West, R. G., Hellier, C., Almenara, J. M., et al. 2016, A&A, 585, A126

Woitke, P. & Helling, C. 2003, A&A, 399, 297

Woitke, P., Helling, C., Hunter, G. H., et al. 2018, A&A, 614, A1

Woitke, P. & Niccolini, G. 2005, A&A, 433, 1101

Wolszczan, A. & Frail, D. A. 1992, Nature, 355, 145

Youdin, A. N. & Mitchell, J. L. 2010, ApJ, 721, 1113

Yurchenko, S. N., Amundsen, D. S., Tennyson, J., & Waldmann, I. P. 2017, A&A, 605, A95

Yurchenko, S. N., Mellor, T. M., Freedman, R. S., & Tennyson, J. 2020, MNRAS, 496, 5282

Zakhozhay, O. V., Launhardt, R., Trifonov, T., et al. 2022, A&A, 667, L14

Zhang, K., Bosman, A. D., & Bergin, E. A. 2020, ApJ, 891, L16

Zhang, S., Zhu, Z., Huang, J., et al. 2018, ApJ, 869, L47

Zhang, X. 2020, Research in Astronomy and Astrophysics, 20, 099